Unsteady Cavitation in Separating and Re-attaching Shear Flows

by

Anubhav Bhatt

A dissertation submitted in partial fulfillment
of the requirements for the degree of
Doctor of Philosophy
(Mechanical Engineering)
in the University of Michigan
2021

Doctoral Committee :

Professor S. L. Ceccio, Chair
Assistant Research Scientist Harish Ganesh, Co-chair
Assistant Professor Jesse Capecelatro
Professor David R. Dowling
Associate Professor Eric Johnsen
Professor Yin Lu Young

Anubhav Bhatt

anubhavb@umich.edu

ORCID ID : 0000-0002-6287-8156

©Anubhav Bhatt 2021

Dedication

I dedicate this work to loving memory of my grandfather Mr K.D. Bhatt. May your soul rest in peace. Without his endless support and encouragement through all these years none of this would have been possible. Hopefully I can make you proud one day.

Acknowledgments

This thesis work was supported by Office of Naval Research under stewardship of program officer Dr. Ki-Han Kim and guidance of Dr. Steven L. Ceccio(PI) as part of Multidisciplinary University Research Initiative (MURI, Grant N00014-17-1-2676) titled 'MURI: Predicting Turbulent Multi-Phase Flows with High Fidelity - A Physics-Based Approach'. The MURI is a collaborative effort to model turbulent cavitating flows over different scales with contributions from researchers at U. Minnesota, Caltech, UC Santa Barbara, U. Iowa, U. Michigan, MIT, Johns Hopkins and Australian Maritime College.

Thank you Prof. Steven L. Ceccio, my research advisor for providing this unique opportunity to perform fundamental cavitation research as part of your esteemed research group. Thank you for your patience and guidance throughout my graduate curriculum, especially through a tough 2020. I have gained invaluable insight into the world of fluid dynamics, experimental research methodology and interpersonal skills. I cannot thank you enough for being my research advisor always helping me in and out of lab.

I would also like to thank my doctoral committee members Prof. David Dowling, Prof. Julie Young, Associate Prof. Eric Johnsen and Assistant Prof. Jesse Capecelatro for graciously agreeing to be on my committee. Thank you for your patience, invaluable inputs and encouragement throughout the evolution of this thesis work.

Special thanks to Dr. Harish Ganesh, my research co-advisor for his endless support and guidance throughout these years. Thank you for going out of your way to guide me not only through the research work but also personal life. I greatly appreciate all your inputs that have helped me grow as a researcher and as a person. Without your constant words of encouragement this dissertation work would not have been possible.

My colleagues at lab, both current and in the past deserve a special mention. Thank you Dr. Juliana Wu, Dr. Joel Hartenberger, Dr. Seongjin Yoon, Kevin Xu, Daniel Knister, Nicholas Lucido and Elizabeth Callison for all your help and support during my tenure as a Ph.D. student in the research group. Thank you Lisa Deijlen (visiting from TU Delft, Wake cavitation project), Guy Laignelot and Pierre-Edouard Bertin (visiting students from French Naval Academy, Pitching foil project) for collaborating with me during your stay.

I would like to thank everyone that helped me with administrative and logistical needs as a graduate student. Thank you Kent Pruss for his time and patience in making the fabrication of models a breeze and managing technical issues with the water tunnel easier. Coleen Root, Martha Sweigert, Karen Brown, Lisa Kisabeth, Nicole Cheesman and Adam Mael have my gratitude in helping me navigate the administrative process as a graduate student.

Thank you to the people I met at 2010AL that helped me socialize during and after the work hours. I am thankful for the company of Brian Worthmann, Tyler Flynn, Alex Douglass, Brandon Patterson, Brandon Lee and David Geroski that made pre-covid workdays entertaining and welcoming. Thank you to current and previous members of ME Graduate Council for providing me with an opportunity to engage with ME community outside the regular curriculum. Also, thank you to the volunteers at Humane Society of Huron Valley for welcoming me to the shelter and giving me exposure to adorable animals each week.

I cannot thank my parents enough for their emotional and financial support for everything I have done thus far. Thank you ma, papa and Aditi for always being there through ups and

downs in my life and helping me get past 2020. I would not have pursued what I wanted with confidence and reached this far in my academic career without you all. Also, thank you Buddy for existing and motivating me each day.

Table of Contents

Dedication ii

Acknowledgments iii

List of Figures xi

List of Tables xxix

List of Appendices xxxi

Abstract xxxii

1 Introduction 2

1.1 Background 2

1.2 Cavitation Inception 3

1.3 Partial/Cloud Cavitation 3

1.4 Compressibility of bubbly mixtures 5

1.4.1 Speed of sound in bubbly mixtures 5

1.4.2 Shock waves in bubbly flows 10

1.5 Current Study 11

1.5.1 Contributions of backward facing step study 13

1.5.2 Contributions of NACA0015 hydrofoil study 13

2 Experimental Setup **15**

2.1 Flow loop 15

2.2 Backward Facing Step 16

2.2.1 Particle Image Velocimetry (PIV) 18

2.3 NACA0015 Hydrofoil 19

2.4 High-speed cinematography system 22

2.5 X-ray Densitometry System 23

3 Backward Facing Step Background **25**

3.1 Single-phase flow properties 25

3.2 Cavitating Shear Layers 28

3.3 Effect of vapor-liquid compressibility 30

3.4 Road map 31

4 Backward Facing Step : Experimental Results **33**

4.1 2-D planar PIV 33

4.2 Visual Observation of Cavitation 35

4.2.1 A Typical Shedding Cycle 36

4.3 Void Fraction Measurements 37

4.3.1 Average Cavity Length 37

4.3.2 Mean void fraction profiles 39

4.3.3 Instantaneous Void Fraction fields 39

4.4 Cavity Shedding Dynamics 44

4.5 Cavity Static Pressure 45

5 Backward Facing Step : Analysis **49**

5.1 Bubbly Shock Properties 49

5.1.1 Synchronized pressure and void fraction measurements 51
5.1.2 Shock properties from void fraction fields 51
5.1.3 Validity of 1-D jump relations 52
5.2 Speed of sound 52
5.2.1 Speed of sound estimation 53
5.2.2 Mach number based on step velocity u_H 54

6 Conclusions of Backward Facing Step Study **57**

7 NACA0015 Hydrofoil : Background **59**
7.1 Overview 59
7.1.1 Re-entrant liquid flows 60
7.1.2 Bubbly shocks 60
7.2 Current Study 64
7.3 Roadmap 66

8 NACA0015 Hydrofoil : Experimental Results **68**
8.1 Cavity Length 68
8.2 Visual Observation of Cavitation 69
8.2.1 Type(i) cavities 72
8.2.2 Type(ii) & (iii) cavities 72
8.3 Type(iv) shedding regime: effect of trailing edge cavitation 73
8.4 X-ray densitometry based void fraction measurements 76
8.4.1 Type(i) cavity: Oscillatory Cavity 76
8.4.2 Type(ii) shedding cavity: Shedding driven equally by re-entrant flows and bubbly shocks 78

8.4.3 Type(iii) shedding cavity: Cavity shedding mostly driven by shocks and occasionally by re-entrant flows 80
8.4.4 Type(iv) shedding cavity: trailing edge cavitation 86
8.5 Review of flow features observed 92

9 Spectral Content in Cavity Dynamics Data of NACA0015 Hydrofoil 98
9.1 Power spectral density 98
9.2 Time-frequency analysis 102
9.3 Spectral POD to identify the shedding modes 105
9.3.1 Methodology 105
9.3.2 SPOD of void fraction fields 108
9.3.3 Type(ii) cavity shedding modes 108
9.3.4 Type(iii) cavity shedding modes 109
9.3.5 Type(iv) cavity shedding modes 109

10 NACA0015 Hydrofoil : Analysis 113
10.1 Bubbly shock properties 113
10.1.1 Comparison with Wu (2019) 114
10.2 Event probability of re-entrant flow/shockwaves to cause cavity pinch-off . . 114
10.3 Probability and Mach number relationship 118
10.3.1 Cavity pressure 118
10.3.2 Mach number within the cavity 118
10.3.3 Mach number and event probability relationship 120

11 Conclusions of NACA0015 study 121

A Charge Amplifier Circuit for Dynamic Pressure Measurement 123
A.1 Calibration circuit 125

B Single Phase Flow Measurements on Backward Facing Step **128**

C Mean and RMSD Void Fraction Profiles for Backward Facing Step **129**

D Estimated Speed of Sound for Backward Facing Step **132**

E Measurement of Bubble Size Distribution Downstream of NACA0015 Hydrofoil **137**

E.1 Post-processing 139

F Mean and RMSD β Values for NACA0015 Hydrofoil **141**

G Spectral Content in Cavitating NACA0015 Hydrofoil **144**

G.1 Waterfall Plots for Pressure (dp_1, dp_2) and Void Fraction (β_{LE}, β_{TE}) Signals 144

G.2 Multiple Peaks in type (iii) and (iv) cavities 148

G.3 Hydrophone signal for type(iv) cavities 150

Bibliography **153**

List of Figures

1.1 Inception in turbulent shear layer occurs in stream-wise vortices (braids) rather than stronger spanwise vortices (rollers) as shown by Iyer and Ceccio (2002). Pressure drop due to the stretching of the weaker braids by the stronger rollers is hypothesized as the reason for observation of inception in the weaker stream-wise rollers. The flow is from left to right. 3

1.2 Schematic depicting re-entrant liquid flow at cavity closure. Flow is from left to right. 4

1.3 A propagating bubbly shock moving towards the apex of the wedge reported by Ganesh et al. (2016). Flow is from left to right. 5

1.4 Plot depicting variation in speed of sound in a bubbly air-water mixture at atmospheric pressure with mixture volume fraction summarized by Brennen (2005). The experimental data is plotted against the analytical expressions under adiabatic and isothermal phase change assumptions respectively. . . . 6

1.5 Plot depicting changes in the two-phase mixture before ($t = 0$) and after ($t = 0^+$) the passage of a pressure wave. The change in continuous phase(A) and dispersed phase(B) leads to change in total volume of the mixture (∂V). The change in volume is used to obtain the sonic speed expression shown in equation 1.6 7

1.6 Speed of sound in water with bubbles estimated using Crespo's expressions (b,c) (Crespo (1969)) plotted against findings of Campbell and Pitcher($\triangle$) . 10

1.7 Schematic depicting pre- and post shock propagation properties in the vapor-liquid mixture. When the shock propagates into stationary vapor-liquid mixture, $u_2 = u_s$ 11

2.1 Schematic of the flow loop depicting Michigan 9" water tunnel testing facility 16

2.2 Schematic of the backward facing step mounted in the water tunnel. Top and side field of view configurations for the high speed videography are shown. For x-ray densitometry a 115 mm by 28 mm view similar to the highlighted side view is chosen (see figure 4.5) 17

2.3 Schematic of the backward facing step mounted in the water tunnel depicting the location of pressure ports in the test section and corresponding pressure tap. $f(x) \approx 2.5{\cdot}10^{-9}x^5 - 7.95{\cdot}10^{-7}x^4 + 6.5{\cdot}10^{-5}x^3$, $0 < x < L_2$ and $f(x) \approx H$, $L_2 < x < L_3$ (Coefficients of $f(x)$ are truncated here for brevity. All dimensions are in mm). $L = 46.08(L_1) + 122.89(L_2) + 30.72(L_3) + 3.11$. Between 0 & 1 (Static) : $(L, (h - H)/2$; Between 0 & 2 (Static): $(L + 1.5H, h/2)$; Between 0 & 3 (Static) : $(L + 8H, h/2)$; Between 0 & 4 (Static) : $(608mm, 0)$; Between 0 & Dynamic Pressure Transducer (Φ 5.54 mm) : $L_{dp} = L + 3H$ 18

2.4 The field-of-view used for boundary layer thickness measurements near the separation point. The velocity profile in 14 mm x 7.5 mm FOV is also shown for set tunnel velocity (u_H) of 10.9 m/s. Flow from right to left. 20

2.5 The two field of views used for the single phase flow measurements. X_R is the re-attachment point. Flow from right to left. 20

2.6 Schematic of hydrofoil mounted in the tunnel. Top and side view used for high speed videography are shown. For void-fraction flow field 135 mm by 85 mm field of view covering roughly 80 % of the chord is used. 21

2.7 Schematic of the x-ray densitometry system depicting source, test section and the imager. A water phantom is used to set/calibrate the range of void fraction values to be investigated. The imager screen has settling time of 1 ms. . . . 24

3.1 Topology of the non-cavitating flow behind a backward facing step. 26

3.2 Re-attachment lengths of different experiments across different expansion ratios show that reattachment length lies between 5 to 8H (Eaton and Johnston (1981)). 27

3.3 Mean flow distribution presented by Scarano et al. (1999) showing location of shear layer and flow reversal inside recirculation zone behind a backward facing step. The velocity profile is depicted over normalized spanwise vorticity distribution. Flow is from left to right. 27

3.4 General behavior of typical reattaching flow and the distortion region near re-attachment seen by Bradshaw and Wong (1972). Flow is from left to right. 28

3.5 Top and side view photographs of shear-layer cavitation inception at u=7.81 m/s, σ =1.52, Re = 1.42x10^6 (O'hern (1990)). Flow is from right to left. . . 29

3.6 Snapshot of instantaneous void fraction(%) flow regime formed in the cavitating shear layer downstream of a sharp separation(Aeschlimann et al. (2011)). Flow is from right to left. 30

4.1 Depiction of process of measuring (a) Boundary layer thickness (b) Collapse of u^+ and y^+ for three flow speeds used for comparison with JHU 34

4.2 Cavitation inception in the streamwise direction is highlighted (streamwise 'braids' , Katz and O'hern (1986)). Intermittent cavitation occurs at $\sigma_0 = 0.98$ for $u_H = 10$ m/s. The red lines highlight the edge of the step. 35

4.3 High speed snapshots of three different cavitation regimes (a, b, c for σ_0=0.78, 0.72, 0.60 respectively) at u_H = 10 m/s. Type A comprises of cavitation in shear layer mostly near reattachment region(away from separation point). Types B and C shedding regimes are of primary interest in this study. 36

4.4 The time-series of high speed snapshots of a periodic Type B shedding cycle. Case at σ_0 = 0.72 for u_H = 10 m/s. Cycle starts with visible cavitation in spanwise vortex(b). The recirculation bubble and shear layer continue to fill with vapor (e)-(g), until an adverse flow front (i) causes the cavity to disappear(shed cavity in (k)). 38

4.5 The mean void fraction fields (snapshots) of the three cavitation regimes (a, b, c for σ_0=0.78, 0.72, 0.60 respectively) at u_H = 10 m/s. The mean length of cavity $< L_C > /H$ and distance to maximum void fraction value (in the mean field, $< L_M > /H$ are shown. The actual densitometry data captures entire 0-100 % void fraction scale, but color scale artificially limited to 0-2% for Type A and 0-25% for the rest. 39

4.6 Mean cavity length($< L_c >$) and location of maximum void fraction($< L_M >$) for $u_H = 8m/s$(■,□), $10m/s$(▲,△), $12m/s$(○,●) for different σ_0. Closed symbols are for $< L_c >$ and open symbols for $< L_M >$. 40

4.7 Mean void fraction contours at u_H = (a) 8 m/s, (b) 10 m/s and (c) 12 m/s at σ_0 = 0.72. 5 slices at X/H = -1, -3, -4, -5, -7 are taken to compare void fraction values across the three velocities shown in Figures 4.8,C.1, C.2. Flow is from left to right. 40

4.8 Mean void fraction values (2% uncertainty) along slices Y/H = -1 to 1.5; $u_H = 8m/s$(□), 10 m/s (△) and $12m/s$(○) at $\sigma_0 = 0.72$ (Type B). The mean void fraction values are comparable across three Re. 41

4.9 X-ray timeseries of a typical Type B shedding cycle at σ_0=0.72 for u_H = 10 m/s. The void fraction ($\beta(X,Y,t)$) range is set to 0-70%. The adverse flow front highlighted in (h) is the bubbly shock front. 42

4.10 X-ray timeseries of a typical Type C shedding cycle at σ_0 = 0.60 for u_H = 10 m/s . The void fraction ($\beta(X,Y,t)$) range is set to 0-85%. Compared to type B, type C cavities are longer, have higher vapor content and collapse at a slower rate. High speed snapshots of type C appear quasi steady, unlike the x-ray timeseries which clearly show shedding. 43

4.11 Dynamic pressure signal(a,$\cdots$) synchronized with time varying void fraction signal (b,$-$) and corresponding power spectral density(c) for a type B cavitating case at σ_0 = 0.73 at u_H = 10 m/s. The highest energy peaks are close. 44

4.12 Dynamic pressure signal(a,$\cdots$) synchronized with time varying void fraction signal(b,$-$) and corresponding power spectral density for a Type C cavitating case at σ_0 = 0.59 at u_H = 10 m/s. Compared to Type B, a lower shedding frequency and lower pressures dp can bee observed. 46

4.13 The change in shedding frequency (St) with decreasing σ_0. u_H = 8 m/s (□■), 10 m/s (△▲) and 12m/s (○●). The St obtained through the void fraction signals(β) are shown in filled symbols, while open symbols depict St from dp signal. 46

4.14 The values of $-Cp_1$ (filled, ■▲●) and $-Cp_2$ (open, □△○) as σ_0 is reduced across three Re; u_H = 8 m/s (□■), 10 m/s (△▲) and 12m/s (○●). Magnitude of Cp_2 is higher than Cp_1 for all three Re indicating that behind the step, the pressure drops between pressure taps at location 1 and 2. 47

4.15 σ_c with decreasing σ_0 (Closer look at -Cp_1). $u_H = 8m/s$(■), $10m/s$(▲), $12m/s$(●). At lower cavitation numbers, pressure inside the cavity approaches vapor pressure. 47

4.16 The values of $-Cp_3$ (■▲●) and $-Cp_4$ (□△○) as σ_0 is dropped across three Re; $u_H = 8m/s$(□■), $10m/s$(△▲) and $12m/s$(○●) 48

5.1 The differential pressure (dp) and corresponding X-ray densitometry snapshots as the shock-front moves past the transducer and hits the step during a shedding cycle. σ_0=0.72 for u_H = 10 m/s. 50

5.2 X-T diagram at Y/H = -0.25; σ_0=0.72 for u_H = 10 m/s. The shock propagation is assumed to be linear and inverse of the slope of X-T diagram gives shockspeed. 51

5.3 Comparison of computed shock-speed, U_{RH}(□) and shock-speed estimated from X-T diagrams, U_S(○) for varying σ_0 shows a good agreement between U_S and U_{RH}. 52

5.4 M_i estimated using the 'homogeneous equilibrium model' (★♦ ►) and 'homogeneous frozen model' (☆ ◊ ▷) for speed of sound; M_1 (★☆) M_2 (♦◊) & M_3 (► ▷). $u_H = 10m/s$. (–) depicts $M_H = 1$ and indicates when the flow becomes supersonic 56

5.5 The variation of M_{Hi} with decreasing σ_0 across three different Re estimated using 'homogeneous frozen model'; $u_H = 8m/s$ (□□□), $10m/s$ (△△△) & $12m/s$ (○ ○ ○); M_{H1} (□△○), M_{H2} (□△○) & M_{H3} (□△○). (–) depicts $M_H = 1$. 56

7.1 Cavitation map for different cavitation regimes over a plano-convex foil depicting main cavity patterns. l/c and e/c are maximum cavity length and maximum cavity thickness non-dimensionalized by chord length respectively. The unsteady regime is highlighted as periodic zone where partial cavitation occurs (Le et al. (1993)). The flow direction is from left to right for each schematic. 61

7.2 Periodic shedding mechanism caused by re-entrant flow at cavity closure for thick cavities(Le et al. (1993)). Time period of a shedding cycle is T. Flow is from right to left. 62

7.3 Cavitation map for different cavitation regimes over a NACA0015 hydrofoil presented by Kjeldsen et al. (2000).The lines l/c=constant are obtained from a linear fit to the cavity length data shown in figure 7.4. 63

7.4 Classical cavity length versus cavitation parameter ($\sigma/2\alpha$) plot against thin flat plate theory suggested by Watanabe (1998) shows how cavity length scales with cavitation number. 64

7.5 JTFA of suction side pressure transducer at $\alpha = 7°$. Similar observation in lift fluctuation spectral content is reported by Kjeldsen et al. (2000). 65

7.6 Shock induced shedding of partial cavities on a NACA0015 hydrofoil from Wu et al. (2019) 65

7.7 Acoustic pressure signal showcasing a transition from Style 1 cavitation (low frequency) to Style 2 (high frequency) with corresponding void fraction measurements for each cycle reported by Barwey et al. (2020). Flow is from right to left. 66

8.1 Definition of cavity length on (a) High speed snapshot of maximum cavity length (b) X-ray densitometry snapshot of maximum cavity length. 69

8.2 Comparison of Lc/C for current model from maximum cavity length measurements at two angle of attack ($\alpha = 10^\circ$ ($\square$(HS), $\blacktriangleright$ (XR)) and $\alpha = 7^\circ(\circ)$) where cavitation parameter ($\sigma_c/2\alpha$) has been corrected for blockage. Cavities formed over the hydrofoil model used in current study(filled symbols) are compared with those observed by Wu (2019) (open symbols). Also the cavity length reported by Obernach ($\dagger$) and Arndt($\lozenge$) are included to show good agreement in cavity lengths reported in the current study. Obernach NACA0015 hydrofoil: 0.128 m C, 0.3 m by 0.3 m test section, aspect ratio (AR) = 2.35, $Re = 1.02 \cdot 10^6$ and $\alpha = 8^\circ$; Arndt NACA0015 hydrofoil : 0.081 m C, 0.19 m by 0.19 m test section, AR = 3 and $\alpha = 7^\circ$. Outside the steady sheet cavity regime, four types of cavitating regimes a marked to show different cavity dynamics observed. These flow regimes are discussed in detail later in section 8.5. The maximum uncertainty in measurement of $\sigma_0 = \pm$ 0.07 and $Lc/C = \pm$ 0.1 70

8.3 Top view snapshot of incipient cavity patches at high cavitation numbers for the NACA0015 hydrofoil; Flow from top to bottom $\alpha = 10^\circ$ and $\sigma_0/2\alpha = 10.8$; $u_0 = 8\ m/s$. 71

8.4 Successive frames from a high-speed video of a type(i) cavity shedding over the foil at $\sigma_0 = 3.2(\sigma_0/2\alpha = 9.18)$. The arrows track the flow-front trapped underneath the cavity, moving from the cavity closure all the way to the leading edge. 72

8.5 Successive frames from a high-speed video of both re-entrant flow and shock-wave driven shedding over the foil for a type(ii) cavity at $\sigma_0 = 2.6$ ($\sigma_0/2\alpha = 7.6$). Despite visualization of flow fronts in the high-speed video, it is not possible to identify a flow front as a shock or liquid re-entrant flow with certainty. 74

8.6 Time-series depiction of one flow front (orange arrows) co-existing with the other (red arrows). The high speed video snapshots do not confirm the presence of either of the flow fronts and the arrows are only for illustration. $\sigma_0 = 1.91(\sigma_0/2\alpha = 5.5)$ 75

8.7 Timeseries of high speed snapshots for a type (iv) cavity highlighting the collapse of the shed vapor cloud downstream of the hydrofoil as a primary initiator for cavity collapse. (a) Acoustic pressure from the hydrophone (p_a) with points before and after cloud collapse (b) Corresponding side view snapshots showing cloud collapse (c) Corresponding top view snapshots depicting cavity collapse process. $\sigma_0 = 1.5(\sigma_0/2\alpha = 4.3)$ 77

8.8 Mean void fraction field of a stable cavity with nearly constant cavity length at $\sigma_0 = 3.6$ ($\sigma_0/2\alpha = 10.3$). Flow is always from right to left for void fraction fields. The void fraction value (β) ranges from 0-0.924. 78

8.9 Time series of void fraction flow fields for a type(i) shedding cavity. The cavity oscillates periodically. The void fraction fields are shown very close to the surface of the foil to highlight the difficulty in resolving flow-fronts that cause cavity pinch-off. The thin cavities restrict the ability to observe any flow front trapped underneath the main cavity. $\sigma_0 = 3.15$ ($\sigma_0/2\alpha = 9.04$), $\beta = 0 - 0.7$. 79

8.10 Time series depicting the type(ii) shedding cycle where re-entrant liquid jet causes cavity pinch-off. $\sigma_0 = 2.65$ ($\sigma_0/2\alpha = 7.6$), $\beta = 0 - 0.924$. 81

8.11 Time series showing shockwave driven cavity-pinch-off during the shedding cycle of a type(ii) cavity. $\sigma_0 = 2.65$ ($\sigma_0/2\alpha = 7.6$), $\beta = 0 - 0.924$. 82

8.12 Unsteady surface pressure signal near leading edge (dp_1) for type(ii) shedding cavity; $\sigma_0 = 2.65$ ($\sigma_0/2\alpha = 7.6$), $\beta = 0 - 0.924$. 83

8.13 Time resolved void fraction time-series of cavitation shedding cycle for a type(iii) cavity. From (4) to (7) trapped re-entrant flow front is unable to cause pinch-off. (5)-(7) shows the advancing shockwave front dominating to cause pinch-off; $\sigma_0 = 1.91$ ($\sigma_0/2\alpha = 5.5$), $\beta = \ 0 - 0.924$ 84

8.14 Synchronized unsteady surface pressure measurements through dp_1 and dp_2 are presented for cavitation shedding cycle for a type(iii) cavity. Ten snapshots presented on timeseries in figure 8.13 are marked on the dynamic pressure signals. From (4) to (7) trapped re-entrant flow front does not significantly affect the unsteady surface pressure at dp_1. 14.6 kPa pressure rise occurs due to the shockwave front passing over dp_1 between (7)-(8) in (a). Similarly a 5.9 kPa pressure rise over dp_2 occurs between (5)-(6) in (b). $\sigma_0 = 1.91$ ($\sigma_0/2\alpha = 5.5$), $\beta = \ 0 - 0.924$ 85

8.15 Timeseries of void fraction field depicting the re-entrant flow causing cavity pinch-off near leading edge (LE) of the hydrofoil for a type(iii) cavity. Liquid re-entrant flow is still able to cause cavity shedding. $\sigma_0 = 1.91$ ($\sigma_0/2\alpha = 5.5$) , $\beta = \ 0 - 0.924$. 87

8.16 Void fraction time-series for cavitation shedding cycle for a type(iv) cavity. $\sigma_0 = 1.4$ ($\sigma_0/2\alpha = 4.1$), $\beta = \ 0 - 0.924$ 89

8.17 Timeseries of void fraction field depicting the re-entrant flow causing cavity pinch-off near leading edge (LE) for a type(iv) cavity. Although shockwaves are dominant mechanism of shedding, liquid re-entrant flow is still able to cause cavity shedding. $\sigma_0 = 1.4$ ($\sigma_0/2\alpha = 4.1$) , $\beta = \ 0 - 0.924$. 90

8.18 Synchronized unsteady pressure measurements through dp_1 and dp_2 are presented for cavitation shedding cycle for a type(iv) cavity. $\sigma_0 = 1.4$ ($\sigma_0/2\alpha = 4.1$), $\beta = \ 0 - 0.924$. The pressure fluctuation recorded between (4)-(5) for both (a) and (b) is similar to the pressure fluctuation in dp_1 and dp_2 seen in figure **??** near (1) where collapse of the vapor cloud is recorded in the hydrophone signal (p_a) 91

8.19 Depiction of trailing edge cavitation on the hydrofoil in type(iv) shedding regime. FOV has been moved downstream. Shedding cycle similar to the bluff body shedding cavitation is seen in (3)-(8); $\sigma_0 = 1.4$ ($\sigma_0/2\alpha = 4.1$) , $\beta = \ 0 - 0.924$. 93

8.20 Synchronized unsteady pressure measurements through dp_1, dp_2 and acoustic pressure measured through a top wall mounted hydrophone (p_a) for trailing edge cavitation seen on the hydrofoil in type(iv) shedding regime. $\sigma_0 = 1.4$ ($\sigma_0/2\alpha = 4.1$) , $\beta = \ 0 - 0.924$. 94

8.21 Schematic depicting different flow fronts governing cavity pinch-off (i) Re-entrant jet driven (ii) Re-entrant jet + Shockwave driven (iii) Shockwave driven but unaffected by TE cavitation (iv) Shockwave driven but TE cavitation actively interacts with the main cavity to cause a shear-layer shedding phenomenon identical to shedding in wake of bluff bodies 95

8.22 Comparison of Lc/C for current model from maximum cavity length measurements at two angle of attack ($\alpha = 10°$ (□ (HS), ▶ (XR)) and $\alpha = 7°$(○)) where cavitation parameter ($\sigma_c/2\alpha$) has been corrected for blockage. Cavities formed over the hydrofoil model used in current study (filled symbols) are compared with those observed by Wu (2019) (open symbols). Also the cavity length reported by Obernach (†) and Arndt(◊) are included. Four types of cavitating regimes are marked as type(i)-(iv) where re-entrant flow and shockwaves affect the cavity shedding dynamics. 97

9.1 Schematic showing the location of (a) Dynamic surface pressure measurement locations (dp_1 and dp_2) on suction side of the hydrofoil (b) Space averaged void fraction probe volumes near the leading edge (LE) and trailing edge (TE) of the hydrofoil (β_{LE} andβ_{TE}). The probes are 5 mm by 2.5 mm and located near the unsteady surface pressure transducers (dp_1 and dp_2). 99

9.2 Space averaged void fraction probe volume near the maximum cavity length(β_{Lc}). The probe is 5 mm by 2.5 mm in size, moves with maximum cavity length from mean void fraction field and captures the dynamics at the aft of the cavity. 99

9.3 Raw time signals for each of the surface pressure transducers and void fraction (β) probes for the 0.787 s acquisition period of the densitometry system where (a) dp_1 (b) void fraction probe near the LE ($\beta_{LE}(t)$) (c) dp_2 (b) void fraction probe near the TE ($\beta_{TE}(t)$). The signals are time synchronized which means similar flow features are seen. The signals are presented for a type(iv) shedding cavity at $\sigma_0 = 1.5$ ($\sigma_0/2\alpha = 4.3$), $\alpha = 10°$). Four instances of shockwaves passing over surface pressure transducer are marked as I, II, III and IV where change in density values due to passage of shocks is important. 100

9.4 Power specrtal density curves for the corresponding time signals presented in figure 9.3; As in the previous figure (a) dp_1 (b) void fraction probe near the LE ($\beta_{LE}(t)$) (c) dp_2 (b) void fraction probe near the TE ($\beta_{TE}(t)$). The peak characteristic frequency and uncertainty in the frequency values for those peaks are marked on each curve. The signals are presented for a type(iv) shedding cavity at $\sigma_0 = 1.5$ ($\sigma_0/2\alpha = 4.3$) 101

9.5 Change in shedding frequency with changes in cavitation number shows how close the peak shedding frequencies obtained from void fraction signal are to those from dynamic pressure transducers and the St reported in previous literature. Maximum uncertainty in $\sigma_0 = \pm$ 0.07, $Lc/C = \pm$ 0.1, $St = \pm$ 0.08 103

9.6 Change in shedding frequency with changes in cavitation number for a cavitation probe moving with cavity length (β_{LC}). A good agreement with literature and peaks seen in dp_1 and dp_2 is seen for peak1. Maximum uncertainty in $\sigma_0 = \pm$ 0.07, $Lc/C = \pm$ 0.1, $St = \pm$ 0.08 104

9.7 Spectrograms of type(iii) shedding cavity at $\sigma_0 = 2.1$ ($\sigma_0/2\alpha = 6.2$) are shown in (a) dp_1 (b) dp_2 and for a type(iv) shedding cavity at $\sigma_0 = 1.6$ ($\sigma_0/2\alpha = 4.7$) are shown in (c) dp_1 (d) dp_2. The flow timescale τ is used to non-dimensionalize time. $\tau = \frac{C}{u_0}$, $\alpha = 10°$. The colorbar represents the magnitude of fft of each signal. 106

9.8 Spectrogram from the hydrophone signal for (a) Type(iii) shedding cavity at $\sigma_0 = 2.1$ ($\sigma_0/2\alpha = 6.2$) (b) Type(iv) shedding cavity at $\sigma_0 = 1.6$ ($\sigma_0/2\alpha = 4.7$). $\tau = \frac{C}{u_0}$, $\alpha = 10°$. 107

9.9 Mode energy distribution for first 5 SPOD modes. Energy of mode1 is dominant. Type(ii) cavity at σ_0 =2.6 ($\sigma_0/2\alpha = 7.6$) 108

9.10 Figure highlighting (a) The FOV chosen for SPOD analysis, (b) Waterfall plot showing mode energy distribution at different cavitation parameters $\sigma_0/2\alpha$. 109

9.11 (a) The peaks detected in transducer signals dp_1 and dp_2 along with mode energy distribution at two different resolved frequencies (b)The spatial SPOD modes corresponding to dominant peaks seen in resolved frequency of mode1 along with mean void fraction field for type(ii) cavity. The peaks detected by dp_1 and dp_2 are also shown. σ_0 =2.6 ($\sigma_0/2\alpha = 7.6$) 110

9.12 (a) The peaks detected in transducer signals dp_1 and dp_2 along with mode energy distribution at two different resolved frequencies (b)The spatial SPOD modes corresponding to dominant peaks seen in resolved frequency of mode1 along with mean void fraction field for type(iii) cavity. The peaks detected by dp_1 and dp_2 are also shown. Peak1 corresponds to shedding of the dominant shedding frequency seen in shockwave driven shedding. σ_0 =1.9 ($\sigma_0/2\alpha = 5.5$). 111

9.13 (a) The peaks detected in transducer signals dp_1 and dp_2 along with mode energy distribution at two different resolved frequencies (b) The spatial SPOD modes corresponding to dominant peaks seen in resolved frequency of mode 1 along with mean void fraction field for type(iv) cavity. The peaks detected by dp_1 and dp_2 are also shown. Peak2 resembles a mid-way shedding cavity cycle where flow-front has reached Lc/C=0.4($\sim$). σ_0 =1.5 ($\sigma_0/2\alpha = 4.3$) . . 112

10.1 Variation of ratio of measured pre- and post-shock void fractions β_1(black) and β_2 (red) with inlet cavitation number σ_0 for present study (corrected) (■) and Wu et al. (2019) (►). 115

10.2 Changes in ratio of measured shock speed U_s/U_b with variation of inlet cavitation number σ_0. U_b is the velocity near the leading edge of the foil based on blockage. Current hydrofoil's shock-speeds (■) are compared to the hydrofoil from previous study by Wu et al. (2019) (►). 115

10.3 pressure rise ($p_2 - p_1$), with inlet cavitation number σ_0 for present study (estimated ■, measured □) and Wu et al. (2019) (▶). Pressure rise estimates for the current study are higher, and can be attributed to the increased mean pressures at which cavitation events are observed. 116

10.4 Event probability plot showing the probability of re-entrant jet causing cavity pinch-off (○) along with shockwaves causing pinch-off (□). For longer type(iii) and type(iv) cavities, shockwaves are the dominant mechanism of shedding. Uncertainty in $\sigma_0 = \pm$ 0.07. 117

10.5 Pressure inside the cavity at different cavitation regimes. This static pressure is used for speed of sound calculations. 119

10.6 The box plot depicting variation of M_0 with decreasing σ_0 across the different cavitation regimes. Speed of sound is estimated using 'homogeneous frozen model and maximum, minimum and median can be seen. $M_0 > 1$ when shockwaves begin to cause cavity pinch-off. 119

10.7 The box plot depicting variation of M_0 with decreasing σ_0 across the different cavitation regimes juxtaposed against the even probability plot to illustrate prevalence of shockwaves when $M_0 > 1$. 120

A.1 Schematic showing the skeleton of the charge amplifier circuit for each sensor. The voltage ± Vss is the activation/source voltage required for the integrated circuit (AD625 instrumentation amplifier) set to 18 V. 124

A.2 Assembled charge amplifier box with grounded instrument casing and BNC connections. 125

A.3 In-house calibration system used to obtain calibration curve of unsteady pressure transducer *dp*. Standard hydrophone(Bruel and Kjaer hydrophone No. 2241694) with trusted calibration curve is used as calibration basis. The dynamic pressure transducer is 290 mm from the walls of the tank and 160 mm away from the bottom of the tank. A 20 kHz source signal generated by the ultrasonic horn is detected equally at the hydrophone and the unsteady pressure transducer as seen in the PSD curves (equal frequency response) at all source signal amplitudes. The horn broadcasts a sinusoidal signal. 126

A.4 Plot depicting accuracy of the calibration system. Higher amplitudes are required to obtain calibration curves/values closer to the manufacturer reported charge sensitivity. 127

C.1 Mean void fraction values for type C; u_H = 8 m/s (□), 10 m/s (△) and 12 m/s (○) at $\sigma_0 = 0.60$. No significant change in void fraction values due to Re is seen. 130

C.2 RMSD values for the three Re; $u_H = 8m/s$(□), 10 m/s (△) and $12m/s$(○);(a) Type B;(b) Type C. RMSD values for Type B are comparable, meanwhile for Type C, RMSD of cavity void fraction is sensitive to *Re*. This can be partially attributed to different mean pressures at these *Re* that affect local pressure fluctuations. 131

D.1 The variation of c_i with decreasing σ_0 across three different *Re* estimated using 'homogeneous frozen model' (open symbols) and 'homogeneous equilibrium model' (filled symbols) ; $u_H = 8m/s$ (□□□), $10m/s$ (△△△) & $12m/s$ (○ ○ ○); c_1 (□△○), c_2(□△○) & c_3(□△○). 136

E.1 Cavitation over the symmetric hydrofoil used in current study (a) High speed snapshot showing a typical shedding cavity over the surface of the foil (b) Schematic depicting classical understanding of different flow features (not to scale). 137

E.2 Questar FOV selected downstream of the cavitating hydrofoil for bubble size and distribution estimations. 138

E.3 Figure depicting the post processing step for each frame of the Questar FOV (a) Raw image captured through the Questar lens (b) Final processed image used for edge detection. 139

E.4 Figure depicting the bubble size distribution downstream of the cavity for (a) σ_0 = 2.2, Lc/C=0.15 (b) σ_0 = 1.6, Lc/C=0.87. Higher cavitation intensity leads to higher vapor bubble size and concentration downstream of the hydrofoil. 140

F.1 Mean and RMSD flow fields of the different cavitation shedding regimes. Mean cavity length progressively increases. The striation in RMSD field occurs due to minimum change in measured x-ray intensity across 0.787s. 142

G.1 Waterfall plot depicting variation of normalized power spectral density with cavitation parameter ($\sigma_0/2\alpha$), where (a) unsteady surface pressure signal near leading edge (dp_1) (b) unsteady surface pressure signal near trailing edge(dp_2). Presence of two peaks in St for the $\sigma_0/2\alpha$ range between 4 to 8 in signal dp_2. The multiple peaks for type(iv) cavities can be visualized in figure G.3 . . . 145

G.2 Waterfall plot depicting variation of normalized power spectral density with cavitation parameter ($\sigma_0/2\alpha$), where (a) static void fraction probe near dp_1 (β_{LE}) (b) static void fraction probe near dp_2 (β_{TE}). Presence of two peaks in St can be seen in figure G.4 146

G.3 The variation of St with $\sigma_0/2\alpha$ from surface pressure signals (a) dp_1 (b) dp_2. Two peaks can be seen in the plot for type(iv) and type(iii) cavities. 148

G.4 The variation of St with $\sigma_0/2\alpha$ from surface pressure signals (a) β_{LE} (b) β_{TE}. Two peaks can be seen in the plot for type(iv) and type(iii) cavities. 149

G.5 PSD plots of transducer signals (a) dp_1 and (b) dp_2 along with void fraction signal (c) and acoustic pressure power spectral density (PSD) from hydrophone (d). The peak frequency 50Hz is not seen on either of the transducers. σ_0 =1.5 ($\sigma_0/2\alpha = 4.3$) 151

G.6 Waterfall plot showing PSD from hydrophone signal. The TE cavitation occurs as early as $\sigma_0/2\alpha = 6$ and becomes a dominant shedding flow feature for type(iv) cavities. The 50Hz peak is explored further using SPOD. 151

G.7 Resolved frequencies and the model energy (%) at each frequency (a) Three peaks in the resolved frequency, with 15 Hz mode having the highest energy (b) The 48Hz mode is closet to 50Hz peak seen on the hydrophone and is the alternating lobe cavitation shown in figure 8.19. σ_0 =1.5 ($\sigma_0/2\alpha = 4.3$) . . . 152

List of Tables

2.1 Inlet parameters and geometry of the backward facing step. 19

2.2 Inlet parameters and location of transducers/pressure ports dp_1, dp_2 and p_c as shown in Figure 2.6 22

5.1 Speed of sound estimation using 'homogeneous frozen model' and 'homogeneous equilibrium model' for $u_H = 8$ m/s. 54

8.1 Calculation of correction factor(CF) used to compare cavity lengths with Wu et al. (2019). 71

8.2 Inlet cavitation number (σ_0) and uncorrected cavitation parameter ($\sigma_0/2\alpha$) values at different cavitating flow regimes at two α. 96

B.1 Table comparing boundary layer thickness(δ) and re-attachment length(X_R) between current study and setup at Johns Hopkins cavitation tunnel (JHU). 128

D.1 Speed of sound estimation using 'homogeneous frozen model' and 'homogeneous equilibrium model' for $u_H = 8$ m/s. 133

D.2 Speed of sound estimation using 'homogeneous frozen model' and 'homogeneous equilibrium model' for $u_H = 10$ m/s. 134

D.3 Speed of sound estimation using 'homogeneous frozen model' and 'homogeneous equilibrium model' for $u_H = 12$ m/s. 135

F.1 Max void fraction values in mean and RMSD void fraction filed at $\alpha = 10^{\circ}$ for different cavitation shedding regimes. 143

G.1 Table summarizing the change in normalized PSD ($\widehat{PSD}$) for the dominant and secondary peak in St for different σ_0. Only dp_2 sees two peaks for longer type (iv) cavities. 147

List of Appendices

A Charge Amplifier Circuit for Dynamic Pressure Measurement **123**

B Single Phase Flow Measurements on Backward Facing Step **128**

C Mean and RMSD Void Fraction Profiles for Backward Facing Step **129**

D Estimated Speed of Sound for Backward Facing Step **132**

E Measurement of Bubble Size Distribution Downstream of NACA0015 Hydrofoil **137**

F Mean and RMSD β Values for NACA0015 Hydrofoil **141**

G Spectral Content in Cavitating NACA0015 Hydrofoil **144**

Abstract

This study is an experimental investigation of cavitation occurring behind a backward facing step, and partial cavity shedding mechanisms on a NACA0015 hydrofoil, using time-resolved x-ray densitometry, high-speed videography, and pressure measurements.

Backward facing step

Understanding of the barotropic relationship, defined by the speed of sound, in a bubbly mixture is essential to predict the occurrence of bubbly shocks in cavitating flows. Cavitating flow behind a backward facing step is studied to understand the effect of mixture compressibility at high void fractions. Using x-ray densitometry, high-speed cinematography, and pressure measurements, cavitation occurring on a backward facing step is studied for a range of inlet cavitation numbers σ_0 and flow speeds u_0. Three types of cavities, designated as type A, B, and C, are identified depending on the extent of cavitation in the shear layer. Developing cavitation (Type A) regime occurs at $\sigma_0 > 0.8$, and in this regime cavitation occurs in the stream-wise vortices of the separated shear layer. For type A cavities, the presence of vapor does not affect the underlying single phase flow, and mean void fraction values of $\beta < 0.2$ is observed. As σ_0 is reduced to 0.77, self-sustained periodic cavity shedding designated as type B, occurs. Type B cavities are characterized by the presence of bubbly shocks that cause cavity shedding, and maximum averaged void fraction increases to $\beta > 0.5$. Type C cavities are similar to type B cavities but with longer lengths and higher void fraction β. Based on x-ray densitometry measurements, properties of bubbly shocks

such as shock speed U_s, pre- and post-shock void fraction, β_1 and β_2, are estimated from void fraction flow fields. The pressure rise across the bubbly shock $(p_2 - p_1)_s$ is measured using a dynamic pressure transducer. Measured β_1, β_2, and $(p_2 - p_1)_s$ are used to estimate the bubbly shock speed U_{RH} is estimated using 1-D Rankine-Hugonoit relations. Estimated 1-D shock speeds U_{RH} are compared with measured shock speeds U_s, and a good agreement is found. Based on the void fraction and the static pressure within the cavity, the local speed of sound based on the 'homogeneous frozen model' and the 'homogeneous equilibrium model' is estimated. Cavity Mach number, M_H, based on the speed of sound estimated using two models and velocity at the step u_H is calculated for all cavitating conditions. It is found that M_H based on the 'homogeneous frozen model' transitions from subsonic to supersonic when bubbly shocks appear in the cavitating flows. In contrast, the 'homogeneous equilibrium model' over-predicts M_H, with values of $M_H \sim O(10^2)$. This suggests that the speed of sound based on the 'homogeneous frozen model' represents the cavitating flow with bubbly shocks.

NACA0015 Hydrofoil

Despite previous studies, the role of liquid re-entrant flows and bubbly shocks in causing sheet-to-cloud transition and cavity shedding is not well understood. In this study, x-ray densitometry, high-speed cinematography and surface pressure measurements are used to study partial cavity shedding dynamics on a NACA0015 hydrofoil. Based on x-ray densitometry measurements of void fraction β, cavities observed at various σ_0 are classified as type(i)-(iv), depending on flow structures that cause shedding. Type(i) are oscillatory cavities where vapor cloud is shed. They occur for $\sigma_0 = 2.8 - 3.2$ for attack angle $(\alpha) = 10°$. Type(ii) cavities ($\sigma_0 = 2.2 - 2.7$ at $\alpha = 10°$) are shed from the leading edge and cavity pinch off is caused either by a re-entrant liquid flow or a bubbly shock. Observed mechanism of cavity pinch off for any given cycle is stochastic in nature with no preference for

either a re-entrant flow or a bubbly shock. At lower cavitation numbers ($\sigma_0 = 1.9 - 2.2$ at $\alpha = 10°$) type(iii) cavities occur and cavity shedding is caused mostly by bubbly shocks and occasionally by liquid re-entrant flows. With $\sigma_0 \leq 1.8$, cavities continue to grow in length and cavitation near the trailing edge affects the shedding cycle. These cavities are designated as type (iv). Shedding in type(iv) cavities are predominantly driven by bubbly shocks and rarely by liquid re-entrant flows. From the x-ray observations, the probability of shedding caused either by a liquid re-entrant flow or bubbly shocks are estimated for all cavities. Estimated probabilities are then compared with cavity Mach number (M_0) based on the 'homogeneous frozen model' and inlet speed (u_0). It is found that the probability of bubbly shocks to cause pinch off increases to over 60% when M_0 exceeds unity.

Chapter 1

Introduction

This thesis is an experimental study of unsteady cavitation occurring on two geometries using time-resolved x-ray densitometry, high-speed cinematography, and synchronized pressure measurements. The first study on unsteady cavitation on a backward facing step investigates the validity of mixture speed of sound based on 'the homogenous frozen model' in predicting the onset of bubbly shocks. The second study focuses on the relative importance of re-entrant liquid flow and bubbly shock waves in causing partial cavity shedding on a NACA0015 hydrofoil. Experimental set-up and methods used for both studies are reported in chapter 2. Chapters 3 through 6 discuss the backward facing step portion of the thesis and chapters 7 through 11 discuss the study on a cavitating NACA0015 hydrofoil.

1.1 Background

Cavitation is a phase change phenomenon from liquid to vapor when the local pressure in the liquid falls below the liquid vapor pressure. The local pressure of a flowing liquid depends on underlying flow field, while the liquid vapor pressure depends on the local temperature. For most hydrodynamic flows of naval interest, the change in water temperature due to the flow is negligible, and occurrence of cavitation depends on the local pressure distribution. Low pressure regions in the flow susceptible to cavitation can exist in cores of vortices, high-shear regions, and detached zones.

1.2 Cavitation Inception

Cavitation inception is the first observed form of cavitation, characterized by presence of small amount of vapor in the the low pressure regions of the flow. Katz and O'hern (1986) and O'hern (1990) observed that cavitation inception in a turbulent shear layer occurred in weaker streamwise vortices (braids) rather than in stronger spanwise vortices (rollers). Iyer and Ceccio (2002) observed a similar behavior for inception in turbulent shear flow. Figure 1.1 shows cavitation inception occurring in a turbulent shear layer.

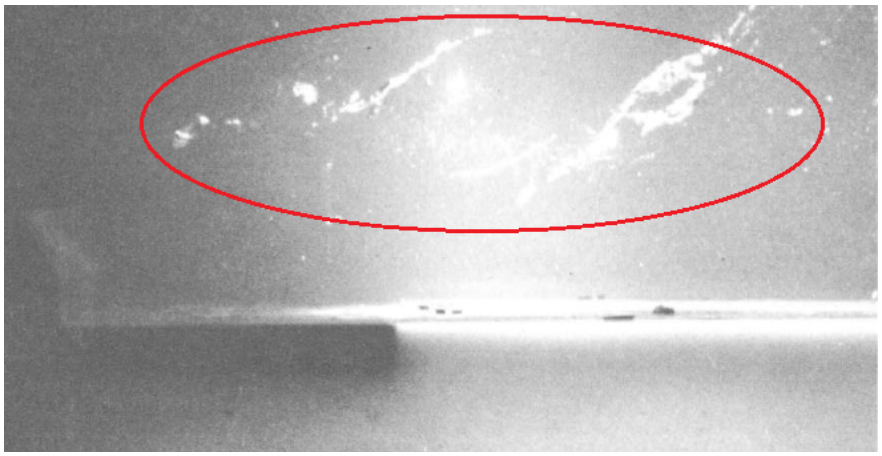

Figure 1.1: Inception in turbulent shear layer occurs in stream-wise vortices (braids) rather than stronger spanwise vortices (rollers) as shown by Iyer and Ceccio (2002). Pressure drop due to the stretching of the weaker braids by the stronger rollers is hypothesized as the reason for observation of inception in the weaker stream-wise rollers. The flow is from left to right.

1.3 Partial/Cloud Cavitation

Partial/Cloud cavitation is characterized by the presence of vapor bubbles in larger area/volume when compared to inception. Partial cavities are usually stable but can experience a transition to self-induced volume oscillations when cavitation number σ reduces. The non-dimensional cavitation number (σ) shown in equation 1.1, defines the ratio between difference of local pressure (p) from liquid vapor pressure (p_v) and the kinetic energy per unit volume

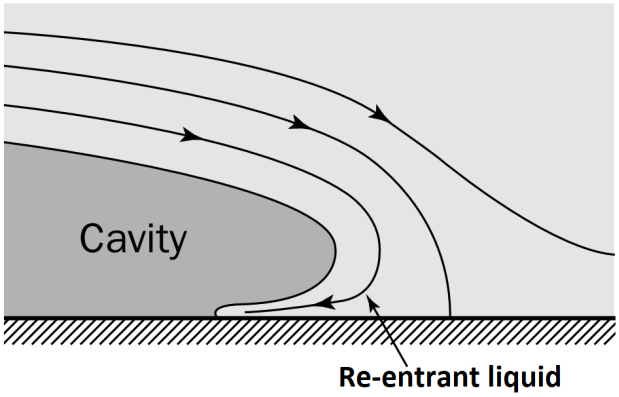

Figure 1.2: Schematic depicting re-entrant liquid flow at cavity closure. Flow is from left to right.

($\frac{1}{2}\rho u^2$). The value of σ characterizes the potential of the flow to cavitate. The self-induced volume oscillations in partial cavities are characterized by shedding of vapor clouds, and the collapse of these shed clouds can cause significant erosive damage, performance deterioration, and noise.

$$\sigma = \frac{p - p_v}{\frac{1}{2}\rho u^2} \tag{1.1}$$

The underlying mechanism that causes shedding has been attributed to the presence of a liquid re-entrant flow originating at cavity closure and a bubbly shock. A liquid re-entrant flow originates at the cavity close where the liquid re-attaches to the surface. A schematic of flow at the cavity closure with a re-entrant flow is shown in figure 1.2. Callenaere et al. (2001) performed a systematic study on the development of re-entrant liquid flows and found the adverse pressure gradient at the cavity closure to be the most important parameter that influences the occurrence and strength of these liquid re-entrant flows.

Recently Ganesh et al. (2016) reported the presence of propagating bubbly shock waves as a dominant mechanism of partial cavity shedding on a wedge. By using time-resolved x-ray densitometry, they were able to identify the presence of bubbly shocks as a cause of shedding. Figure 1.3 shows a snapshot of a shedding cycle caused by a propagating bubbly shock. Similar observation of bubbly shocks causing cavity shedding was reported in

numerical studies by Bhatt and Mahesh (2020) and Budich et al. (2018). Unlike the liquid re-entrant flow which has its origin from the presence of a stagnation point at cavity closure, the bubbly shock wave occurs due to increased mixture compressibility in the cavitation region.

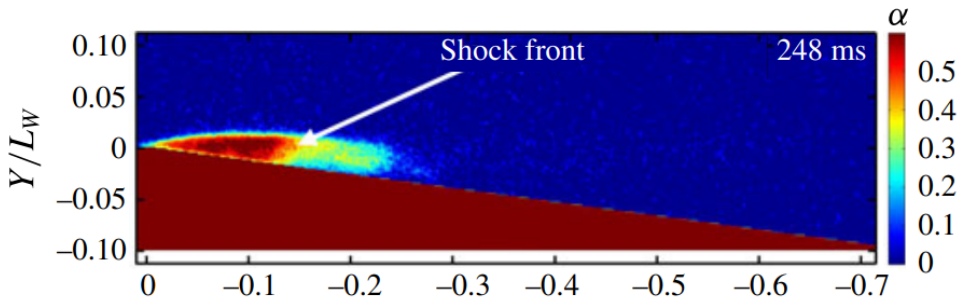

Figure 1.3: A propagating bubbly shock moving towards the apex of the wedge reported by Ganesh et al. (2016). Flow is from left to right.

1.4 Compressibility of bubbly mixtures

The vapor-liquid compressibility is important and can result in the occurrence of bubbly shocks in cavitating flows. Higher vapor content at lower σ can result in reduced local speed of sound (c) and the local velocity becoming comparable to c. The compressibility effects such as shocks can manifest. Figure 1.4 shows the variation of speed of sound of a gas-liquid mixture at different air volume fractions. It is seen that the speed of sound varies from its value of $\sim$ 1500 m/s in water to $\sim$ 330 m/s in air and reduces significantly for volume fractions between 20-80%.

1.4.1 Speed of sound in bubbly mixtures

Speed of sound (c) in a bubbly mixture defines the pressure-density relationship of the mixture under a given thermodynamic assumption,and is difficult to obtain analytically. Depending on the processes considered (heat transfer, mass transfer, and relative motion between phases) the difficulty in obtaining a solution and the complexity of the resulting

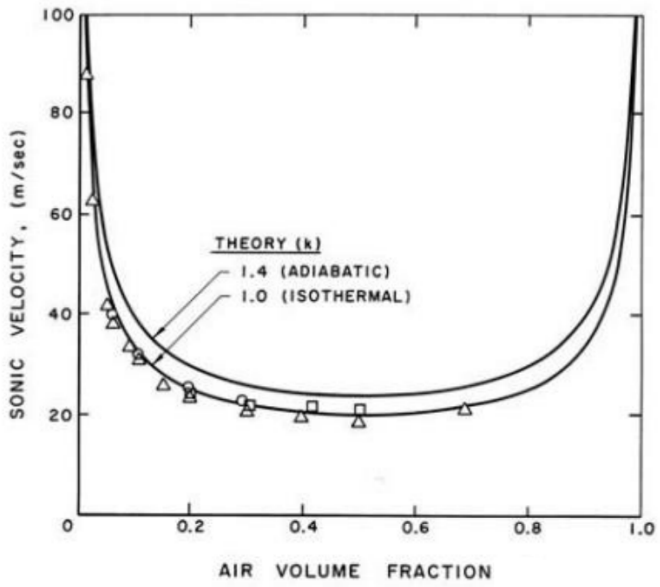

Figure 1.4: Plot depicting variation in speed of sound in a bubbly air-water mixture at atmospheric pressure with mixture volume fraction summarized by Brennen (2005). The experimental data is plotted against the analytical expressions under adiabatic and isothermal phase change assumptions respectively.

expression increases. This has resulted in different 'models' being used for estimating the sound speed in bubbly mixtures. Lack of experimental measurement of sound speed in high void fraction bubbly flows makes the validation of these models difficult. This has resulted in a lack of consensus on the appropriate speed of sound expression that best represents cavitating bubbly flows (Budich et al. (2018)). This section provides the background necessary to understand the importance of two common thermodynamic assumptions and their effect on the mixture speed of sound.

The speed of sound (c) relates to mixture density (ρ) and pressure (p) through a barotropic relation at a constant thermodynamic property, as shown in equation 1.2.

$$c = \sqrt{\frac{dp}{d\rho}} \tag{1.2}$$

For a two-phase mixture shown in figure 1.5, an expression for speed of sound can be obtained by considering a pressure wave passing through the mixture. The summary pro-

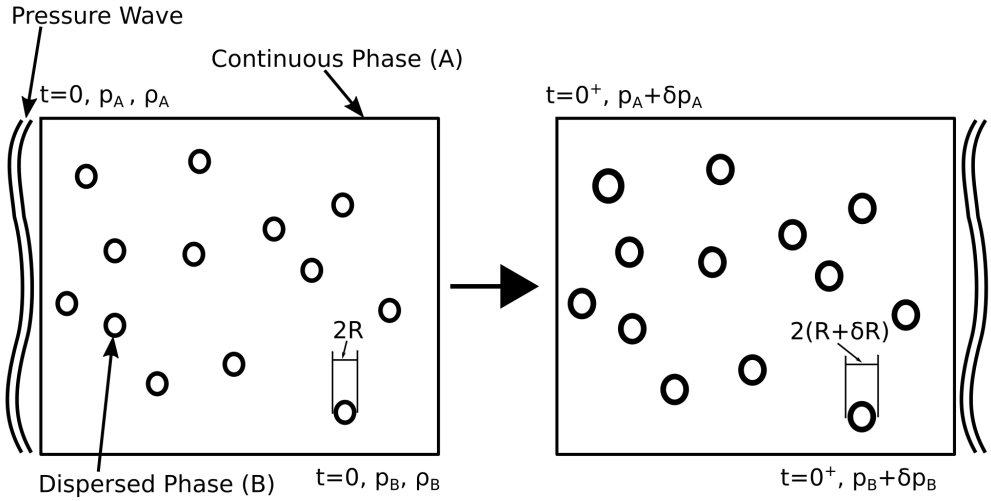

Figure 1.5: Plot depicting changes in the two-phase mixture before ($t = 0$) and after ($t = 0^+$) the passage of a pressure wave. The change in continuous phase(A) and dispersed phase(B) leads to change in total volume of the mixture (∂V). The change in volume is used to obtain the sonic speed expression shown in equation 1.6

vided here is based on discussion on homogeneous mixture models by Brennen (2005). A continuous phase (A) and a dispersed phase (B), before and after the passage of an infinitesimal pressure wave, are shown in figure 1.5 (a) and (b) respectively. The initial pressure at $t = 0$ is given by $p_A = p_B + 2S/R$, where S is the surface tension and R is the radius of the dispersed phase particles. Also, the initial volume (V) of the mixture is unity ($V_A + V_B = 1$). After the pressure wave passes through the two-phase mixture, p_A changes to $p_A + \partial p_A$, and a new equilibrium state of the mixture is reached at $t = 0^+$. Mass (∂m) is exchanged between the continuous and dispersed phases. This changes the volume of the two-phases, and is given by equations 1.3 and 1.4. The change in total volume of the mixture (∂V) and the relationship to sonic velocity are given in equations 1.5 and 1.6. Speed of sound for each phase can be defined as c_A and c_B as shown in equation 1.7 satisfying thermodynamic constraints QA and QB respectively. No dispersed particles are created or destroyed during $t = 0 \rightarrow 0^+$ (propagation of sound does not destroy particles) and the ratio $\frac{\partial p_A}{\partial p_B}$ can be

determined using $\partial p_A = \partial p_B - \frac{2S}{R^2}\partial R$. Upon substitution in equation 1.6, an expression for the sonic speed shown in equation 1.8 can be obtained.

In the absence of surface tension ($S = 0$) equation 1.8 reduces to equation 1.9. However, this reduced expression for speed of sound still requires definition of thermodynamic constraints QA and QB.

$$V_A(t = 0^+) = [\rho_A V_A + \partial m] \,/\, \left[\rho_A + \frac{\partial \rho_A}{\partial p_A}\Big|_{QA} \partial p_A\right] \tag{1.3}$$

$$V_B(t = 0^+) = [\rho_B V_B + \partial m] \,/\, \left[\rho_B + \frac{\partial \rho_B}{\partial p_B}\Big|_{QB} \partial p_B\right] \tag{1.4}$$

$$\partial V = V_A(t = 0^+) + V_B(t = 0^+) - 1 \tag{1.5}$$

$$c^{-2} = -\rho_m \frac{\partial V}{\partial p_B}\Big|_{\partial p_B \to 0} = \rho_m \left[\frac{V_A}{\rho_A}\frac{\partial \rho_A}{\partial p_A}\Big|_{QA}\frac{\partial p_A}{\partial p_B} + \frac{V_B}{\rho_B}\frac{\partial \rho_B}{\partial p_B}\Big|_{QB} - \frac{\rho_B - \rho_A}{\rho_B \rho_A}\frac{\partial m}{\partial p_B}\right] \tag{1.6}$$

$$c_A^{-2} = \frac{\partial \rho_A}{\partial p_A}\Big|_{QA}; c_B^{-2} = \frac{\partial \rho_B}{\partial p_B}\Big|_{QB} \tag{1.7}$$

$$\frac{1}{\rho_m c^2} = \frac{V_B}{\rho_B c_B^2} + \frac{\left[\frac{V_A}{\rho_A c_A^2} - \frac{\partial m}{\partial p_B}\left\{\frac{1}{\rho_A} - \frac{1}{\rho_B} + \frac{2S}{3\rho_A \rho_B c_A^2 R}\right\}\right]}{\left[1 - \frac{2S}{3\rho_A c_A^2 R}\right]} \tag{1.8}$$

$$\frac{1}{\rho_m c^2} = \frac{V_B}{\rho_B c_B^2} + \left[\frac{V_A}{\rho_A c_A^2} - \frac{\partial m}{\partial p_B}\left\{\frac{1}{\rho_A} - \frac{1}{\rho_B}\right\}\right] \tag{1.9}$$

QA and QB can be chosen depending on assumption of the underlying thermodynamic process occurring during phase change. When the two phases are in thermodynamic equilibrium, heat transfer occurs instantaneously during the phase change and this is the 'homogeneous equilibrium model' of speed of sound. For this model QA = QB = isentropic process (s). If zero heat transfer occurs between the phases during phase change, the two phases are insulated. This is 'the homogeneous frozen model' of speed of sound where QA = QB

= phase equilibrium (e). The actual behavior of the two phases is expected to lie between these two assumptions.

If ϵ_A is the fraction of the continuous phase (A) that exists in thermodynamic equilibrium, then $(1-\epsilon_A)$ fraction will be insulated (similarly, ϵ_B and $(1-\epsilon_B)$ fractions are defined for dispersed phase (B)). Similar to equations 1.3 and 1.4, the change in volume of each fraction due to incremental change in pressure ($\partial p_A = \partial p_B = \partial p$) can be calculated as shown in equation 1.10. Substituting this into equation 1.9 gives the general qualitative expression of speed of sound for a homogeneous two-phase mixture as shown in equation 1.11.

$$\begin{matrix} \dfrac{(1-\epsilon_A)(\rho_A V_A + \partial m)}{\rho_A + \frac{\partial \rho_A}{\partial p}\Big|_s \partial p}; \dfrac{\epsilon_A(\rho_A V_A + \partial m)}{\rho_A + \frac{\partial \rho_A}{\partial p}\Big|_e \partial p} \\ \dfrac{(1-\epsilon_B)(\rho_B V_B + \partial m)}{\rho_B + \frac{\partial \rho_B}{\partial p}\Big|_s \partial p}; \dfrac{\epsilon_B(\rho_B V_B + \partial m)}{\rho_B + \frac{\partial \rho_B}{\partial p}\Big|_e \partial p} \end{matrix} \tag{1.10}$$

$$\begin{aligned} \frac{1}{\rho_m c^2} = (1-\epsilon_A)\frac{V_A}{\rho_A}\left(\frac{\partial \rho_A}{\partial p}\right)_s + \epsilon_A \frac{V_A}{\rho_A}\left(\frac{\partial \rho_A}{\partial p}\right)_e + (1-\epsilon_B)\frac{V_B}{\rho_B}\left(\frac{\partial \rho_B}{\partial p}\right)_s \\ + \epsilon_B \frac{V_B}{\rho_B}\left(\frac{\partial \rho_B}{\partial p}\right)_e - \frac{\partial m}{\partial p}\left(\frac{1}{\rho_A} - \frac{1}{\rho_B}\right) \end{aligned} \tag{1.11}$$

In the above analysis, relative motion between the phases in neglected. (Crespo (1969)) derived an expression for the speed of sound, including relative motion, heat and mass transfer between phases by using linearized governing equations of motion. It is one of the most complex and complete representation of sonic speed, and it provides a good representation of measurements of speed of sound, as seen in figure 1.6. Despite simplification, the expression for mixture speed of sound suggested by Crespo (1969) requires precise knowledge of thermodynamic parameters like heat exchange rate at interface for a given mixture component and temperatures, that are difficult to measure experimentally.

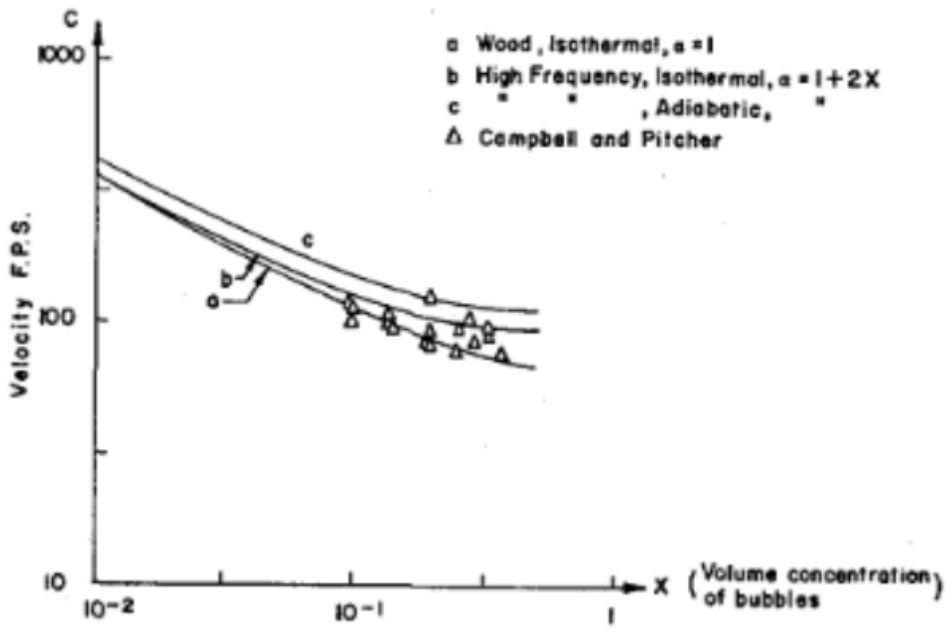

Figure 1.6: Speed of sound in water with bubbles estimated using Crespo's expressions (b,c) (Crespo (1969)) plotted against findings of Campbell and Pitcher(△)

1.4.2 Shock waves in bubbly flows

As discussed earlier, the speed of sound in a two-phase mixture can get significantly lower than the speed of sound in either of the two components at moderate void fractions, $\beta \sim 0.5$. When this low mixture speed of sound is comparable with local flow velocity, compressibility effects such as shocks can occur within the bubbly mixture.

A bubbly shock is a discontinuity across which mass, momentum, and energy are conserved. Figure 1.7 shows a schematic of stationary bubbly shock with pre- and post-shock conditions designated as '1' and '2' respectively. Conservation of mass and momentum across the shock are shown in equations 1.12 and 1.13. From these relations, an expression for shock speed (u_S) is obtained in terms of $\beta_1, \beta_2, p_1, p_2$. This expression, shown in equation 1.15, is the Rankine-Hugonoit jump relations for a bubbly shock.

$$\rho_1 u_1 = \rho_2 u_2 \tag{1.12}$$

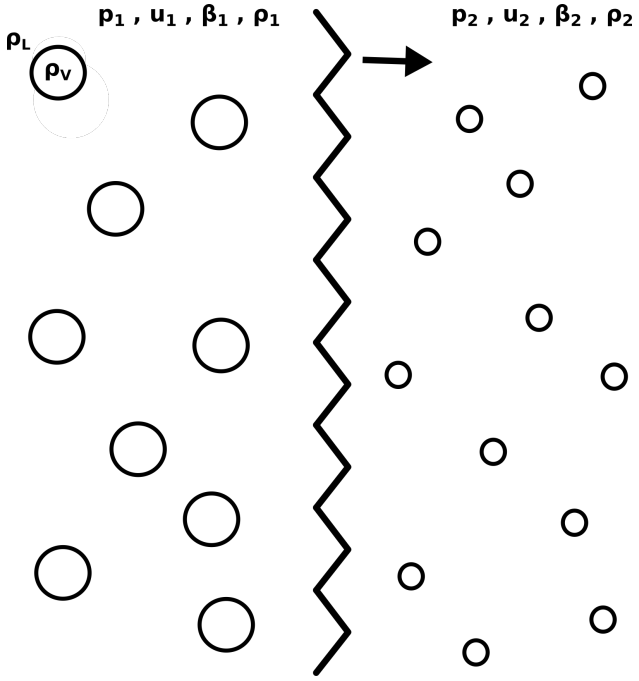

Figure 1.7: Schematic depicting pre- and post shock propagation properties in the vapor-liquid mixture. When the shock propagates into stationary vapor-liquid mixture, $u_2 = u_s$

$$\rho_1 u_1^2 + p_1 = \rho_2 u_2^2 + p_2 \tag{1.13}$$

$$\rho_1 \approx \rho_L(1-\beta_1); \rho_2 \approx \rho_L(1-\beta_2) \tag{1.14}$$

$$u_s = \frac{p_2 - p_1}{\rho_L}\left[\frac{(1-\beta_2)}{(1-\beta_1)*(\beta_1-\beta_2)}\right] \tag{1.15}$$

1.5 Current Study

Current study advances the findings of previous studies by Ganesh et al. (2016) and by Wu (2019). Ganesh et al. (2016) reported the shedding of partial cavities caused by bubbly shocks and attributed compressibility of the cavitating mixture for their occurrence. Despite identifying the mechanism, Ganesh et al. (2016) was not able elucidate on the barotropic relation that best described the cavitating flow. Since the publication of Ganesh et al. (2016), the field has advanced, and the validity of an appropriate speed of sound expression that best

represents these cavitating flows is one of the open questions. This study will address the importance of underlying thermodynamic assumptions used to estimate local sound speed by using two extreme thermodynamic assumptions during the phase change and comparing with experimental observation of onset of shockwaves. The local speed of sound expression helps quantify the mixture compressibility.

Wu (2019) hypothesized and tested the importance of mixture compressibility in altering the shedding dynamics of a cavitating wake. In that study, Mach number based on Wood's formula (and wedge velocity) was used to quantify compressibility in the near-wake of a bluff body. They reported that the Strouhal number (St) of a cavitating wake increased when the Mach number in the near wake transitioned from sub- to supersonic. Despite the findings no explicit measure of compressibility effects (such as shock pressure rises) were made other than Mach number estimation using Wood's formula. Also, the Mach number estimated based on Wood's formula, which is close to the 'homogeneous frozen model' of speed of sound was not compared with Mach numbers based on other speed of sound models.

In the backward facing step portion of the study, speed of sound expression that best represents the observed bubbly cavitating flow is identified. This is done by identifying a Mach number, estimated based on two speed of sound models, that best predicts the onset of bubbly shocks by a subsonic to supersonic transition. In addition, the validity of one-dimensional Rankine-Hugonoit jump relations for propagating bubbly shocks observed in cavitating flows is explored.

Re-entrant liquid flow and propagating bubbling shocks are two mechanisms that cause shedding of partial cavities. The transition from stable sheet cavities to shedding cavities occur when the conditions conducive for one of the mechanisms occur. Wu (2019) reported the presence of propagating bubbly shocks as a dominant mechanism of shedding on a NACA0015 hydrofoil. However, the existence and role of the liquid re-entrant flow in causing shedding was not discussed in that study. Lack of pressure measurements resulted in no

estimation of cavity Mach numbers and pressure rises across propagating shocks. The current study on a NACA0015 hydrofoil addresses the inadequacies in the findings of Wu (2019) by investigating the underlying flow features that cause shedding using time-resolved x-ray densitometry synchronized with pressure measurements. By using a larger scale model, the presence of both liquid re-entrant flow and bubbly shocks is identified and the relative importance of each flow front as a dominant cavity shedding mechanism is identified. By estimating the Mach number within the cavity, it is shown that the likelihood of shedding caused by a re-entrant flow or a bubbly shock is related to the cavity Mach number.

1.5.1 Contributions of backward facing step study

Time-synchronous measurements of void fraction flow fields and cavity pressures on a cavitating backward facing step have not been reported before. One of the contributions of this study is the experimental verification of the validity of 1-D jump conditions across a propagating bubbly shock observed in the cavitating bubbly flow. This is done by comparing the measured shock speeds from x-ray densitometry with the estimated shock speed from pressure measurements using 1-D conservation relations. The cornerstone contribution of this portion of the study is the finding that the Mach number based on step velocity and 'the homogeneous frozen speed' of sound predicts the experimentally observed onset of bubbly shocks. An application of this finding is providing a barotropic relation that can be used in numerical simulations to predict the onset of shocks. A high-fidelity experimental data-set that can be used for the validation of CFD codes is also obtained from the study.

1.5.2 Contributions of NACA0015 hydrofoil study

Observation of simultaneous occurrence of both a re-entrant liquid flow and a bubbly shock wave for a range of cavitation numbers have not been reported before. Occurrence of both these flow fronts and their role in causing cavity pinch-off at different cavitating conditions

is shown using time-resolved x-ray densitometry. In addition, the probability of each flow structure to cause cavity pinch-off is also presented. Increased probability of the occurrence of shock waves is shown to coincide with transition of Mach number (M_0) from subsonic to supersonic values. M_0 is based on inlet velocity (u_0) and speed of sound estimated by 'homogeneous frozen model'. There is no known experimental study that discusses this important phenomenon of partial cavity shedding by re-entrant flows and shocks on the same cavitating geometry in such detail. The data and the results from the present study will significantly improve the numerical modeling of cavitating flows.

Chapter 2

Experimental Setup

2.1 Flow loop

Cavitation experiments were performed in the Michigan 9" recirculating cavitation channel shown in figure 2.1. The flow loop of has 6:1 contraction leading to 228.6 mm diameter section that transitions to 209.6 mm by 209.6 mm square section with filleted corners. The flow velocity and static pressure in the tunnel test section can be varied from 0 to 18 m/s, and from near-vacuum to 200 kPa gauge pressure. Dissolved gas content, which determines the distribution of nucleation sites (nuclei) in the liquid, was controlled using a de-aeration system. The dissolved oxygen content of the liquid (DO) was measured to estimate the overall gas content in water. The DO was measured with a Thermo-Scientific Orion Star A113 Dissolved Oxygen bench-top meter with a range of 0-20 $\pm$ 0.2 mg/L. The meter was also used to measure the temperature of water within a range of 0-50 $\pm$ 0.1 °C.

The inlet velocity (u_0) was measured through the pressure drop across the contraction using Setra 230, 0-68 kPa, differential pressure transducer with an accuracy of 0.25 % of full scale (FS). Inlet pressure (p_0) was measured using Omega PX409-030A5V, 0-206 kPa static pressure transducer (0.08 % FS accuracy). u_0 and p_0 were used to calculate inlet cavitation number (σ_0), defined in equation 2.1, where p_v is the vapor pressure.

$$\sigma_0 = \frac{(p_0 - p_V)}{\frac{1}{2}\rho u_0^2} \tag{2.1}$$

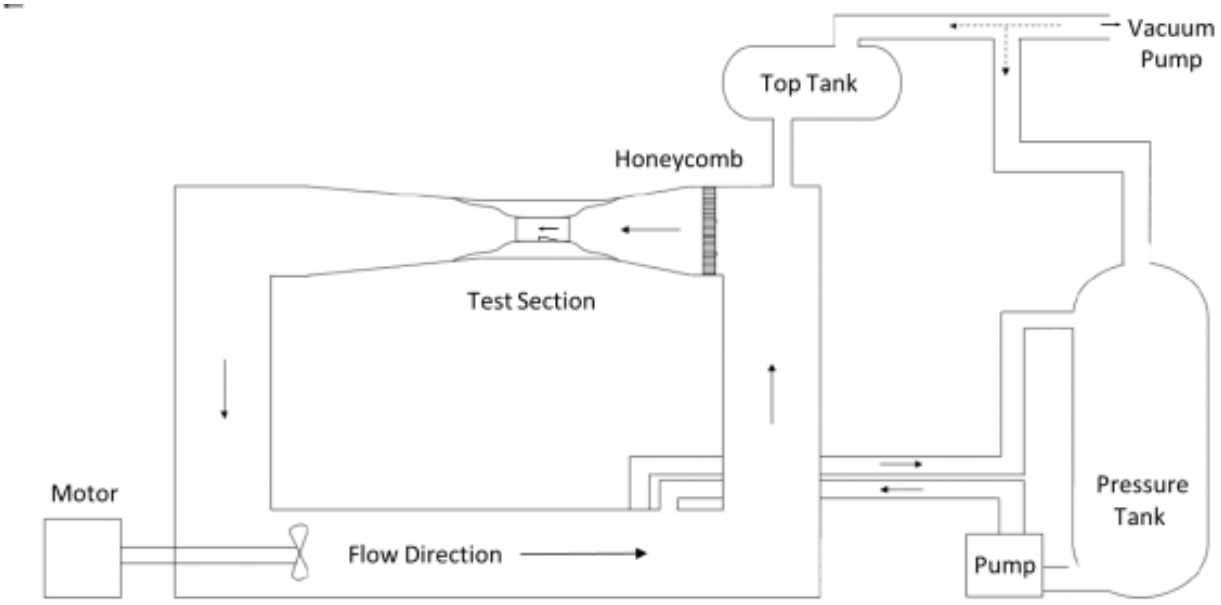

Figure 2.1: Schematic of the flow loop depicting Michigan 9" water tunnel testing facility
.

2.2 Backward Facing Step

The backward facing step experiments were performed in a test-section of reduced area (78.4 mm by 78.4 mm) within the original test-section using custom made windows. This was done to minimize baseline x-ray attenuation of the non-cavitating liquid. Details of the reduced test section geometry can be found in Ganesh (2015).

The backward facing step consists of a ramp that leads to step height of (H) of 12.1 mm. The ramp follows a fifth order polynomial profile ($y = f(x)$), where y denotes the height from the wall that increases to step height (H). Figure 2.2 shows a schematic of the test-section with the backward facing step.

Cavitation measurements were performed for step velocities $u_H = 8, 10, 12\ m/s$ with a corresponding Reynolds number of $Re_H = 9.8 \cdot 10^4$, $12.3 \cdot 10^4$ and $14.8 \cdot 10^4$ respectively. The step velocity u_H was estimated from the measured inlet velocity u_0 and mass conservation given in equation 2.2.

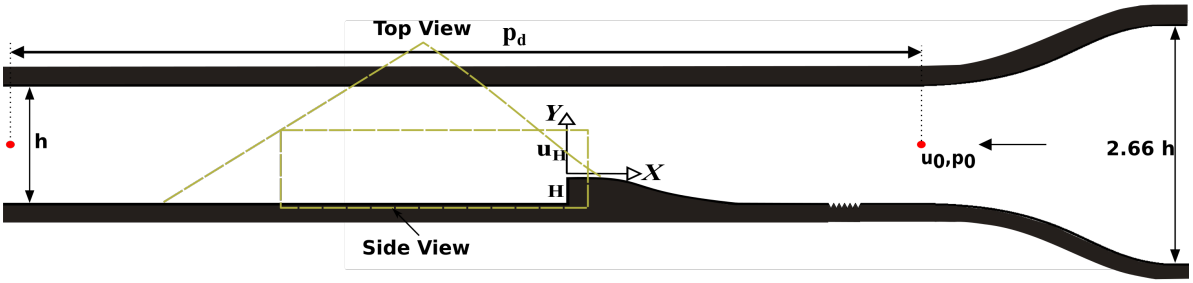

Figure 2.2: Schematic of the backward facing step mounted in the water tunnel. Top and side field of view configurations for the high speed videography are shown. For x-ray densitometry a 115 mm by 28 mm view similar to the highlighted side view is chosen (see figure 4.5)

.

$$u_H = \frac{h \cdot u_0}{h - H} \tag{2.2}$$

Inlet pressure p_0 was measured using Omega PX409-030A5V, 0-206 kPa static pressure transducer (0.08 % FS accuracy). Static pressure p_1 was measured using differential pressure transducer Omega PX2300, 0-34 kPa (0.25 % FS accuracy) between pressure taps at p_0 and p_1. Omega PX409-005AI-EH, 0-34 kPa (0.08 % FS accuracy) static pressure transducer measures static pressure at X = -1.5H (p_2); while Omega PX203, 0-206 kPa (0.25 % FS accuracy) static pressure transducer measures static pressure at X = -8H (p_3). The overall pressure drop across the test section between p_0 and p_4 was measured using Omega RX2300, 0-34 kPa (0.25 % FS accuracy). All pressure taps have a diameter of 1.6 mm.

Dynamic pressure transducer PCB 113M231, with 7.04 μA/kPa sensitivity, was used to measure the fluctuation in local surface pressure (dp). This CVLD piezoelectric sensor was capable of acquiring a maximum pressure rise of 6895 kPa. A charge amplifier unit was custom built (Appendix A) for the sensor to acquire the signal at f_{3dB} = 1.04-10300Hz, at a fixed gain of 10. Additional gain was provided by Krohn-Hite 3944 multichannel filter. The signal was acquired at a sampling frequency of 50 kHz for 3 seconds. All the static and dynamic pressure measurement locations are summarized in figure 2.3. The dissolved oxygen was maintained below 20 % of saturation for all experiments and the water temperatue was

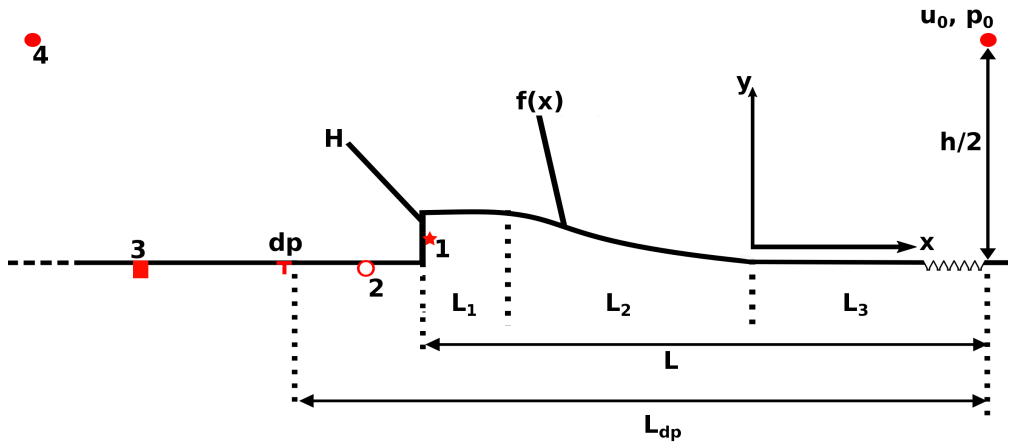

Figure 2.3: Schematic of the backward facing step mounted in the water tunnel depicting the location of pressure ports in the test section and corresponding pressure tap. $f(x) \approx 2.5 \cdot 10^{-9}x^5 - 7.95 \cdot 10^{-7}x^4 + 6.5 \cdot 10^{-5}x^3$, $0 < x < L_2$ and $f(x) \approx H$, $L_2 < x < L_3$ (Coefficients of $f(x)$ are truncated here for brevity. All dimensions are in mm). $L = 46.08(L_1) + 122.89(L_2) + 30.72(L_3) + 3.11$. Between 0 & 1 (Static) : $(L, (h-H)/2$; Between 0 & 2 (Static): $(L{+}1.5H, h/2)$; Between 0 & 3 (Static) : $(L{+}8H, h/2)$; Between 0 & 4 (Static) : $(608mm, 0)$; Between 0 & Dynamic Pressure Transducer (Φ 5.54 mm) : $L_{dp} = L + 3H$

.

close to room temperature ($20° - 23°C$).

2.2.1 Particle Image Velocimetry (PIV)

2-D planar PIV was done to characterize the liquid flow boundary layer thickness at the separation point near step (δ), and the re-attachment length X_R. The laser light beam postion and PIV field-of-view for boundary layer measurements near the step are shown in figure 2.4. An 80 mJ, 200 kHz pulsed laser (green beam of 532 nm wavelength) from New Wave Solo PIV system was used to illuminate the FOV. LaVision FlowMaster 3 camera with a 1Mpix (1280 pix by 1024 pix) resolution of was used for acquisition at 1000 frames per second. The flow was seeded using Titanium Dioxide (TiO_2, 0.2 μm). The laser pulse trigger and camera acquisition were synchronized and controlled through Davis 8.0 software. All the post processing was done in Davis 8.0 using built-in algorithms.

Boundary layer measurements near the separation point (δ) were made in a 14 mm by

Parameter	Symbol	Value
Step Height	H	12.1 mm
Channel Height	h	78.4 mm
Channel Span	S	78.4 mm
Expansion Ratio	$ER = \frac{h}{h-H}$	1.2
Inlet Velocity	u_0	($\approx$) 6.77, 8.46, 10.16 $\pm$ 0.15 m/s
Mean Velocity at the step	u_H	($\approx$) 8, 10, 12 $\pm$ 0.18 m/s
Inlet Pressure	p_0	17-55 $\pm$ 0.16 kPa
Vapor Pressure	p_{vap}	3 kPa
Inlet cavitation number	$\sigma_0 = \frac{p_0 - p_{vap}}{\frac{1}{2}\rho {u_0}^2}$	0.50-1.00 $\pm$ 0.07
Boundary Layer Thickness (non cavitating, $u_H = 10$ m/s)	δ/H	0.33 $\pm$ 0.01
Reattachment Length (non cavitating, $u_H = 10$ m/s)	X_R/H	5.4 $\pm$ 0.1
Reynolds number based on H	$Re_H = \frac{u_H H}{\nu}$	98700-148000

Table 2.1: Inlet parameters and geometry of the backward facing step.

7.5 mm observation window. A 16 by 16 pixel sized interrogation windows with 50% overlap were selected for this field-of-view. In addition, a larger field-of-view near the re-attachment zone, downstream of the step was chosen to determine the re-attachment point. A 33 mm x 19 mm field-of-view was chosen with a 32 by 32 pixel interrogation window (50% overlap). The point of flow turning was identified by examining the streamlines in this field-of-view. The location of the two fields-of-view is shown in figure 2.5.

2.3 NACA0015 Hydrofoil

The NACA0015 hydrfoil used in this study had a chord of 165.6 mm, a span of 209.5 mm which corresponds to an aspect ratio (AR) of 1.27. The hydrofoil model was machined out of brass. Unlike the backward facing step, hydrofoil experiments were performed in the original test-section to facilitate better spatial resolution. The suction side of the foil was equipped with pressure ports to measure unsteady surface pressure and static cavity pressure as shown in figure 2.6.

Omega PX409-110 005AI-EH, 0-34 kPa (0.08 % FS accuracy) and Omega PX203, 0-206

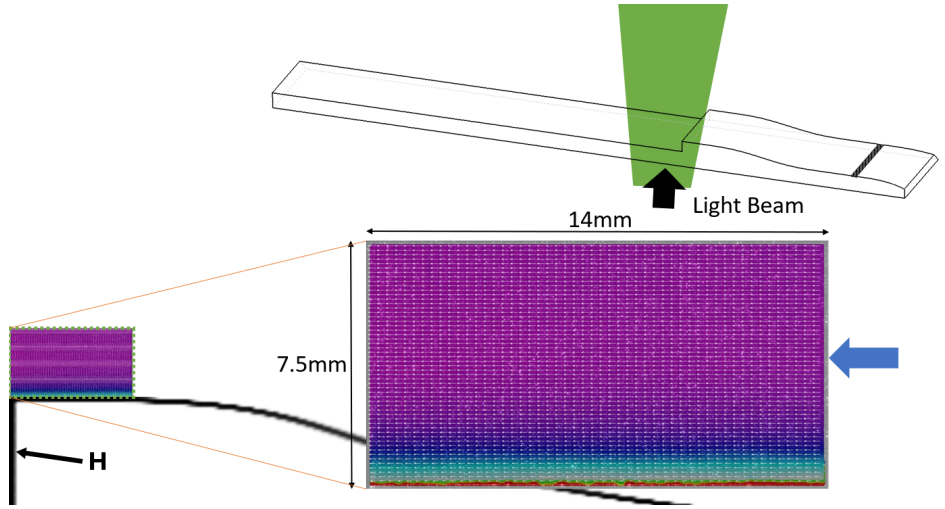

Figure 2.4: The field-of-view used for boundary layer thickness measurements near the separation point. The velocity profile in 14 mm x 7.5 mm FOV is also shown for set tunnel velocity (u_H) of 10.9 m/s. Flow from right to left.

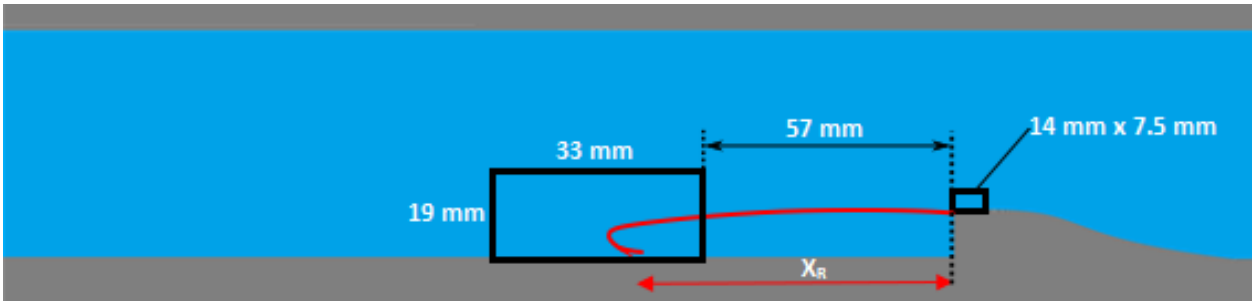

Figure 2.5: The two field of views used for the single phase flow measurements. X_R is the re-attachment point. Flow from right to left.

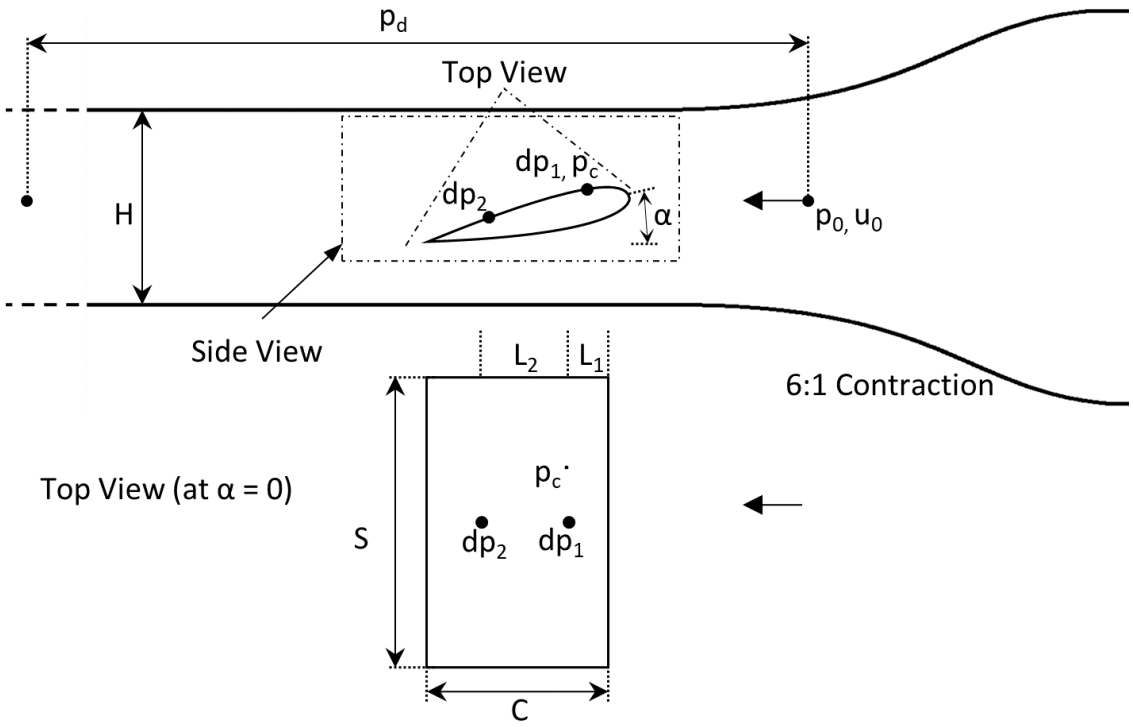

Figure 2.6: Schematic of hydrofoil mounted in the tunnel. Top and side view used for high speed videography are shown. For void-fraction flow field 135 mm by 85 mm field of view covering roughly 80 % of the chord is used.

kPa (0.25 % FS accuracy) static pressure transducers were used to measure the pressure on the hydrofoil surface (p_c). The overall pressure drop across the test section (p_d) was measured using Omega RX2300, 0-34 kPa (0.25 % FS accuracy) transducer. All pressure taps had a diameter of 1.6 mm. A schematic of the test section with the location of all the pressure transducers/ports is shown in figure 2.6. The dissolved oxygen content was maintained below 15% of saturation at room temperature ($20°C$ to $23°C$). The inlet parameters used for NACA0015 hydrofoil experiments is shown in table 2.2.

Two dynamic pressure transducers PCB 113M231 were surface mounted on the foil to measure dynamic pressure at dp_1 (7.59 $\mu A/kPa$, 0.2 % full-scale linearity) and dp_2 (7.28 $\mu A/kPa$, 0.1 % full-scale linearity) as shown in figure 2.6. These CVLD differential pressure sensors have a piezoelectric membrane that produces current when subjected to pressure pulses in the tunnel. Pressure transducer signals were acquired by the in-house charge

Parameter	Symbol	Value
Chord	C	165.6 mm
Span	S	209.6 mm
Angle of attack (AOA)	α	7° , 10°
Aspect Ratio	AR=S/C	1.27
Inlet velocity	u_0	8 ± 0.14 m/s
Inlet pressure	p_0	35 - 120 ± 0.16 kPa
Vapor Pressure	p_{vap}	3 kPa
Inlet cavitation number	$\sigma_0 = \frac{p_0 - p_{vap}}{\frac{1}{2}\rho {u_0}^2}$	1 - 3.6 ± 0.07
Location of transducers	L_1	40.6 mm
	L_2	69.8 mm

Table 2.2: Inlet parameters and location of transducers/pressure ports dp_1, dp_2 and p_c as shown in Figure 2.6

amplifier used in the backward facing step setup. Signals were sampled at a frequency of 50-100 kHz for 1.5 seconds.

2.4 High-speed cinematography system

Cavitation events were visualized, for both experiments, with two Phantom v730 high-speed video cameras. The cameras were mounted to provide top and side views of cavitation events, and the high-speed videography field-of-view for backward facing step and NACA0015 hydrofoil are shown in figure 2.2 and figure 2.6. The two high-speed video cameras were time synchronized and triggered simultaneously. A Nikon AF-P DX NIKKOR 18-55 mm f/3.5-5.6 G VR zoom lens was used in observing top-view and a Nikon Micro-NIKKOR-P 55m f/3.5-32 auto lens was attached to the side-view camera. Video recording was done at 5000 frames per second for a duration for 1.5s for backward facing step experiments, and at 7500 frames per second for hydrofoil experiements.

2.5 X-ray Densitometry System

Time-resolved measurements of void fraction flow fields was performed using an x-ray densitometry system. X-ray densitometry system used in the current study, described in Makiharju (2012), Ganesh et al. (2016) and Mäkiharju et al. (2013), measured spanwise-averaged void fraction (β) measurements at 1000 fps for 0.787 s exposure time and 0.125 mm spatial resolution. A brief summary of the system is presented here.

X-ray densitometry is a non-intrusive method to estimate density of materials in the flow field. For optically opaque multiphase flows, x-ray radiation based densitometry has been used to measure void fraction flow fields. The x-ray densitometry system used in current study has a medical x-ray source capable of producing 430 mA at 150 kV peak output, and the imaging system is comprised of a scintillator. An image intensifier (1 ms de-excitation period) and a high-speed camera (Phantom V9.0) were to record video images obtained in the scintillator. A schematic of the image acquisition system is shown in figure 2.7.

The intensity of the radiation beam (photons) passing through the test section is related to the mass attenuation coefficients, material densities, and thicknesses of all the materials present along the path of the beam. For a domain with N materials Beer Lambert's law states that the ratio of transmitted intensity (I) to original source intensity (I_0) depends on the mass attenuation and thickness of the material given by :

$$\frac{I}{I_0} = e^{-\sum_{i=1}^{N}[\frac{\mu_i x_i}{\rho_i}]} = \prod_{i=1}^{N} e^{-\sum_{i=1}^{N}[\frac{\mu_i x_i}{\rho_i}]} \tag{2.3}$$

where, $\frac{\mu_i}{\rho_i}$ is the mass attenuation coefficient, ρ_i is the material density, x_i is the mass thickness ($x_i = \rho_i \cdot h_i$) and h_i is the beam length traversed through the material i. The attenuation coefficient is a known property of photon energy and any material in the domain, and is related to the material density and its atomic properties as discussed by Hubbell and Seltzer (2004). Therefore for a single material, $i = 1$, a measure of the change in intensity

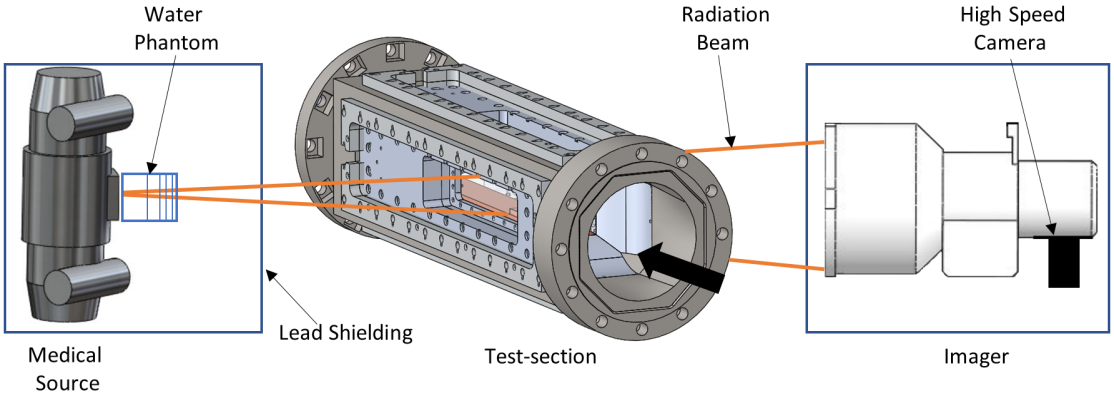

Figure 2.7: Schematic of the x-ray densitometry system depicting source, test section and the imager. A water phantom is used to set/calibrate the range of void fraction values to be investigated. The imager screen has settling time of 1 ms.

can be converted into a measure of the average density of the material along the beam path.

Chapter 3

Backward Facing Step Background

Backward facing step provides a canonical single phase flow configuration that has been extensively studied and reported in literature. Key non-cavitating flow features behind a backward facing step and observations of cavitation in shear layers/mixing layers are presented in the following sections.

3.1 Single-phase flow properties

Figure 3.1 shows a schematic of the non-cavitating flow over a backward facing step. A boundary layer separates from the sharp separation point, becoming a free shear layer. As the flow separates from the sharp separation point at the edge, shear layer flow rolls up to create large-scale spanwise vortices, similar to a mixing free shear layer structure observed by Troutt et al. (1984). The separated shear layer grows and curves, re-attaching to the bottom wall. Upstream of the re-attachment point, the flow re-circulates, and depending on the pressure at the stagnation point, the recirculating bubble can affect the shear layer as shown by Eaton and Johnston (1981). In the reattachment region, the shear layer is subjected to distorting forces due to effects of stabilizing curvature, adverse pressure gradient, and strong interaction with the wall (Eaton and Johnston (1981)). In addition, the length of the recirculating bubble formed underneath the shear layer fluctuates in a random manner introducing low frequency unsteadiness (Eaton and Johnston (1981)). This geometrically simple flow has all the features of separating and reattaching shear flows including a mixing

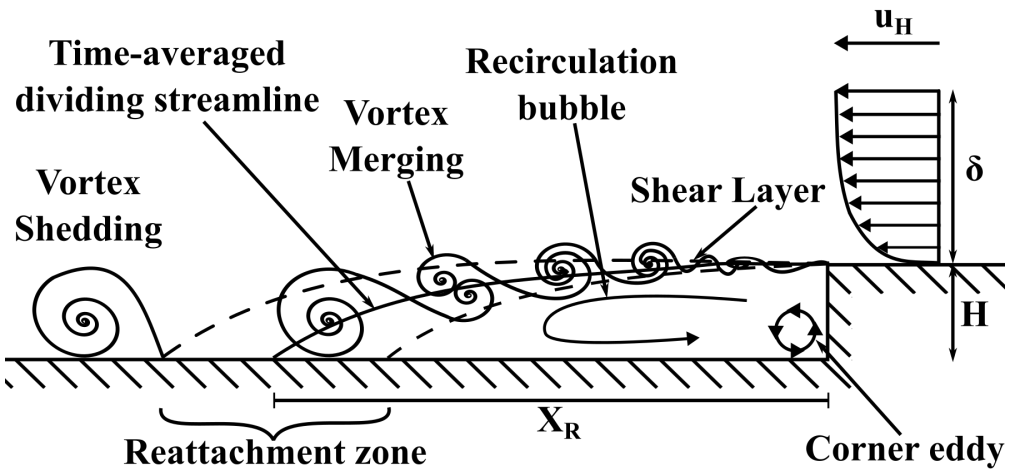

Figure 3.1: Topology of the non-cavitating flow behind a backward facing step.

layer, recirculation, re-attachment and a redeveloping boundary layer.

The variation of reattachment length X_R is discussed in detail in the review article by Eaton and Johnston (1981). This length varies from five to eight step heights ($5 < X_R/H < 8$) for well known experiments shown in figure 3.2. The parameters which have significant effect on the reattachment length are the expansion ratio of the geometry, boundary layer thickness, boundary layer state (laminar/turbulent) at separation, free-stream turbulence levels and pressure gradient in the re-attachment region.

Using PIV measurements and pattern recognition Scarano et al. (1999) presented the flow structures observed within the shear layer. Their velocity profile downstream of a step is shown in figure 3.3 where the magnitude and direction of flow reversal can be observed. Bradshaw and Wong (1972) studied the recovery of the boundary layer downstream of reattachment region as shown in figure 3.4. Their results demonstrated the importance of understanding the turbulence structure in the reattachment zone. The overall geometry determined the stream-wise pressure gradient in the reattachment zone.

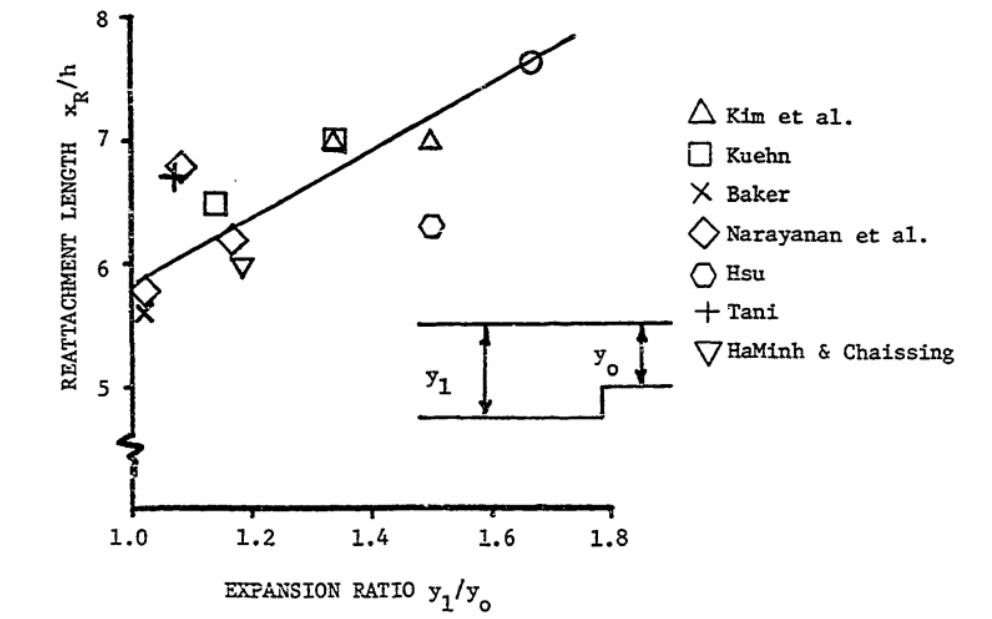

Figure 3.2: Re-attachment lengths of different experiments across different expansion ratios show that reattachment length lies between 5 to 8H (Eaton and Johnston (1981)).

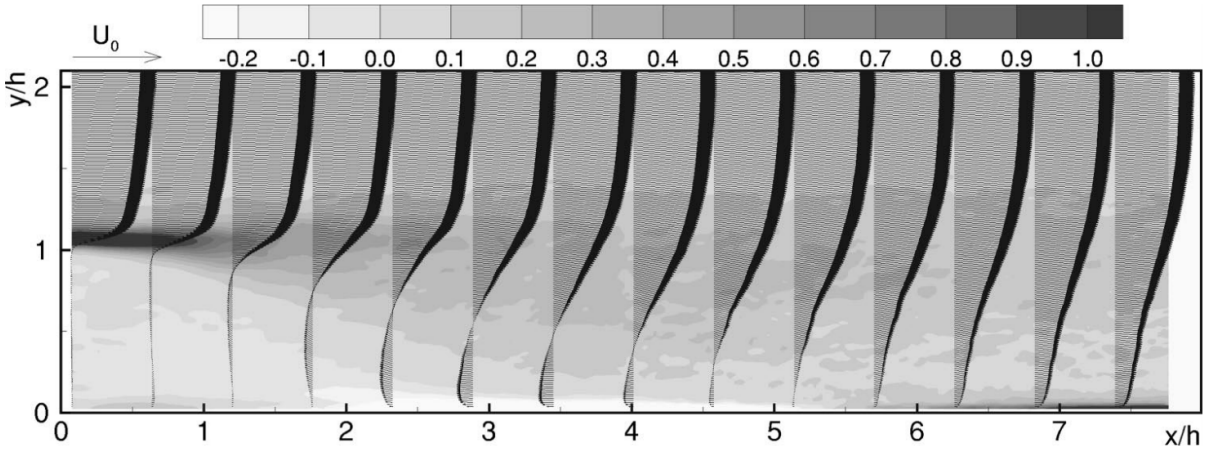

Figure 3.3: Mean flow distribution presented by Scarano et al. (1999) showing location of shear layer and flow reversal inside recirculation zone behind a backward facing step. The velocity profile is depicted over normalized spanwise vorticity distribution. Flow is from left to right.

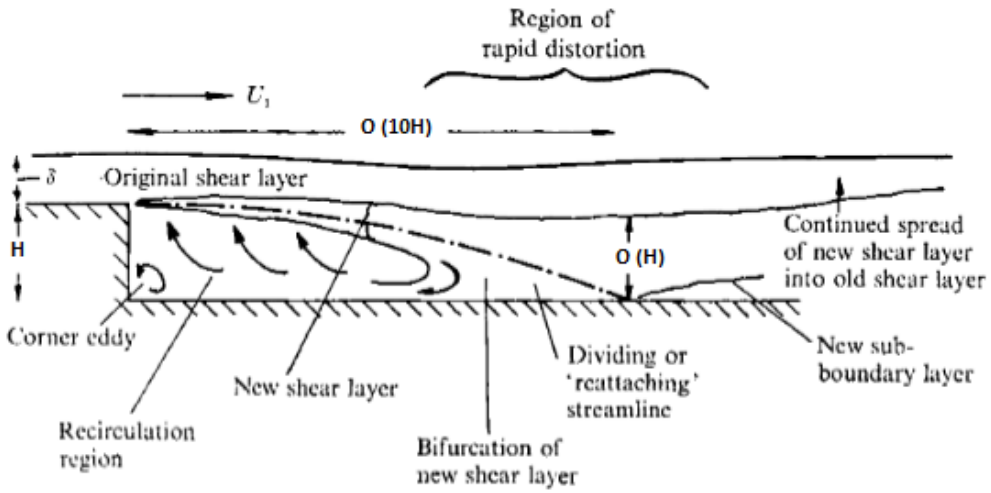

Figure 3.4: General behavior of typical reattaching flow and the distortion region near reattachment seen by Bradshaw and Wong (1972). Flow is from left to right.

3.2 Cavitating Shear Layers

Liquid flows in the wake of a backward facing step can experience cavitation if the local pressure in the shear layer falls below the vapor pressure. Katz and O'hern (1986) and O'hern (1990) reported that cavitation inception in a shear layer first occurs in streamwise braids as shown in figure 3.5 (a). Belahadji et al. (1995) postulated that during inception, cavitation bubbles decouple the stretching and rotation rates of streamwise vortices, but do not significantly alter bulk flow properties. Iyer and Ceccio (2002) reported that the overall formation, growth and convection of the primary and secondary vortical structures in the shear layer remains unaffected during inception.

Cavitation occurring in large scale structures within the shear layer was studied by Aeschlimann et al. (2011) by investigating void fraction field as shown in figure 3.6. As the extent of the cavitation increases, the void fraction values increase along with the convection speed of large-scale spanwise cavitating vortices. For cavitating wakes of bluff bodies, the presence of developed cavitation has a significant impact on large scale structure dynamics like vortex spacing, shedding frequency and convective speeds of spanwise structures reported by Franc and Michel (1983), Young and Holl (1966), Aeschlimann et al. (2011) and

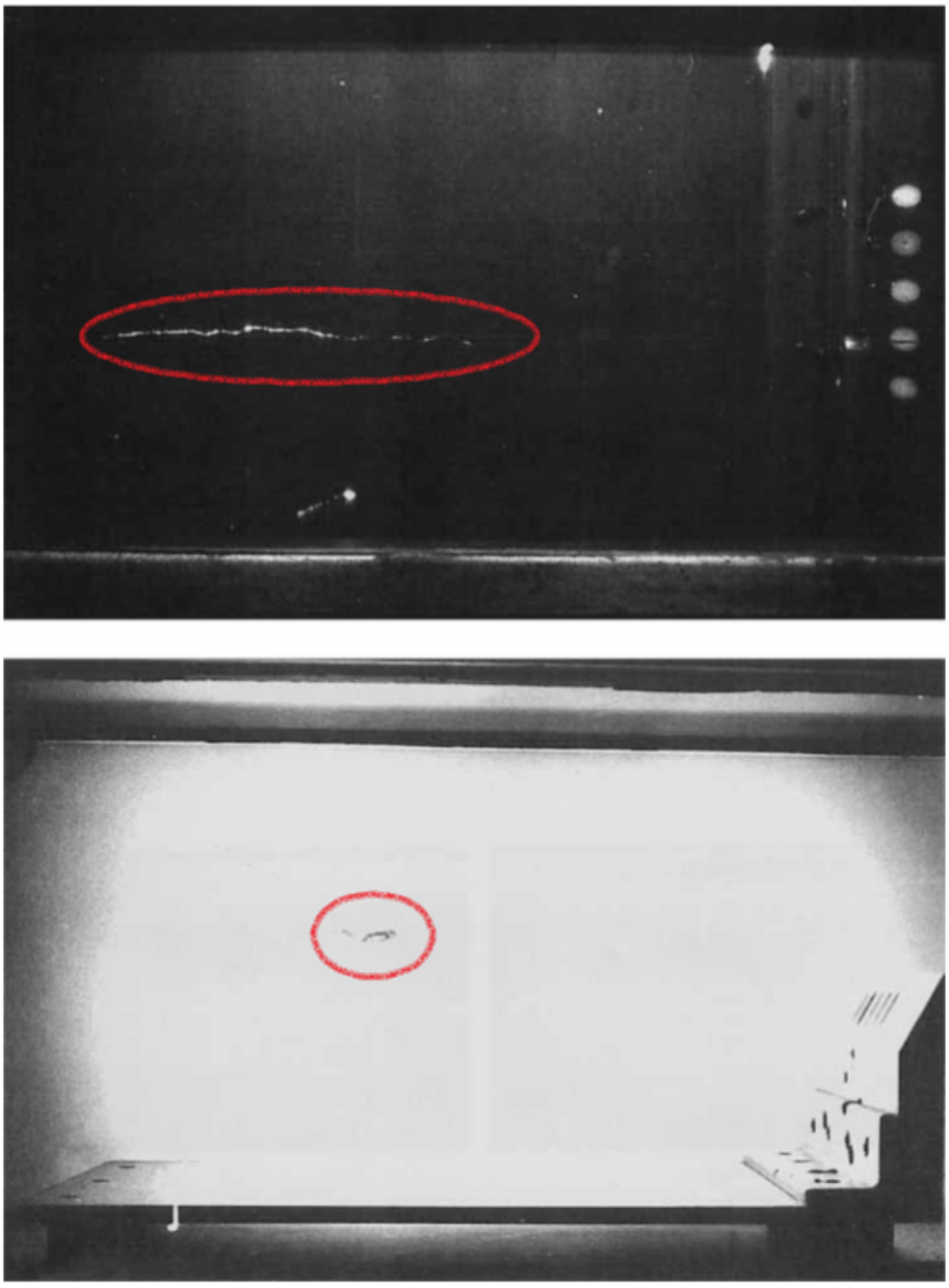

Figure 3.5: Top and side view photographs of shear-layer cavitation inception at u=7.81 m/s, σ =1.52, Re = 1.42x10^6 (O'hern (1990)). Flow is from right to left.

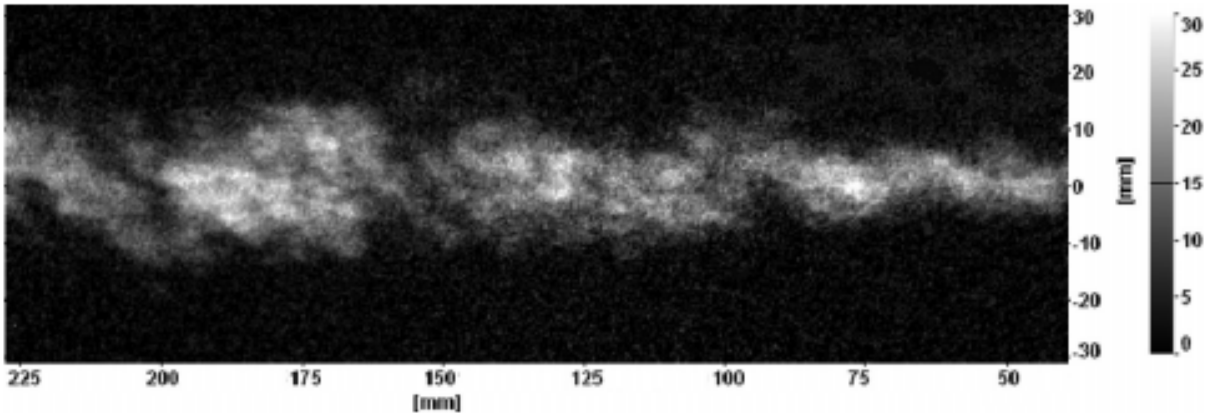

Figure 3.6: Snapshot of instantaneous void fraction(%) flow regime formed in the cavitating shear layer downstream of a sharp separation(Aeschlimann et al. (2011)). Flow is from right to left.

Wu et al. (2021).

3.3 Effect of vapor-liquid compressibility

As discussed in section 1.4, under certain cavitating conditions, mixture compressibility effects can become important. Compressibility effects can be quantified by estimating the local speed of sound and comparing it with a relevant velocity scale. Ganesh et al. (2016) and Wu et al. (2021) used simplified speed of sound expression suggested by Brennen (2005), and reported significant change in observed flow physics when the Mach number transitioned from subsonic to supersonic.

Both these studies used a simple isothermal expression for speed of sound, which does not take properly account for the heat transfer between the liquid-vapor phases during the phase change process. Budich et al. (2018) discusses the importance of taking into account the heat transfer between the phases during sound propagation in a vapor-liquid mixture. Two simple heat transfer scenarios are represented by 'the homogeneous equilibrium model' and 'the homogeneous frozen model'. The equilibrium model assumes instantaneous heat transfer between phases and mixture existing in thermodynamic equilibrium. The frozen

model assumes zero heat transfer between phases. According to Brennen (2005), the real two-phase mixture sound speed should lie somewhere between these two limiting assumptions.

Section 1.4 discussed a generalized expression for sonic-speed for two generic phases. By considering homogeneously dispersed phase (V: vapor) in carrier fluid (L: water), ϵ_L is the fraction of the liquid phase in thermodynamic equilibrium, and $(1 - \epsilon_L)$ fraction will be insulated (similarly for ϵ_V fraction of the vapor phase). The general qualitative expression that can be used for both the models to estimate the speed of sound (c) based on the general equation 1.11 is given by equation 3.1. Here, the mixture density is $\rho_m = \beta\rho_V + (1 - \beta)\rho_L$. Quantities f and g define thermodynamic properties of respective phase. For water $g^* = 1.67$, $\eta = 0.73$, $g_V = 0.91$ and $f_V = 0.73$ (Brennen (2005)). The pressure p_c (= 22.06 MPa) is the critical pressure of water. $\epsilon_V = \epsilon_L = 1$ corresponds to 'homogeneous equilibrium model' while $\epsilon_V = \epsilon_L = 0$ gives the 'homogeneous frozen model' from equation 3.1.

$$\frac{1}{\rho_m c^2} = \frac{\beta}{p}\left[(1 - \epsilon_V)f_V + \epsilon_V g_V\right] + \frac{1 - \beta}{p^{1+\eta}}\epsilon_L g^* {p_c}^{\eta} \tag{3.1}$$

In this study, 'homogeneous frozen' and 'homogeneous equilibrium' speed of sound in the mixture is estimated based on measurments of void fraction β and cavity pressure p. Mach number based on these estimations are examined for subsonic to supersonic transition that coincides with the onset of first observation bubbly shocks. The speed of sound expression that best represents the observed physics in the current experimental setup is then identified.

3.4 Road map

In the current study, flow features of developed cavities forming in the wake of a backward facing step are examined using high speed videography and time resolved x-ray densitometry. First, the experimental results are presented in chapter 4. The velocity profile and single phase flow measurements near separation point are presented in section 4.1. The cavity

topology and three flow regimes of interest (Type A, B and C) are presented in section 4.2. Instantaneous void fraction timeseries of snapshots describing a typical shedding cycle for each of type B and C are shown and important flow features are identified in section 4.3. Cavity shedding frequency detailing the dynamics of the cavity are discussed for each shedding regime in section 4.4. Static pressures within/outside cavity are discussed in section 4.5. In chapter 5, bubbly shock properties are presented along with 1D jump conditions. Finally, the observations are related to compressibility effects, and expression for local speed of sound that best represents experimental observations are presented in section 5.2. The final conclusions of the backward facing step study are presented in chapter 6.

Chapter 4

Backward Facing Step : Experimental Results

This chapter presents Particle Image Velocimetry (PIV), high-speed cinematography, pressure measurements and time-resolved x-ray densitometry results.

4.1 2-D planar PIV

Velocity profile slightly upstream of the step is measured using PIV. For boundary layer thickness (δ) measurements, a 14 mm X 7.5 mm field-of-view shown in figure 2.4, is used. Boundary layer upstream of the step ramp is tripped to ensure transition to turbulence. The measured velocity profile is fit with a $1/7^{th}$ power law, shown in figure 4.1(a), and boundary layer thickness(δ) is determined as the location of 99% free-stream velocity. The log-law plot in the linear region using u^+ and y^+, estimated using equation 4.1, is shown in figure 4.1(b). PIV measurements were also performed in the separated region behind the step to determine the reattachment length, X_R.

$$u^+ = \frac{1}{\kappa} ln y^+ + C^+ \tag{4.1}$$

In equation **??**, $y^+ = \frac{y u_\tau}{\nu}$, $u^+ = \frac{u}{u_\tau}$, $u_\tau = \sqrt{\frac{\tau_w}{\rho}}$, $\tau_w = \rho\nu \frac{du}{dy}\Big|_{y=0}$, $\kappa = 0.41$, $C^+ = 5.1$ and $\nu = 1.05 \cdot 10^{-6}\ m^2 s^{-1}$. u is the velocity parallel to the wall, and y is the distance from the wall.

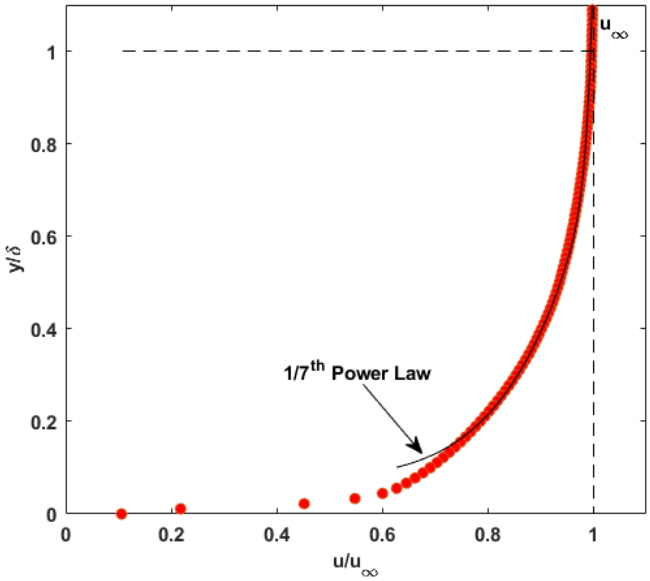

(a) The velocity profile at $u_H = 10.9$ m/s and $1/7^{th}$ power law used to fit the profile

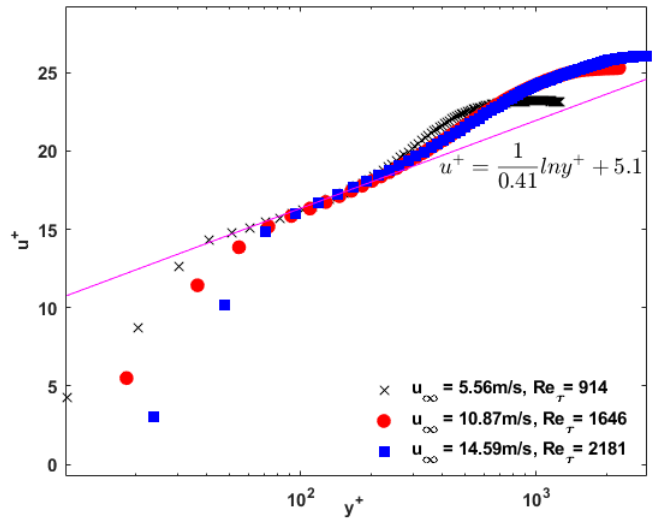

(b) The semilog u^+ vs y^+ plot shows the curve for the three compared speeds, collapse in the linear region. u_τ is calculated near the wall using $u_\tau = \sqrt{\nu \cdot \frac{du}{dy}\Big|_{y=0}}$ where $\nu = 1.05 \cdot 10^{-6}\ s^{-1}$. u_τ has an uncertainty of $\pm$ 0.03

Figure 4.1: Depiction of process of measuring (a) Boundary layer thickness (b) Collapse of u^+ and y^+ for three flow speeds used for comparison with JHU

4.2 Visual Observation of Cavitation

To observe cavitation events, cavitation number (σ_0) is changed by reducing inlet pressure (p_0) from inception (near $\sigma_0 = 1$) to near super-cavitation (near $\sigma_0 = 0.6$), at a fixed inlet speed u_0. Inception first occurs in streamwise braids, as observed in previous studies (O'hern (1990)). A high-speed video snapshot of an incipient cavity is shown in figure 4.2. On reducing p_0 further, extent of cavitation in the shear layer increases, between X = -3H to -5H. The location of X=0 is given in figure 2.2. These cavities shown in figure 4.3(a), were classified as type A or 'developing cavitation'. Developing cavitation is characterized by the presence of vapor bubbles in both streamwise and spanwise vortices of the shear layer. Type A cavities do not experience large-scale shedding of vapor clouds, but the location of the cavitating region oscillates.

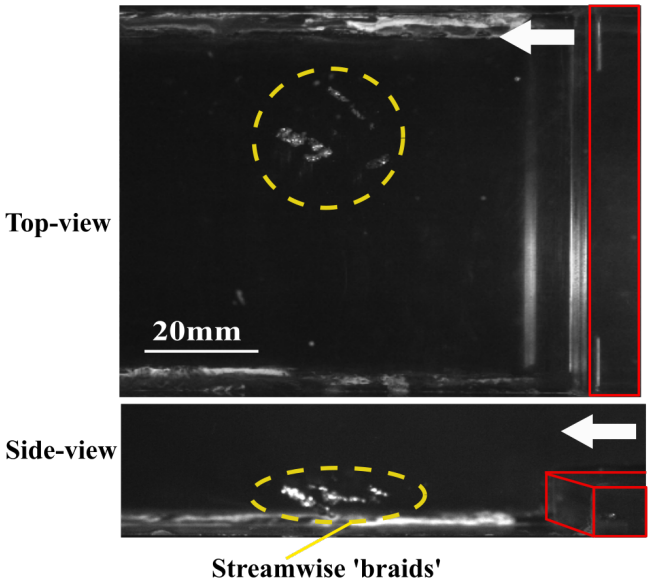

Figure 4.2: Cavitation inception in the streamwise direction is highlighted (streamwise 'braids' , Katz and O'hern (1986)). Intermittent cavitation occurs at $\sigma_0 = 0.98$ for $u_H = 10$ m/s. The red lines highlight the edge of the step.

With a reduction in inlet pressure p_0, unsteady cavitation designated as type B is observed. Type B is a self-sustained shedding cavitation regime with periodic oscillation of the cavity length. As p_0 is reduced further, type C cavitation is observed. Type C cavitation

has a lower shedding rate than type B, and occurs before super-cavitation. Maximum cavity lengths for type C start to extend beyond the field of view of the x-ray densitometry system. Figure 4.3 (b) and figure 4.3 (c) show high-speed video snapshots of type B and type C cavities respectively.

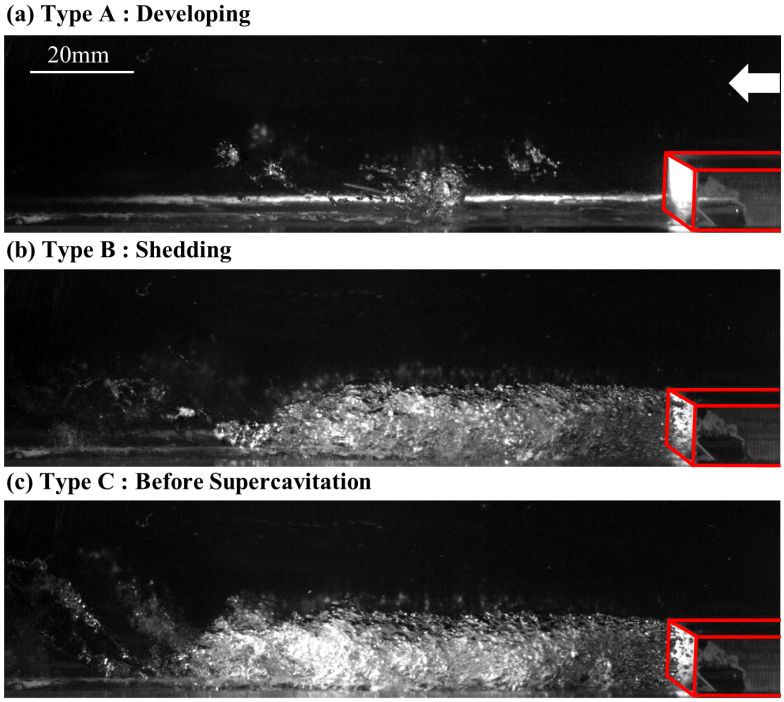

Figure 4.3: High speed snapshots of three different cavitation regimes (a, b, c for σ_0=0.78, 0.72, 0.60 respectively) at $u_H = 10$ m/s. Type A comprises of cavitation in shear layer mostly near reattachment region(away from separation point). Types B and C shedding regimes are of primary interest in this study.

4.2.1 A Typical Shedding Cycle

Type B and type C cavities have similar shedding cycles, and a typical shedding cycle of type B cavitation is shown in figure 4.4. Cavitation occurs in both strong spanwise vortices and weaker streamwise vortices. Shedding cycle begins with cavitation occurring in the core of the spanwise vortex (green in figure 4.4(b)). As this spanwise vortex moves downstream, the extent of cavitation in this vortical structure increases. At the same, cavitation begins in the upstream spanwise vortical structure closer to the step (blue in figure 4.4(c)). Both these

structures convect downstream and become indistinguishable with large amounts of vapor in the region between them (green and blue in figure 4.4(d)(f)). At this point the separated region begins to fill from the aft of the cavity with vapor and cavity collapse follows.

4.3 Void Fraction Measurements

Time-resolved spanwise averaged void fraction are measured for type A, B, and C cavities using x-ray densitometry. For inception and developing cavitation (Type A) regime, the measured mean void fraction values are less than 10%. Mean void fraction fields obtained from x-ray densitometry measurements of type A, B and C cavities, and the definition of the cavity length are shown in figure 4.5. Cavity length ($< L_C >$) is measured from the base of the step to a region where mean void fraction falls below 5%. For shedding cavities, cavity length ($< L_C >$) is estimated as maximum length observed in a given cycle. In addition, distance to the maximum mean void fraction ($max(\beta_{MEAN})$) in the field is defined as $< L_M >$. Figure 4.5(b) shows the definition of $< L_C >$ and $< L_M >$. Variation of $< L_C >$ and $< L_M >$ is shown in figure 4.6.

$$\beta_{MEAN} = \sum_{N=0}^{786} \frac{\beta(X, Y, N)}{787} \tag{4.2}$$

4.3.1 Average Cavity Length

From figure 4.6, it is observed for a given σ_0 higher Re have lower the mean cavity lengths. L_M, which signifies the location of maximum averaged void fraction, lies between 3 to 4 H, and does not have a Re dependence. The location of maximum void fraction, L_M, occurs at the location of maximum shear stress as reported by Jovic and Driver (1995).

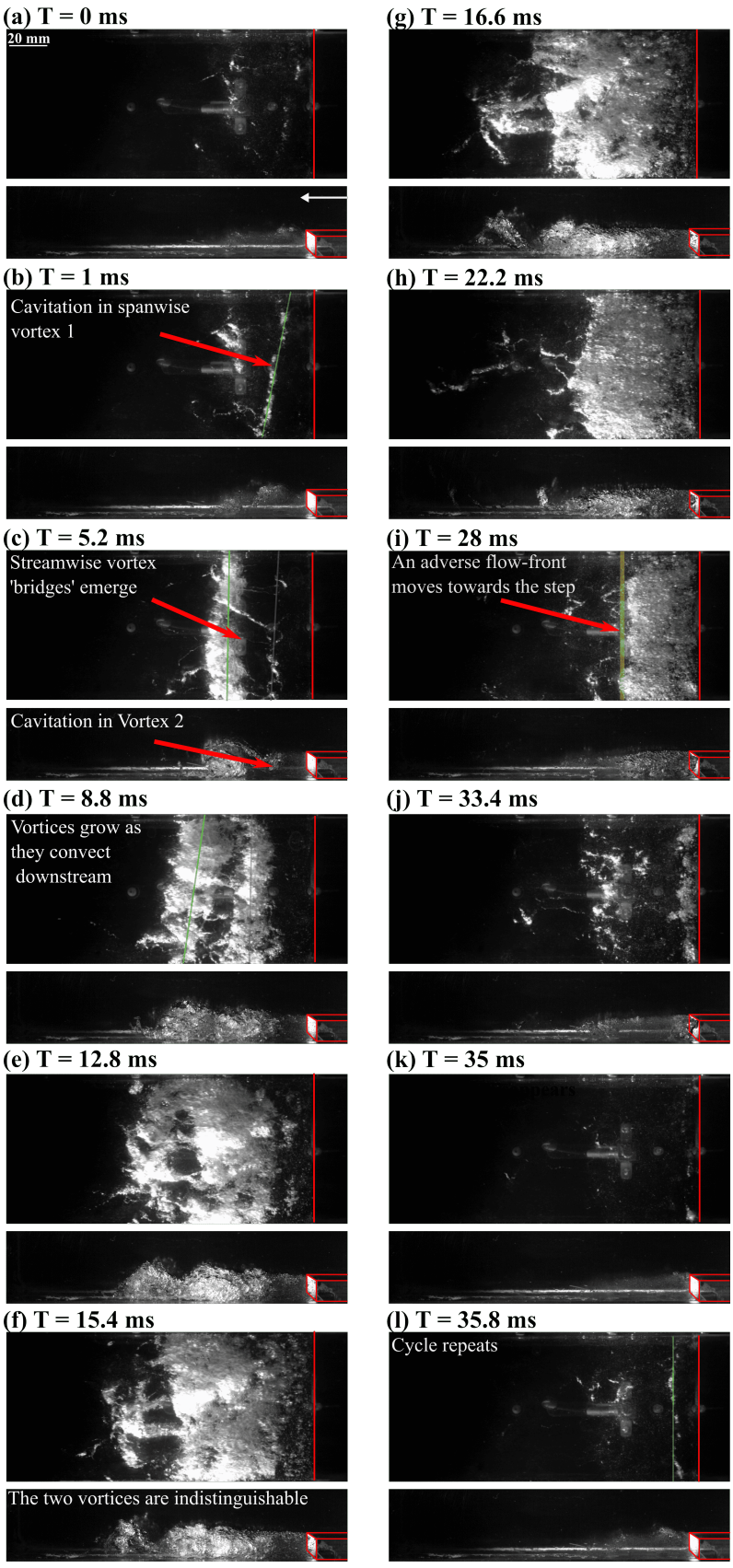

Figure 4.4: The time-series of high speed snapshots of a periodic Type B shedding cycle. Case at $\sigma_0 = 0.72$ for $u_H = 10$ m/s. Cycle starts with visible cavitation in spanwise vortex(b). The recirculation bubble and shear layer continue to fill with vapor (e)-(g), until an adverse flow front (i) causes the cavity to disappear(shed cavity in (k)).

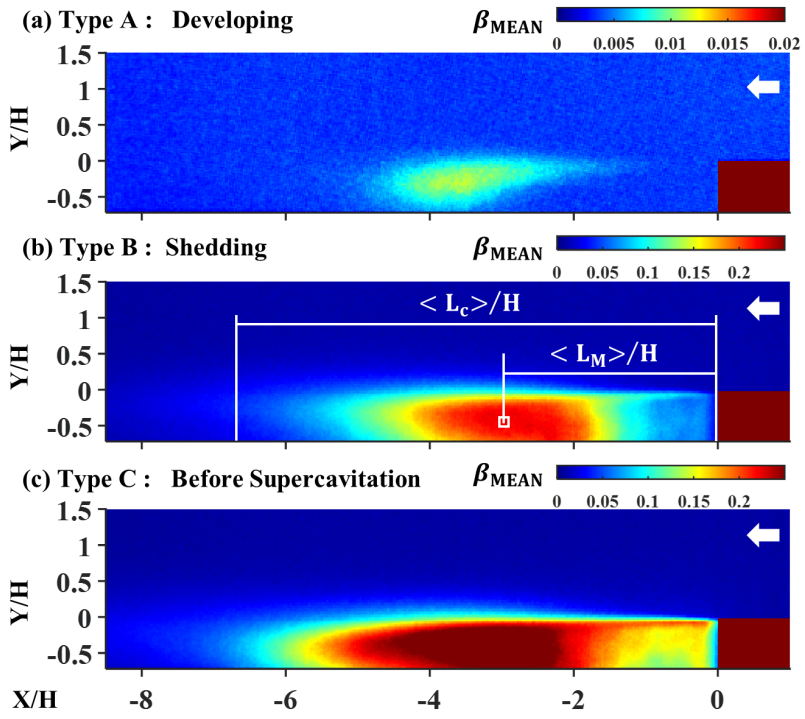

Figure 4.5: The mean void fraction fields (snapshots) of the three cavitation regimes (a, b, c for σ_0=0.78, 0.72, 0.60 respectively) at $u_H = 10$ m/s. The mean length of cavity $< L_C > /H$ and distance to maximum void fraction value (in the mean field, $< L_M > /H$ are shown. The actual densitometry data captures entire 0-100 % void fraction scale, but color scale artificially limited to 0-2% for Type A and 0-25% for the rest.

4.3.2 Mean void fraction profiles

The mean void fraction profiles for Type B cavitation at different Re are shown in figure 4.7. The profiles, with an uncertainty of 2%, for Type-B are similar across the three Re. X-slices of the mean void fraction field for Type B shedding regime at $X = -H, -3H, -4H, -5H$ & $-7H$ are shown in figure 4.8. RMSD void fraction of type B and void fraction profiles for type C are shown in Appendix C.

4.3.3 Instantaneous Void Fraction fields

Instantaneous void fraction fields of a typical type-B shedding cycle are shown in figure 4.9. The cycle begins with cavitation in the core of a spanwise vortex (vortex 1), highlighted in

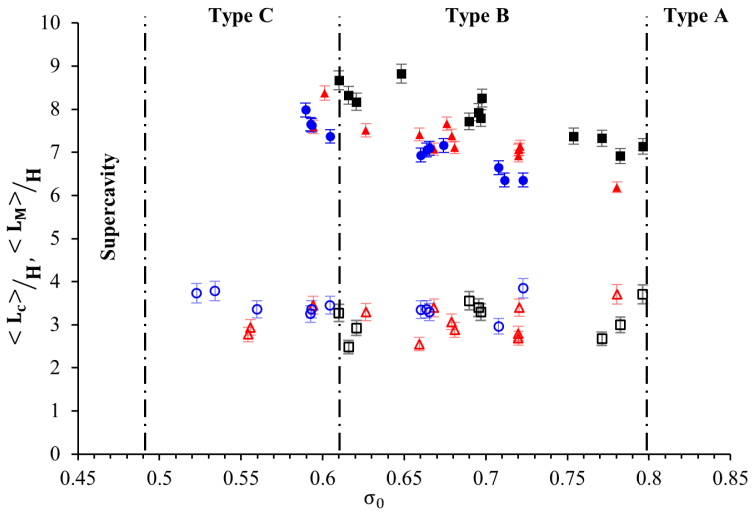

Figure 4.6: Mean cavity length($< L_c >$) and location of maximum void fraction($< L_M >$) for $u_H = 8m/s$(■,□), $10m/s$(▲,△), $12m/s$(○,●) for different σ_0. Closed symbols are for $< L_c >$ and open symbols for $< L_M >$.

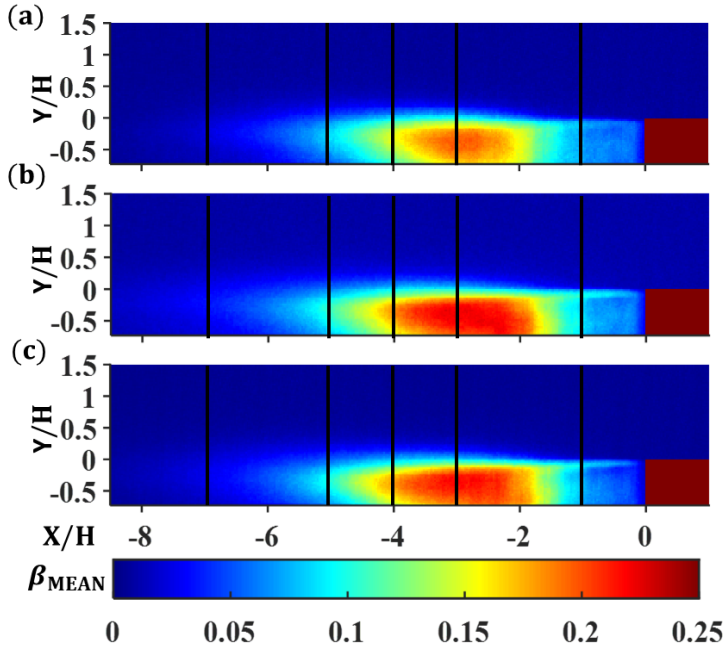

Figure 4.7: Mean void fraction contours at u_H = (a) 8 m/s, (b) 10 m/s and (c) 12 m/s at $\sigma_0 = 0.72$. 5 slices at X/H = -1, -3, -4, -5, -7 are taken to compare void fraction values across the three velocities shown in Figures 4.8,C.1, C.2. Flow is from left to right.

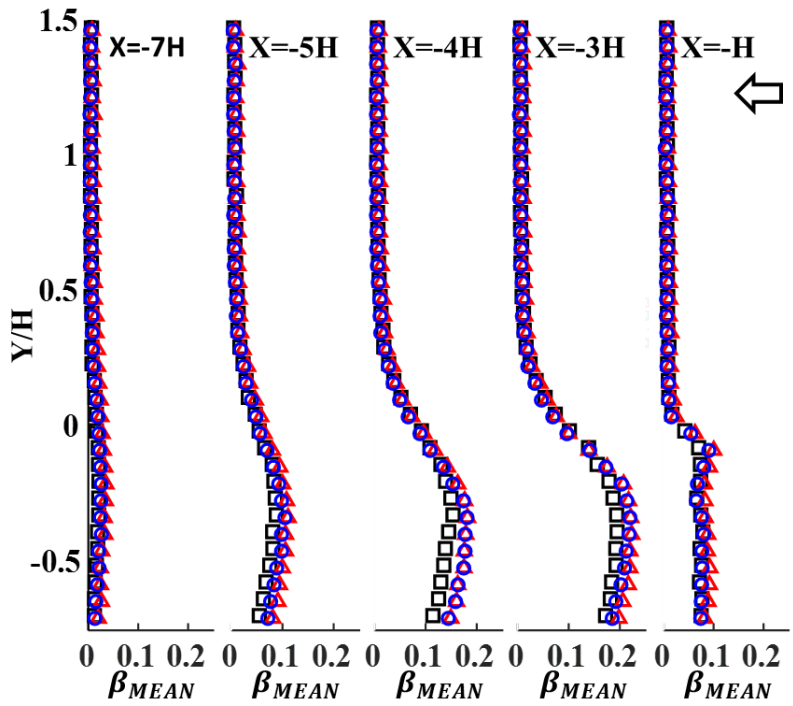

Figure 4.8: Mean void fraction values (2% uncertainty) along slices Y/H = -1 to 1.5; u_H = $8m/s$(□), 10 m/s (△) and $12m/s$(○) at $\sigma_0 = 0.72$ (Type B). The mean void fraction values are comparable across three *Re*.

green between X = -0.5H to X = -2H in figure 4.9(a). As this structure convects downstream, it grows in size and interacts with the upstream spanwise vortex, highlighted in blue in figure 4.9(c)-(d). Subsequently the vortex pair becomes indistinguishable and a filled cavity starts to emerge between X = -2H to X = -6H seen in figure 4.9(e)-(g). High-speed snapshots of fully grown type B cavity in figure 4.4(f)-(g) appear to be quasi-steady. However, x-ray measurements in figure 4.4(f)-(g) reveal that the bubbly mixture undergoes changes in its composition during this portion of the cavity shedding cycle.

Instantaneous void fraction fields of type C shedding case is depicted in figure 4.10. Upon comparison with type B cavities, it is observed that type C cavities have higher vapor content. Lower cavitation numbers leads to fuller/longer cavity with a consistently filled shear layer. At maximum cavity length in a given cycle, a bubbly shock propagating upstream is seen more clearly compared to Type B, as shown in figure 4.10(g)-(h). As the bubbly shock reaches the step, the cavity collapses, and a cavitating spanwise vortex is shed from the step.

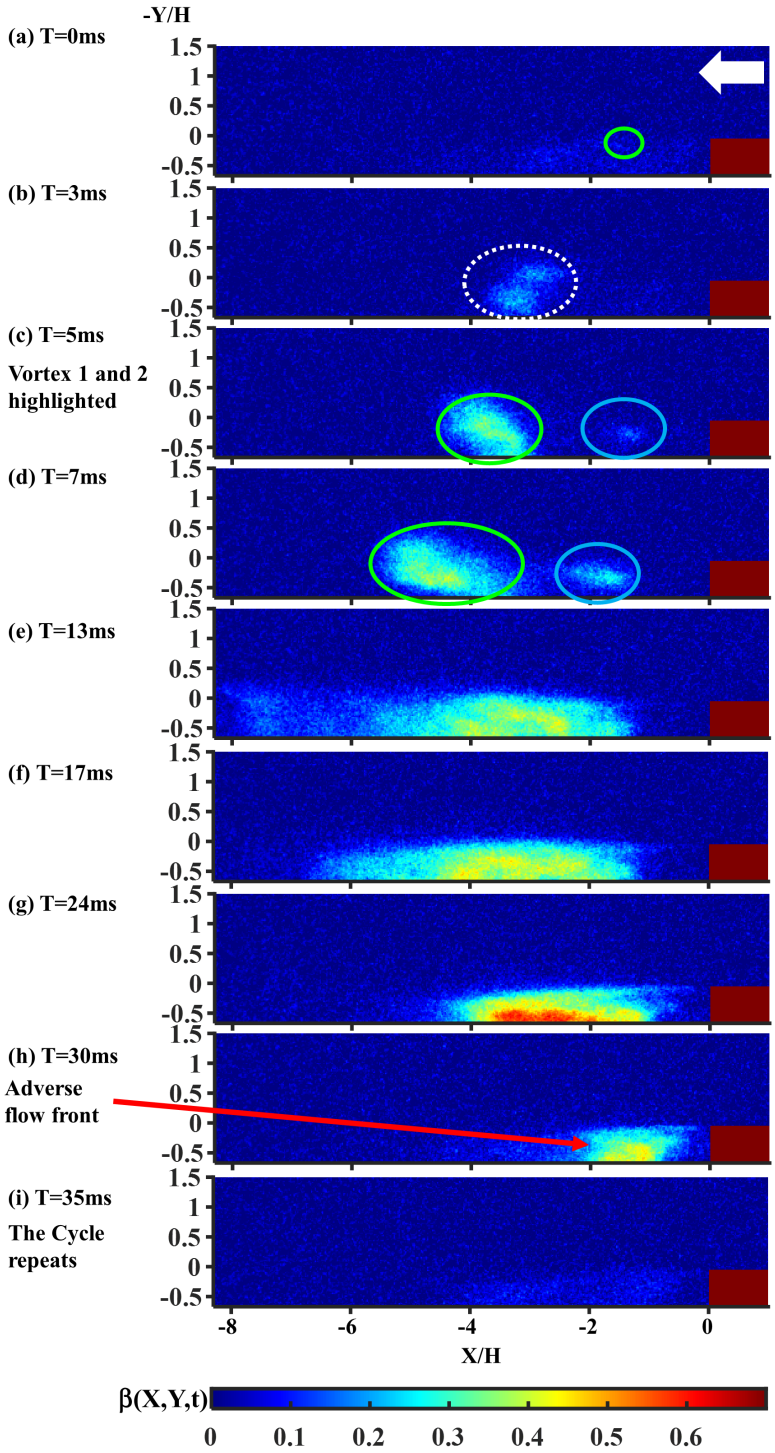

Figure 4.9: X-ray timeseries of a typical Type B shedding cycle at σ_0=0.72 for $u_H = 10$ m/s. The void fraction ($\beta(X, Y, t)$) range is set to 0-70%. The adverse flow front highlighted in (h) is the bubbly shock front.

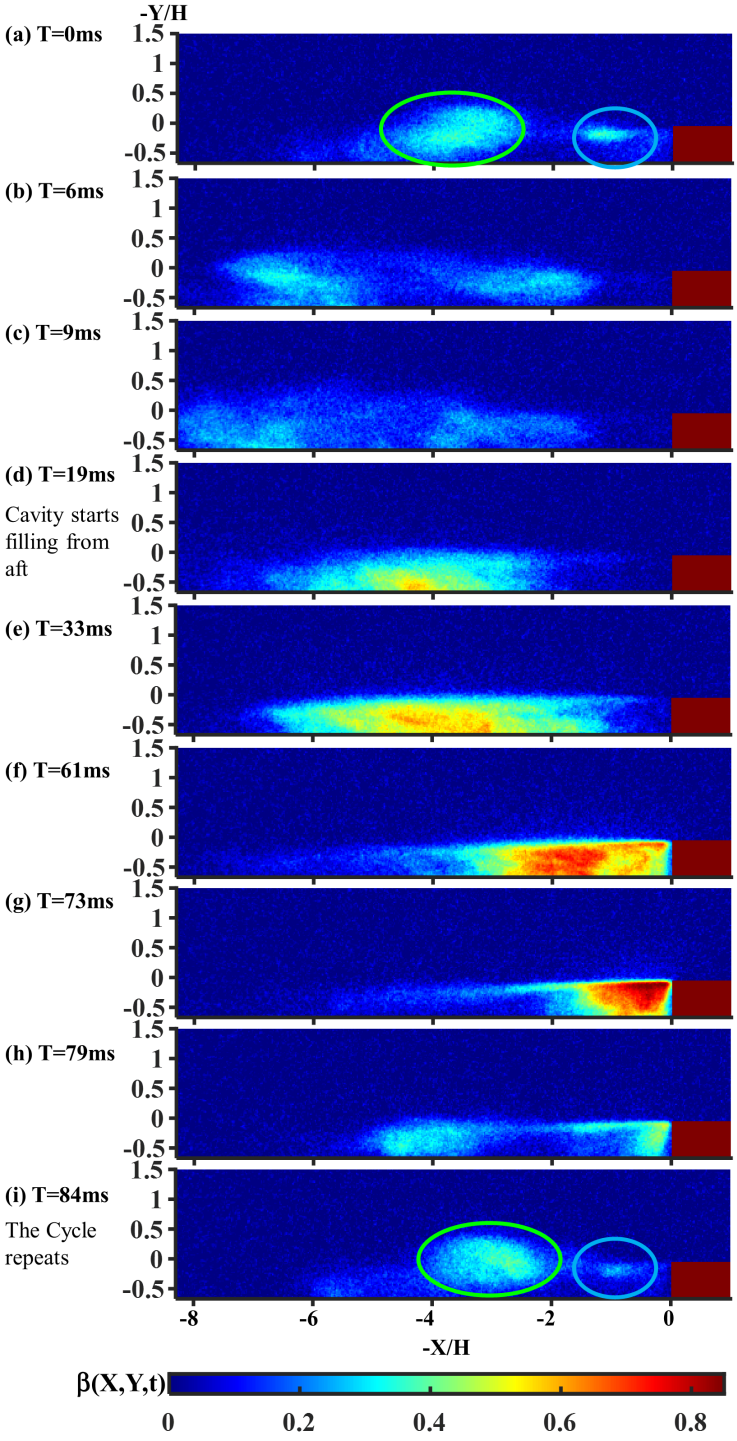

Figure 4.10: X-ray timeseries of a typical Type C shedding cycle at $\sigma_0 = 0.60$ for $u_H = 10$ m/s . The void fraction ($\beta(X, Y, t)$) range is set to 0-85%. Compared to type B, type C cavities are longer, have higher vapor content and collapse at a slower rate. High speed snapshots of type C appear quasi steady, unlike the x-ray timeseries which clearly show shedding.

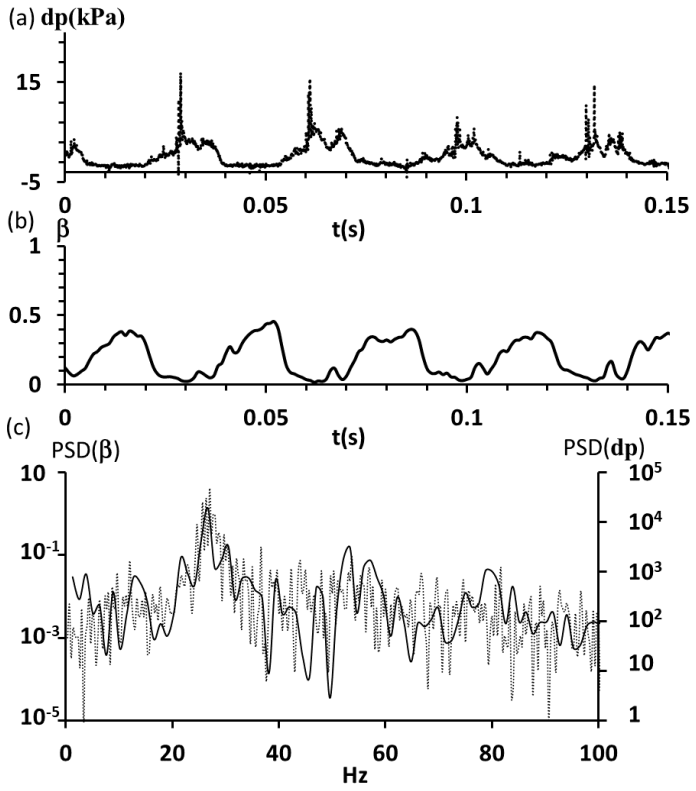

Figure 4.11: Dynamic pressure signal(a,$\cdots$) synchronized with time varying void fraction signal (b,$-$) and corresponding power spectral density(c) for a type B cavitating case at $\sigma_0 = 0.73$ at $u_H = 10$ m/s. The highest energy peaks are close.

4.4 Cavity Shedding Dynamics

Cavity shedding cycle shown in figure 4.4 and figure 4.9 occurs periodically. As the flow transitions from type A to type C, the shedding frequency, f, also changes. Periodicity observed in the shedding regimes is quantified by measuring the time variation in flow properties such as void fraction (β) and unsteady pressure within the cavity (dp). The location of the unsteady pressure transducer is shown in figure 2.3. The Strouhal number (St) used to non-dimensionalize the shedding frequency is given by equation 4.3.

$$St = \frac{f \cdot H}{u_0} \tag{4.3}$$

Shedding frequency from void fraction field is determined by spatially averaging local void

fraction over a 1.25 mm by 0.875 mm probe area located at (-5.5H, -0.5H). The shedding frequency determined from the void fraction signal is independent of the probe location, in the range X = -6.5H to -0.5H (Y= -H to 0). In addition, the shedding frequency is also determined from the dynamic pressure transducer (dp) measurements. Figure 4.11 and figure 4.12 show the dynamic pressure signal (dp), the time varying void fraction signal, and corresponding power spectral densities for type B and type C cavities.

Dominant shedding frequencies observed at different σ_0 lie between 10-70 Hz. The resulting St estimated from strongest frequency peak monotonically decreases with decreasing σ_0 as shown in figure 4.13. Note that St is not strongly influenced by changes in Re. Similar trend in St vs σ_0 is observed from void fraction measurements. Type-B shedding cavities are more aggressive with higher magnitudes of PSD than type-C cavities. When the inlet cavitation number is reduced ($\sigma_0 < 1.0$) the cavitation regime approaches the supercavitation state and unsteadiness in the cavity shedding process decreases.

4.5 Cavity Static Pressure

Static pressure along the wall is measured at different stream-wise locations within the cavity. Figure 2.3 shows the location of the static pressure taps, p_1, p_2, p_3, p_4, and the dynamic pressure transducer dp. The $-C_p$ values, based on equation 4.4 where where $i = 1, 2, 3$ corresponds to the pressure measured at the three static pressure taps underneath the cavity, at different σ_0 for p_1 and p_2 are shown in figure 4.14. $-Cp_2$ is higher than $-Cp_1$ for all Re. Both $-Cp_1$ and $-Cp_2$ peak around σ_0 = 0.71-0.78, which corresponds to onset of type B shedding. As cavity fills with vapor, $-Cp$ decreases. Cavitation number based on cavity pressure can be defined as σ_c, where $\sigma_c = -Cp_1$. In figure 4.15, the cavity pressure is seen to approach vapor pressure (–) as σ_0 is reduced. This suggests that during type B and type C shedding cycles, the cavity is not homogeneously filled with vapor, as also evidenced by the void fraction measurements.

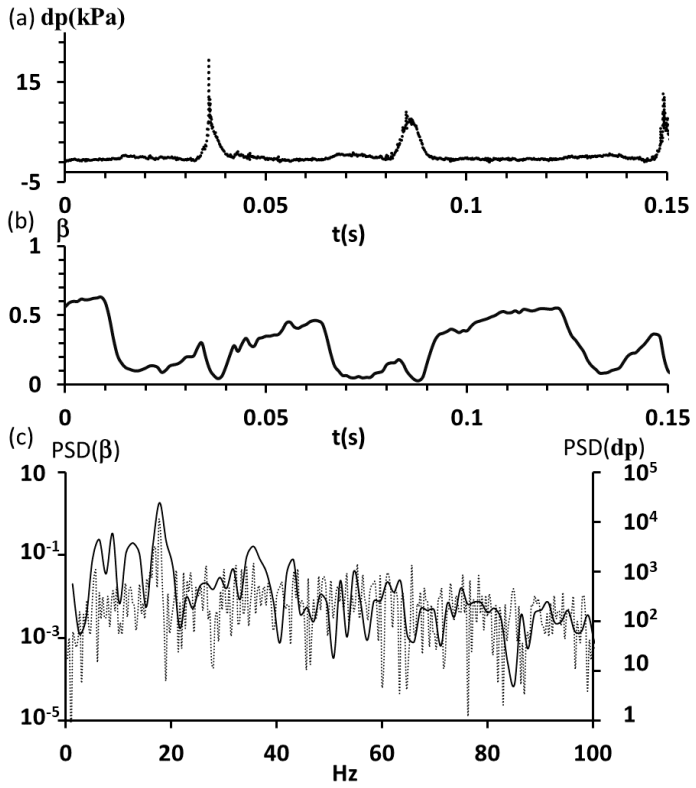

Figure 4.12: Dynamic pressure signal(a,$\cdots$) synchronized with time varying void fraction signal(b,$-$) and corresponding power spectral density for a Type C cavitating case at $\sigma_0 = 0.59$ at $u_H = 10$ m/s. Compared to Type B, a lower shedding frequency and lower pressures dp can bee observed.

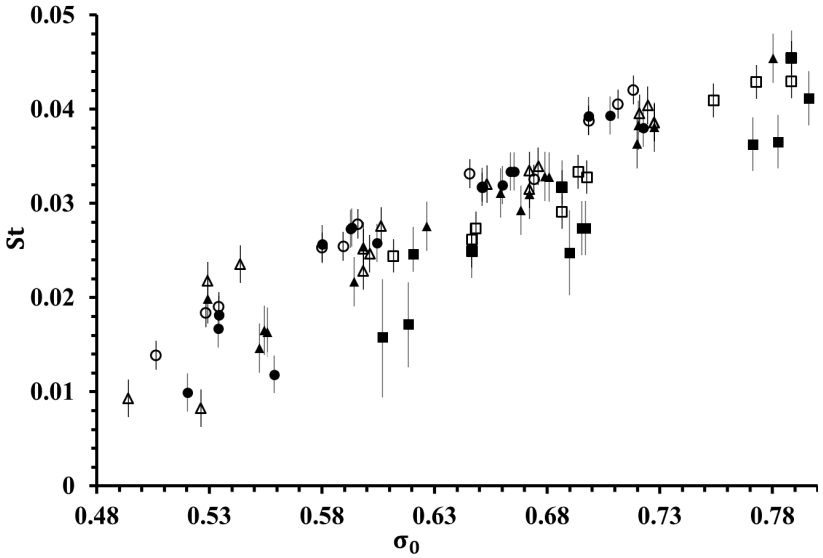

Figure 4.13: The change in shedding frequency (St) with decreasing σ_0. $u_H = 8$ m/s (□■), 10 m/s (△▲) and $12m/s$ (○●). The St obtained through the void fraction signals(β) are shown in filled symbols, while open symbols depict St from dp signal.

$$Cp_i = \frac{p_i - p_0}{\frac{1}{2} \cdot \rho \cdot {u_0}^2} \tag{4.4}$$

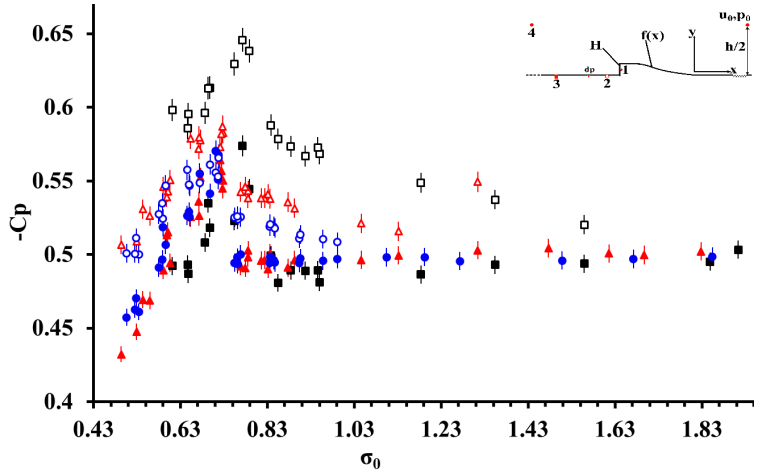

Figure 4.14: The values of $-Cp_1$ (filled, ■▲●) and $-Cp_2$ (open, □△○) as σ_0 is reduced across three Re; u_H = 8 m/s (□■), 10 m/s (△▲) and $12m/s$ (○●). Magnitude of Cp_2 is higher than Cp_1 for all three Re indicating that behind the step, the pressure drops between pressure taps at location 1 and 2.

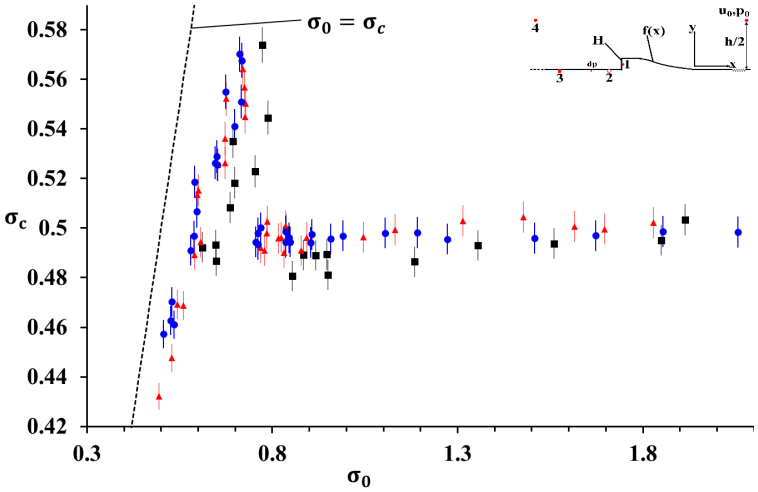

Figure 4.15: σ_c with decreasing σ_0 (Closer look at -Cp_1). $u_H = 8m/s$(■), $10m/s$(▲), $12m/s$(●). At lower cavitation numbers, pressure inside the cavity approaches vapor pressure.

$-Cp$ for p_3 and p_4 are shown in figure 4.16. $-Cp_4$ remains comparatively unchanged across different cavitation regimes. At high cavitation numbers $-Cp_3$ is negative, indicative of higher pressure in the re-attachment region compared to the inlet pressure as suggested in previous literature (Jovic and Driver (1995)). $-Cp_3$ increases as flow transitions from type

B to type C. This is due to drop in p_3 as the cavity grows longer.

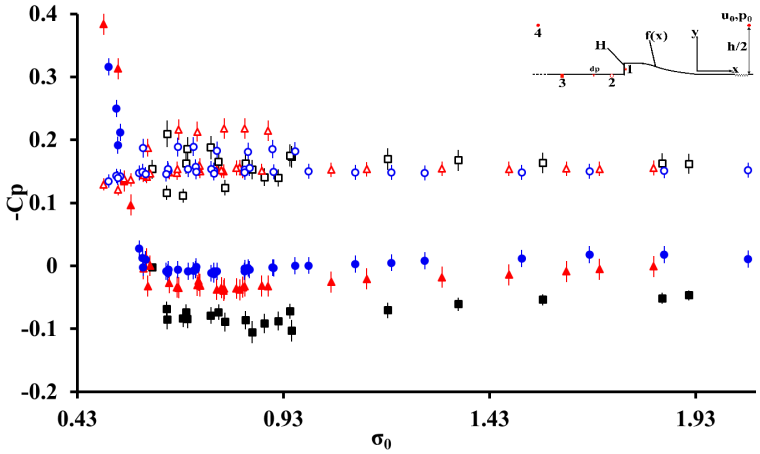

Figure 4.16: The values of $-Cp_3$ (■▲●) and $-Cp_4$ (□△○) as σ_0 is dropped across three Re; $u_H = 8m/s$(□■), $10m/s$(△▲) and $12m/s$(○●)

Chapter 5

Backward Facing Step : Analysis

This chapter presents the analysis of time resolved void fraction fields and pressure measurements to understand compressibility effects. Properties of propagating bubbly shocks such as pressure rise, void fraction jump, and shock speeds are presented. Speed of sound estimated from static pressure measurements and void fraction fields based on two speed of sound models and the corresponding Mach numbers (M_H) are presented.

5.1 Bubbly Shock Properties

Bubbly shock waves, shown in figure 4.9(h), cause the collapse and shedding of the cavity behind the step. Ganesh et al. (2016), Budich et al. (2018), and Bhatt and Mahesh (2020) discuss the conditions needed for the occurrence of bubbly shock waves. As σ_0 is reduced, and as flow transitions from type A to B, the vapor content in shear layer and recirculation bubble increases. Such an increase in vapor volume fraction causes the local speed of sound values to reduce. From instantaneous void fraction fields and dynamic pressure measurements, shocks speed and their associated pressure rise can be inferred. Measured shock speed can then be compared with the shock speed estimated from 1-D jump relations. Such a comparison will provide insight on the validity of such a simple 1-D relation in modeling of these flows.

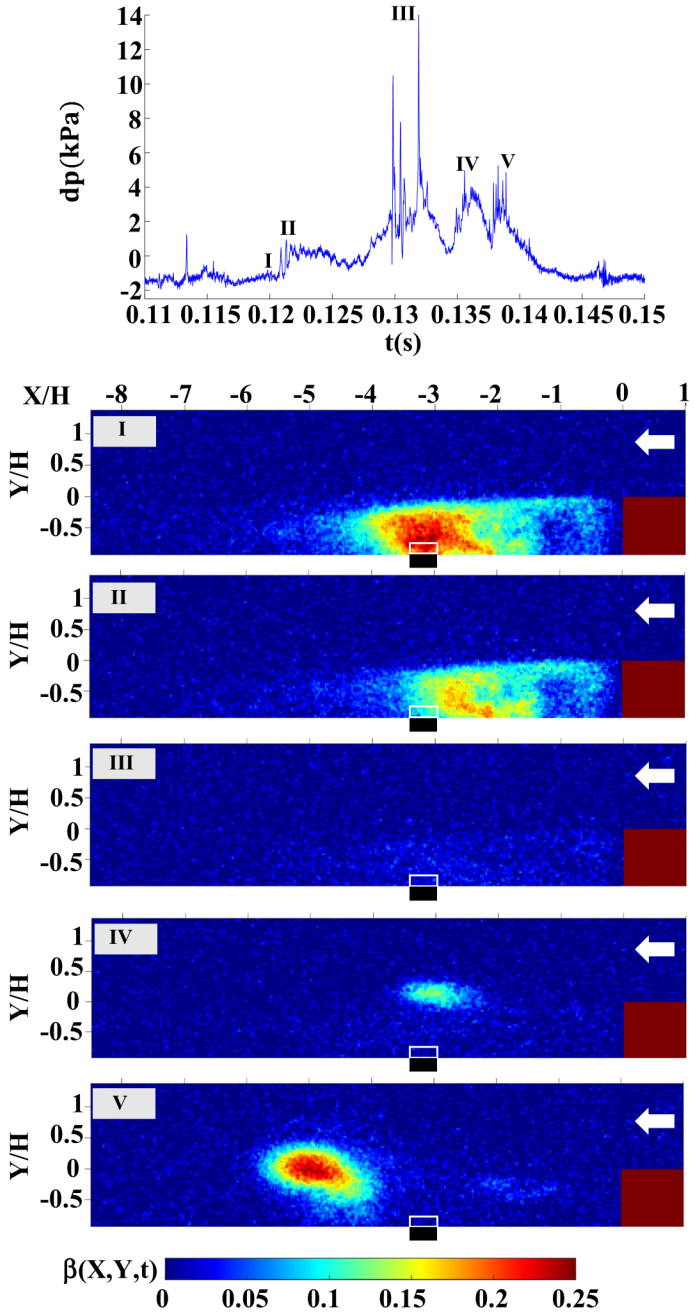

Figure 5.1: The differential pressure (dp) and corresponding X-ray densitometry snapshots as the shock-front moves past the transducer and hits the step during a shedding cycle. σ_0=0.72 for u_H = 10 m/s.

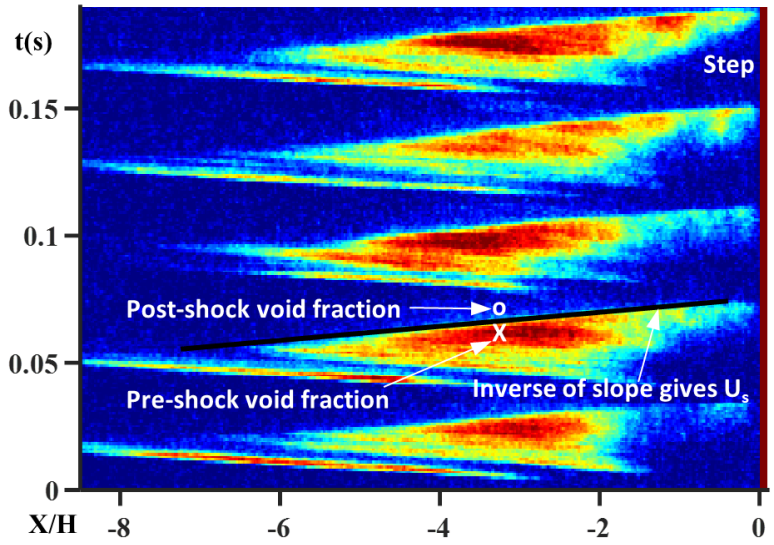

Figure 5.2: X-T diagram at Y/H = -0.25; σ_0=0.72 for u_H = 10 m/s. The shock propagation is assumed to be linear and inverse of the slope of X-T diagram gives shockspeed.

5.1.1 Synchronized pressure and void fraction measurements

Figure 5.1 shows synchronized variation of void fraction fields (β) and dynamic pressure measurements (dp) during a shedding cycle. In figure 5.1, (I) corresponds to the instance when the bubbly shock is downstream of the transducer. As the shock wave passes over the transducer, the pressure increases, and void fraction decreases as shown in (II). After shock passage the dynamic pressure transducer detects a large pressure rise at (III) when the shock impinges on the base of the step. Passage of the shed cavitating spanwise vortex causes the pressure to increase as shown in (IV) and (V).

5.1.2 Shock properties from void fraction fields

Shock propagating velocity (U_S) is estimated from void fraction flow fields using an X-T diagram. Figure 5.2 shows an X-T diagram, where X is the co-ordinate along the streamwise direction at a height of $Y/H = 0.25$ from the bottom wall. Shock speed U_S is determined by estimating the inverse of slope shown in figure 5.2. In addition, the pre- and post-shock void fraction, β_1 and β_2, are also determined at the location of the dynamic pressure transducer.

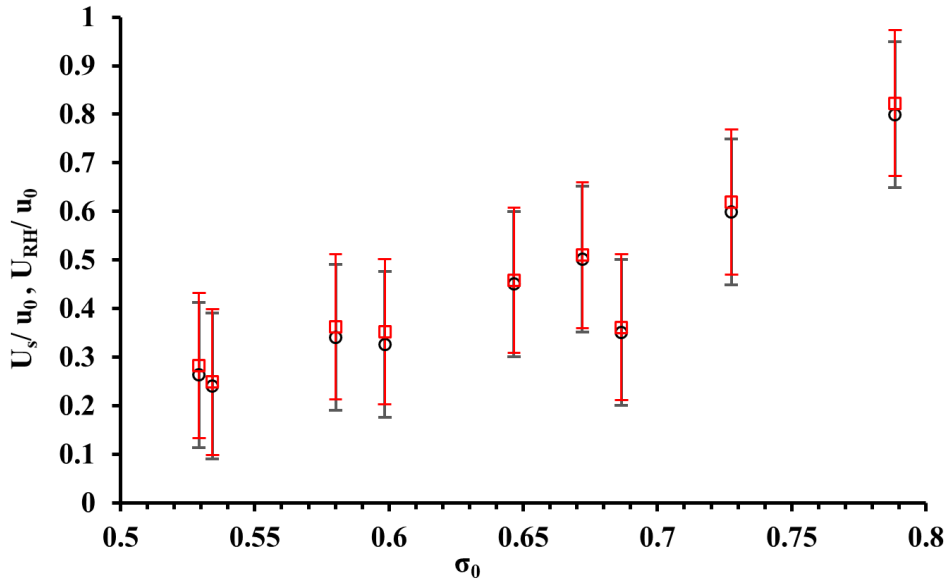

Figure 5.3: Comparison of computed shock-speed, $U_{RH}(\square)$ and shock-speed estimated from X-T diagrams, $U_S(\circ)$ for varying σ_0 shows a good agreement between U_S and U_{RH}.

Using pressure rise across the shock measured by the surface pressure transducer ($dp = (p_2 - p_1)_s$) in figure 5.1 and equation 1.15, shock speed, U_{RH}, is estimated. Pre- and post-shock void fractions values β_1 and β_2, are estimated by spatially averaging void fraction fields using a void fraction probe (5 mm x 5 mm) shown in figure 5.1.

5.1.3 Validity of 1-D jump relations

Measured shock speed from the X-T diagram, U_S, and U_{RH} calculated using measured quantities based on equation 1.15 is compared to check the validity of 1-D jump relations. This comparison is shown in figure 5.3. It is evident from figure 5.3 that 1-D jump relations based on the conservation of mass and momentum across a moving bubbly shock represents a bubbly shock observed in this flow well.

5.2 Speed of sound

Speed of sound in a compressible mixture defines the pressure-density relationship for the mixture. For gas-liquid two phase flows, it is not straightforward to identify this relationship.

Depending on thermodynamic processes, relative motion between phases, mass exchange during phase and distribution of phases the speed of sound expression can vary. Irrespective of the speed of sound expression (and the assumptions), for bubbly shocks to occur, the flow within the vapor-liquid mixture has to be supersonic.

Even though it is not possible to identify the exact expression for speed of sound based on experimental measurements, it is possible to investigate which qualitative speed of sound expression, based on a given set of assumptions best indicates the *first* observance of bubbly shocks. By estimating local Mach number based on a local speed of sound and a velocity scale, it is possible to identify a speed of sound expression that indicates the *first* occurrence of bubbly shocks by predicting a subsonic to supersonic Mach number transition. In this section, the validity of speed of sound based on 'the homogeneous frozen model' and 'the homogenous equilibrium model' in predicting the onset of bubbly shocks is discussed.

5.2.1 Speed of sound estimation

Section 3.3 discusses the underlying assumptions used in estimating the 'homogeneous frozen model' and 'homogeneous equilibrium model' of speed of sound. Speed of sound based on the 'homogeneous frozen model' and the 'homogeneous equilibrium model' is estimated by setting $\epsilon_V = \epsilon_L = 0$ and $\epsilon_V = \epsilon_L = 1$ in the general expression given in equation 3.1 respectively. The resulting expressions for the 'homogeneous frozen model' and the 'homogeneous equilibrium model' of speed of sound is shown in equation 5.1 and 5.2 respectively.

$$\frac{1}{\rho_m c^2} = \frac{\beta f_V}{p} \tag{5.1}$$

$$\frac{1}{\rho_m c^2} = \frac{\beta}{p} g_V + \frac{1-\beta}{p^{1+\eta}} g^* p^\eta \tag{5.2}$$

In equations 5.1 and 5.2, β is the local void fraction and p is the local pressure measured at static pressure ports underneath the cavity. f_V, g_V, p_c, and η are thermodynamic properties

u_0 (m/s)	u_H (m/s)	σ_0	Static Pressure (kPa)			Frozen Model (m/s)			Equilibrium Model (m/s)		
			p_1	p_2	p_3	c_1	c_2	c_3	c_1	c_2	c_3
6.75	8.02	0.88	12	10.08	25.23	13.21	12.11	19.16	0.17	0.15	0.33
6.76	8.03	0.79	8.57	6.43	23.05	7.06	6.11	11.57	0.13	0.1	0.3
6.77	8.04	0.60	6.37	3.87	14.08	5.86	4.57	8.71	0.1	0.06	0.2
6.77	8.04	0.69	7.17	5.44	20.59	6.33	5.52	10.73	0.11	0.09	0.28
6.77	8.05	0.61	6.49	4.02	16.54	5.88	4.63	9.39	0.1	0.07	0.23
6.77	8.05	0.86	11.83	9.72	24.93	11.98	10.86	17.39	0.17	0.14	0.32
6.77	8.05	0.65	6.52	4.4	19.39	5.89	4.84	10.17	0.1	0.07	0.26
6.77	8.05	0.92	12.83	11.04	26.05	13.75	12.76	19.6	0.18	0.16	0.34
6.78	8.06	0.69	7.37	5.34	20.50	6.37	5.42	10.62	0.11	0.09	0.27
6.78	8.06	0.86	11.71	9.56	24.94	11.93	10.78	17.42	0.17	0.14	0.32
6.78	8.06	0.69	7.1	5.08	20.73	6.25	5.29	10.68	0.11	0.08	0.28
6.79	8.07	0.76	8.37	6.70	22.63	7.07	6.32	11.63	0.13	0.1	0.3
6.80	8.09	0.75	8.41	6.59	22.41	7.07	6.26	11.54	0.13	0.1	0.3

Table 5.1: Speed of sound estimation using 'homogeneous frozen model' and 'homogeneous equilibrium model' for $u_H = 8$ m/s.

of water-vapor mixture discussed in section 3.3. Table 5.1 shows estimated speed of sound based on local pressure measurements (figure 2.3) at locations p_1, p_2, p_3, and void fraction measurements near these locations at $u_H = 8m/s$. Table 5.1 shows that the speed of sound based on 'the homogeneous frozen model' is an order of magnitude higher than the speed of sound estimated by 'the homogeneous equilibrium model'. Sound speed estimation for $u_H = 10m/s$ and $u_H = 12m/s$ are summarized in Appendix D.

5.2.2 Mach number based on step velocity u_H

Mach number based on the estimated speed of sound and a velocity scale can now be estimated. Due to lack of local velocity measurements, velocity at the step u_H is used to define Mach number M_{Hi}, as shown in equation 5.3. Since most flow processes are scaled based on the step velocity, the choice of this velocity scale is justified. In equation 5.3, the suffix 'i'

refers to the speed of sound, both 'homogeneous' and 'frozen', estimated based on the static pressure and void fraction at locations 1, 2, and 3 shown in figure 2.3.

$$M_{Hi} = \frac{u_H}{c_i} \tag{5.3}$$

Figure 5.4 shows the variation of M_{Hi} with σ_0, estimated by 'the homogeneous frozen' (open symbols) and 'the homogeneous equilibrium' (filled symbols) speed of sound expressions, $u_H = 10$ m/s. M_H estimated using the 'the homogeneous equilibrium' model is about two orders of magnitude higher than M_H estimated using 'the homogeneous frozen model'. This suggests that the local Mach based on the equilibrium model is *always* supersonic. However, experimental observations show that first onset of bubbly shocks occur during the transition from type A to type B cavities. Upon examining figure 4.9, it is evident that M_H based on the frozen model shows a transition from subsonic to supersonic values. Specifically, the flow is seen to transition from subsonic regime ($M_H < 1$) at type A to supersonic ($M_H > 1$) at the onset of type B regime for M_{H1} and M_{H2}. M_{H3} being subsonic(< 1) can be attributed to the selection of u_H in defining M_H instead of the local mean velocity near p_3. The homogeneous equilibrium model, on the other hand, consistently overestimate M_{Hi} and does not capture the subsonic to supersonic transition as the cavitating flow transitions from type A to type B regime. Figure 5.5 shows the M_H based on the frozen model for $u_H = 8, 10$ & $12m/s$. It is seen that M_{Hi} decreases monotonically with increasing σ_0. M_{H1}, M_{H2} and M_{H3} do not have a clear Re dependency.

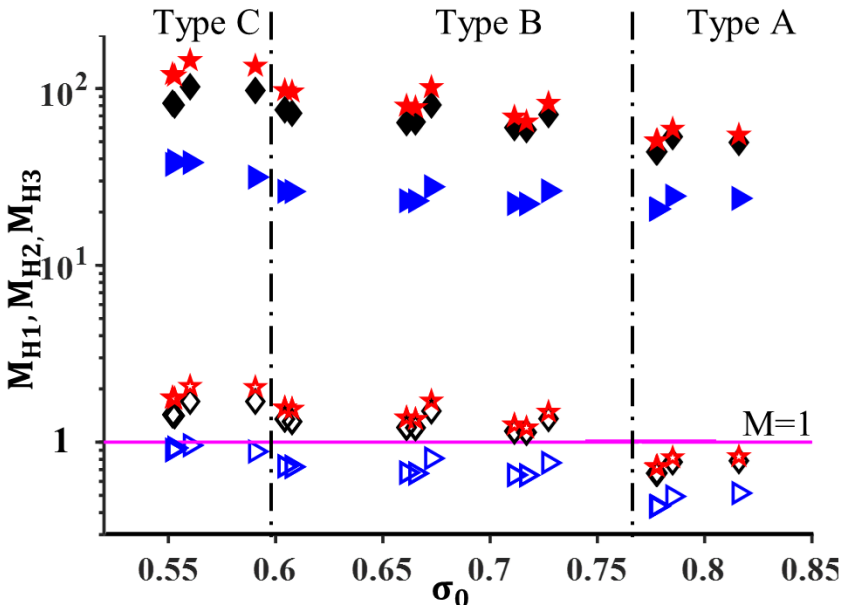

Figure 5.4: M_i estimated using the 'homogeneous equilibrium model' (★♦ ▶) and 'homogeneous frozen model' (☆ ◊ ▷) for speed of sound; M_1 (★☆) M_2 (♦◊) & M_3 (▶ ▷). $u_H = 10m/s$. (−) depicts $M_H = 1$ and indicates when the flow becomes supersonic

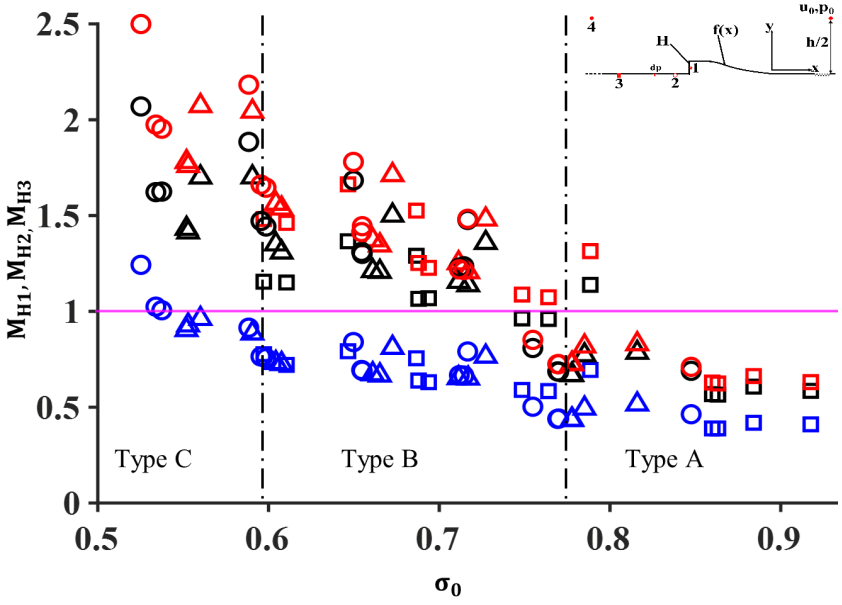

Figure 5.5: The variation of M_{Hi} with decreasing σ_0 across three different Re estimated using 'homogeneous frozen model'; $u_H = 8m/s$ (□□□), $10m/s$ (△△△) & $12m/s$ (○ ○ ○); M_{H1} (□△○), M_{H2} (□△○) & M_{H3} (□△○). (−) depicts $M_H = 1$.

Chapter 6

Conclusions of Backward Facing Step Study

Cavitation on a backward facing step at three cavitating regimes was investigated using x-ray densitometry, high-speed cinematographic system, and synchronized pressure measurements. During a shedding cycle the stronger spanwise vortices incept and grow in size as they convect away from the separation point. The vortex-pair interaction dominates the cavity filling part of the shedding cycle as visualized in figure 4.4. A bubbly shock moving towards the step collapses the cavity (figure 4.9(g)-(i)) causing shedding. Shedding frequency decreases monotonically with decreasing σ_0 and does not have Re dependence. Mean void fraction values in the cavity are comparable across the three Re.

Static pressure p_1, p_2 and p_3 inside/around the cavity were measured. The local pressure drops and recovers between p_1 and p_3. Time-synchronous measurement of void fraction and dynamic pressure facilitated the characterization of bubbly shock properties. The shock speed estimated using a simple 1-D Rankine-Hugoniot jump condition compares well with the shock-speed measured through the X-T diagram from void fraction measurements. Validity of the 'homogeneous frozen model' and the 'homogeneous equilibrium model' based speed of sound expressions in predicting the onset of bubbly shocks was examined. It was found that onset of bubbly shocks observed in type B cavities coincided with the subsonic to supersonic transition of the Mach number, M_H, estimated based on 'homogeneous frozen' speed of sound and velocity at the step u_H. M_H based on the 'homogeneous equilibrium model' were $\sim$ O(10^2) irrespective of the cavity shedding dynamics. Thus 'homogeneous equilibrium

model' over-predicts M_H and is unable to capture subsonic to supersonic transition when bubbly shockwaves appear in type B cavities.

This work has been published as a research article in the International Journal of Multiphase Flow, Volume 139 on June, 2021. The paper was titled *Cavitating flow behind a backward facing step* and authored by Bhatt, A., Ganesh, H., and Ceccio, S. L. (Bhatt et al. (2021)). The work was also presented at 71^{st} and 72^{nd} annual meeting of APS DFD (2018, 2019) and at 33^{rd} Symposium of Naval Hydrodynamics (2020).

Chapter 7

NACA0015 Hydrofoil : Background

7.1 Overview

Cavitation on a canonical geometry such as 2D hydrofoil has been studied extensively due to its similarity with the flow over propulsor passages. Most studies focus on the mechanisms that cause the transition from a stable sheet cavity to a shedding cloud cavity as the cloud cavitation regimes are undesirable in hydrodynamic applications. Re-entrant liquid flow and propagating bubbly shocks are two dominant mechanisms reported to cause the shedding of a partial cavity. This portion of the thesis investigates the relative importance of re-entrant liquid flows and bubbly shocks in causing cavity shedding on a NACA0015 hydrofoil at different cavitation numbers σ.

One of the earliest studies on 2D hydrofoils was done by Wade and Acosta (1966) in which detailed measurements were made for both cavitating and non-cavitating flow past a plano-convex foil. They reported oscillations in maximum cavity length and hydrodynamic forces when the cavity length exceeded 60% of the chord. These oscillations continued to persist until the cavity length reached 120% of the chord, after which supercavitation was observed. The cavitation regimes over the plano-convex foil were identified as partially cavitating regime, fully cavitating regime, and an unsteady (oscillating) regime between the two.

7.1.1 Re-entrant liquid flows

Le et al. (1993) studied partial cavitation dynamics on the flat side of a plano-convex hydrofoil, and identified different regimes of shedding as shown in figure 7.1. Based on surface pressure measurements at cavity closure and high-speed images they reported that shedding was caused by presence of liquid re-entrant flow originating at cavity closure. They reported that the development of this liquid re-entrant flow depended on the pressure gradient at the cavity closure, mainly for long cavities. A schematic of the periodic cloud cavity shedding due to liquid re-entrant flow is shown in 7.2.

Callenaere et al. (2001) performed a detailed study on the development and propagation of liquid re-entrant flow to cause shedding. By controlling cavity thickness and pressure gradient at cavity closure, the conditions necessary for the development of a liquid re-entrant flow to cause shedding was reported. Presence of a strong adverse pressure gradient was found to be necessary for the development of a liquid re-entrant flow. If adverse pressure gradient was high enough, a re-entrant flow formed at the aft of the cavity can cause shedding. The relative thickness of the re-entrant liquid flow with respect to the cavity thickness was also identified as an important factor is causing shedding. When the cavity thickness was significantly higher than re-entrant flow thickness, the re-entrant flow can get trapped underneath the cavity. If enough flow accumulated at the aft of the cavity, then the trapped flow can reach the leading edge and pinch-off the cavity.

7.1.2 Bubbly shocks

One of the earliest suggestion on the existence of bubbly shocks on a NACA0015 hydrofoil was provided by Arndt et al. (2000) and Kjeldsen et al. (2000). Kjeldsen et al. (2000) studied cavitation on a 2D NACA0015 hydrofoil and identified different regimes based on the cavitation number (σ) and attack angle (α). These cavitation regimes were similar to

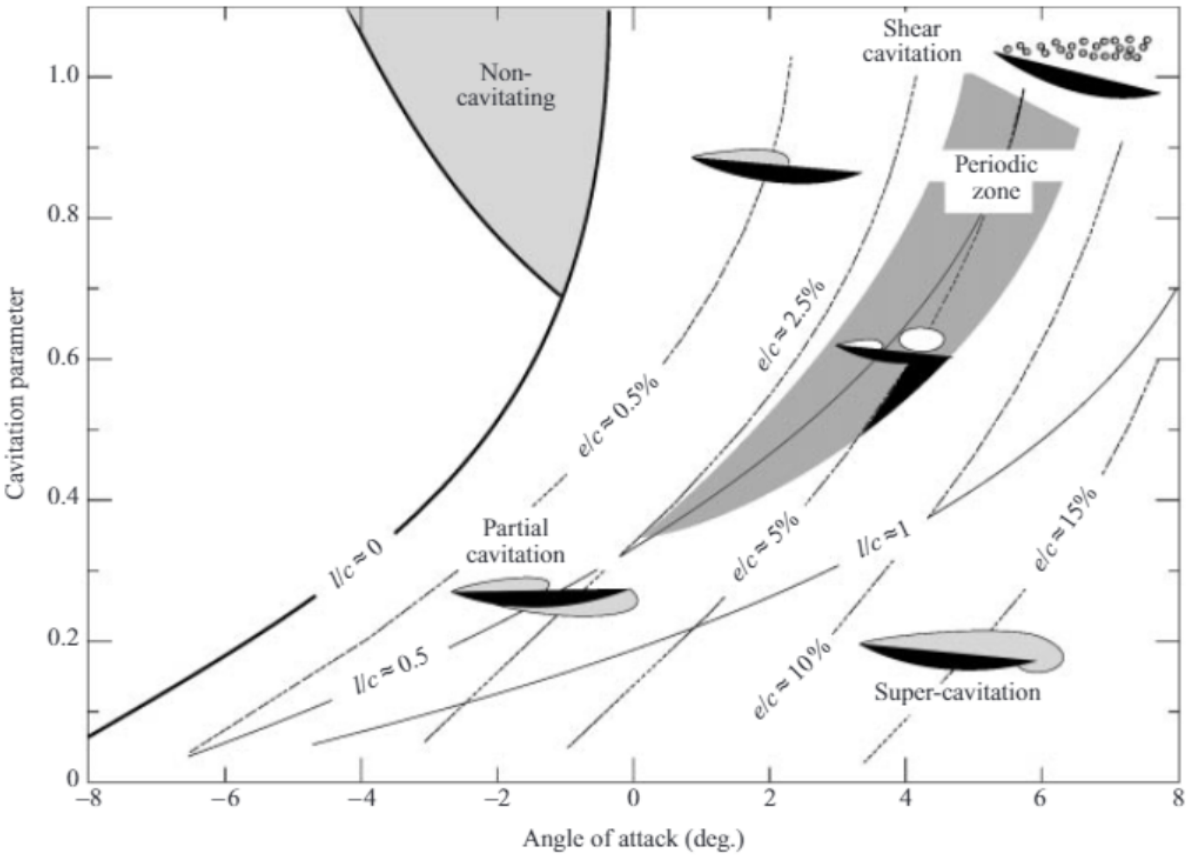

Figure 7.1: Cavitation map for different cavitation regimes over a plano-convex foil depicting main cavity patterns. l/c and e/c are maximum cavity length and maximum cavity thickness non-dimensionalized by chord length respectively. The unsteady regime is highlighted as periodic zone where partial cavitation occurs (Le et al. (1993)). The flow direction is from left to right for each schematic.

those reported by Le et al. (1993) for a plano-convex hydrofoil as seen in figure 7.3. The variation in cavity length (l/c) with cavitation parameter ($\sigma/2\alpha$) is shown in figure 7.4. The l/c increases with decreasing $\sigma/2\alpha$. One of the key findings of the study by Kjeldsen et al. (2000) was the abrupt change of shedding Strouhal number (St) with σ. Figure 7.5 shows this variation of St at $\alpha = 7^{\circ}$ with decreasing σ from the ramp tests using Joint Time-Frequency Analysis (JTFA). St is based on fluctuations in pressure measurements on the suction side of the hydrofoil. The explanation for this abrupt transition in St from 'St dependent on σ' regime to '$St \approx 0.15$ and does not depend on σ' was given using potential flow theory based quarter-chord instability observed on the cavitating hydrofoils.

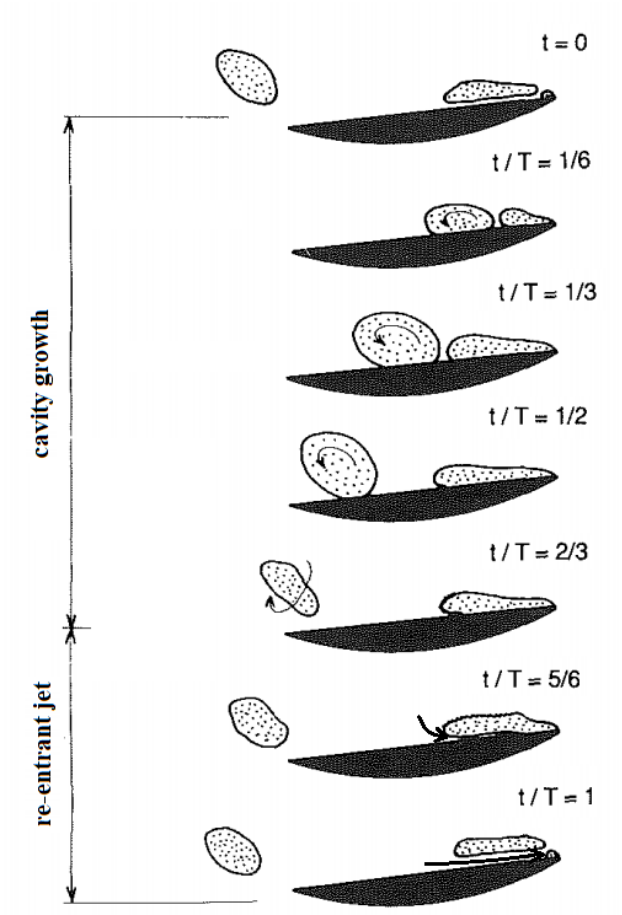

Figure 7.2: Periodic shedding mechanism caused by re-entrant flow at cavity closure for thick cavities(Le et al. (1993)). Time period of a shedding cycle is T. Flow is from right to left.

Arndt (2012) suggested that the proximity of shed cloud collapse to the growing cavity affected the overall growth and cavity shedding dynamics. They also postulated the presence bubbly shocks at lower σ as the reason for occurrence of abrupt St transition but couldn't observe them experimentally.

Recent studies such as Ganesh et al. (2016), Wu (2019), Wu et al. (2021), Bhatt and Mahesh (2020) and Budich et al. (2018) have shown the presence of bubbly shocks as a dominant mechanism of shedding of partial cavities. Wu et al. (2019) used time-resolved x-ray densitometry to identify bubbly shocks as a dominant mechanism of shedding in partial cavities on a NACA0015 hydrofoil. Figure 7.6 shows a shedding cycle caused by a bubbly shock on a NACA 0015 hydrofoil observed by Wu (2019). They also reported that occurrence

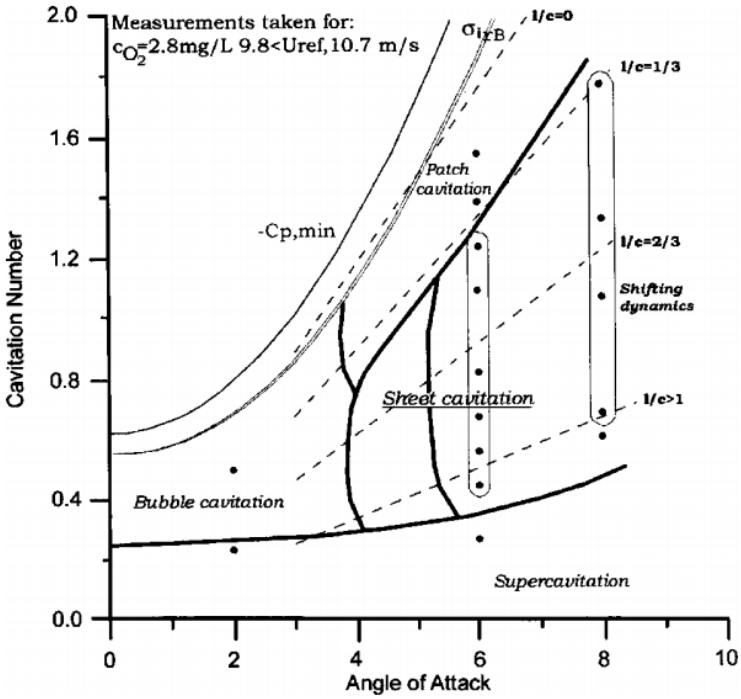

Figure 7.3: Cavitation map for different cavitation regimes over a NACA0015 hydrofoil presented by Kjeldsen et al. (2000).The lines l/c=constant are obtained from a linear fit to the cavity length data shown in figure 7.4.

of these bubbly shocks coincided with the change in dynamics associated with cavitation aligning with observations made by Arndt (2012). Barwey et al. (2020) used data-driven decomposition of void fraction fields obtained by Wu et al. (2019) to explain the observed change in dynamics by identifying the relationship between shed cloud collapse at trailing edge and bubbly shock occurrence, as shown in figure 7.7.

Based on σ, a cavitating NACA0015 hydrofoil can undergo sheet-to-cloud transition and experience periodic cloud shedding. This periodic cavity shedding can be driven either by bubbly shocks or by liquid re-entrant flow. It is important to understand the relative importance of these flow fronts in causing shedding for better modeling and prediction of such flows. Despite the detailed experimental study, Wu et al. (2019) were unable to identify the presence of liquid re-entrant flow induced shedding on the NACA0015 hydrofoil. This was mainly due to the lack of spatial resolution of the measurement area. Due to lack of pressure

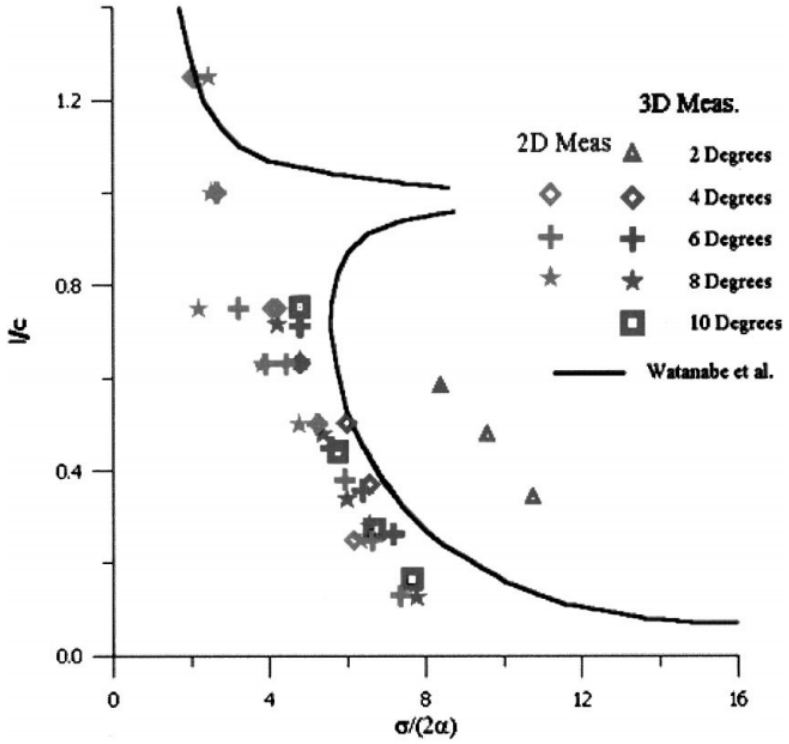

Figure 7.4: Classical cavity length versus cavitation parameter ($\sigma/2\alpha$) plot against thin flat plate theory suggested by Watanabe (1998) shows how cavity length scales with cavitation number.

measurements Wu et al. (2019) were unable to quantify compressibility by estimating the cavity Mach number.

7.2 Current Study

In the current study, unsteady partial cavitation over a symmetric NACA0015 hydrofoil will be investigated using time-resolved x-ray densitometry data, high-speed cinematography and synchronous static and unsteady pressure measurements on the hydrofoil surface. The model dimensions are chosen to facilitate better spatial resolution to aid in the identification of flow structures within and near the cavity. In addition, synchronized unsteady surface pressure measurements using flush mounted pressure transducers with time-resolved x-ray densitometry measurements will be performed. Measured cavity static pressure will be used to estimate speed of sound values within the cavity similar to the previous study on a

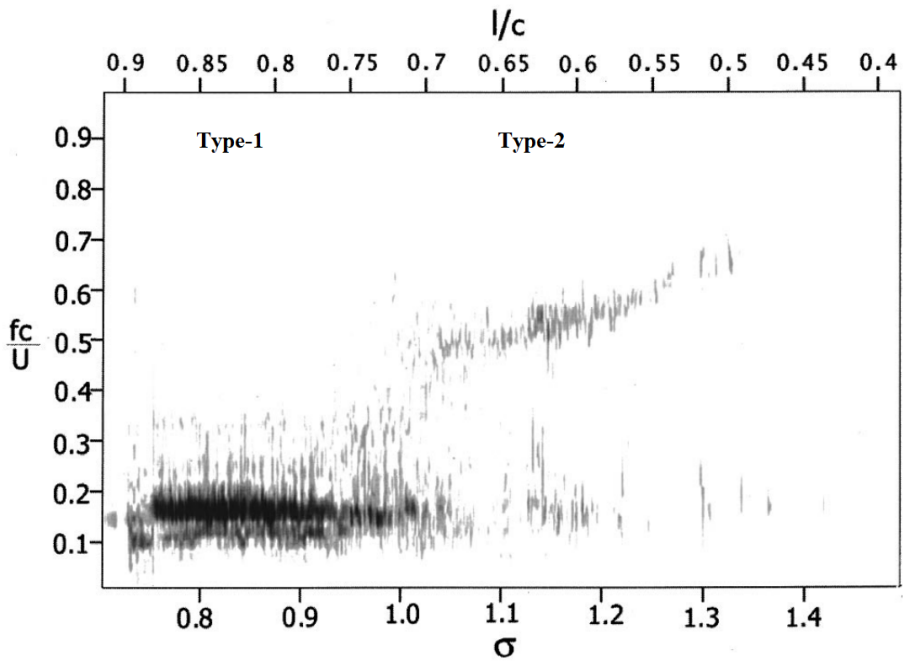

Figure 7.5: JTFA of suction side pressure transducer at $\alpha = 7°$. Similar observation in lift fluctuation spectral content is reported by Kjeldsen et al. (2000).

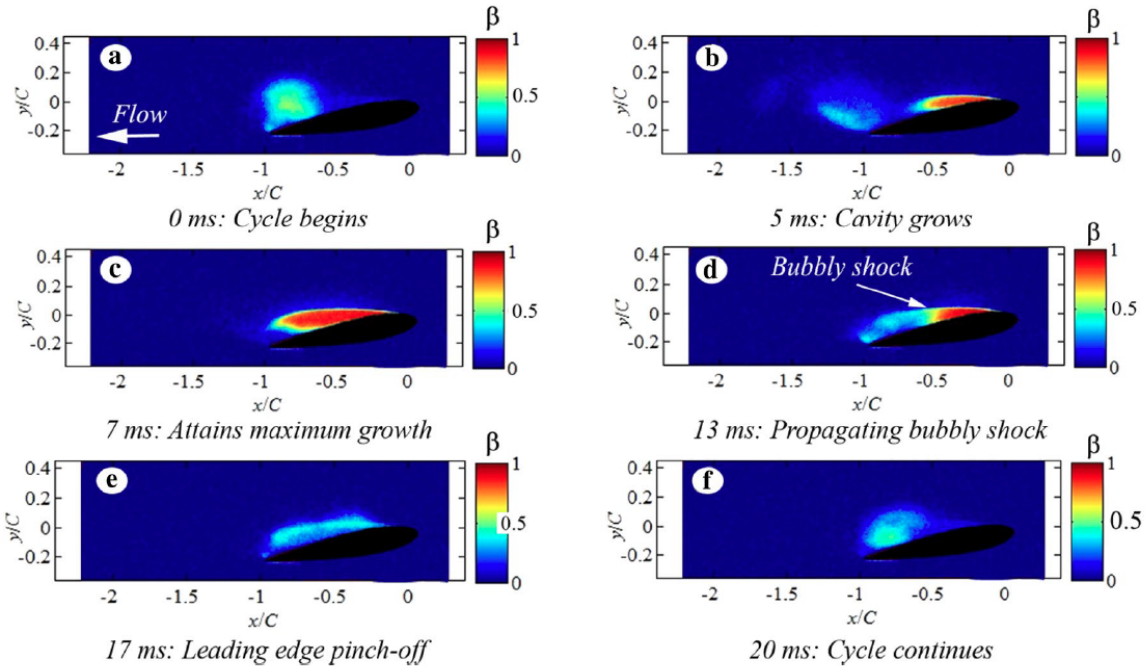

Figure 7.6: Shock induced shedding of partial cavities on a NACA0015 hydrofoil from Wu et al. (2019)

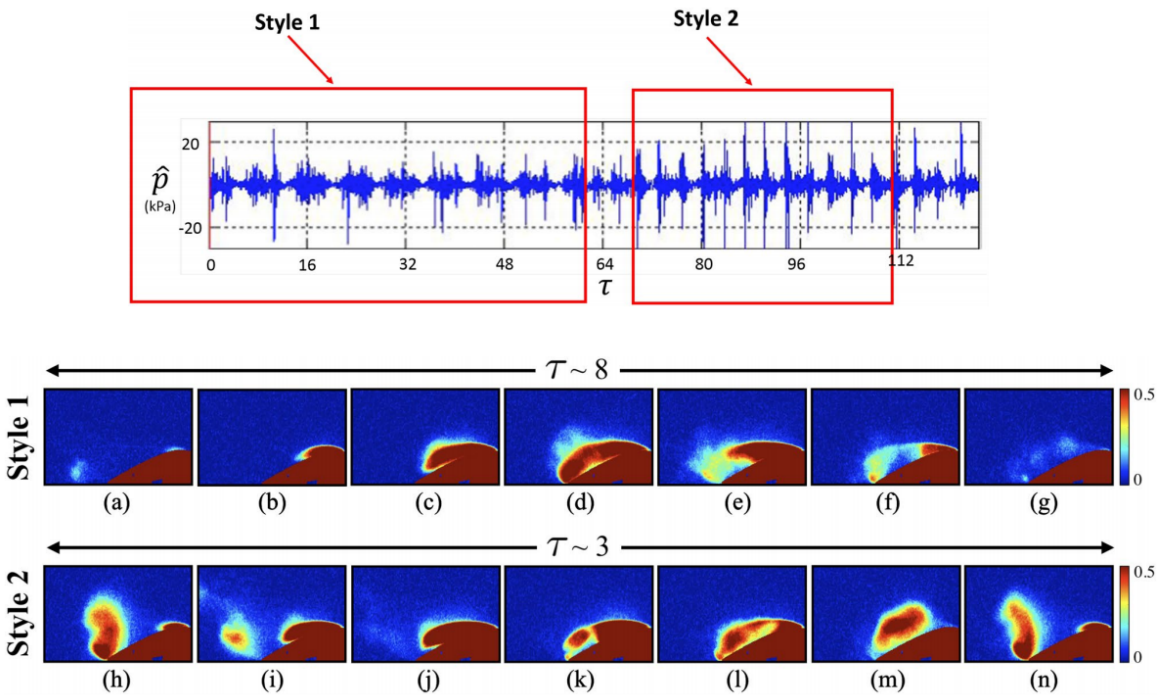

Figure 7.7: Acoustic pressure signal showcasing a transition from Style 1 cavitation (low frequency) to Style 2 (high frequency) with corresponding void fraction measurements for each cycle reported by Barwey et al. (2020). Flow is from right to left.

cavitating backward facing step. From the x-ray measurements, the probability of re-entrant flow or a bubbly shock to cause a cavity shedding cycle and its relationship to the observations of changes in vapor-liquid compressibility will be made. Relationship between cloud collapse and the onset of propagating bubbly shocks that cause shedding will also be studied by using a synchronous hydrophone measurements, located downstream of the hydrofoil trailing edge. Finally, an effort will be made to understand the effect of model scale on the observed dynamics by comparison with Wu et al. (2019).

7.3 Roadmap

Chapter 8.1 discusses the estimation of cavity lengths and classification of different cavity topology. In chapter 8.1, cavities are classified as type(i)-(iv) based on visual observations of different flow fronts in the cavitation regimes in section 8.2. Void fraction measurements

($\beta(x, y, t)$) for each shedding cavity type along with surface pressure transducer measurements are presented in section 8.4. Both re-entrant jets and shockwaves, along with cavitation at trailing edge are visualized. A summary of the identified flow features is presented in section 8.5. The spectral content of the dynamics data acquired through void fraction fields and surface pressure measurements are presented in chapter 9. Time frequency analysis is presented in section 9.2. Spectral POD to identify specific shedding modes is discussed in section 9.3. The analysis of shock-properties and compressibility effects are presented in chapter 10. The shockspeeds are measured and compared with Wu (2019) in 10.1. The analysis of event probability of re-entrant flow/shockwave to cause cavity pinch-off is presented in section 10.2. The speed of sound estimations using homogeneous frozen model are presented in section 10.3. Conclusion of the hydrofoil study is made in chapter 11.

Chapter 8

NACA0015 Hydrofoil : Experimental Results

Cavitation on the NACA0015 hydrofoil is observed using high-speed cinematography and time-resolved x-ray densitometry. Both these measurements are time-synchronized with unsteady surface pressure and static pressure measurements inside the cavity. Cavity length, visual observations, void fraction flow fields and unsteady surface pressure measurements are presented in the following sections.

8.1 Cavity Length

Cavitation experiments were performed at two attack angles of $\alpha = 10^\circ$ & 7°. Cavitation observations are made at a fixed inlet velocity $u_0 =$ 8 m/s and reducing inlet pressure p_0. This resulted in cavities growing in length from stable sheet cavities to shedding cavities. For shedding cavities, the average of maximum length in each cycle is designated as the cavity length. This cavity length is measured using both the snapshots from high-speed videos and instantaneous void fraction flow fields from x-ray densitometry data. The definition of cavity length (Lc) for high speed top-view snapshots and mean void fraction field is shown in figure 8.1.

In order to compare observations at different α, cavitation parameter $\sigma_0/2\alpha$ is used. Also, to compare current cavitation observations with Wu et al. (2019), a blockage correction is used. The blockage correction factor (CF) is obtained by using appropriate blockages across the two experimental configurations as shown in table 8.1. The corrected cavitation number

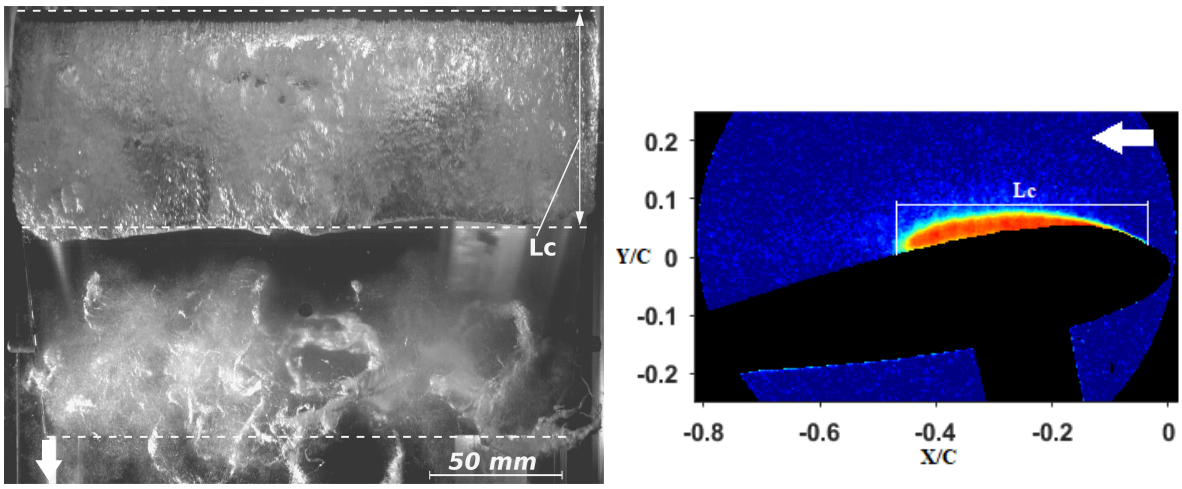

(a) (b)

Figure 8.1: Definition of cavity length on (a) High speed snapshot of maximum cavity length (b) X-ray densitometry snapshot of maximum cavity length.

(σ_c) is given in equation 8.1. Cavity length variation shown in figure 8.2 is seen to adhere to the classical Lc vs $\sigma_c/2\alpha$ profile shown in figure 7.4. Cavity lengths are seen to be in good agreement with previous studies reported by Arndt (2012).

$$\sigma_c = CF \cdot \sigma_0 \tag{8.1}$$

8.2 Visual Observation of Cavitation

Cavitation dynamics at two angle of attack ($\alpha = 7°$ and $10°$) are similar, hence high-speed video and x-ray measurements are discussed only for $\alpha = 10°$.

As σ_0 is reduced, cavitation first appears in patches on the suction side of the hydrofoil near the leading edge as shown in figure 8.3. Visible cavitation inception on the suction side of the hydrofoil starts at $\sigma_0/2\alpha = 10.8$ for $\alpha = 10°$ and $\sigma_0/2\alpha = 11.1$ for $\alpha = 7°$. At these conditions, cavity lengths are small with very low vapor content($\beta < 5\%$) and the cavity lengths are stable.

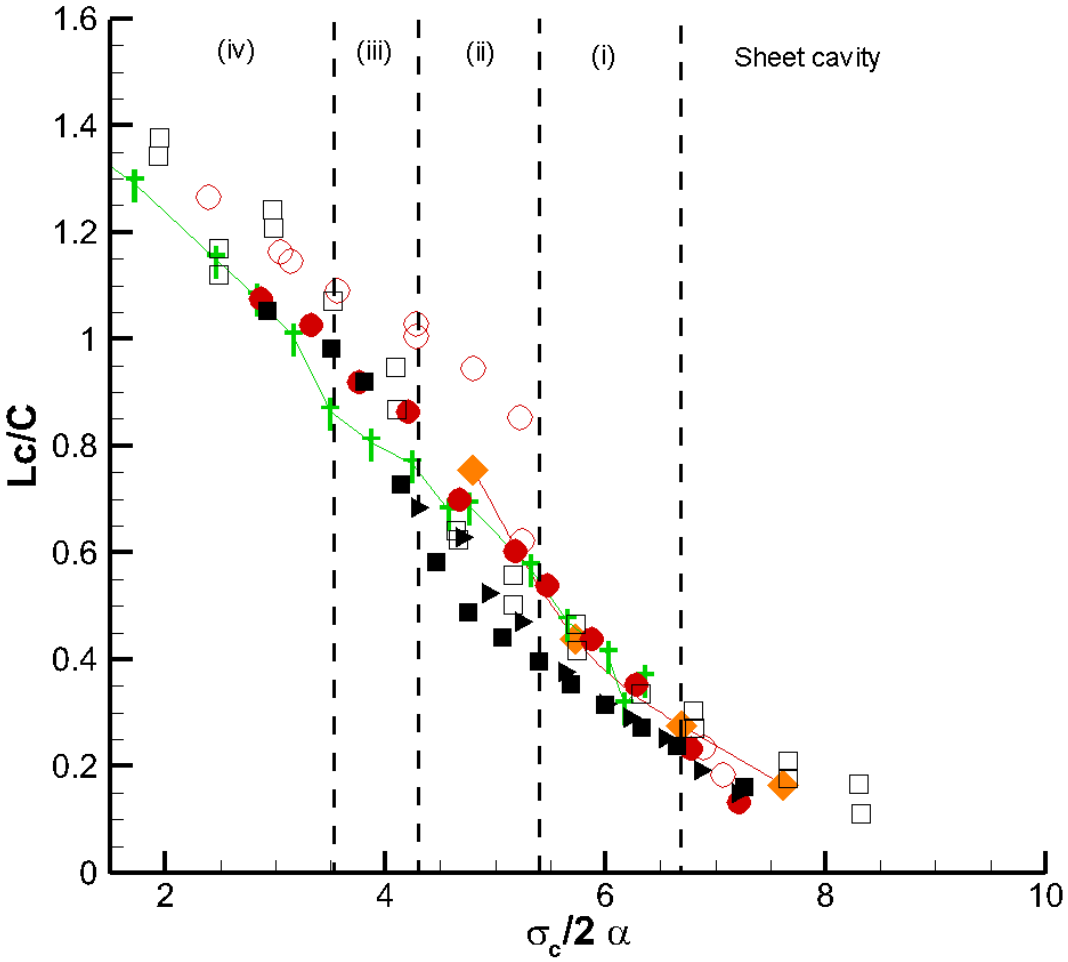

Figure 8.2: Comparison of Lc/C for current model from maximum cavity length measurements at two angle of attack ($\alpha = 10°$ (□(HS), ▶ (XR)) and $\alpha = 7°$(○)) where cavitation parameter ($\sigma_c/2\alpha$) has been corrected for blockage. Cavities formed over the hydrofoil model used in current study(filled symbols) are compared with those observed by Wu (2019) (open symbols). Also the cavity length reported by Obernach (†) and Arndt(◊) are included to show good agreement in cavity lengths reported in the current study. Obernach NACA0015 hydrofoil: 0.128 m C, 0.3 m by 0.3 m test section, aspect ratio (AR) = 2.35, $Re = 1.02 \cdot 10^6$ and $\alpha = 8°$; Arndt NACA0015 hydrofoil : 0.081 m C, 0.19 m by 0.19 m test section, AR = 3 and $\alpha = 7°$. Outside the steady sheet cavity regime, four types of cavitating regimes a marked to show different cavity dynamics observed. These flow regimes are discussed in detail later in section 8.5. The maximum uncertainty in measurement of $\sigma_0 = \pm\ 0.07$ and $Lc/C = \pm\ 0.1$

Wu et al. (2019)	Chord(C)	50 mm
	Tunnel Height(h)	76.2 mm
	Blockage(C·sin(α))	8.68
	$\lambda_1 = \frac{C \cdot sin(\alpha)}{h}$	0.114
Current NACA0015 foil	Chord(C)	165.6 mm
	Tunnel Height(h)	209.6 mm
	Blockage(C·sin(α))	28.75
	$\lambda_2 = \frac{C \cdot sin(\alpha)}{h}$	0.137
Correction Factor (CF) $= \left(\frac{\lambda_1}{\lambda_2}\right)^2$		0.689

Table 8.1: Calculation of correction factor(CF) used to compare cavity lengths with Wu et al. (2019).

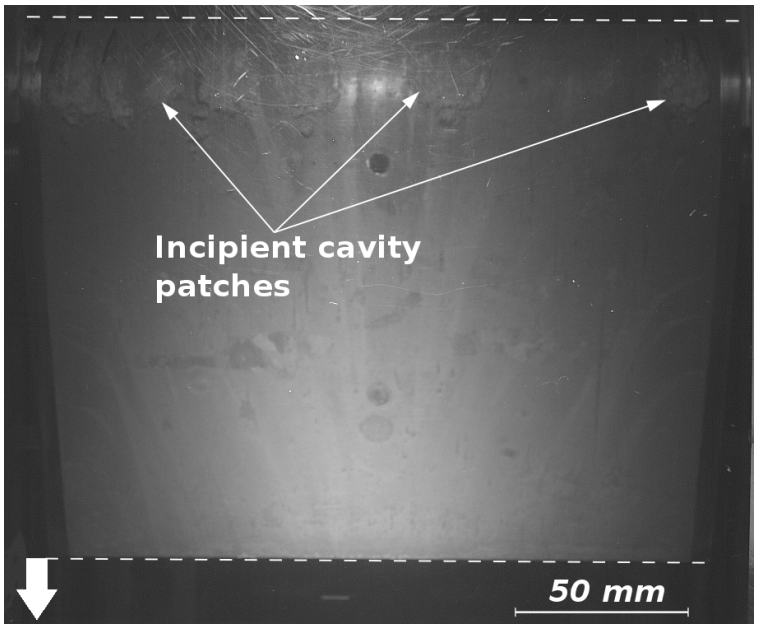

Figure 8.3: Top view snapshot of incipient cavity patches at high cavitation numbers for the NACA0015 hydrofoil; Flow from top to bottom $\alpha = 10°$ and $\sigma_0/2\alpha = 10.8$; $u_0 = 8\ m/s$.

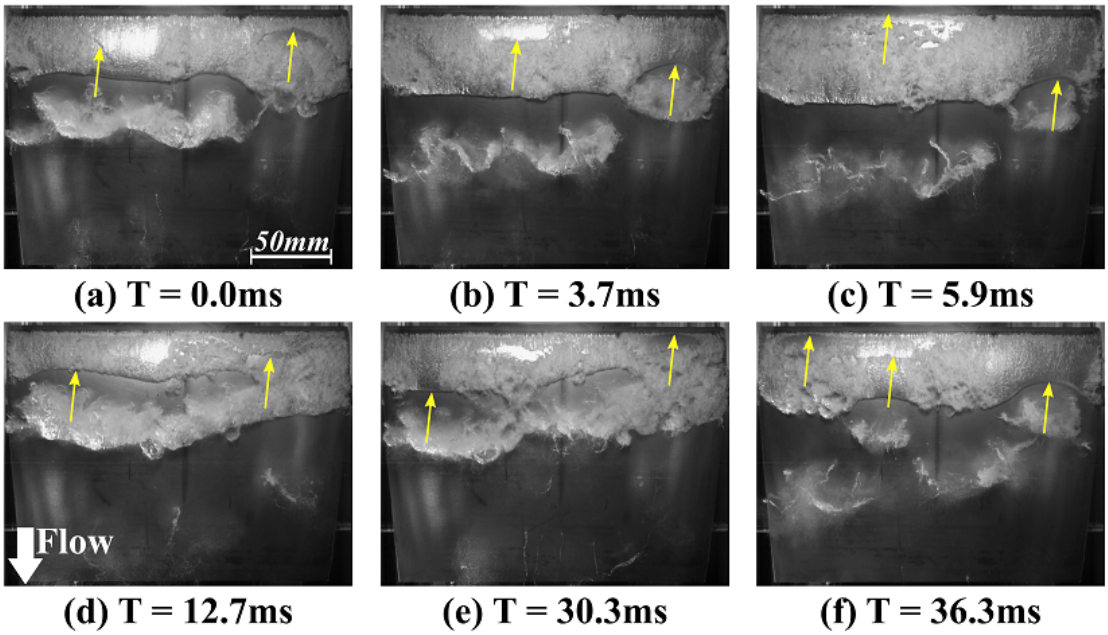

Figure 8.4: Successive frames from a high-speed video of a type(i) cavity shedding over the foil at $\sigma_0 = 3.2(\sigma_0/2\alpha = 9.18)$. The arrows track the flow-front trapped underneath the cavity, moving from the cavity closure all the way to the leading edge.

8.2.1 Type(i) cavities

The onset of periodic shedding occurs at type(i) oscillating cavities and figure 8.4 shows a type (i) shedding cycle. Type (i) cavities are characterized by the pinch-off due to flow feature underneath the cavity. This is shown as yellow arrows in figure 8.4 that highlight the presence of flow structures that causes cavity pinch off. These cavities typically exist for $\sigma_0 = 3.2 - 2.8$ ($\sigma_0/2\alpha = 7.6$ to 9.8). On some occasions, the cavities are not span-wise uniform, having a 'W' or a 'U' shape.

8.2.2 Type(ii) & (iii) cavities

With a reduction in cavitation number σ_0, cavity length increases and type (ii) and type (iii) cavitation occurs at $\sigma_0 = 2.2 - 2.7$ and $\sigma_0 = 1.8 - 2.2$ respectively. Visual observation of type (ii) and type (iii) cavities are similar in high-speed video. A time-series depicting a type (ii) shedding cycle at $\sigma_0 = 2.6$ is shown in figure 8.5. Two flow fronts, marked in red

and yellow, cause the cavity to pinch off from the leading edge. The mechanism of shedding and the observed flow features are discussed using the void fraction measurements in section 8.4.

When cavitation number (σ_0) is reduced below $\sigma_0 = 2.2$, type (iii) shedding occurs and two flow features are observed. Figure 8.6 shows a time-series of shedding observed for a type (iii) cavity at $\sigma_0 = 1.3$. After attaining a length of about 40% of the chord length(C), a flow structure originates at the cavity closure region, shown in orange in figure 8.6 (b)-(e), similar to the flow front seen in type(i) & (ii). However, this flow front does not cause the cavity to pinch off from the leading edge, as observed in type (ii). Instead, another flow front shown in red in figure 8.6 (d)-(f), causes the cavity to pinch off. Nature of these flow fronts and their role in shedding is discussed in section 8.4.

8.3 Type(iv) shedding regime: effect of trailing edge cavitation

When $\sigma_0 \leq 1.8$ and $Lc/C \geq 0.85$, the region near trailing edge of the hydrofoil begins to cavitate. Trailing edge cavitation is initiated by the passage of a shed cloud. In addition, from the observations, it is seen that rotation of the trailing edge cavitation cloud is opposite signed when compared with the shed cloud from the leading edge. Figure 8.7 shows high-speed video snapshots of a type (iv) cavity and its corresponding hydrophone signal. The cavity begins to grow, and at the same time the shed cloud convects downstream, shown as instance '1' and '2' in figure 8.7(a), (b), (c). At instance '3' in figure 8.7(a), (b), (c) the cloud collapses and cavity growth stops. At instance '4' in figure 8.7(a), (b), (c) a flow front is seen to travel upstream. This front causes the cavity to collapse and shed, as shown by '5' and '6' in figure 8.7(a), (b), (c).

The shedding cycle starts with a spike in acoustic pressure due to cavitation cloud collapse downstream of the hydrofoil, recorded at (3). This cloud collapse triggers a flow front at cavity closure, and as this flow front moves upstream cavity begins to collapse as seen in

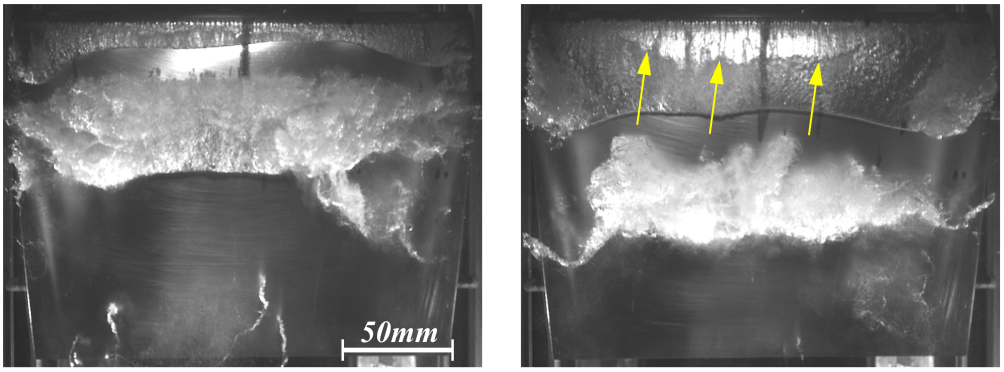

(a) T = 0.0ms (b) T = 6.5ms

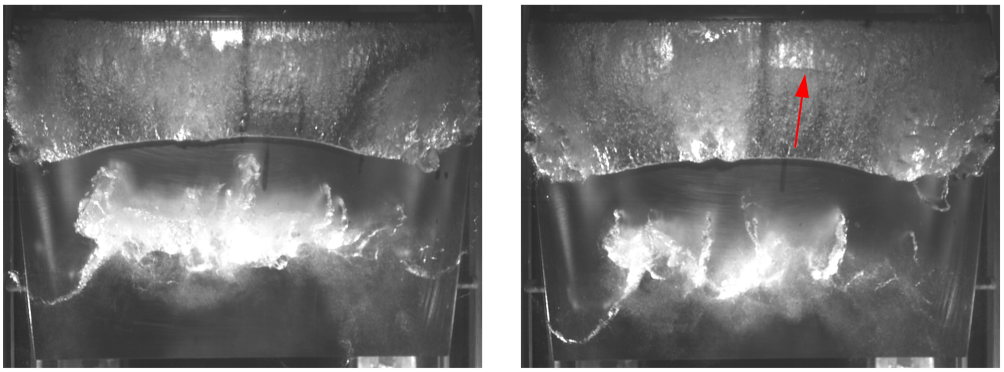

(c) T = 9.2ms (d) T = 12.1ms

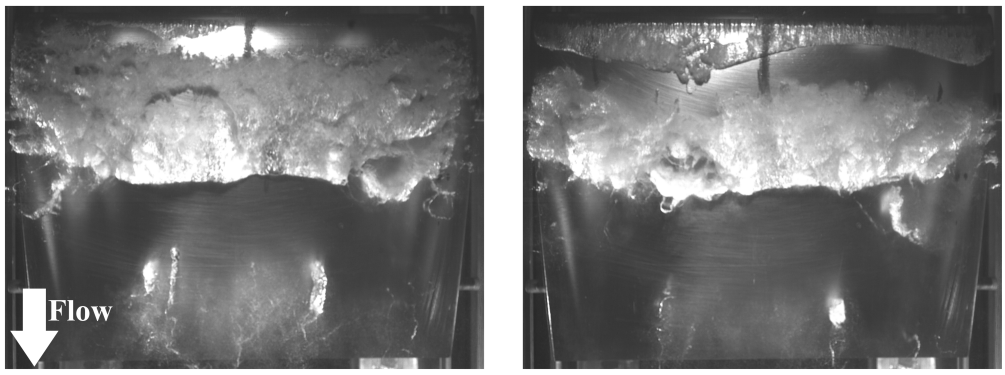

(e) T = 17.9ms (f) T = 21.7ms

Figure 8.5: Successive frames from a high-speed video of both re-entrant flow and shockwave driven shedding over the foil for a type(ii) cavity at $\sigma_0 = 2.6$ ($\sigma_0/2\alpha = 7.6$). Despite visualization of flow fronts in the high-speed video, it is not possible to identify a flow front as a shock or liquid re-entrant flow with certainty.

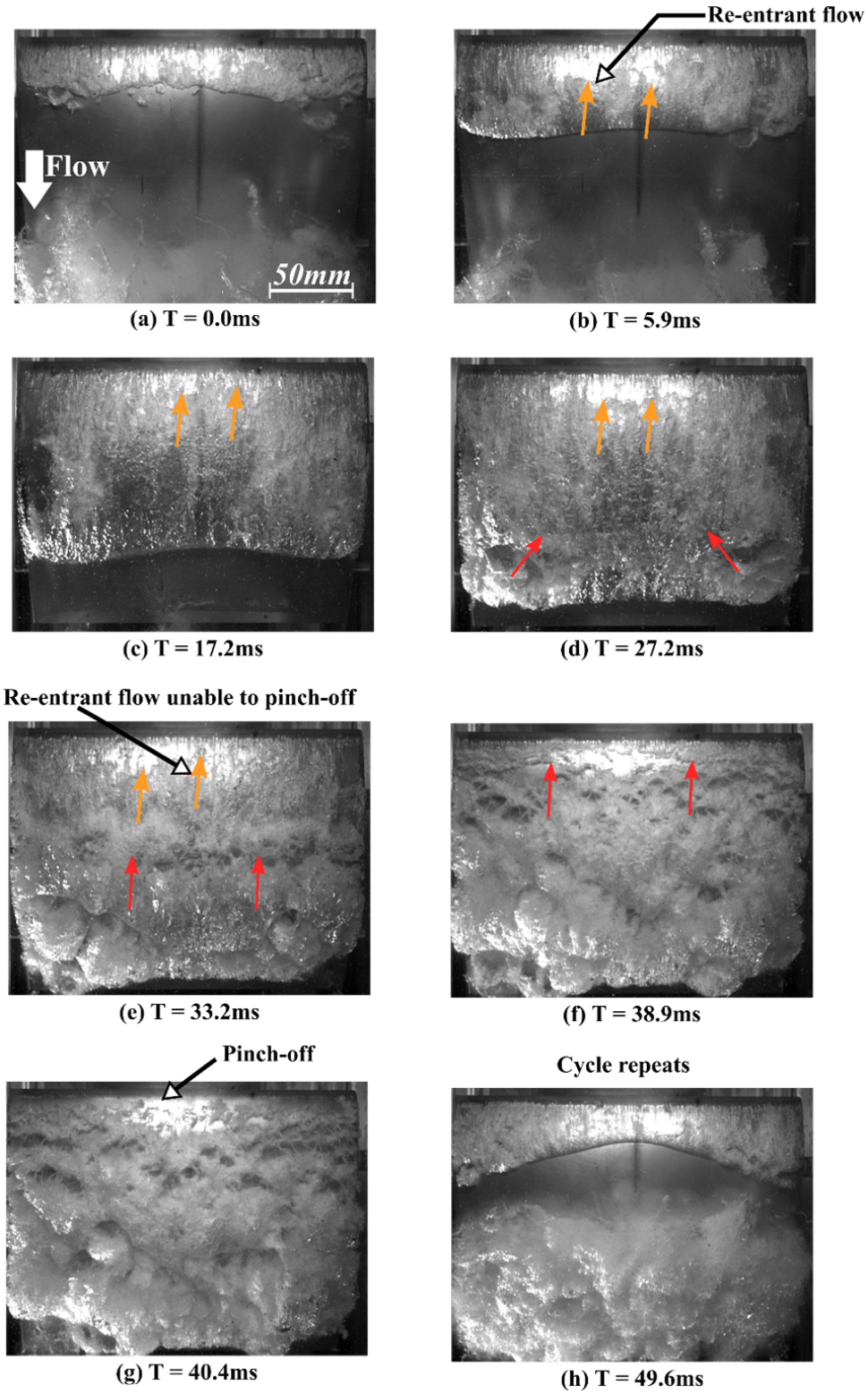

Figure 8.6: Time-series depiction of one flow front (orange arrows) co-existing with the other (red arrows). The high speed video snapshots do not confirm the presence of either of the flow fronts and the arrows are only for illustration. $\sigma_0 = 1.91(\sigma_0/2\alpha = 5.5)$

figure 8.7(c) (4)-(6). By instance '6' the cavity has collapsed (pinch-off). Subsequently, cavity growth occurs beyond '6' and another cloud collapse is recorded at 84 ms with a different peak in p_a. This variation in magnitude occurs due to different cloud size and proximity of the cloud to hydrophone.

8.4 X-ray densitometry based void fraction measurements

Time-resolved void fraction flow fields obtained using x-ray densitometry measurements for all cavity types are presented in this section. Flow structures observed in high-speed videos are identified using void fraction flow fields (β) obtained from x-ray densitometry. All void fraction measurements are synchronized with unsteady surface pressure measurements (and hydrophone measurements). The location of dp_1, dp_2 and p_a is shown in figure 2.6.

Figure 8.8 shows the time-averaged void fraction field of a stable incipient cavity at $\sigma_0 = 3.6$ ($\sigma_0/2\alpha = 10.3$). Incipient cavities do not contain much vapor resulting in measured maximum instantaneous void fraction of $\beta < 5\%$.

8.4.1 Type(i) cavity: Oscillatory Cavity

Type(i) cavities occur for $\sigma_0/2\alpha = 7.6$ to 9.8 ($0.2 < Lc/C < 0.4$). These cavities are thin and exhibit periodic oscillation of cavity length. Instantaneous time-resolved void fraction fields for a type (i) cavity shedding is shown in figure 8.9.

Figure 8.9(1)-(3) shows the growth of the cavity to its maximum length. Upon attaining maximum length, a vapor cloud shed as shown in figure 8.9(4)-(5), and new cycle follows (figure 8.9(6)). Despite being small and thin, these cavities have a maximum instantaneous void fraction values of β close to 0.6. X-ray densitometry measurements shown in figure 8.9 do not provide definite information about the flow structure that causes cavity pinch-off.

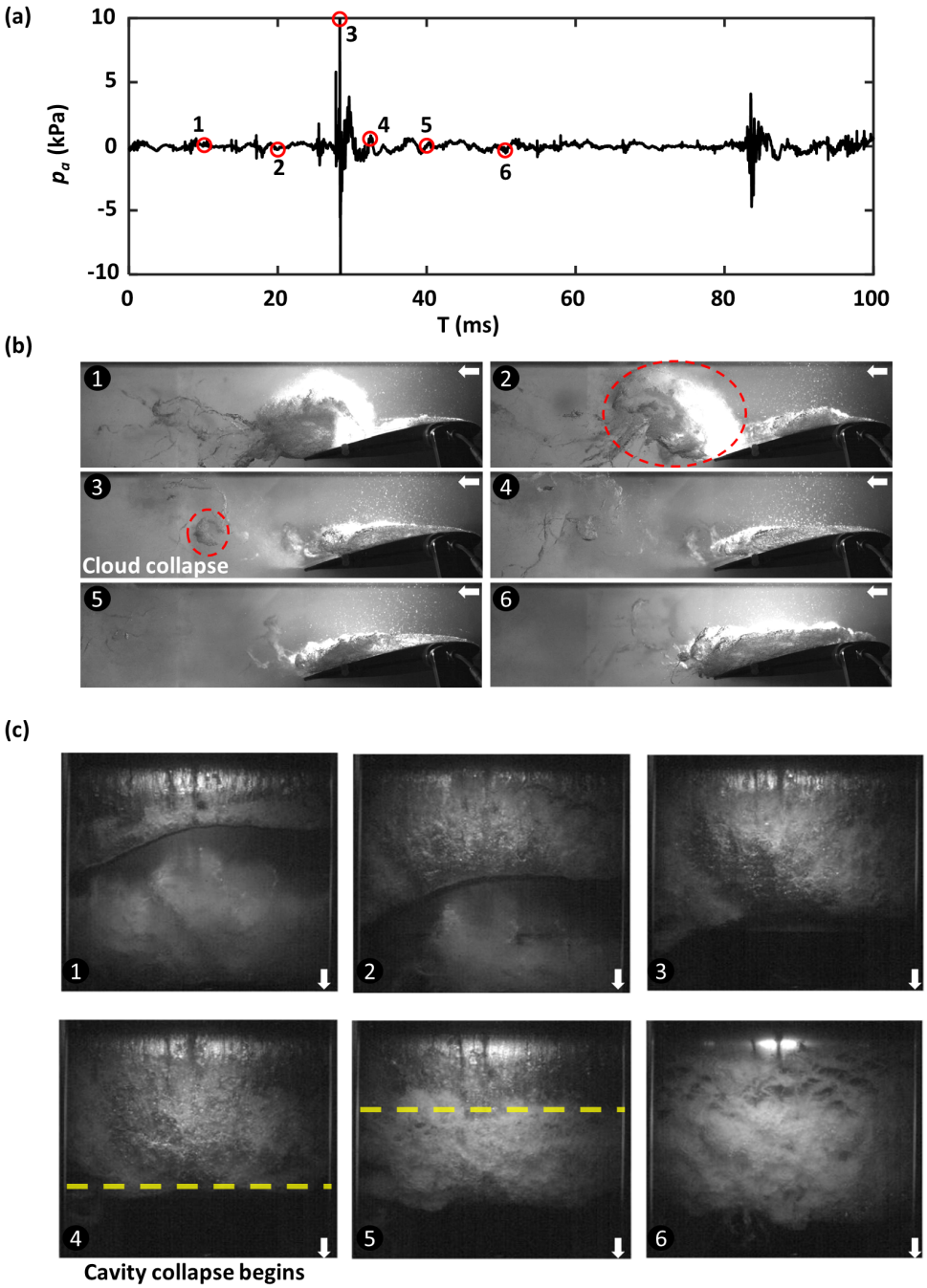

Figure 8.7: Timeseries of high speed snapshots for a type (iv) cavity highlighting the collapse of the shed vapor cloud downstream of the hydrofoil as a primary initiator for cavity collapse. (a) Acoustic pressure from the hydrophone (p_a) with points before and after cloud collapse (b) Corresponding side view snapshots showing cloud collapse (c) Corresponding top view snapshots depicting cavity collapse process. $\sigma_0 = 1.5(\sigma_0/2\alpha = 4.3)$

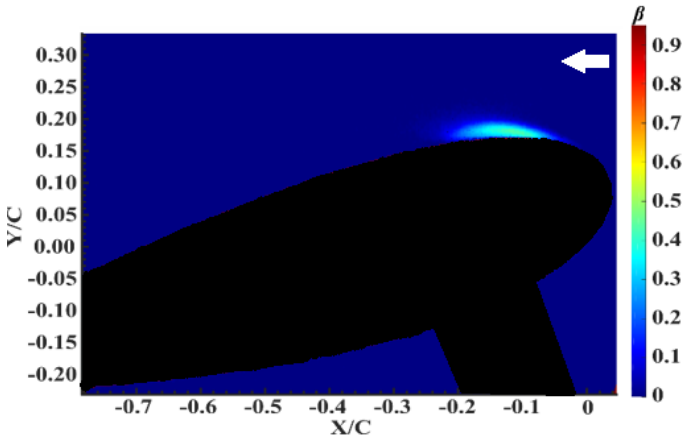

Figure 8.8: Mean void fraction field of a stable cavity with nearly constant cavity length at $\sigma_0 = 3.6$ ($\sigma_0/2\alpha = 10.3$). Flow is always from right to left for void fraction fields. The void fraction value (β) ranges from 0-0.924.

8.4.2 Type(ii) shedding cavity: Shedding driven equally by re-entrant flows and bubbly shocks

Type(ii) cavities are observed for $\sigma_0/2\alpha = 6.2$ to 7.6 ($0.4 < Lc/C < 0.6$). These cavities are shed from the cavity attachment point close to the leading edge. In a given cycle, the cavity is pinched off either by re-entrant liquid flow or a bubbly shock. Figure 8.10 shows the shedding caused by a liquid re-entrant flow and figure 8.11 shows a shedding cycle caused by a bubbly shock.

Shedding cycle caused by a liquid re-entrant flow begins by cavity growth shown in figure 8.10 (1). The cavity continues to grow, as shown in the sequence 8.10 (2)-(4), and attains maximum length (Lc). At this stage, shown in figure 8.10 (4), the liquid re-entrant flow appears to be halfway to the leading edge. The liquid re-entrant flow pinches off the cavity and a vapor cloud is shed downstream, as seen in figure 8.10 (5).

The shedding cycle caused by bubbly shocks is shown in figure 8.11 follows the similar order of events as seen in figure 8.10. However, the flow front that causes shedding is a bubbly shock wave. This is evident by the presence of a discontinuity in the void fraction field (β) along the tangential direction of the suction side of the hydrofoil surface, as seen in

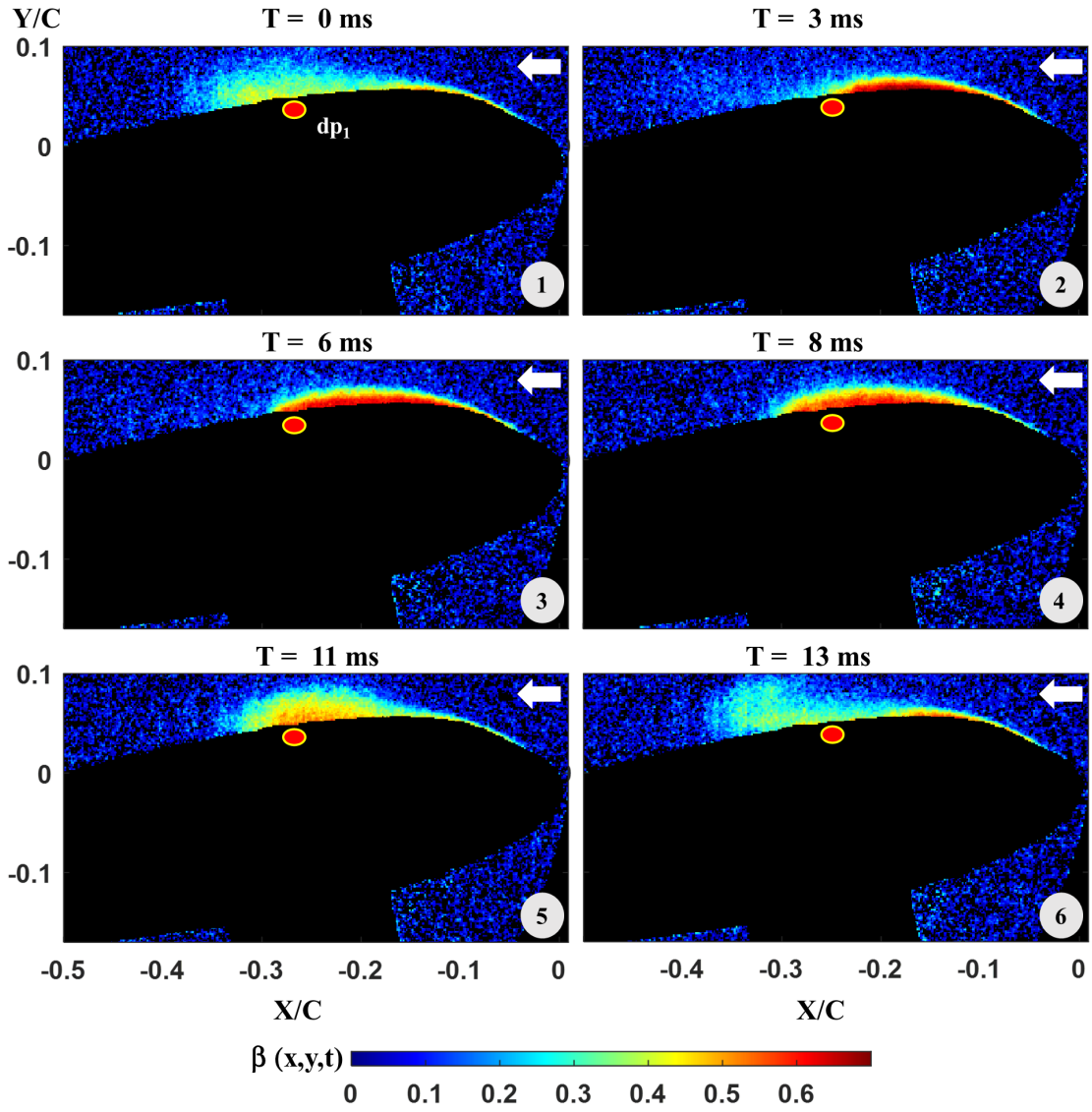

Figure 8.9: Time series of void fraction flow fields for a type(i) shedding cavity. The cavity oscillates periodically. The void fraction fields are shown very close to the surface of the foil to highlight the difficulty in resolving flow-fronts that cause cavity pinch-off. The thin cavities restrict the ability to observe any flow front trapped underneath the main cavity. $\sigma_0 = 3.15$ ($\sigma_0/2\alpha = 9.04$), $\beta = \ 0 - 0.7$.

figure 8.11 (4).

Re-entrant liquid flows and bubbly shocks have different dynamic surface pressure signatures at dp_1 for type(ii) cavities. Figure 8.12(a) and (b) show the synchronous dynamic pressure measured at dp_1 for re-entrant flow and shockwave driven shedding cycle respectively. As the bubbly shock passes over the transducer near leading edge (dp_1), an average 4 kPa pressure rise is recorded by the transducer as seen in figure 8.12(b) (4). However, such a pressure rise is not registered in dp_1 when the re-entrant liquid passes. The mechanism observed during a given cycle that causes shedding is stochastic in nature with no preference of either flow front. Bubbly shockwaves reach the leading edge of the hydrofoil in $\approx$ 11 ms while the re-entrant jet reaches in $\approx$ 7 ms for cavities of similar lengths.

8.4.3 Type(iii) shedding cavity: Cavity shedding mostly driven by shocks and occasionally by re-entrant flows

Type(iii) cavities occur for $\sigma_0/2\alpha = 4.2$ to 6.1 ($0.6 < Lc/C < 0.85$). In this regime, the cavities are longer and both bubbly shocks and liquid re-entrant flow are visualized using x-ray densitometry. However, on most occasions, cavity shedding from the leading edge was caused by bubbly shocks. On few occasions, the liquid re-entrant flow caused the cavity shedding. The observed mechanism of shedding is stochastic with no preference in dominance of either flow front.

Figure 8.13 shows the time varying void fraction flow fields of a shedding cycle caused by a bubbly shock. Corresponding synchronized unsteady surface pressure measurements(dp_1 and dp_2) are shown in figure 8.14.

Figure 8.13 (1)-(3) shows the growth phase of a type (iii) cavity. Accumulation of liquid underneath the cavity is seen in figure 8.13 (3). The cavity continues to grow past the x-ray field-of-view while the liquid re-entrant flow travels upstream towards the leading edge as shown in figure 8.13 (4). A bubbly shock wave is seen near trailing edge of the hydrofoil

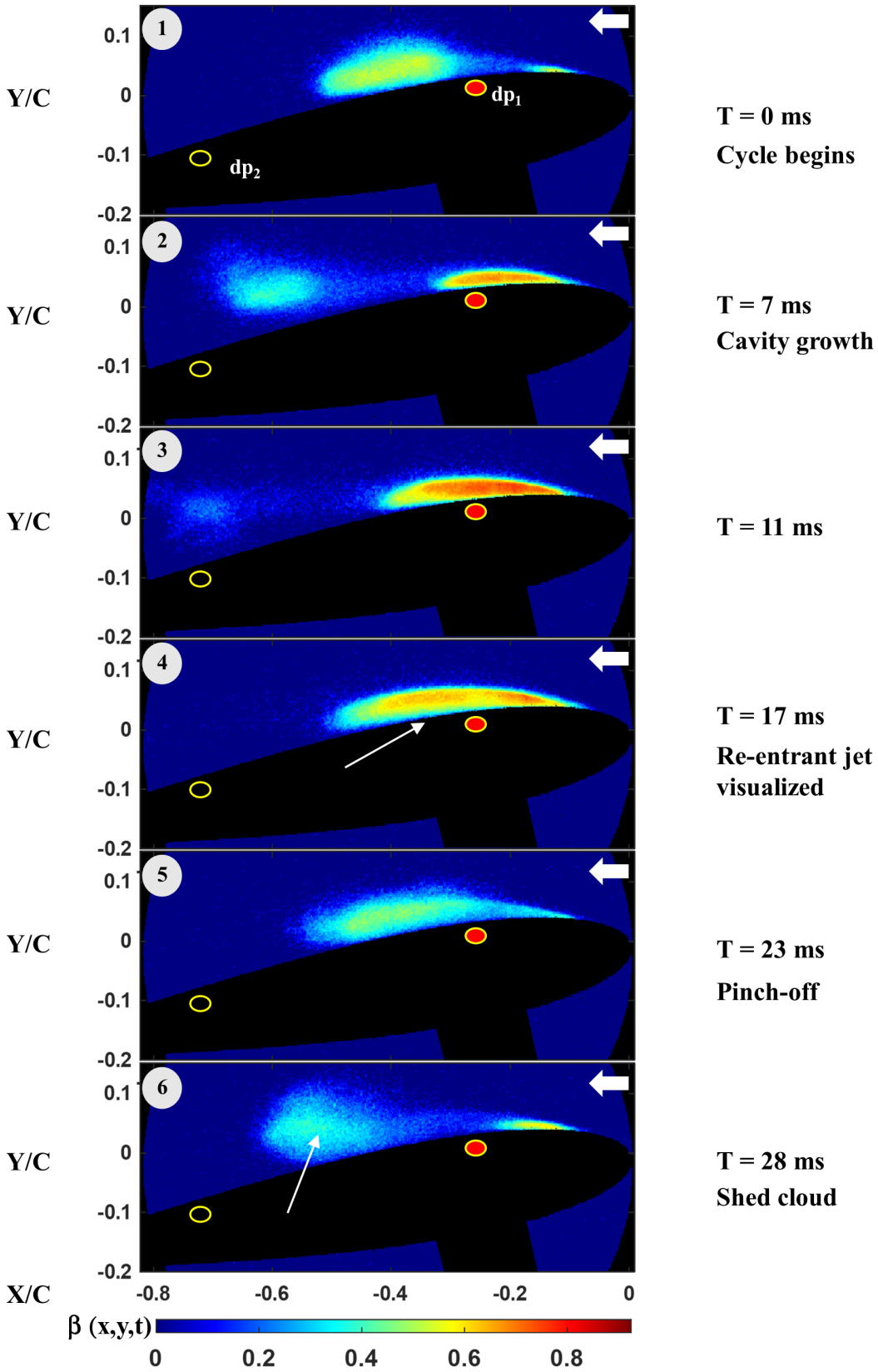

Figure 8.10: Time series depicting the type(ii) shedding cycle where re-entrant liquid jet causes cavity pinch-off. $\sigma_0 = 2.65$ ($\sigma_0/2\alpha = 7.6$), $\beta = \ 0 - 0.924$.

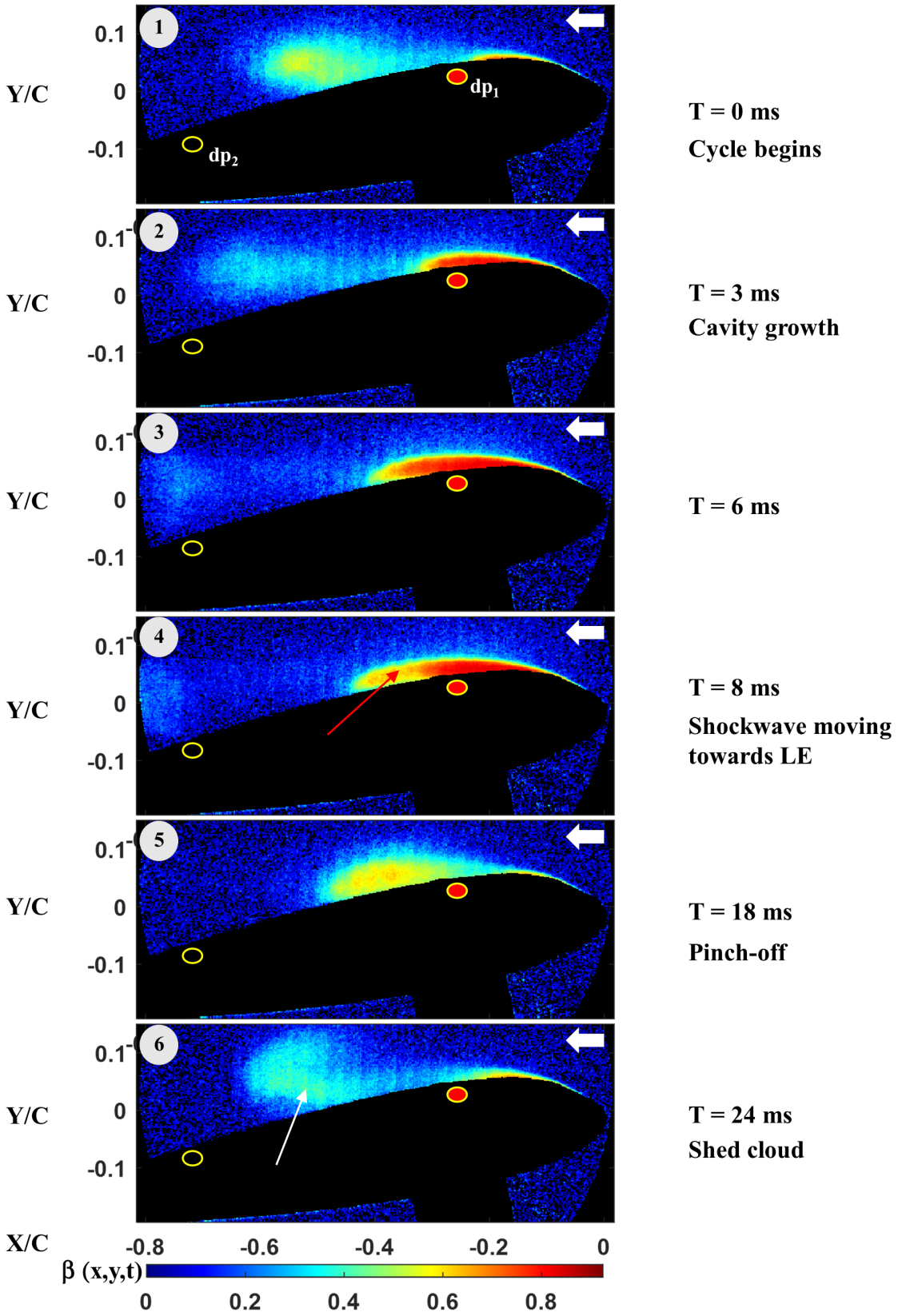

Figure 8.11: Time series showing shockwave driven cavity-pinch-off during the shedding cycle of a type(ii) cavity. $\sigma_0 = 2.65$ $(\sigma_0/2\alpha = 7.6)$, $\beta = \ 0 - 0.924$.

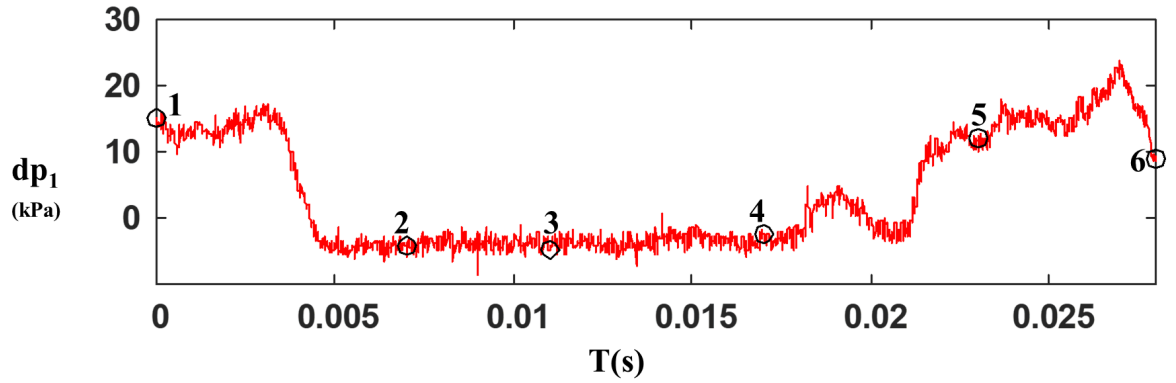

(a) dp_1 for re-entrant liquid jet driven cavity pinch-off shown in figure 8.10.

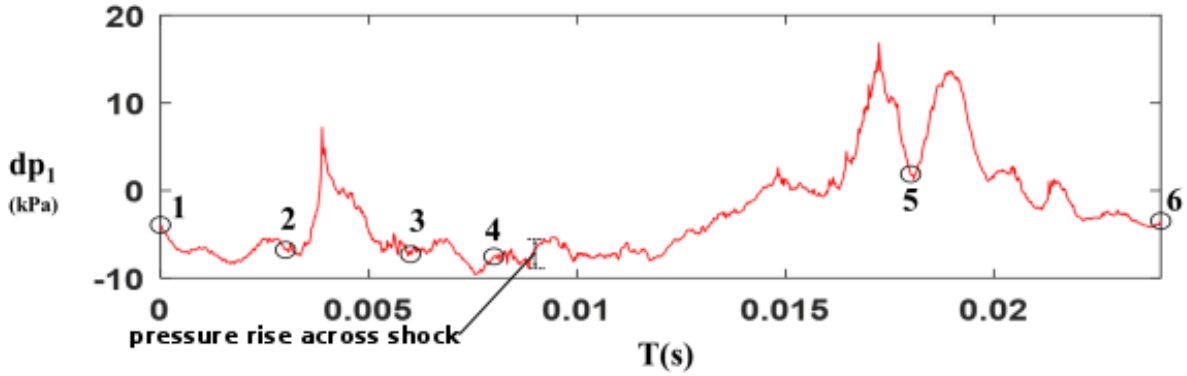

(b) dp_1 for shockwave driven cavity pinch-off shown in figure 8.11

Figure 8.12: Unsteady surface pressure signal near leading edge (dp_1) for type(ii) shedding cavity; $\sigma_0 = 2.65$ ($\sigma_0/2\alpha = 7.6$), $\beta = \ 0 - 0.924$.

in figure 8.13 (5), and this shock travels upstream to cause pinch off. The liquid re-entrant flow is almost stationary, unable to reach the leading edge (figure 8.13 (6)-(7)). The bubbly shock continues to travel upstream to cause cavity pinch-off as seen in figure 8.13 (7)-(9). The cycle then repeats.

On some occasions, liquid re-entrant flow is able to cause the cavity to shed, and one such cycle is shown in figure 8.15. The liquid re-entrant forms during the growth phase and begins to travel upstream as shown in figure 8.15 (1)-(2). While the cavity grows, the re-entrant flows continue to travel upstream towards the leading edge, as seen in figure 8.15 (3)-(5). It then pinches off the cavity from the leading edge as seen in figure 8.15 (6). The residual cavity grows and normal shedding cycle resumes.

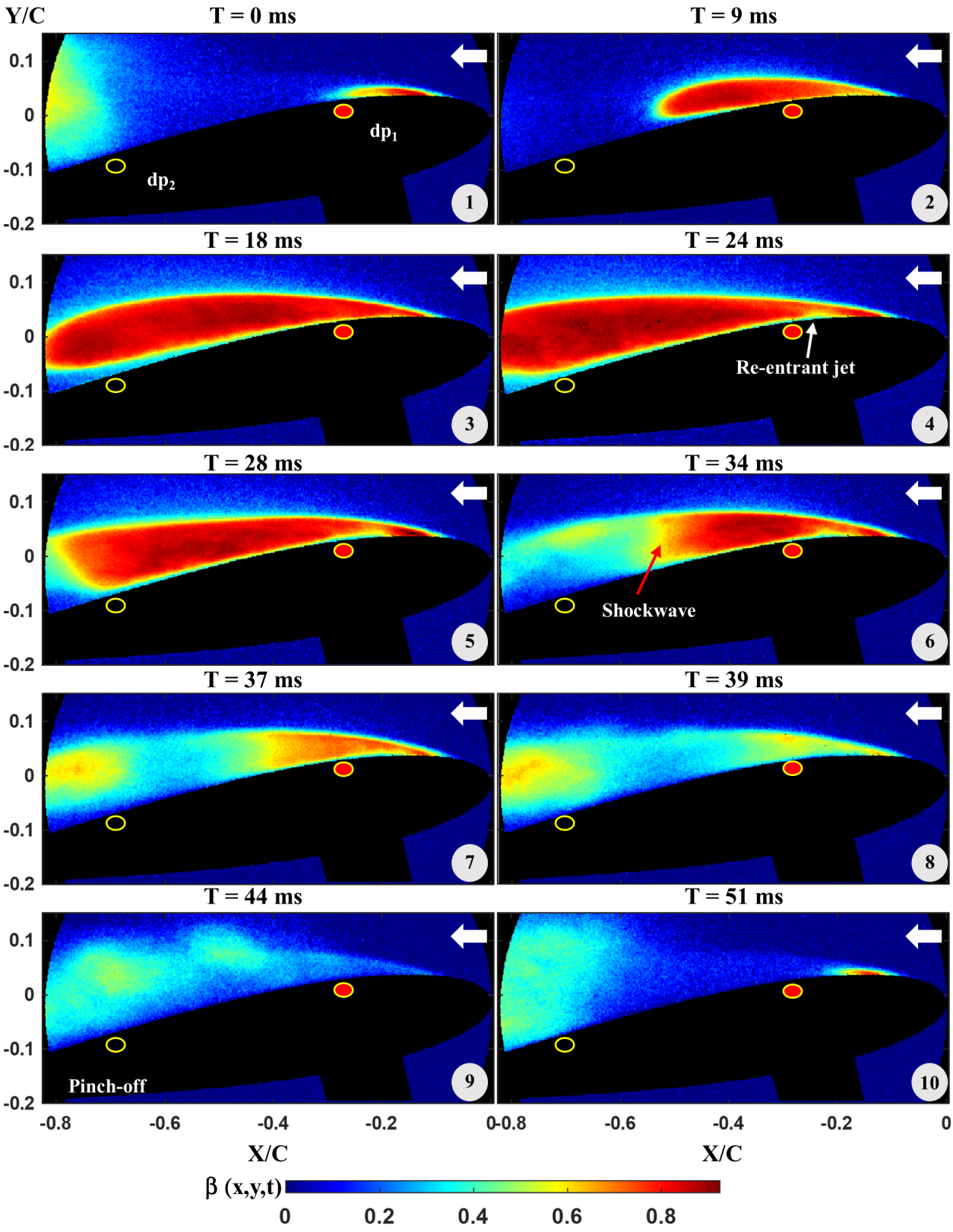

Figure 8.13: Time resolved void fraction time-series of cavitation shedding cycle for a type(iii) cavity. From (4) to (7) trapped re-entrant flow front is unable to cause pinch-off. (5)-(7) shows the advancing shockwave front dominating to cause pinch-off; $\sigma_0 = 1.91$ ($\sigma_0/2\alpha = 5.5$), $\beta = 0 - 0.924$

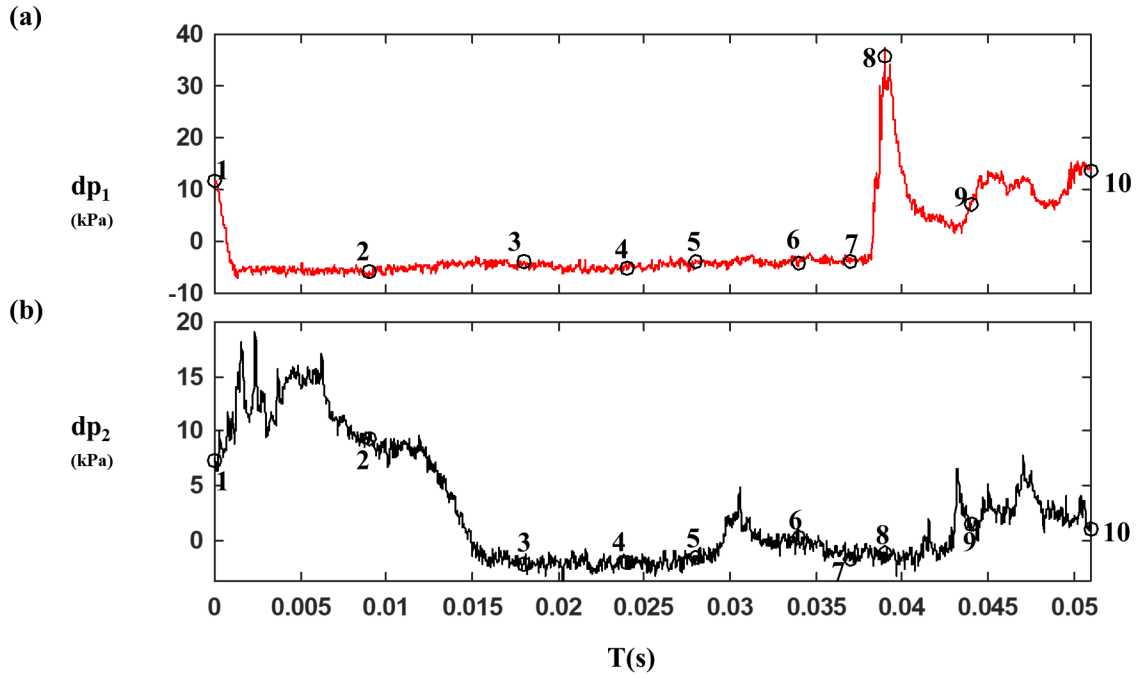

Figure 8.14: Synchronized unsteady surface pressure measurements through dp_1 and dp_2 are presented for cavitation shedding cycle for a type(iii) cavity. Ten snapshots presented on timeseries in figure 8.13 are marked on the dynamic pressure signals. From (4) to (7) trapped re-entrant flow front does not significantly affect the unsteady surface pressure at dp_1. 14.6 kPa pressure rise occurs due to the shockwave front passing over dp_1 between (7)-(8) in (a). Similarly a 5.9 kPa pressure rise over dp_2 occurs between (5)-(6) in (b). $\sigma_0 = 1.91$ ($\sigma_0/2\alpha = 5.5$), $\beta = \ 0 - 0.924$

Figure 8.14 shows the synchronous dynamic pressure signal recorded at dp_1 and dp_2 for the bubbly shock induced shedding cycle shown in figure 8.13. In this cycle both liquid re-entrant flow and bubbly shocks are observed. Figure 8.13 shows that the liquid re-entrant flow is in the vicinity of dp_2 and dp_1 from 18 to 24 ms, and the bubbly shocks pass over the transducers dp_2 and dp_1 close to 28 ms and 37 ms respectively. Upon examining figure 8.14, it is seen that the passage of a bubbly shock over dp_2 and dp_1 results in pressure rise observed between points (5)-(6) and (7)-(8). Such a pressure is not observed for the passage of liquid re-entrant flow which occurs between points (3) and (4).

During the cavity growth phase, as liquid re-entrant jet is trapped beneath the cavity, vapor covers the surface of transducers near the leading edge (dp_1) and trailing edge (dp_2) a pressure drop is recorded as seen in figure 8.14 (dp_1 : (a)(1)-(2); dp_2 : (b)(2)-(3)). The cavity continues to grow until it reaches a critical length (Lc). As the cavity pinches off from the leading edge, a large spike in pressure is registered at dp_1 as the transducer gets exposed to ambient pressure (figure 8.14(a)(8)).

8.4.4 Type(iv) shedding cavity: trailing edge cavitation

When maximum cavity lengths are comparable with chord length (Lc/C$\geq$ 0.85) secondary cavitation near trailing edge actively interacts with the main cavity. Trailing edge cavitation is observed as early as in type(ii) cavities, but it only affects cavity growth and shedding dynamics for longer type(iv) cavities that occur when $\sigma_0/2\alpha \leq 1.8$ and when $Lc/C \geq 0.85$. Similar to type(iii) shedding, both liquid re-entrant jet and bubbly shocks are observed during a cavity shedding cycle. Vapor production at the leading edge is high, as evident by higher instantaneous values of β. On most observed cycles, the weaker liquid re-entrant flow is unable to cause cavity pinch-off.

Time-series depicting shedding process of a type(iv) cavity due to bubbly shocks and liquid re-entrant flow shown in figure 8.16 and 8.17 respectively. Similar to type(iii) shedding,

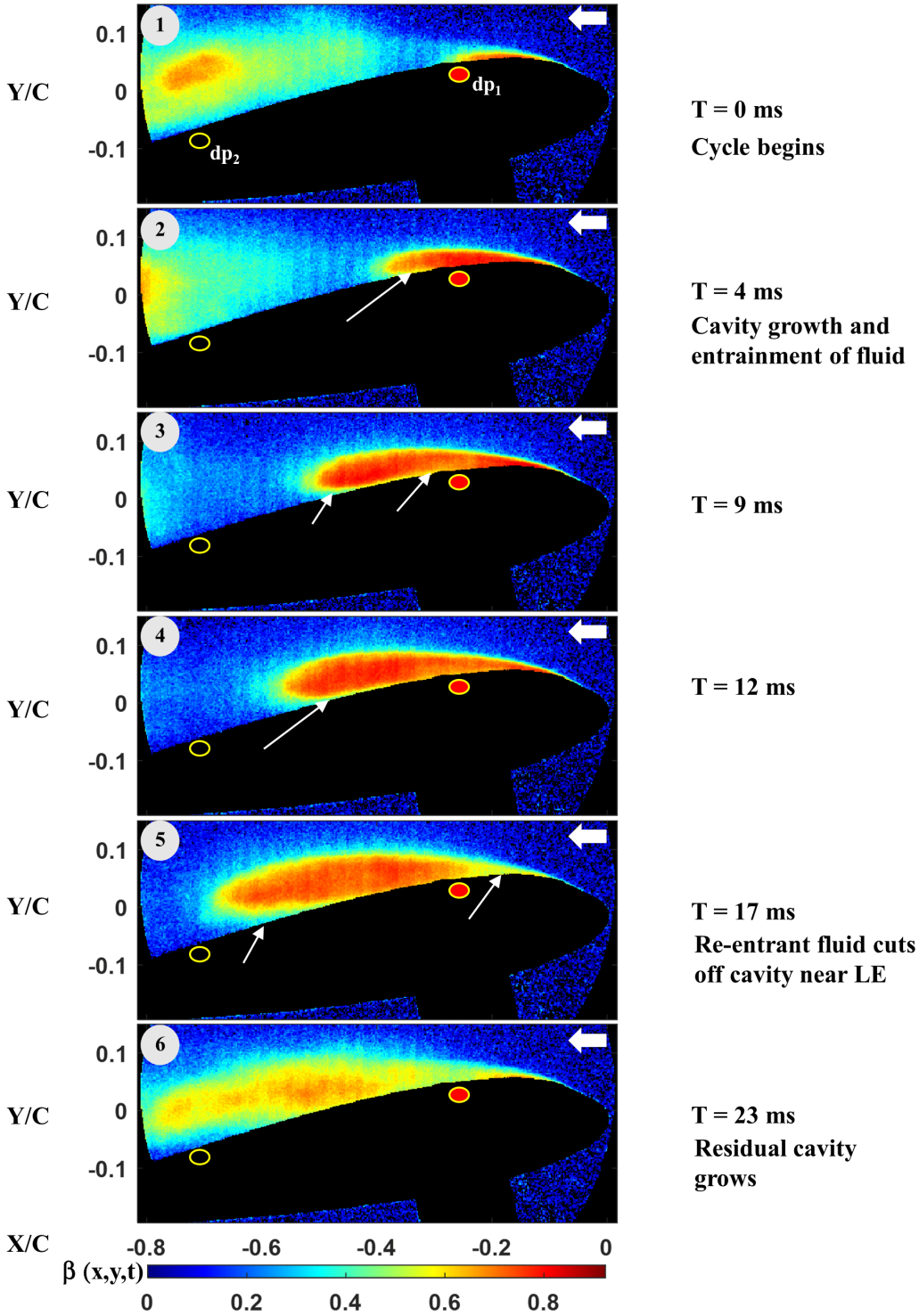

Figure 8.15: Timeseries of void fraction field depicting the re-entrant flow causing cavity pinch-off near leading edge (LE) of the hydrofoil for a type(iii) cavity. Liquid re-entrant flow is still able to cause cavity shedding. $\sigma_0 = 1.91$ $(\sigma_0/2\alpha = 5.5)$, $\beta = \ 0 - 0.924$.

both liquid re-entrant jet and bubbly shocks are observed during a cavity shedding cycle. Figure 8.16(1)-(3) shows the growth phase of the cavity. During the growth phase, liquid begins to accumulate underneath the cavity, and a well defined liquid re-entrant flow forms, as seen in figure 8.16(4). After (4), the cavity continues to grow beyond the x-ray field-of-field. A bubbly shock is observed near the downstream end of the x-ray field-of-view, while the liquid re-entrant flow is downstream of dp_1, as seen in figure 8.16(5). The bubbly shock continues to travel upstream, going past the liquid re-entrant flow, to cause the cavity to pinch off, as seen in figure 8.16(6)-(9).

Occasionally, the liquid re-entrant flow is able to cause cavity pinch off for type (iv) cavities. Such an instance is shown in figure 8.17. During the growth phase a liquid re-entrant flow forms, as seen in figure 8.17 (1)-(4). This liquid flow travels upstream and causes the cavity to pinch off from the leading edge, as seen in figure 8.17 (5)-(6). Like type (ii) and type (iii) cavities, the mechanism of pinch off observed in a given cycle was stochastic with no preference for dominance of either flow front to drive shedding.

Figure 8.18 shows dynamic pressure signal recorded by the transducers dp_1 and dp_2. Similar to type(iii) cavities, passage of the re-entrant flow over the transducer dp_1 does not result in an appreciable pressure rise between instances (5) and (6), as seen in figure 8.18(a). Passage of bubbly shocks over the transducers dp_2 and dp_1, occurring between 19-40 ms and 46-54 ms respectively, registers a pressure rise.

Figure 8.16 and 8.17 have a limited field of view which prevents the observation of cavitation near the trailing edge. In order to visualize cavitation at trailing edge, the field-of-view of the densitometry system is moved downstream, and a time-series of type(iv) cavitation near the trailing edge is shown in figure 8.19. The void fraction flow field is synchronized with surface pressures dp_1 and dp_2. In addition, a hydrophone submerged in a water bath is mounted on top of the tunnel wall at 0.25 C away from the trailing edge of the foil. Figure 8.20 presents the synchronized unsteady pressure and hydrophone measurements cor-

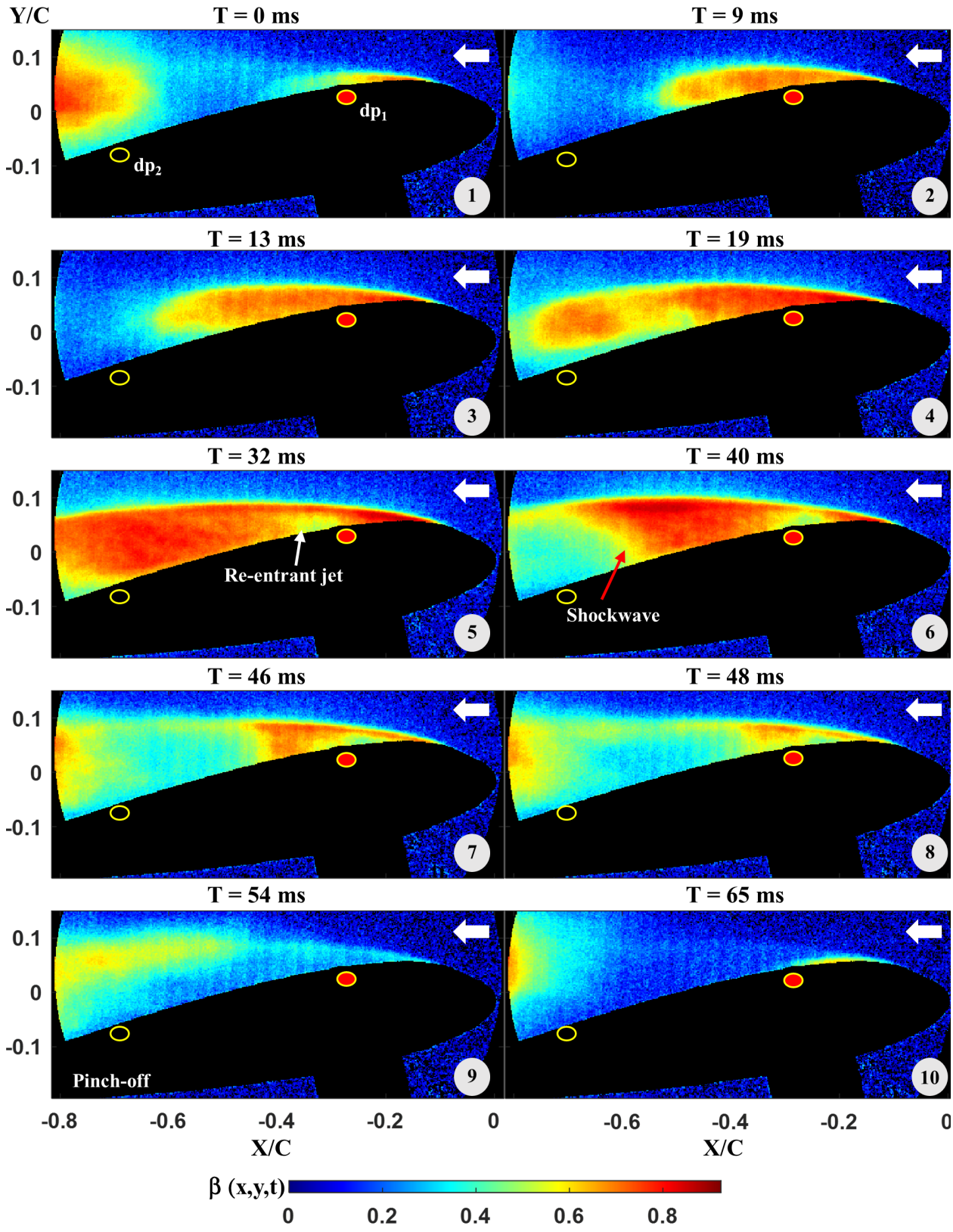

Figure 8.16: Void fraction time-series for cavitation shedding cycle for a type(iv) cavity. $\sigma_0 = 1.4$ ($\sigma_0/2\alpha = 4.1$), $\beta = \ 0 - 0.924$

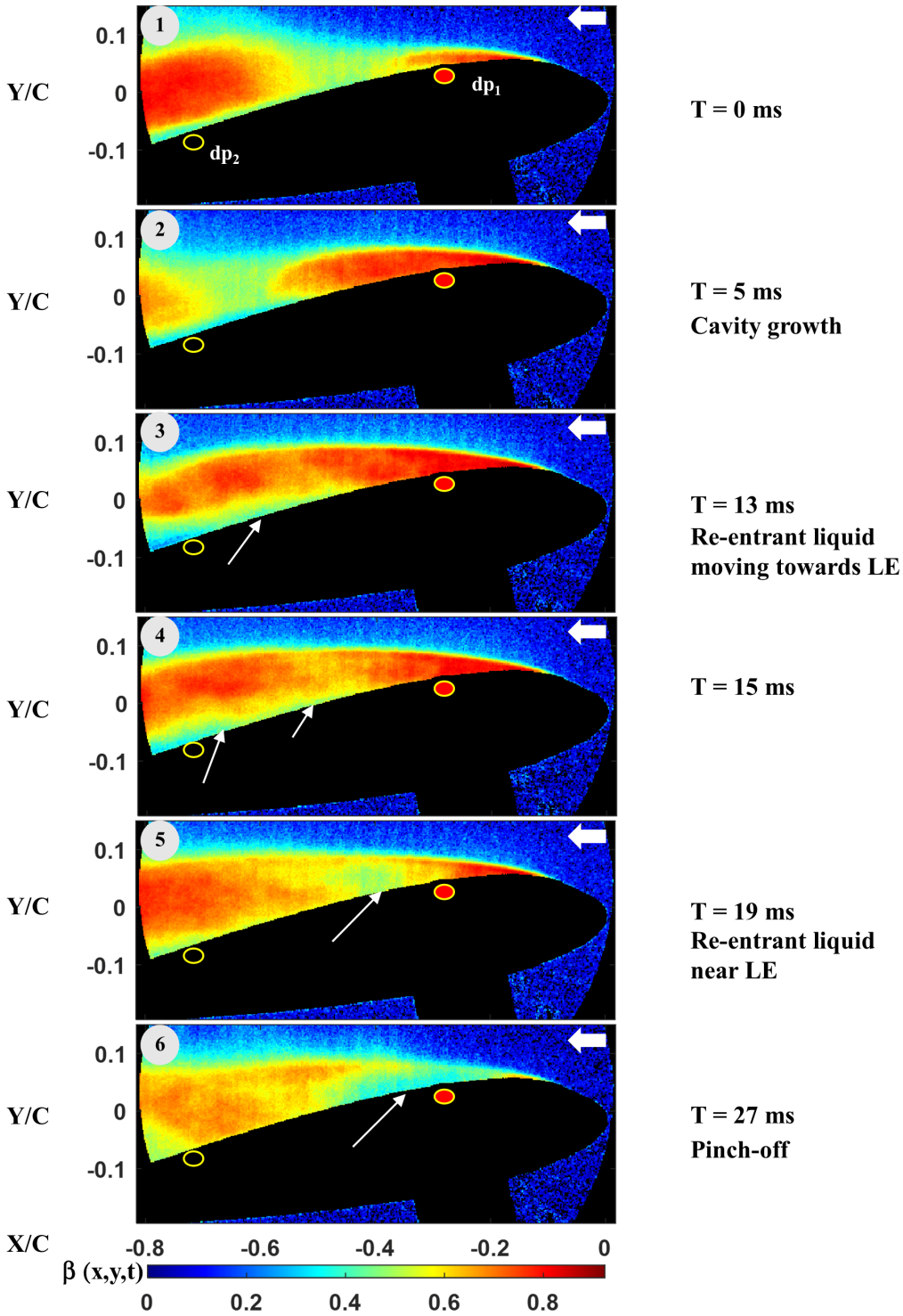

Figure 8.17: Timeseries of void fraction field depicting the re-entrant flow causing cavity pinch-off near leading edge (LE) for a type(iv) cavity. Although shockwaves are dominant mechanism of shedding, liquid re-entrant flow is still able to cause cavity shedding. $\sigma_0 = 1.4$ $(\sigma_0/2\alpha = 4.1)$, $\beta = \ 0 - 0.924$.

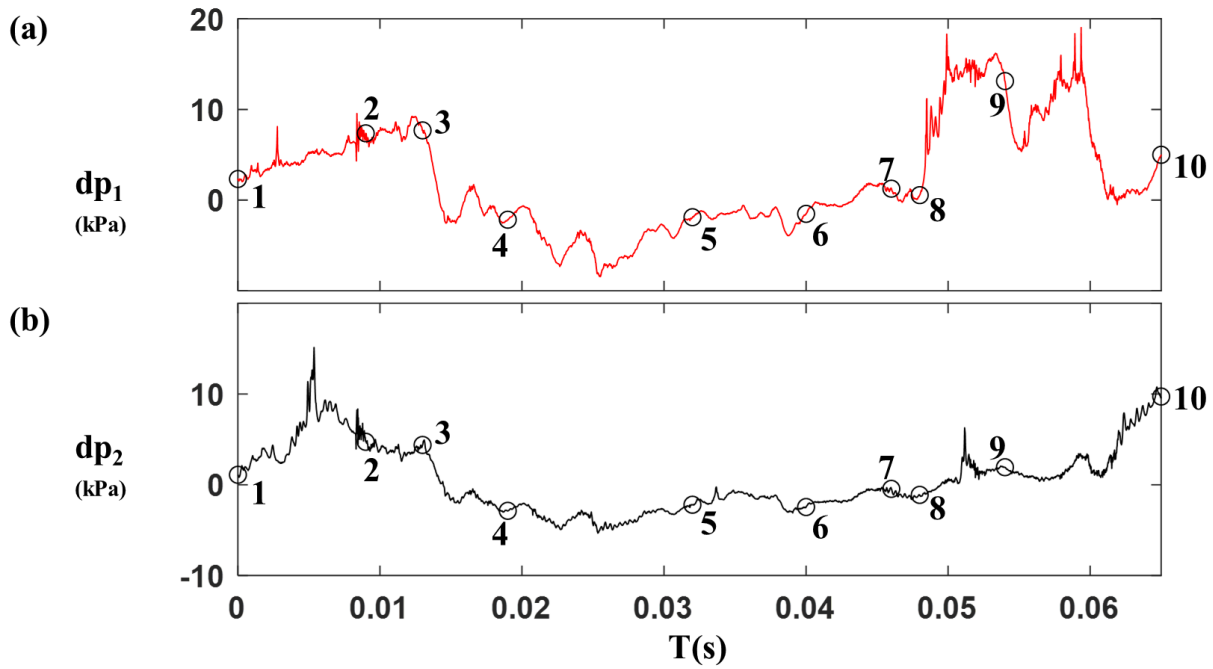

Figure 8.18: Synchronized unsteady pressure measurements through dp_1 and dp_2 are presented for cavitation shedding cycle for a type(iv) cavity. $\sigma_0 = 1.4$ ($\sigma_0/2\alpha = 4.1$), $\beta = 0 - 0.924$. The pressure fluctuation recorded between (4)-(5) for both (a) and (b) is similar to the pressure fluctuation in dp_1 and dp_2 seen in figure **??** near (1) where collapse of the vapor cloud is recorded in the hydrophone signal (p_a)

responding to the shedding cycle shown in figure 8.19.

Time-series of cavitation events occurring near the trailing edge is shown in figure 8.19. The cycle starts with secondary cavitation at the trailing edge of the hydrofoil as the shock-wave travels towards the leading edge. As the main cavity approaches its max-length (Lc), shed vapor from aft of the cavity convects downstream (figure 8.19(1)-(2)). As this shed vapor from the cavity moves downstream, secondary cavitation begins to appear near the trailing edge of the hydrofoil. A cavitating lobe (Lobe 1 in figure 8.19(5)) grows and interacts with oncoming vapor cloud shed from the main cavity. When Lobe 1 reaches its maximum size, another vapor filled lobe designated as Lobe 2 appears as shown in figure 8.19(6). These two lobes interact as shown in figure 8.19(6)-(8). This behavior is similar to the cavitation observed in the near wake of a bluff body. Prior to the final interaction between Lobe 1 to Lobe 2 (figure 8.19(8)) a pressure spike is seen in the hydrophone signal (figure 8.20(c) between (7) and (8)). After the pressure spike, the two cavitating lobes combine and convect downstream (figure 8.19(9)-(10)). The cavity begins to grow towards the trailing edge (figure 8.19(10)) and the cycle repeats.

8.5 Review of flow features observed

As the cavitation number (σ_0) decreases, the cavitation dynamics on suction side of the hydrofoil change. Two flow features, re-entrant liquid jets and bubbly shockwaves affect the cavity dynamics. The schematic of the flow fronts identified and the mechanism of shedding is shown in figure 8.21. Figure 8.22 shows these regimes as a function of σ_0 and Lc/C

Four regimes identified in this study are,

- **Type(i)** : Oscillatory cavities cavities with $0.2 < Lc/C \leq 0.4$ ($\sigma_0/2\alpha = 7.6$ to 9.8), the liquid-flow accumulated under the cavity causes pinch-off as shown in figure 8.21(i). As shown in figure 8.9, this liquid flow cannot be resolved using the densitometry system.

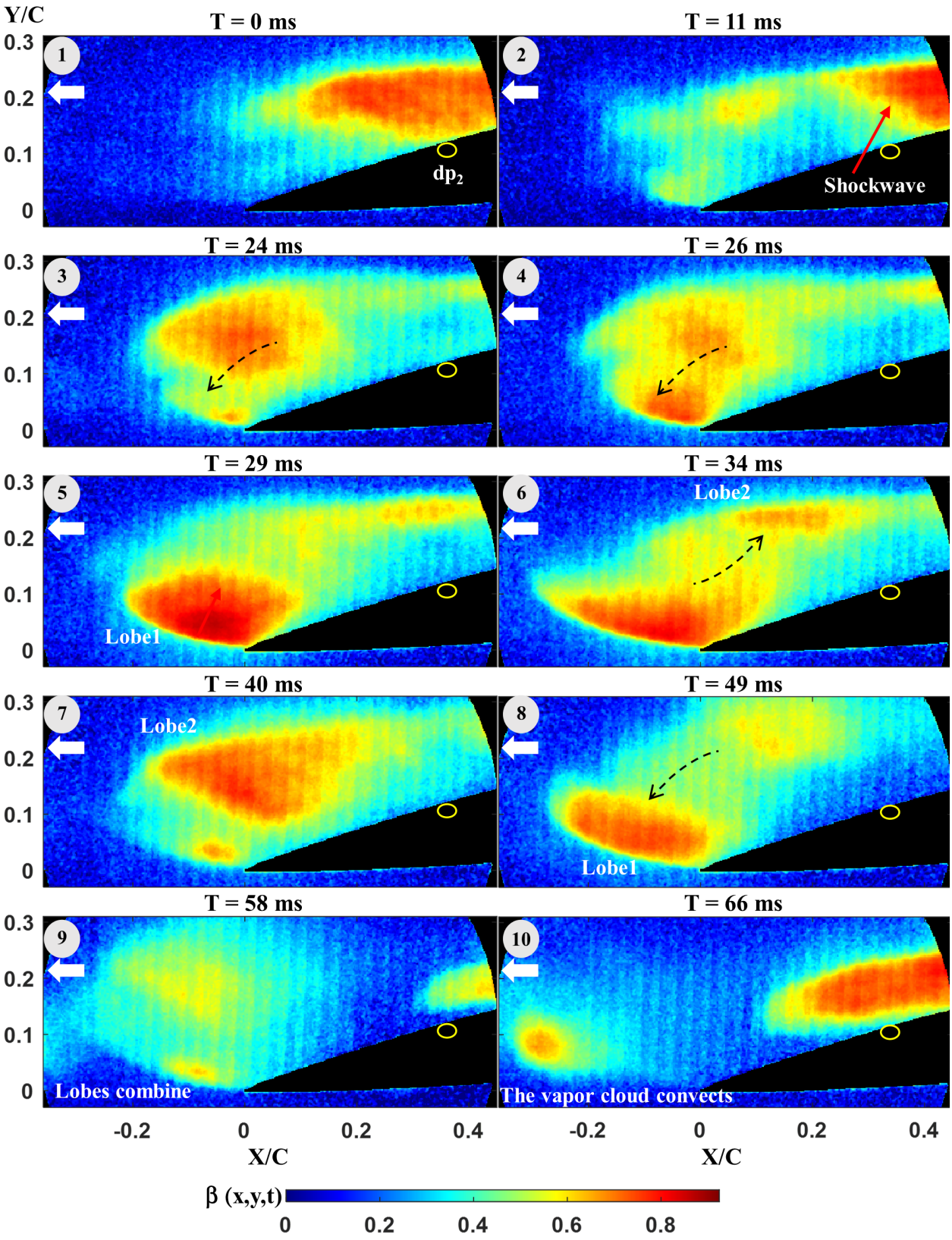

Figure 8.19: Depiction of trailing edge cavitation on the hydrofoil in type(iv) shedding regime. FOV has been moved downstream. Shedding cycle similar to the bluff body shedding cavitation is seen in (3)-(8); $\sigma_0 = 1.4$ $(\sigma_0/2\alpha = 4.1)$, $\beta = \ 0 - 0.924$.

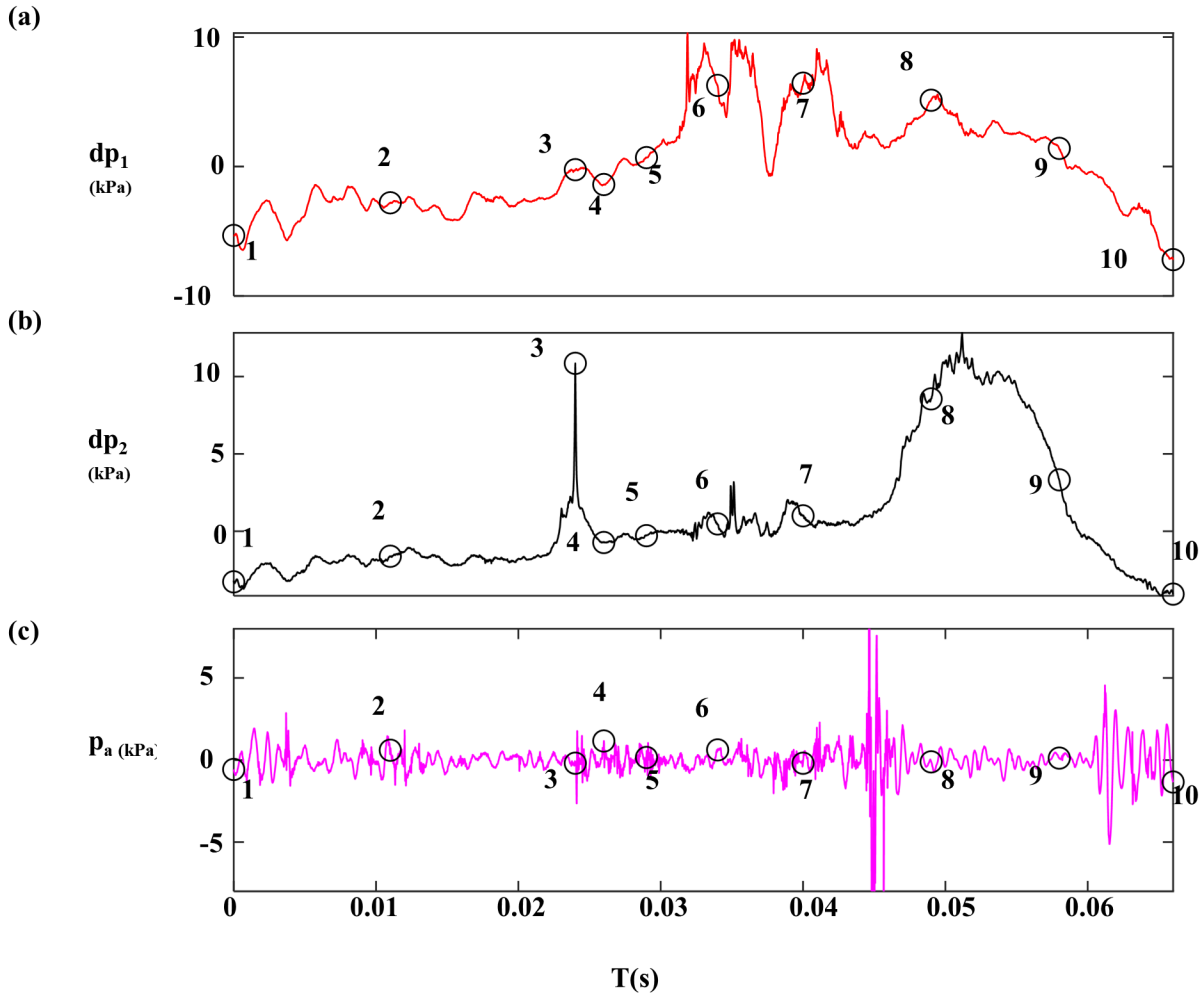

Figure 8.20: Synchronized unsteady pressure measurements through dp_1, dp_2 and acoustic pressure measured through a top wall mounted hydrophone (p_a) for trailing edge cavitation seen on the hydrofoil in type(iv) shedding regime. $\sigma_0 = 1.4$ ($\sigma_0/2\alpha = 4.1$) , $\beta = \ 0 - 0.924$.

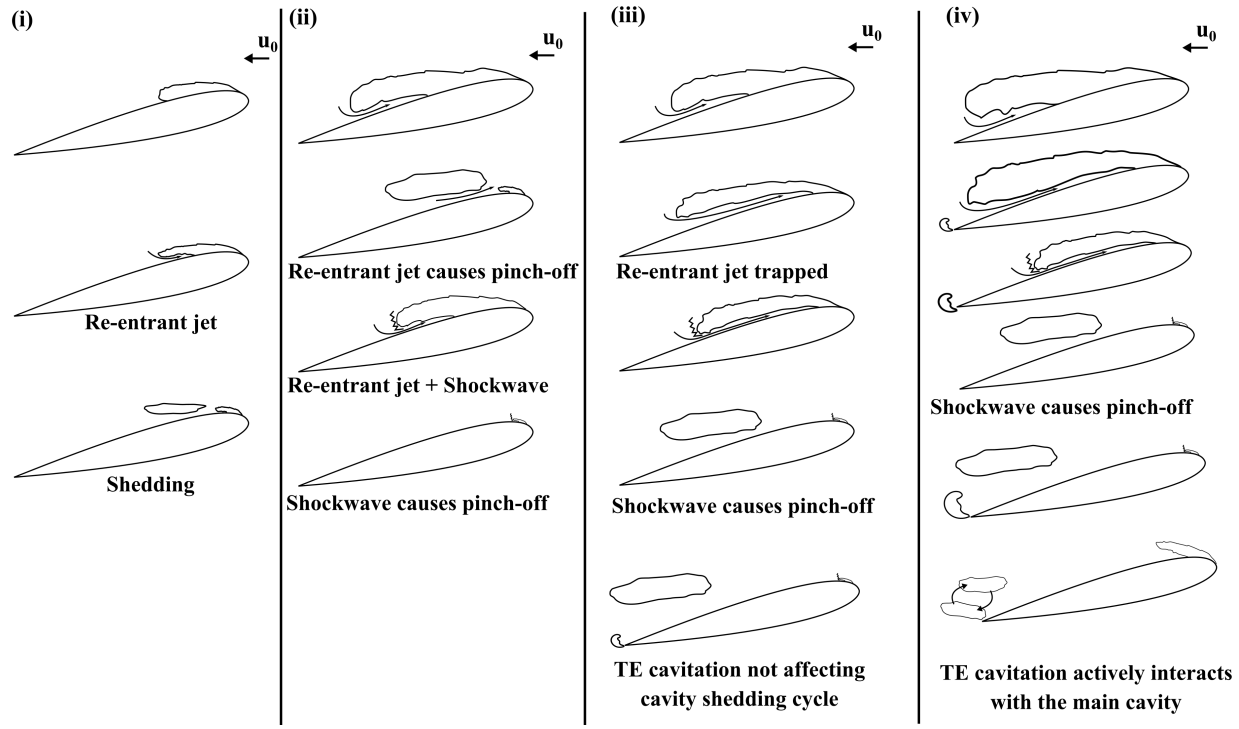

Figure 8.21: Schematic depicting different flow fronts governing cavity pinch-off (i) Re-entrant jet driven (ii) Re-entrant jet + Shockwave driven (iii) Shockwave driven but unaffected by TE cavitation (iv) Shockwave driven but TE cavitation actively interacts with the main cavity to cause a shear-layer shedding phenomenon identical to shedding in wake of bluff bodies

$\alpha = 10^\circ$			$\alpha = 7^\circ$			Flow features
σ_0	$\sigma_0/2\alpha$	Lc/C	σ_0	$\sigma_0/2\alpha$	Lc/C	
3.68	10.54	0.16	2.55	10.46	0.13	Stable sheet cavity
3.36	9.64	0.23	2.40	9.82	0.23	
3.20	9.18	0.27	2.22	9.11	0.35	Type(i) Oscillatory
3.03	8.69	0.31	2.08	8.52	0.43	
2.87	8.24	0.35	1.93	7.92	0.53	
2.73	7.83	0.39				Type(ii) bubbly shockwaves and re-entrant liquid jet co-exist
2.56	7.34	0.44	1.83	7.52	0.60	
2.40	6.89	0.48	1.65	6.78	0.69	
2.26	6.48	0.58				
2.10	6.01	0.72	1.48	6.09	0.86	Type(iii) bubbly shockwaves with no TE cavitation feedback
1.92	5.52	0.91	1.33	5.44	0.91	
1.77	5.08	0.98	1.17	4.82	1.02	Type(iv) bubbly shockwaves + TE cavitation feedback
1.48	4.24	1.05	1.01	4.15	1.07	

Table 8.2: Inlet cavitation number (σ_0) and uncorrected cavitation parameter ($\sigma_0/2\alpha$) values at different cavitating flow regimes at two α.

- **Type(ii)** : Both re-entrant liquid flow and shockwave fronts cause shedding when the cavity length is within $0.4 < Lc/C \leq 0.6$ ($\sigma_0/2\alpha = 6.2$ to 7.6).

- **Type(iii)** : For longer cavities ($0.6 < Lc/C < 0.85$, $\sigma_0/2\alpha = 4.2$ to 6.1) re-entrant jet is unable to cause pinch-off (figure 8.21(iii)). Shockwaves begin to dominate the shedding cycle. There is no significant feedback from the trailing edge cavitation.

- **Type(iv)** : For significantly longer cavities ($Lc/C \geq 0.85$, $\sigma_0/2\alpha$ <5.1) the secondary cavitation at the trailing edge begins to interfere with the main cavity.

Table 8.2 summarizes the different cavity dynamics observed at different cavitation numbers (σ_0) and the associated flow features.

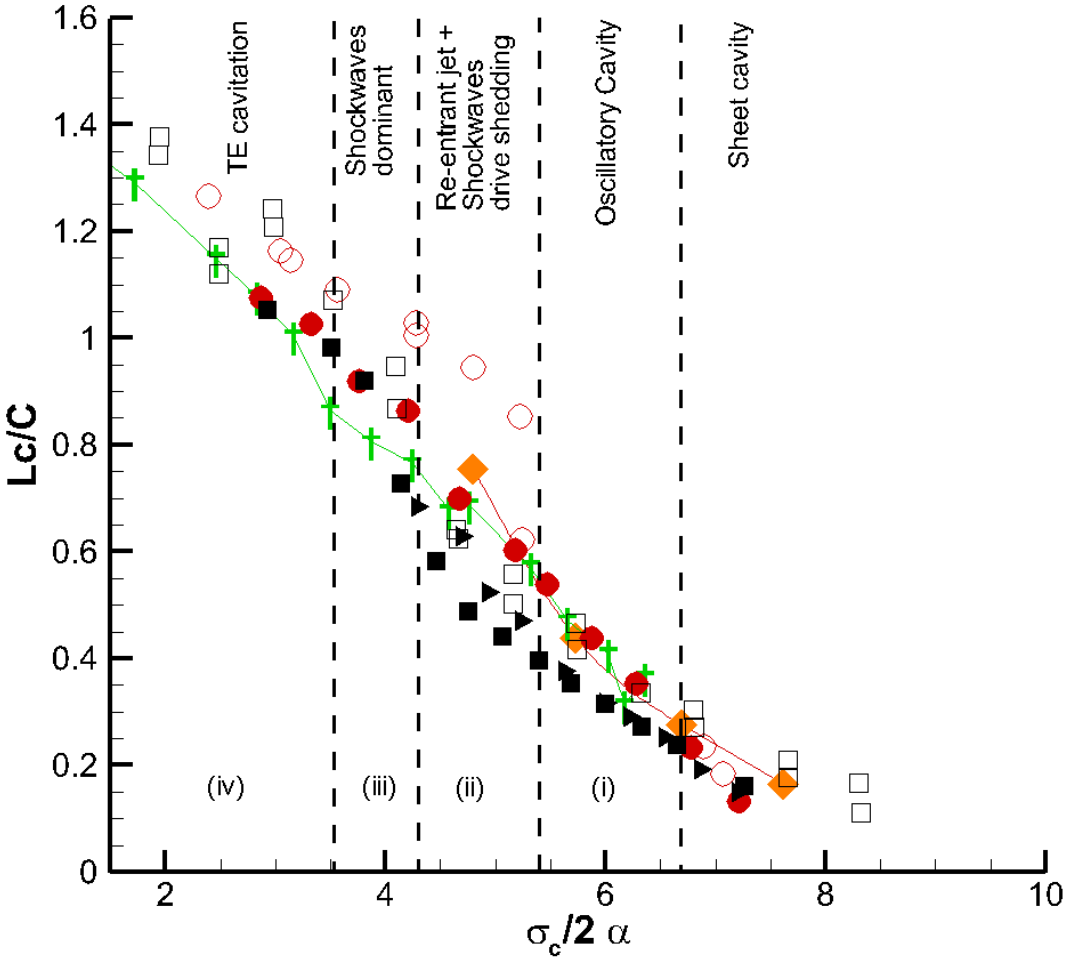

Figure 8.22: Comparison of Lc/C for current model from maximum cavity length measurements at two angle of attack ($\alpha = 10°$ (□ (HS), ▶ (XR)) and $\alpha = 7°$(○)) where cavitation parameter ($\sigma_c/2\alpha$) has been corrected for blockage. Cavities formed over the hydrofoil model used in current study (filled symbols) are compared with those observed by Wu (2019) (open symbols). Also the cavity length reported by Obernach (†) and Arndt(◊) are included. Four types of cavitating regimes are marked as type(i)-(iv) where re-entrant flow and shockwaves affect the cavity shedding dynamics.

Chapter 9

Spectral Content in Cavity Dynamics Data of NACA0015 Hydrofoil

Spectral analysis of dynamic pressure transducer signals dp_1 and dp_2, void fraction signals at spatial locations close to dp_1, dp_2, and cavity closure, and hydrophone signals are presented in this section. In addition, Spectral Proper Orthogonal Decomposition (S-POD) of void fraction fields is performed to identify spatial modes and their associated resolved frequencies.

9.1 Power spectral density

Figures 9.1 and 9.2 shows the location of pressure and void fraction probes. As an example, the dynamic pressure signals (dp_1 and dp_2) and void fraction signal at the two probes (β_{LE} andβ_{TE}) for a type(iv) shedding cavity are shown in figure 9.3. As the bubbly shock passes over the surface pressure transducer, pressure increases and a simultaneous drop in measured void fraction values is seen at locations I, II, III and IV.

Figure 9.4 shows the dominant peak obtained from Fast Fourier Transform of signals shown in figure 9.3. The dp_1 and dp_2 signals are acquired at sampling rate of 50 kHz for a duration of 3s which gives a frequency resolution of 0.33 Hz (or St resolution of 0.007). Pressure transducer dp_1 sees a single dominant peak, whereas transducer dp_2 registers two peaks for a type (iv) cavity. Presence of two peaks is also observed in void fraction probes β_{LE} and β_{TE}. The void fraction signals are sampled at 1 kHz for a duration of 0.787s leading to a frequency resolution of 1.3 Hz.

Figure 9.5(a) and (b) show the variation of the first and second dominant peak, in terms

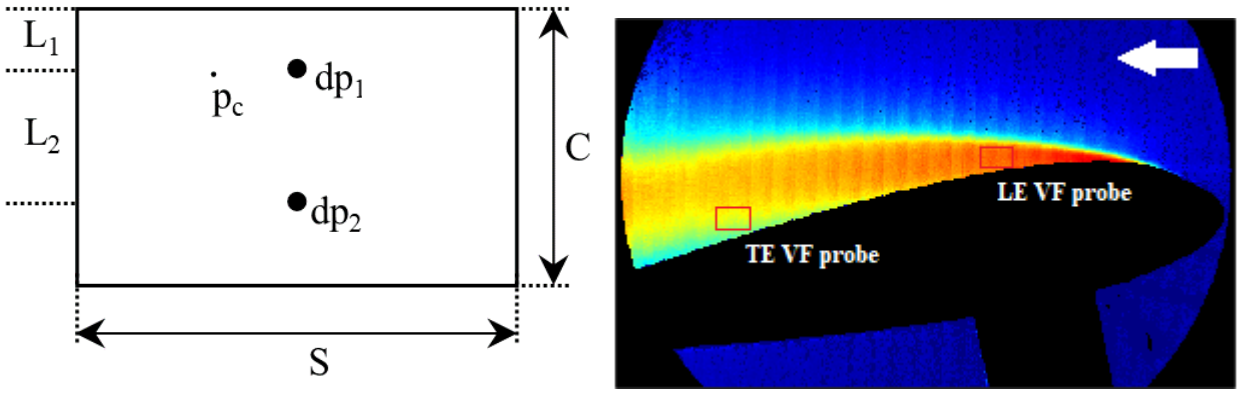

(a) (b)

Figure 9.1: Schematic showing the location of (a) Dynamic surface pressure measurement locations (dp_1 and dp_2) on suction side of the hydrofoil (b) Space averaged void fraction probe volumes near the leading edge (LE) and trailing edge (TE) of the hydrofoil (β_{LE} andβ_{TE}). The probes are 5 mm by 2.5 mm and located near the unsteady surface pressure transducers (dp_1 and dp_2).

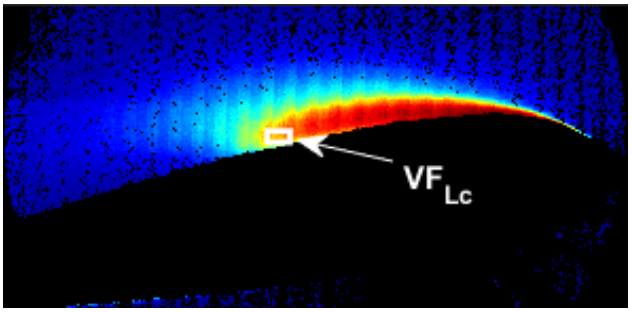

Figure 9.2: Space averaged void fraction probe volume near the maximum cavity length(β_{Lc}). The probe is 5 mm by 2.5 mm in size, moves with maximum cavity length from mean void fraction field and captures the dynamics at the aft of the cavity.

of St (equation 9.1), obtained from dp_1, dp_2, and void fraction probe β_{LE}, with cavitation parameter $\sigma_0/2\alpha$. Figure 9.5 (a) and (b) also shows St reported by Kjeldsen et al. (2000) and Arndt (2012). It is seen that first dominant peak matches well with the St reported by Obernach (Arndt et al. (2000)). St reported by Arndt (2012) is at $\sigma_0/2\alpha$ values lower than the current study. St based on peak 1 is strongly dependent on $\sigma_0/2\alpha$ for type(i) and type(ii) cavities and St decreases monotonically with decreasing $\sigma_0/2\alpha$. For St based on peak 2, there is a change in the slope of the curve from monotonically decreasing with $\sigma_0/2\alpha$

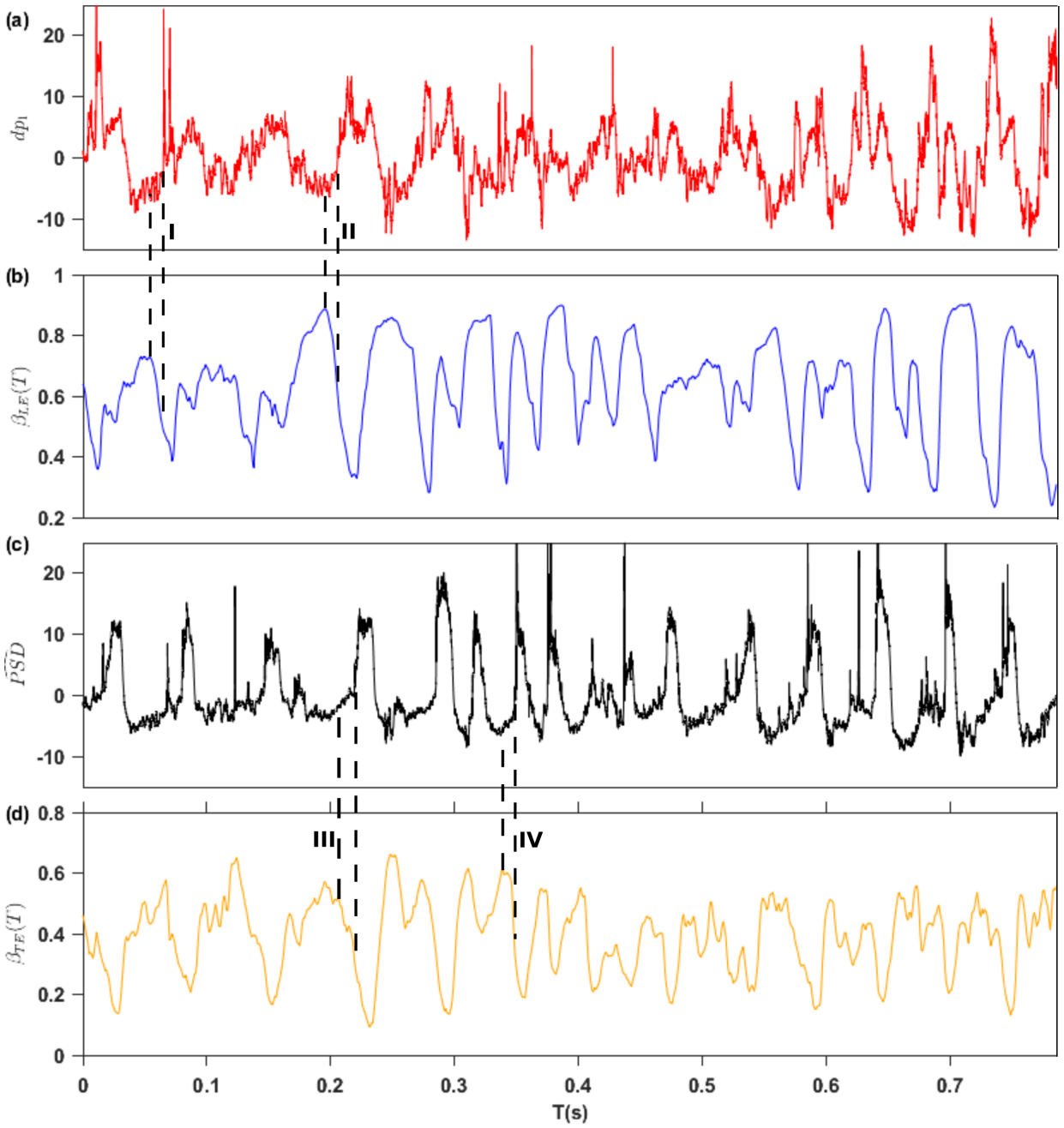

Figure 9.3: Raw time signals for each of the surface pressure transducers and void fraction (β) probes for the 0.787 s acquisition period of the densitometry system where (a) dp_1 (b) void fraction probe near the LE ($\beta_{LE}(t)$) (c) dp_2 (b) void fraction probe near the TE ($\beta_{TE}(t)$). The signals are time synchronized which means similar flow features are seen. The signals are presented for a type(iv) shedding cavity at $\sigma_0 = 1.5$ ($\sigma_0/2\alpha = 4.3$), $\alpha = 10°$). Four instances of shockwaves passing over surface pressure transducer are marked as I, II, III and IV where change in density values due to passage of shocks is important.

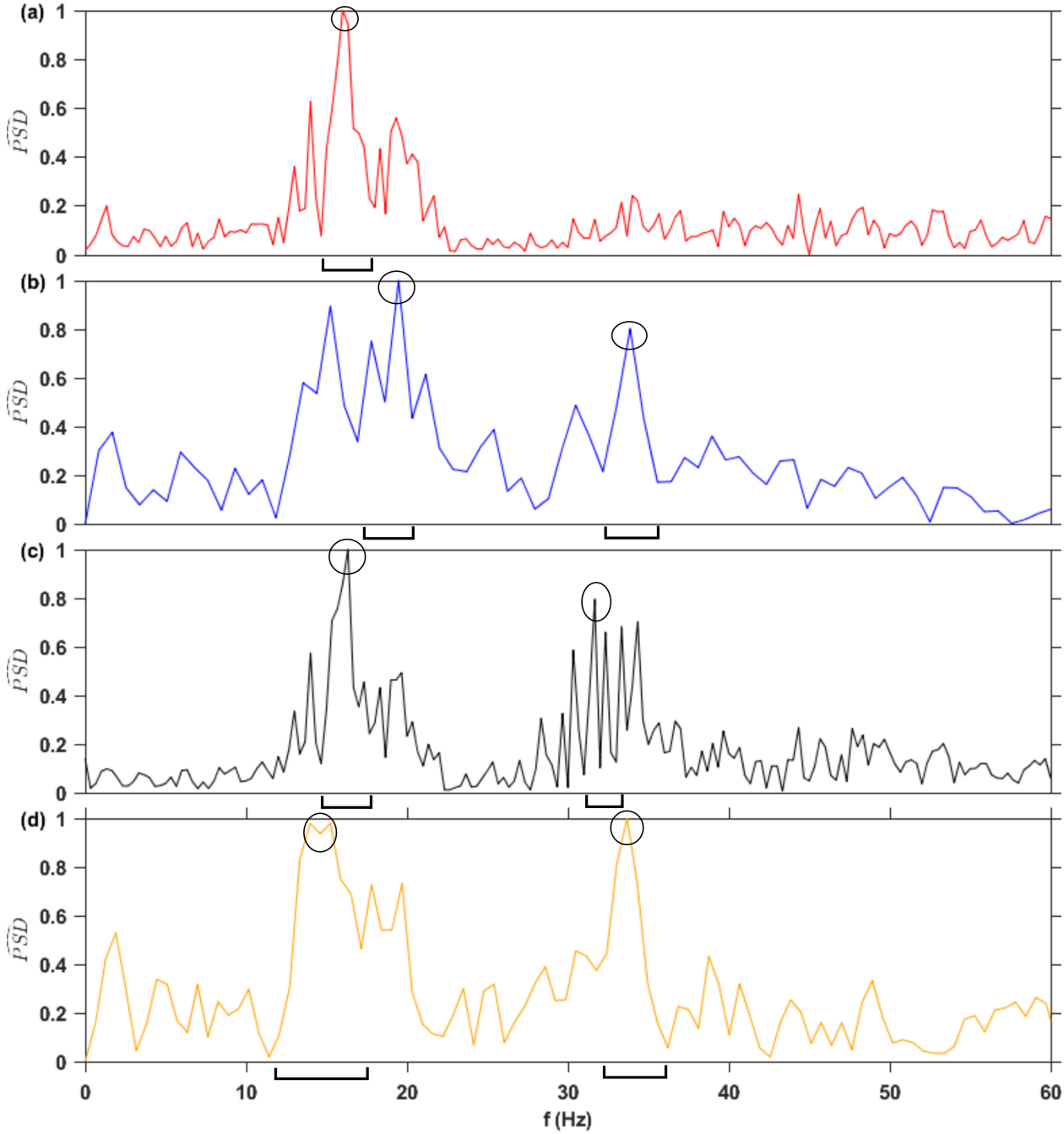

Figure 9.4: Power specrtal density curves for the corresponding time signals presented in figure 9.3; As in the previous figure (a) dp_1 (b) void fraction probe near the LE ($\beta_{LE}(t)$) (c) dp_2 (b) void fraction probe near the TE ($\beta_{TE}(t)$). The peak characteristic frequency and uncertainty in the frequency values for those peaks are marked on each curve. The signals are presented for a type(iv) shedding cavity at $\sigma_0 = 1.5$ ($\sigma_0/2\alpha = 4.3$)

to being independent of $\sigma_0/2\alpha$. This transition occurs at a $\sigma_0/2\alpha \sim 5.7$.

$$St = \frac{f \cdot C}{u_0} \tag{9.1}$$

Figure 9.6 shows first peak and second peak values varying across the moving void fraction probe (β_{LC}) kept at maximum cavity length (Lc), in addition to dp_1 and dp_2 measurements. This moving probe was taken to resolve the variations due to cavity length which is not captured by dp_1, dp_2 and β_{LE}. Upon examination, good agreement with Obernach's experimental data (Arndt et al. (2000)) is seen for the first (dominant) peaks. In addition, St based on first peak for β_{LC} follows the monotonically decreasing sharper than figure 9.5(a). For peak 2, the transition from monotonically decreasing to being independent of $\sigma_0/2\alpha$ occurs at $\sigma_0/2\alpha \sim 5.7$. This transition on St with σ_0 was also reported by Kjeldsen et al. (2000).

9.2 Time-frequency analysis

Wu et al. (2019) reported that cavitation dynamics on NACA0015 hydrofoil can have several dominant shedding frequencies, and under certain conditions these frequencies can change with time. Barwey et al. (2020) found that this change in frequency with time happens due to transition from a 3-step to 2-step shedding process. A time frequency analysis is performed on dp_1, dp_2 and p_a to investigate the temporal variation of dominant frequency.

Figure 9.7 presents the spectrograms of dp_1 and dp_2 signals for a type (iii) and type (iv) cavity. Co-existence of two peaks at a given time and no change in dominant frequency with time is seen. Spectrograms of acoustic pressure signal(p_a) measured by the hydrophone is shown in figure 9.8. As observed in figure 9.7, there are no variations in dominant shedding frequency with time. Current experimental configuration, despite having two frequency peaks, does not have a time variation in frequency caused by transition from 3-step to a

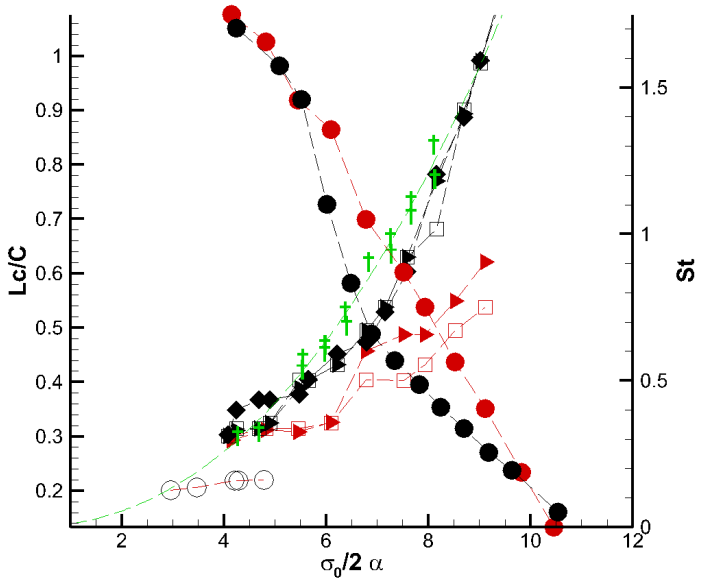

(a) First(dominant) peaks seen in PSD data compared with St reported by Obernach (†) and Arndt(◯). dp_1 (▷), dp_2 (□), β_{LE} (♦), Lc/C (●, ●) for AOA(α) = 10° (black) and 7° (red)

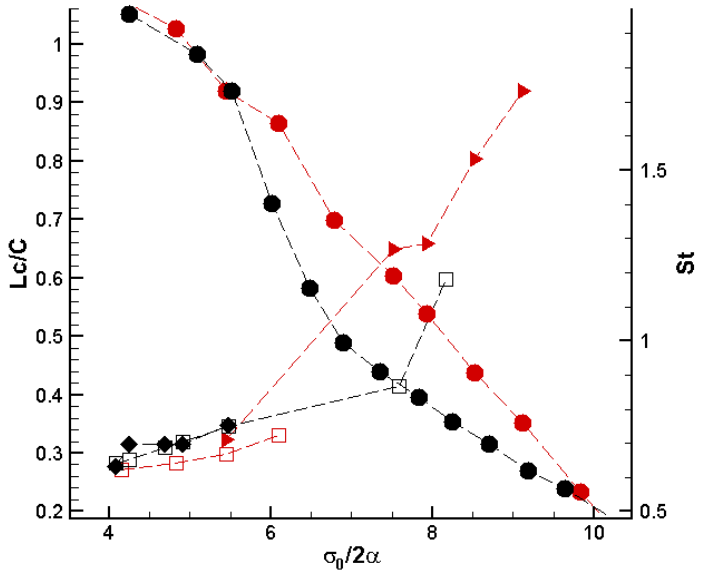

(b) Second peak seen in PSD data through dp_1 (▷), dp_2 (□), β_{LE} (♦), Lc/C (●, ●) for AOA(α) of 10° (black) and 7° (red)

Figure 9.5: Change in shedding frequency with changes in cavitation number shows how close the peak shedding frequencies obtained from void fraction signal are to those from dynamic pressure transducers and the St reported in previous literature. Maximum uncertainty in $\sigma_0 = \pm\ 0.07$, $Lc/C = \pm\ 0.1$, $St = \pm\ 0.08$

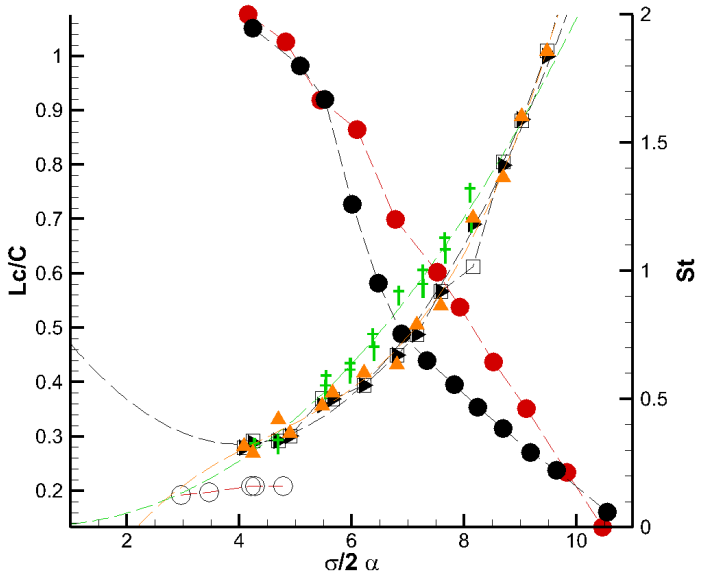

(a) First(dominant) peaks seen in PSD data compared with St reported by Obernach (†) and Arndt(◯). dp_1 (▷), dp_2 (□), β_{Lc} (▲), Lc/C (●, ●) for AOA(α) = 10° (black) and 7° (red)

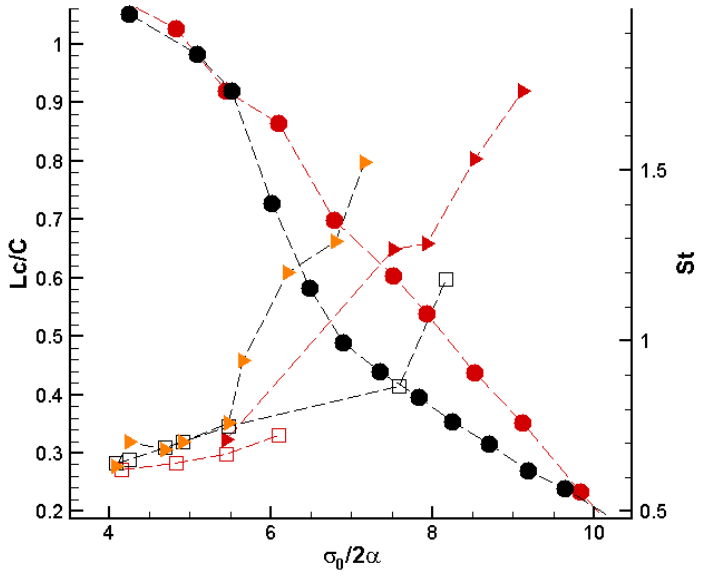

(b) Second peak seen in PSD data through dp_1 (▷), dp_2 (□), β_{Lc} (▲), Lc/C (●, ●) for AOA(α) of 10° (black) and 7° (red)

Figure 9.6: Change in shedding frequency with changes in cavitation number for a cavitation probe moving with cavity length (β_{LC}). A good agreement with literature and peaks seen in dp_1 and dp_2 is seen for peak1. Maximum uncertainty in $\sigma_0 = \pm$ 0.07, $Lc/C = \pm$ 0.1, $St = \pm$ 0.08

2-step process reported by Wu et al. (2019) and Barwey et al. (2020).

9.3 Spectral POD to identify the shedding modes

Spectral proper orthogonal decomposition (SPOD) is a modal decomposition technique used to extract coherent structures from statistically stationary fields. As a result, it is possible to identify spatial modes occurring at a given frequency. The generated modes are harmonic in time, and are computed one frequency at a time. Mathematically, SPOD modes are the eigenvectors of a cross-spectral density (CSD) tensor at each frequency. Schmidt and Colonius (2020) discuss the application of this method in detail. This section presents SPOD analysis of time-resolved void fraction data.

9.3.1 Methodology

The following methodology is deployed to setup SPOD analysis for the current dataset :

- The data matrix is created using all the frames of the void fraction flow field over a capture cycle of 0.787 s. Two different datasets can be combined to form a larger sample to improve statistical convergence. The mean void fraction value is subtracted from each frame to yield matrix with variance data.

- It is important to set appropriate frequency resolution($\triangle f$) for the dataset based on prior knowledge of physically shedding modes.

$$f_{sampling} = \frac{1}{sampling\ time\ step}$$

$$f_{Nyquist,max} = \frac{f_{sampling}}{2}$$

for N_{FFT} = Number of snapshots in one segment of time-series, sets window length; N_{blk} = Number of blocks the data series is broken into; N_{ovlp} = Number of snapshots

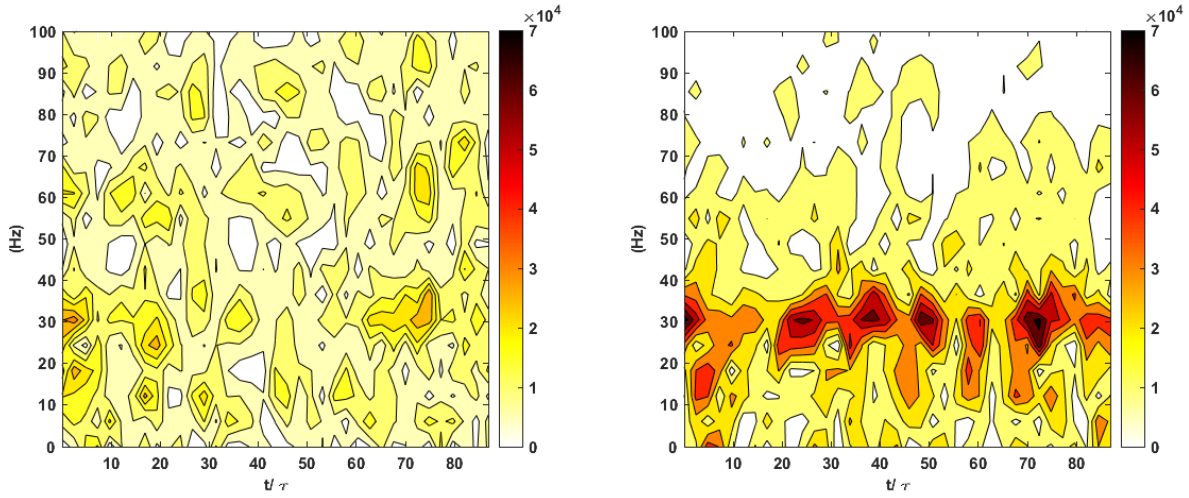

(a) Type(iii), dp_1

(b) Type(iii), dp_2

(c) Type(iv), dp_1

(d) Type(iv), dp_2

Figure 9.7: Spectrograms of type(iii) shedding cavity at $\sigma_0 = 2.1$ ($\sigma_0/2\alpha = 6.2$) are shown in (a) dp_1 (b) dp_2 and for a type(iv) shedding cavity at $\sigma_0 = 1.6$ ($\sigma_0/2\alpha = 4.7$) are shown in (c) dp_1 (d) dp_2. The flow timescale τ is used to non-dimensionalize time. $\tau = \frac{C}{u_0}$, $\alpha = 10°$. The colorbar represents the magnitude of fft of each signal.

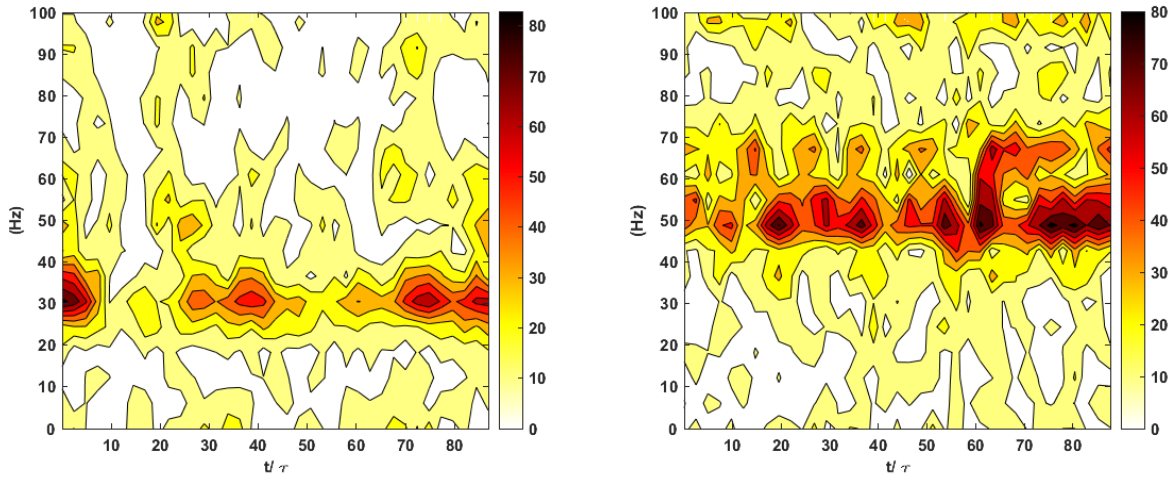

(a) Type(iii), p_a (b) Type(iv), p_a

Figure 9.8: Spectrogram from the hydrophone signal for (a) Type(iii) shedding cavity at σ_0 = 2.1 ($\sigma_0/2\alpha$ = 6.2) (b) Type(iv) shedding cavity at σ_0 = 1.6 ($\sigma_0/2\alpha$ = 4.7). $\tau = \frac{C}{u_0}$, α = 10°.

overlapping between successive blocks; T = Period of each data-block,

$$T = N_{FFT}(sampling\ time\ step) = \frac{N_{FFT}}{f_{sampling}}$$

$$\triangle f = \frac{f_{sampling}}{N_{FFT}}$$

- Based on size of hamming window N_{blk} is given by :

$$N_{blk} = \lfloor \frac{Total snapshots - N_{ovlp}}{N_{ovlp} - N_{FFT}} \rfloor$$

- For current dataset $\triangle f$ =3.9Hz, $f_{sampling}$ = 1000 Hz , N_{FFT} = 256. A 50% overlap of windows is taken. This is the default block overlap set for current SPOD analysis.

- Open source SPOD program by Schmidt and Colonius (2020) is used to obtain the modes and their associated frequencies.

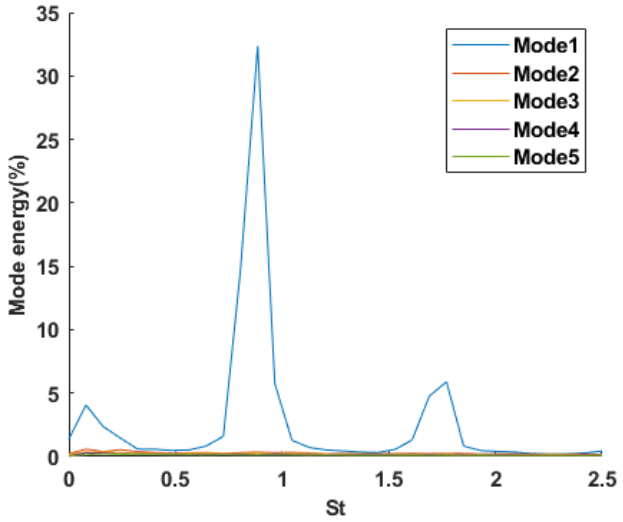

Figure 9.9: Mode energy distribution for first 5 SPOD modes. Energy of mode1 is dominant. Type(ii) cavity at σ_0 =2.6 ($\sigma_0/2\alpha = 7.6$)

9.3.2 SPOD of void fraction fields

After setting up the window size and overlap %, the energy at each mode for all the frequencies are determined. The mode energy distribution for first 5 modes is shown in figure 9.9. Mode 1 is dominant and energy of rest of the modes is negligible.

The field-of-view chosen for SPOD analysis and the shedding mode energy at each of the resolved frequencies is presented in figure 9.10. The resolved frequencies with maximum mode energy are the same as the dominant and secondary shedding frequencies reported in section 9.1. The field-of-view chosen for SPOD analysis is shown in figure 9.10 (a). A waterfall plot showing mode energy at different resolved frequencies for different cavitation shedding regimes is shown in figure 9.10 (b).

9.3.3 Type(ii) cavity shedding modes

The type(ii) shedding cycle is driven by both re-entrant flow and shockwaves. The two peaks of resolved shedding frequency are shown in figure 9.11. Despite having the same frequencies obtained by PSD of surface pressure signals, no clear visual observation can be

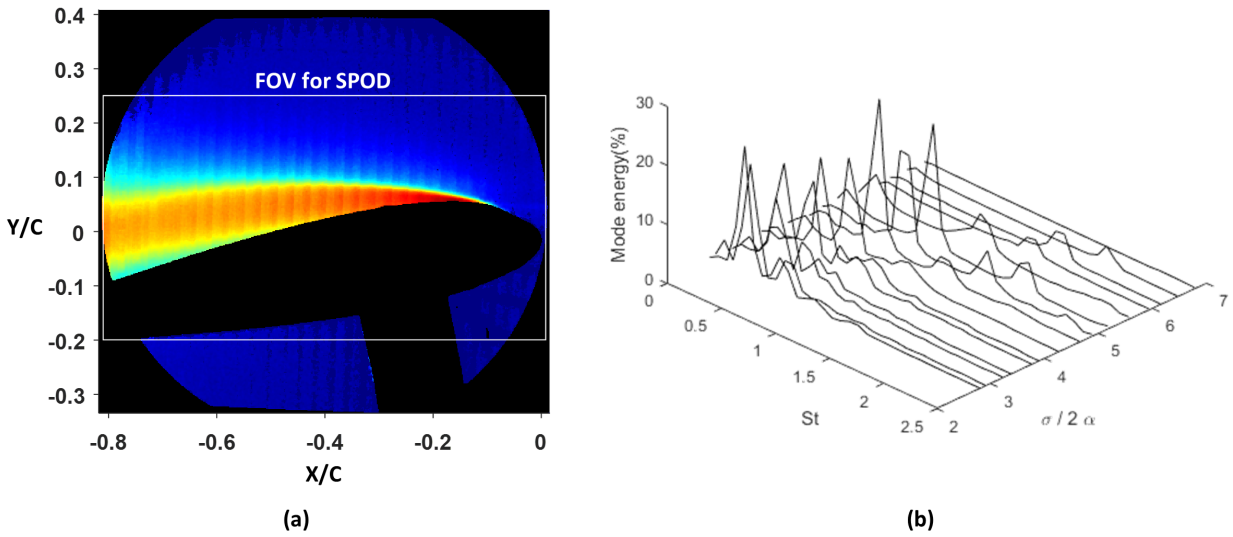

Figure 9.10: Figure highlighting (a) The FOV chosen for SPOD analysis, (b) Waterfall plot showing mode energy distribution at different cavitation parameters $\sigma_0/2\alpha$

made using the spatial modes at the two resolved frequencies. Interpretation of these modes is not straightforward.

9.3.4 Type(iii) cavity shedding modes

The type(iii) shedding cavities are longer and mainly driven by shockwaves, while re-entrant flow is trapped beneath the cavity as seen in figure 8.13. The top two peaks of shedding resolved shedding frequency are shown in figure 9.12. Peak 1 frequency is closest to dominant frequency reported for type(iii) cavities in figure 9.5.

9.3.5 Type(iv) cavity shedding modes

The type(iv) shedding cavities are characterized by presence of bubbly shocks and liquid re-entrant flow, and trailing edge cavitation as seen in figures 8.16 and 8.19. The top two peaks resolved through SPOD analysis are shown in figure 9.13.

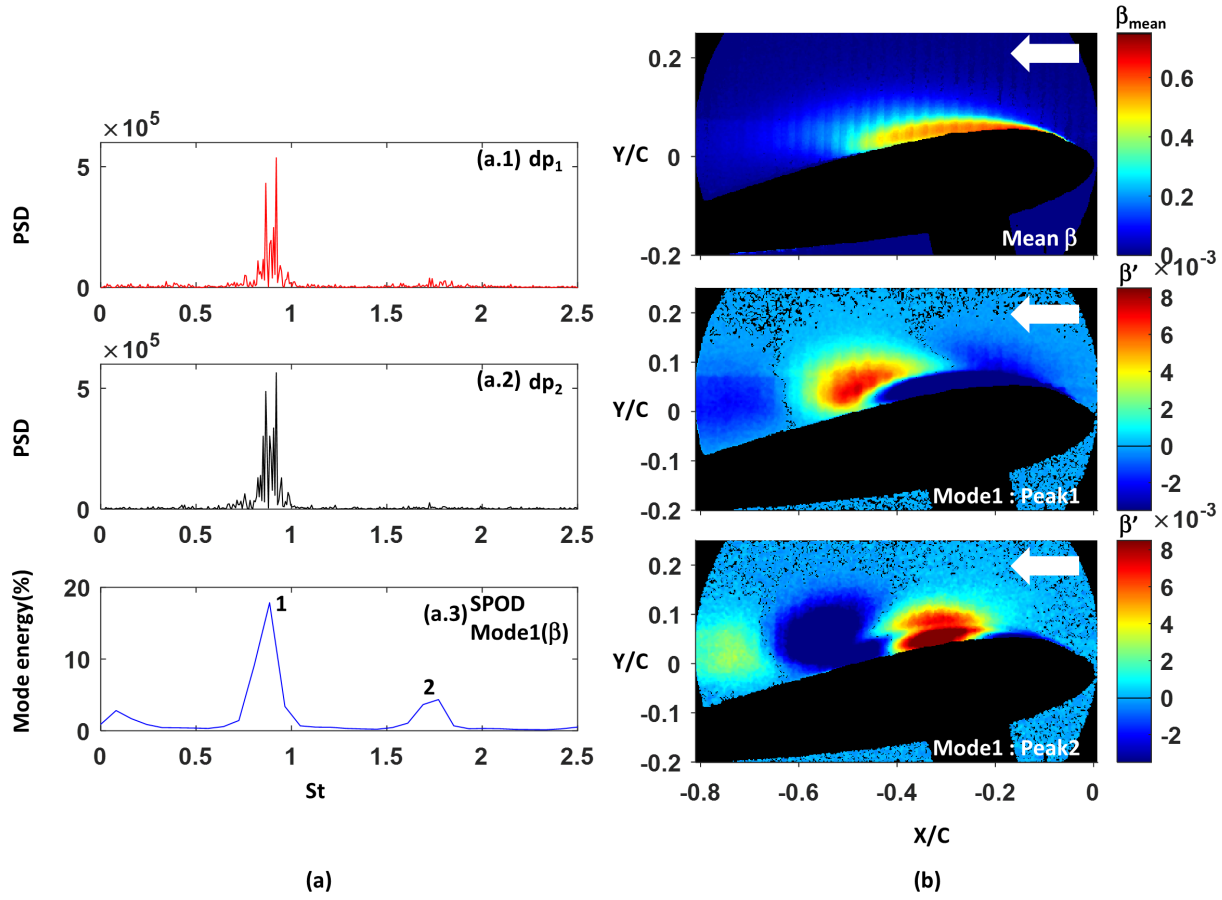

Figure 9.11: (a) The peaks detected in transducer signals dp_1 and dp_2 along with mode energy distribution at two different resolved frequencies (b)The spatial SPOD modes corresponding to dominant peaks seen in resolved frequency of mode1 along with mean void fraction field for type(ii) cavity. The peaks detected by dp_1 and dp_2 are also shown. σ_0 =2.6 ($\sigma_0/2\alpha$ = 7.6)

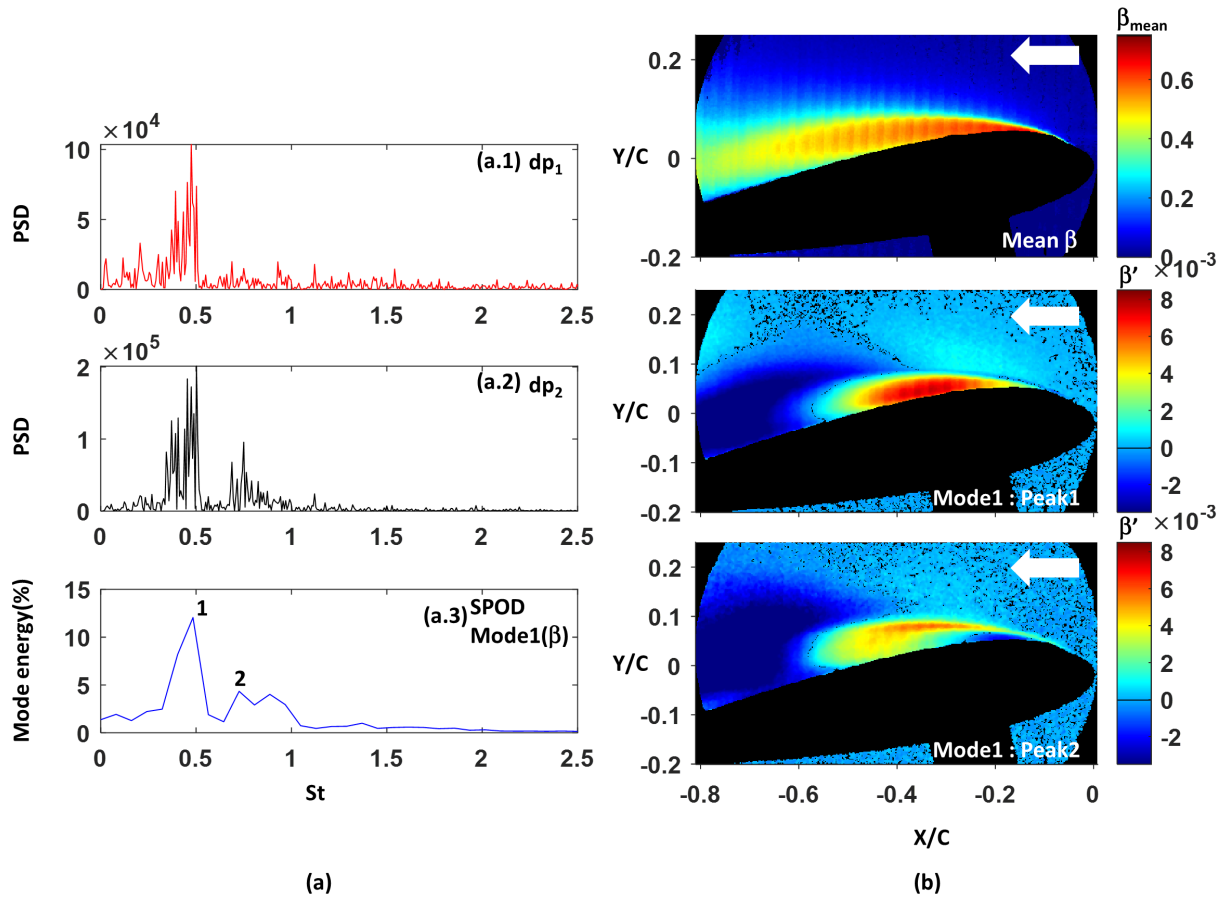

Figure 9.12: (a) The peaks detected in transducer signals dp_1 and dp_2 along with mode energy distribution at two different resolved frequencies (b)The spatial SPOD modes corresponding to dominant peaks seen in resolved frequency of mode1 along with mean void fraction field for type(iii) cavity. The peaks detected by dp_1 and dp_2 are also shown. Peak1 corresponds to shedding of the dominant shedding frequency seen in shockwave driven shedding. σ_0 =1.9 ($\sigma_0/2\alpha = 5.5$).

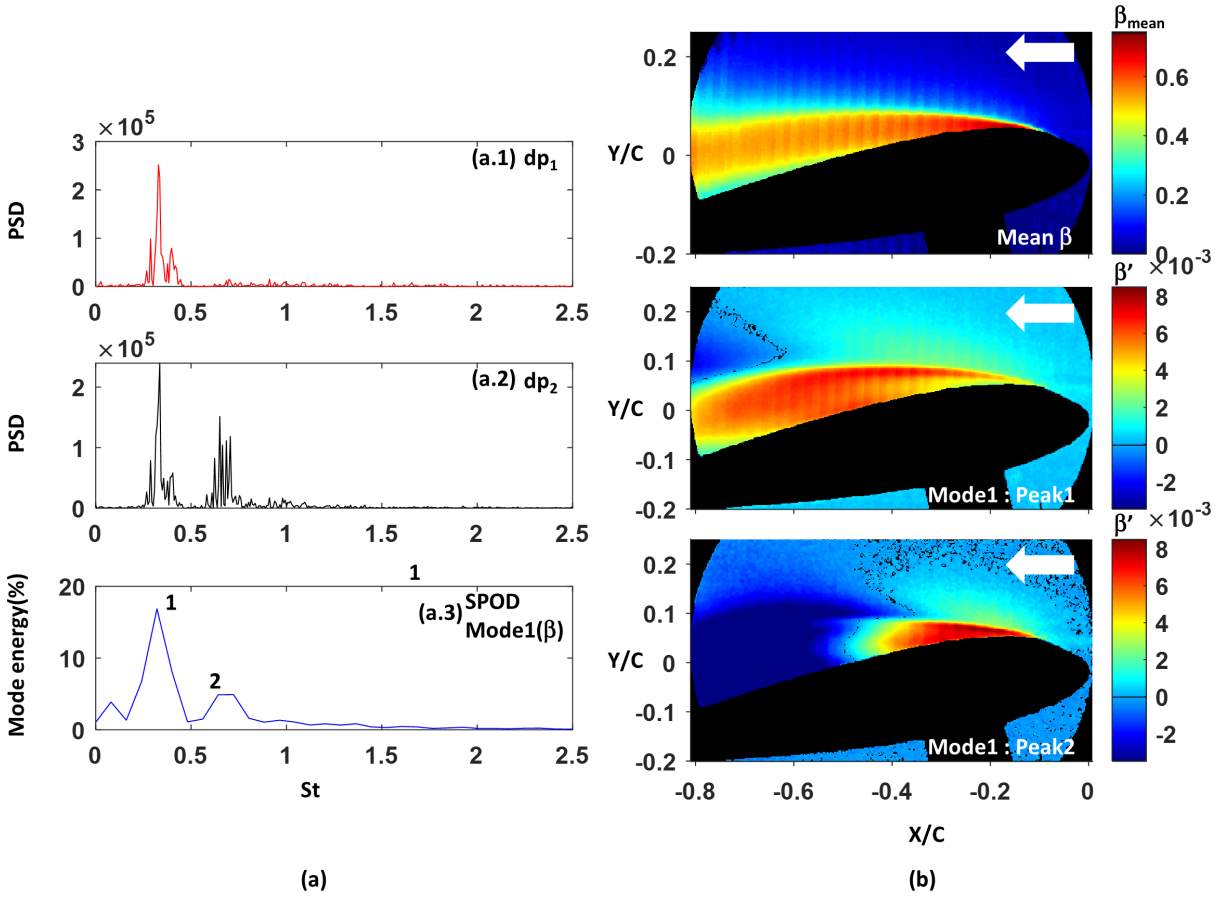

Figure 9.13: (a) The peaks detected in transducer signals dp_1 and dp_2 along with mode energy distribution at two different resolved frequencies (b) The spatial SPOD modes corresponding to dominant peaks seen in resolved frequency of mode 1 along with mean void fraction field for type(iv) cavity. The peaks detected by dp_1 and dp_2 are also shown. Peak2 resembles a mid-way shedding cavity cycle where flow-front has reached Lc/C=0.4($\sim$). σ_0 =1.5 ($\sigma_0/2\alpha$ = 4.3)

Chapter 10

NACA0015 Hydrofoil : Analysis

Void fraction flow fields of shedding cavities are analyzed in this section. Properties of bubbly shocks, probability of shedding caused by a liquid re-entrant flow or a bubbly shock wave, and its relationship to cavity Mach numbers are presented in the following sections.

10.1 Bubbly shock properties

Bubbly shock properties such as shock speed (U_S), pressure rise $(p_2-p_1)_s$, pre- and post-shock void fraction β_1 and β_2 are estimated from void fraction and pressure measurements. U_S, β_1, and β_2 are estimated from void fraction flow fields using the similar procedure described in the backward facing step portion in section 5.1. Estimated quantities are compared with Wu et al. (2019) to understand the effect of scale.

Despite having time-resolved void fraction measurements Wu (2019) did not have static dynamic pressure measurements in the cavity. Figure 10.2 compares the U_s measured in the current study with U_s measured by Wu et al. (2019). Measured shock speeds in the present study are higher than those reported by Wu et al. (2019) by a factor of two. It is shown in section 5.1 that 1-D jump conditions represent bubbly shock very well. Figure 10.1 compares the measured pre- and post-shockwave void fraction values (β_1 and β_2 respectively) between the present study and Wu et al. (2019). Measured pre- and post-shock void fractions between the two studies are similar. Based on the measurements of U_S and, pre- and post void fraction it is possible to estimate the expected pressure rise across bubbly shocks observed by Wu

et al. (2019), using 1-D jump relations. Comparison of the estimated pressure rise between the current study and Wu et al. (2019) is shown in figure 10.3. Measured pressure rise in present study is also plotted in figure 10.3. Figure 10.3 shows that for the present study, measured and estimated pressure rise matches well. However, the pressure rise observed in the present is higher than pressure rise estimated for Wu et al. (2019).

10.1.1 Comparison with Wu (2019)

Billet and Holl (1981b) discuss the effect of scale on limited partial cavitation occurring on a NACA0015 hydrofoil at four different model scales. They reported Re dependence on desinence cavitation number with higher desinence observed at higher Re. Cavitation desinence occurs when any observed cavitation disappears with an increase in pressure. In the present study, which is at a higher Re compared to Wu (2019), cavitation events were observed at higher mean pressure levels. This is consistent with the findings of Billet and Holl (1981a). In addition, blockage between the studies are different. Observed differences between present study and Wu (2019) can be attributed to the effect of Re and blockage. Figure 10.3 suggests that in the present study, the propagating bubbly shocks are stronger than those reported by Wu et al. (2019). This is due to cavitation events occuring at higher pressures because of scale effects and blocakge. Ganesh et al. (2016) reported that the magnitude of the mean pressure level can have an impact on the observed shock speeds due to higher pressures at cavity closure.

10.2 Event probability of re-entrant flow/shockwaves to cause cavity pinch-off

From time-resolved void fraction measurements,the probablity of shedding caused by a liquid re-entrant flow or a bubbly shock wave is estimated based on equation 10.1 and 10.2 respectively. Each occurrence of shedding caused by a given flow front is considered as an independent occurrence during the measurement duration. During 0.787s of x-ray measure-

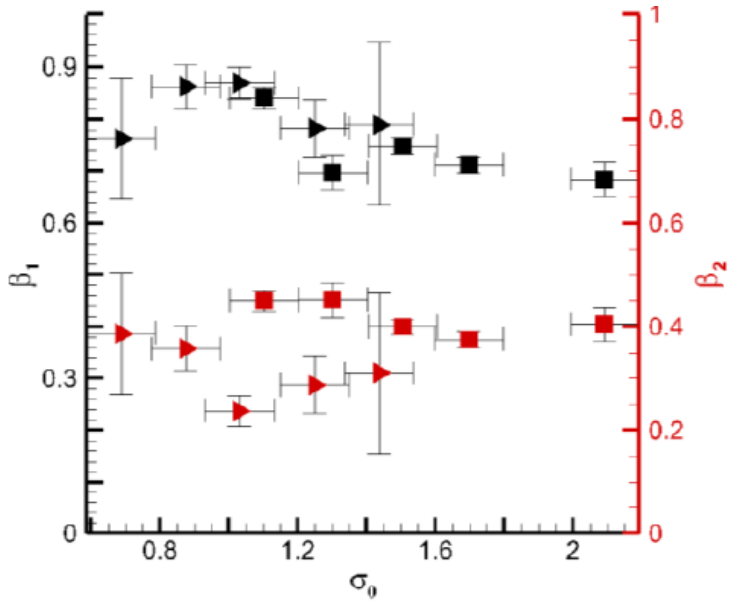

Figure 10.1: Variation of ratio of measured pre- and post-shock void fractions β_1(black) and β_2 (red) with inlet cavitation number σ_0 for present study (corrected) (■) and Wu et al. (2019) (►).

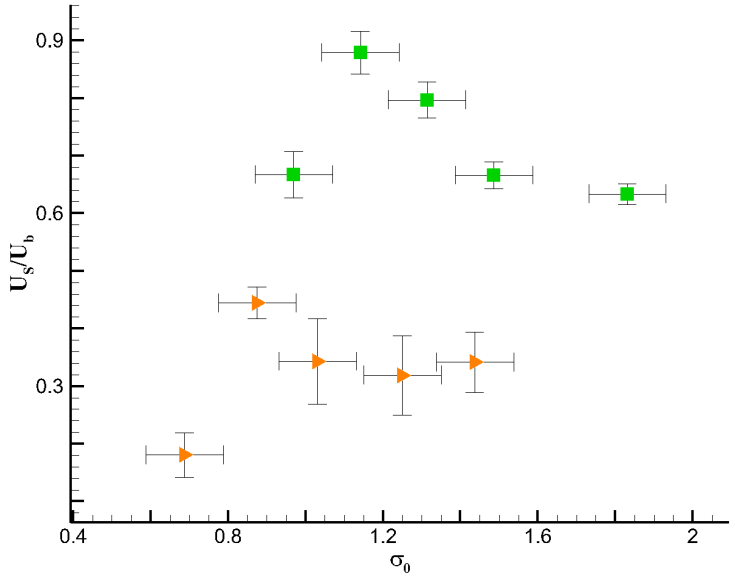

Figure 10.2: Changes in ratio of measured shock speed U_s/U_b with variation of inlet cavitation number σ_0. U_b is the velocity near the leading edge of the foil based on blockage. Current hydrofoil's shock-speeds (■) are compared to the hydrofoil from previous study by Wu et al. (2019) (►).

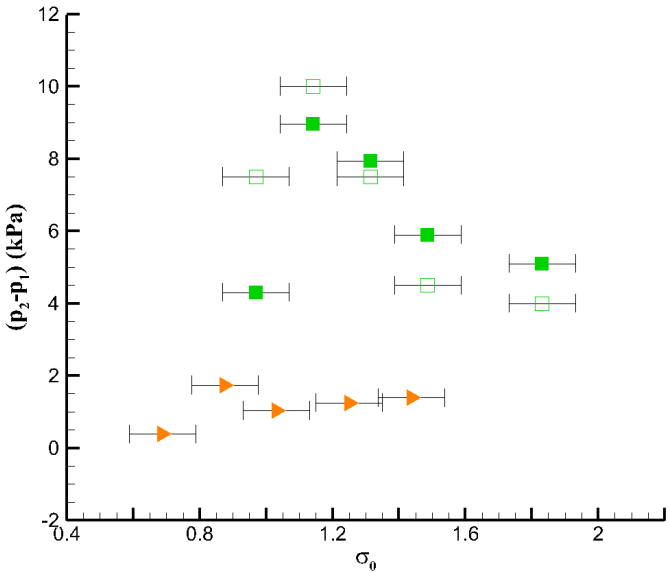

Figure 10.3: pressure rise $(p_2 - p_1)$, with inlet cavitation number σ_0 for present study (estimated ■, measured □) and Wu et al. (2019) (▶). Pressure rise estimates for the current study are higher, and can be attributed to the increased mean pressures at which cavitation events are observed.

ment duration, total number of shedding cycles are counted as N, number of shedding cycles caused by bubbly shocks and liquid re-entrant flows are denoted as N_S and N_R respectively. Probability of shedding due to liquid re-entrant flow $(P(R))$ and bubbly shocks $(P(S))$ are given by equations 10.1 and 10.2.

$$P(R) = \frac{N_R}{N} \tag{10.1}$$

$$P(S) = \frac{N_S}{N} \tag{10.2}$$

Figure 10.4 shows the estimated probability of shedding caused by a liquid re-entrant flow or a bubbly shocks. Two datasets of 0.786s duration are used to create figure 10.4. Probability of liquid re-entrant flow is the highest for type (ii) cavities and the lowest for type (iv) cavities. At $\sigma_0/2\alpha = 7.0$, type (ii) cavities have an equal likelihood of liquid re-entrant and shock induced shedding. As the flow transitions to longer type(iii) and type(iv)

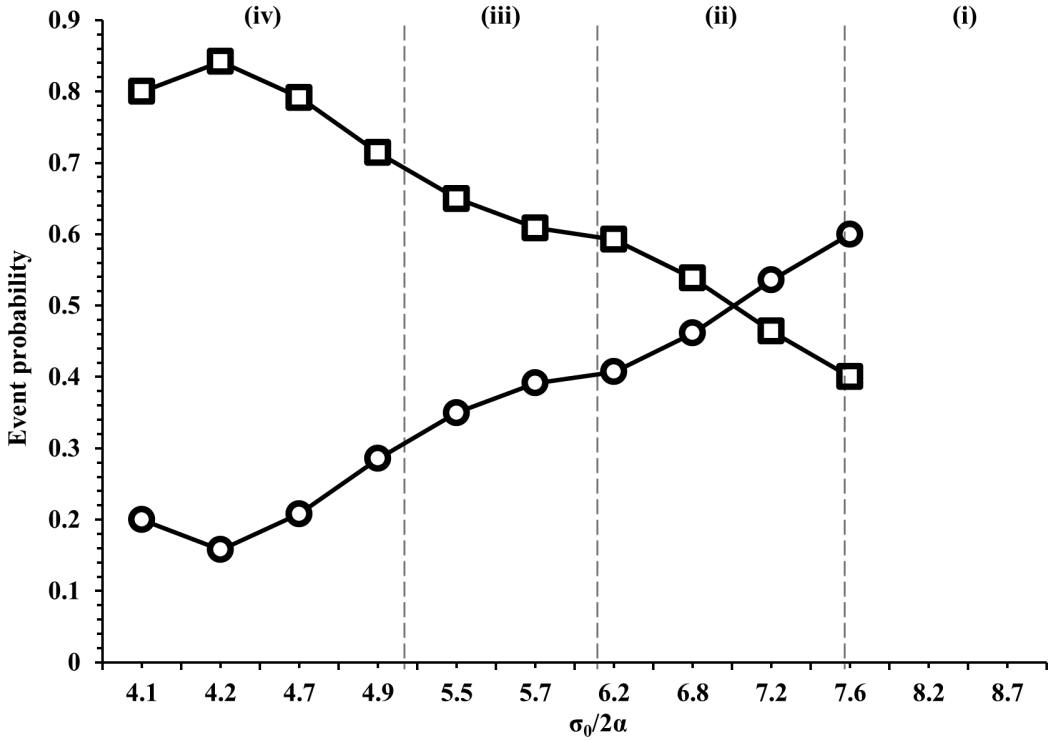

Figure 10.4: Event probability plot showing the probability of re-entrant jet causing cavity pinch-off (○) along with shockwaves causing pinch-off (□). For longer type(iii) and type(iv) cavities, shockwaves are the dominant mechanism of shedding. Uncertainty in $\sigma_0 = \pm\ 0.07$.

cavities, shockwaves dominate as primary shedding mechanism while shedding caused by a liquid re-entrant flow is occasional.

10.3 Probability and Mach number relationship

10.3.1 Cavity pressure

To estimate the speed of sound within the cavity, and hence the Mach number, static pressure inside the cavity is measured. Location of the static pressure tap is shown in figure 2.6. Cavity static pressure is non-dimensionalized using Cp_{cavity} defined in equation 10.3. Figure 10.5 shows the variation of cavity pressure co-efficient with cavitation parameter $\sigma_0/2\alpha$.

$$Cp_{cavity} = \frac{p_{cavity} - p_0}{\frac{1}{2} \cdot \rho \cdot u_0^2} \tag{10.3}$$

10.3.2 Mach number within the cavity

Based on cavity pressure measurements and void fraction measurements, speed of sound (c)within the cavity is estimated using the homogeneous frozen model. Mach number, M_0, within the cavity is then estimated as $M_0 = u_0/c$. Figure 10.6 shows the variation of the M_0 with cavitation parameter ($\sigma_0/2\alpha$) as a box-plot. The boxes represent the minimum, maximum and median M_0 values from a given data-set. The upper whisker represents the 75^{th} percentile and is the median of upper half of the data-set while the lower whisker represents the 25^{th} percentile and is the median of lower half of the M_0 data-set. An M_0 data-set at each $\sigma_0/2\alpha$ represents the peak in M_0 value in 787 frames of the void fraction data (β) at a mean value of cavity pressure (p_c). It is seen that onset of shockwaves coincides with $M_0 > 1$. Type(ii) cavities are still in the sub-sonic region for $\sigma_0/2\alpha > 6.2$ as seen in the box plot. At lower σ_0 the mean inlet mach numbers are supersonic $M_0 > 1$ and the median increases with decreasing cavitation number.

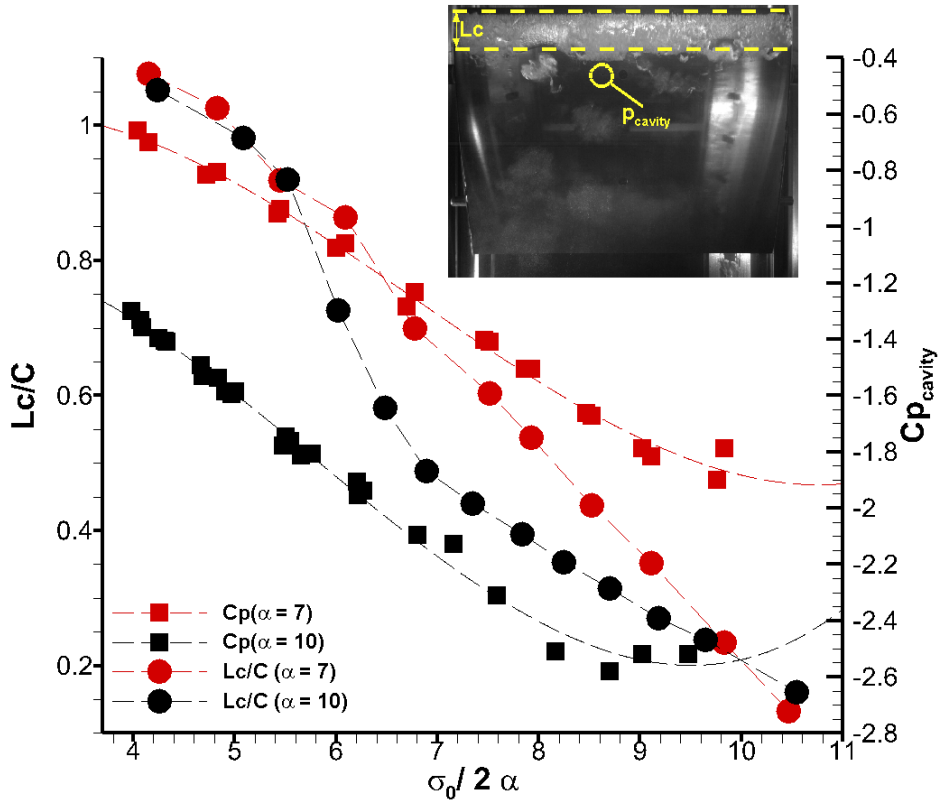

Figure 10.5: Pressure inside the cavity at different cavitation regimes. This static pressure is used for speed of sound calculations.

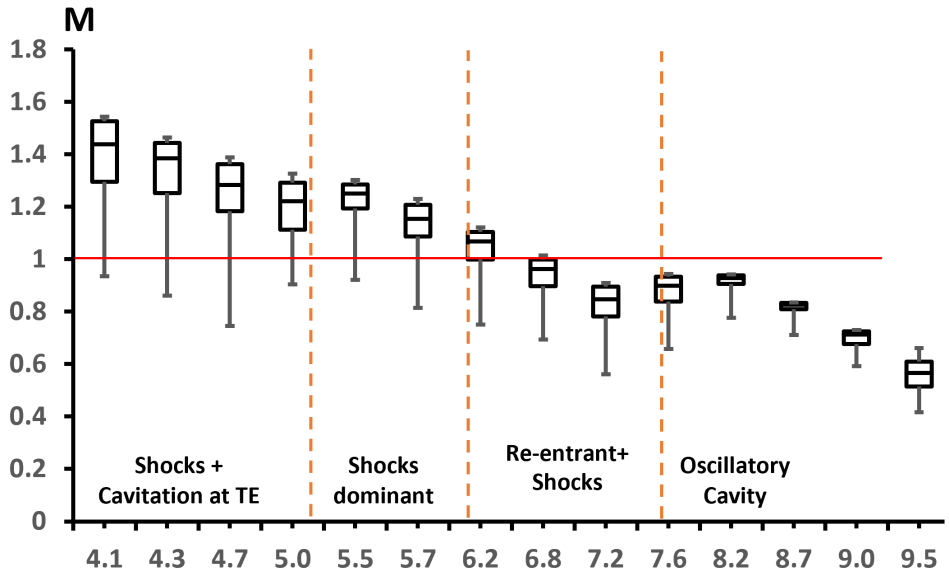

Figure 10.6: The box plot depicting variation of M_0 with decreasing σ_0 across the different cavitation regimes. Speed of sound is estimated using 'homogeneous frozen model and maximum, minimum and median can be seen. $M_0 > 1$ when shockwaves begin to cause cavity pinch-off.

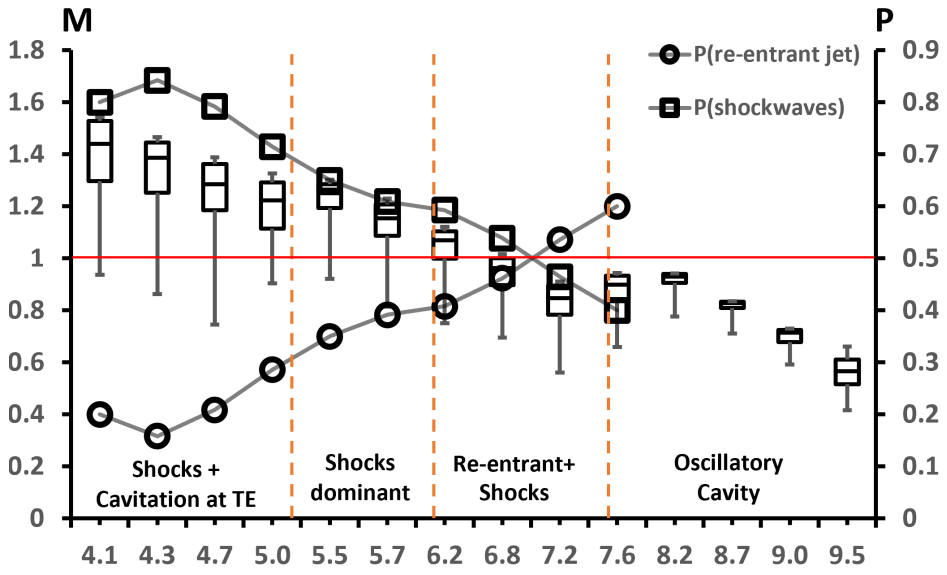

Figure 10.7: The box plot depicting variation of M_0 with decreasing σ_0 across the different cavitation regimes juxtaposed against the even probability plot to illustrate prevalence of shockwaves when $M_0 > 1$.

10.3.3 Mach number and event probability relationship

Figure 10.7 shows a composite plot of probability of observations of re-entrant flows/shocks ($P(R)$ and $P(S)$) and corresponding M_0 based on p_{cavity} and $\beta(X, Y, t)$. At $\sigma_0/2\alpha = 7.52$, $M_0 < 1$ and P(R) is highest at 0.6. As the cavity begins to fill with vapor at lower $\sigma_0/2\alpha = 6.8$, M_0 increases. $P(S)$ increases and $P(R)$ decreases. This trend continues with decreasing $\sigma_0/2\alpha$, and maximum $P(S)$ occurs when maximum M_0 occurs. At high values of M_0, $P(R)$ is still appreciable, suggesting the role of re-entrant flow in causing shedding in predominantly compressible mixture.

Chapter 11

Conclusions of NACA0015 study

Cavitation on a NACA0015 hydrofoil was studied using high-speed cinematography, x-ray densitometry and synchronized pressure measurements. With a reduction in inlet cavitation number σ_0, stable cavities began to exhibit periodic shedding. Type (i) cavities were formed at $\sigma_0/2\alpha = 7.6$ to 9.8 and these cavities exhibited oscillatory behavior. At $\sigma_0/2\alpha = 6.2$ to 7.6, type (ii) cavities were formed and cavity shedding is caused either by a liquid re-entrant flow or a bubbly shock. With reduction in cavitation number, $\sigma_0/2\alpha = 4.2$ to 6.1, type (iii) cavities occurred and these were characterized by the presence of a stationary re-entrant flow unable to cause shedding. On some occasions, the liquid re-entrant flow was able to cause type (iii) cavities to pinch off. At $Lc/C \geq 0.85$, type (iv) cavitation, characterized by occurrence of secondary cavitation in the region near the trailing edge of hydrofoil. In type (iv) cavities, the shed vapor cloud interacted with cavitation near the trailing edge and affected the shedding cycle. Type (iv) cavities shedding was caused mostly by bubbly shocks and rarely by liquid re-entrant flow. Based on x-ray measurements, the probability of re-entrant liquid flow caused shedding and the probability of bubbly shock caused shedding was estimated. Upon comparison with cavity Mach number M_0, it was found that the likelihood of bubbly shock induced shedding increased with increase in M_0. Despite the high likelihood of occurrence of bubbly shocks due to increased compressibility of the bubbly mixture, liquid re-entrant flow exist in such scenarios and can cause cavity shedding.

This work was presented at 32^{nd} Symposium of Naval Hydrodynamics (2018) and 10^{th}

International Symposium of Cavitation (CAV2018). The research work will be submitted as an article to the Journal of Fluid Mechanics, titled '*Role of Re-entrant Flow and Bubbly Shockwaves in Cavity Shedding Dynamics*'.

Appendix A

Charge Amplifier Circuit for Dynamic Pressure Measurement

When subjected to varying mechanical pressure, the charged piezoelectric membrane of the unsteady pressure transducer (CVLD differential pressure sensor) produces a very small current (μA). In order to obtain any meaningful measurements from the transducer, this current needs to be amplified through a charge amplifier circuit. The charge amplifier circuit shown in figure A.1(a), simultaneously supplied a charge voltage to the transducer and detects the current produced when the transducer is under load. The PCB 113M231 sensors need a 15 V operating voltage to charge the piezoelectric membrane and sufficient grounding to prevent current leakage from the face of the sensor when it is submerged in water. The circuit depicting basic layout of the charge amplifier and band-pass filter can be seen in figure A.1(a). AD625 instrumentation amplifier with the pin-configuration shown in figure A.1(b) was used as the basic building block for the charge amplifier and the band-pass circuit.

The current produced by the unsteady pressure transducer under load, passes over a 200 Ω resistor, and the voltage drop across the resistor was used as the base signal for the charge amplifier. The net gain of the amplifier (AD625) was set using an $R_f = 20000\ \Omega$ to set a gain $= \frac{2*R_f(20\ k\Omega)}{R_G(\infty)} = 1$.

A secondary bandpass filter shown in figure A.1a was made for better signal conditioning and reasonable settling times on the amplifier to improve overall response time of the circuit. The highpass and lowpass components were chosen as follows :

- High pass filter : Capacitance $= 0.47\ \mu F$ and Resistance $= 328.1\ \Omega$ for an $f_{3dB} = \frac{1}{2\pi RC}$

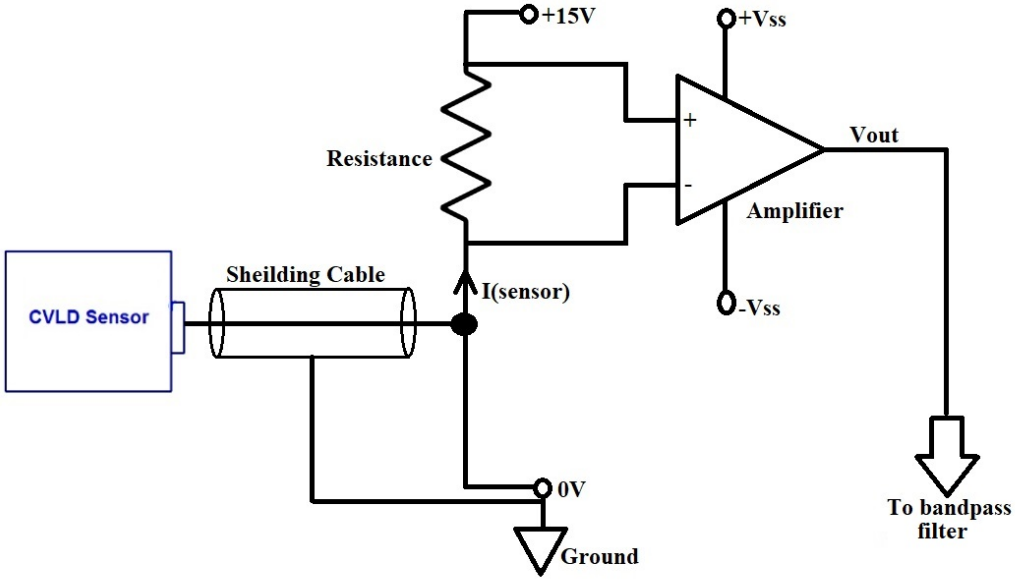

(a) Charge amplifier circuit

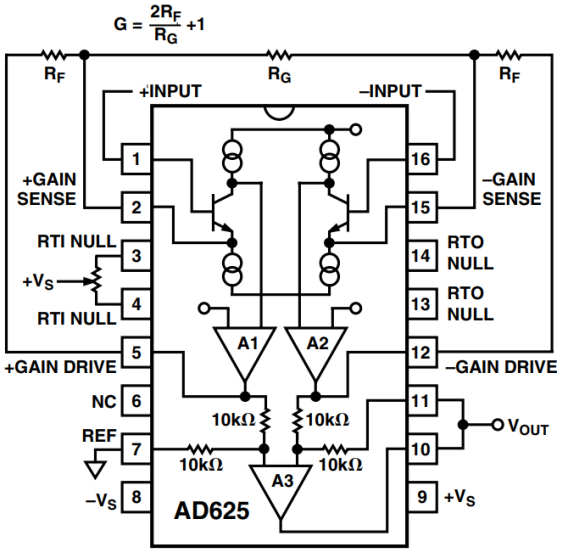

(b) AD625 pin diagram

Figure A.1: Schematic showing the skeleton of the charge amplifier circuit for each sensor. The voltage ± Vss is the activation/source voltage required for the integrated circuit (AD625 instrumentation amplifier) set to 18 V.

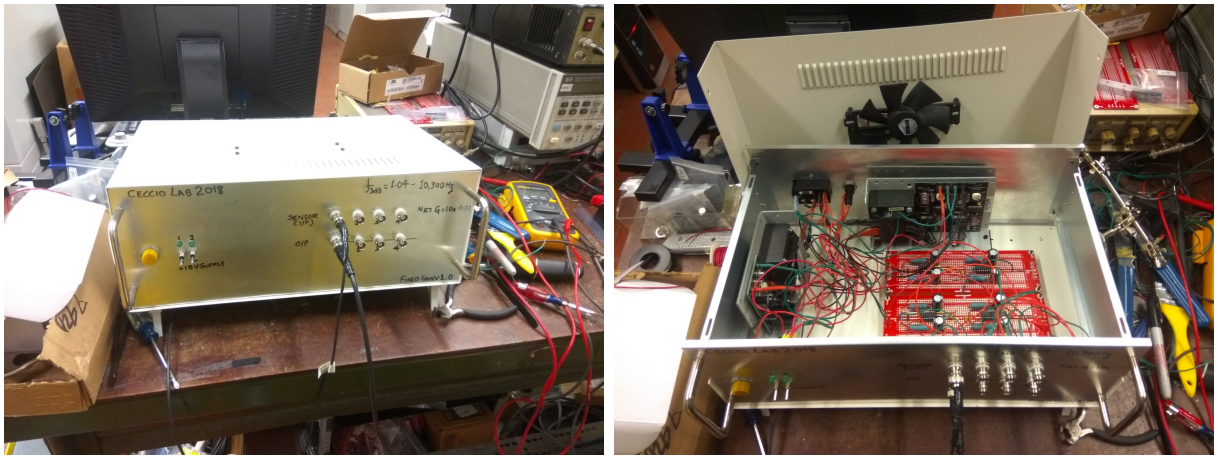

Figure A.2: Assembled charge amplifier box with grounded instrument casing and BNC connections.

$= 1.03$ Hz.

- Low pass filter : Capacitance $= 47\ nF$ and Resistance $= 330\ \Omega$ for an $f_{3dB} = \frac{1}{2\pi RC} =$ 10261 Hz.

- Overall gain of bandpass filter $= \frac{2*R_f(20\ k\Omega)}{R_G(4.42\ k\Omega)} = 10$

A dual channel system (to acquire two unsteady pressure signals simultaneously) was made with appropriate power supply units and grounded instrument casing as shown in figure A.2. Additional gain and butter-worth filtering was provided by KH 3944 multichannel filter.

A.1 Calibration circuit

The in-house setup built to verify the manufacturer calibration values is shown in figure A.3. A 750W Cole Palmer ultrasonic horn (noise generator) was used to create pressure impulses from the top of a water filled tank (large cylindrical tank having a diameter of 580 mm and height of 927 mm was used to minimize the effect of wall reflections on base measurements). The tip of the horn was submerged in water and aligned along the center-line of the water tank. The unsteady pressure transducer (to be calibrated) was mounted 160 mm away from

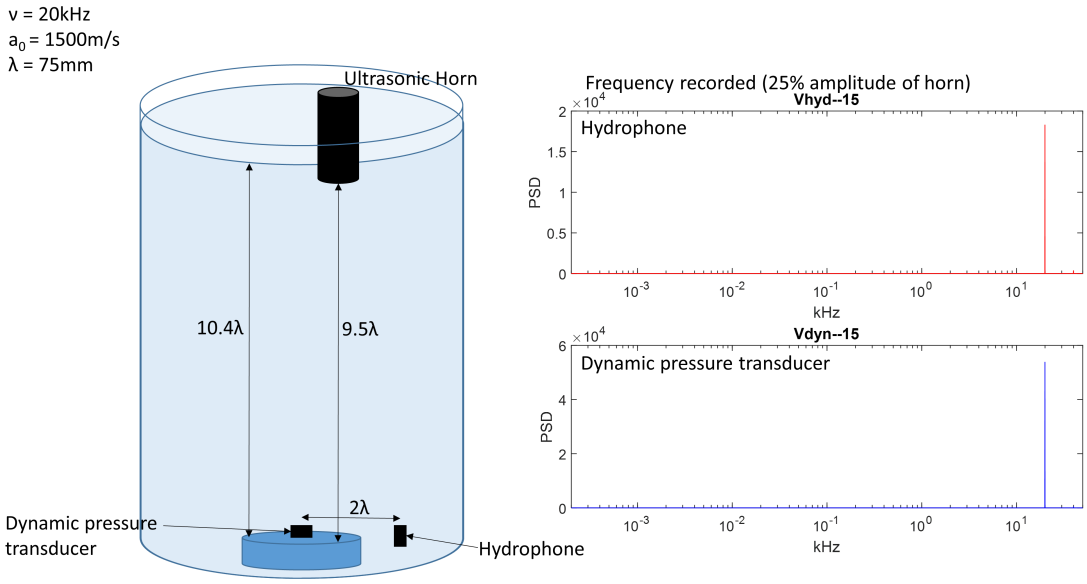

Figure A.3: In-house calibration system used to obtain calibration curve of unsteady pressure transducer *dp*. Standard hydrophone(Bruel and Kjaer hydrophone No. 2241694) with trusted calibration curve is used as calibration basis. The dynamic pressure transducer is 290 mm from the walls of the tank and 160 mm away from the bottom of the tank. A 20 kHz source signal generated by the ultrasonic horn is detected equally at the hydrophone and the unsteady pressure transducer as seen in the PSD curves (equal frequency response) at all source signal amplitudes. The horn broadcasts a sinusoidal signal.

the base of the tank and transducer surface was also aligned along the tank center-line. A Bruel and Kjaer hydrophone (No. 2241694) with a voltage sensitivity of 26.3 $\mu V/Pa$ with 94 x $10^{-3} pC/Pa$ was mounted parallel to the center-line of the water tank, at a distance of 150 mm away from the surface of unsteady pressure transducer and 160 mm away from the base of the water tank.

The pressure impulses produced by the horn were simultaneously recorded by both the unsteady pressure transducer and the standard calibration hydrophone. The standard calibration of the hydrophone was used as the absolute truth to measure the magnitude of pressure impulses (in kPa). This pressure measurement was compared with the current measurement from unsteady pressure transducer to obtain a calibration curve (charge sensitivity) for the transducer.

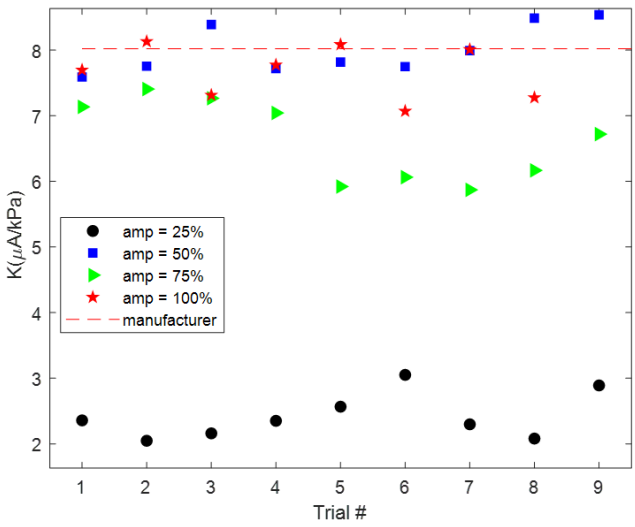

Figure A.4: Plot depicting accuracy of the calibration system. Higher amplitudes are required to obtain calibration curves/values closer to the manufacturer reported charge sensitivity.

The magnitude of the pressure impulses were varied from 25% to 100% of the maximum amplitude of ultrasonic horn. The mean pressure amplitudes for a given trial were recorded as shown in figure A.4. The higher amplitude provided calibration results closer to the manufacturer reported charge sensitivity (figure A.4). For all calibration trials a source amplitude of 100% was set at the ultrasonic horn to obtain the final charge sensitivity for the unsteady pressure transducer.

Appendix B

Single Phase Flow Measurements on Backward Facing Step

PIV Measurements reveal that the values of re-attachment location (X_R) and boundary layer thickness (δ) of the current setup is comparable to the values from the collaborators at Johns Hopkins University (Agarwal et al. (2018)) as shown in table B.1.

u_H (m/s)	5.3	10.5	16	JHU
	5.6	10.9	14.6	UM
u_τ (m/s)	0.24	0.45	0.67	JHU
	0.24± 0.03	0.43± 0.03	0.56± 0.03	UM
Re_τ	807	1504	2345	JHU
	914	1646	2181	UM
δ/H	0.368	0.365	0.384	JHU
	0.331	0.332	0.338	UM
X_R/H	6.19	5.53	5.31	JHU
	5.6±0.1	5.4±0.1	5.4±0.1	UM

Table B.1: Table comparing boundary layer thickness(δ) and re-attachment length(X_R) between current study and setup at Johns Hopkins cavitation tunnel (JHU).

Appendix C

Mean and RMSD Void Fraction Profiles for Backward Facing Step

The mean void fraction values along different X slices are shown in figure C.1, where β values are higher than type B cavities. Mean β values are still similar across the three Re. Taking similar slices on the Root Mean Standard Deviation (RMSD) of void fraction field, defined in equation C.1, yields comparable RMSD values across the three Re for Type B regime as shown in figure C.2(a). Comparatively larger RMSD values are seen in type C shedding regime (Figure C.2(b)). With decreasing cavitation number, void fraction fluctuations increase.

$$\beta_{RMSD} = \sqrt{\frac{\sum_{N=0}^{786} \left(\beta(X,Y,N) - \beta_{MEAN}\right)^2}{787}} \tag{C.1}$$

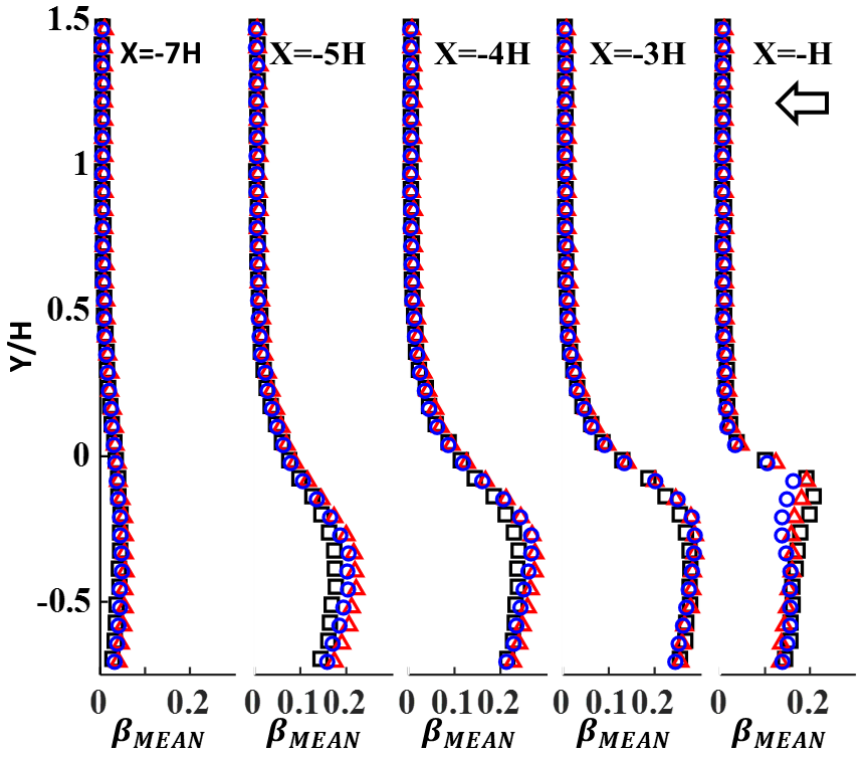

Figure C.1: Mean void fraction values for type C; $u_H = 8$ m/s (□), 10 m/s (△) and 12 m/s (○) at $\sigma_0 = 0.60$. No significant change in void fraction values due to Re is seen.

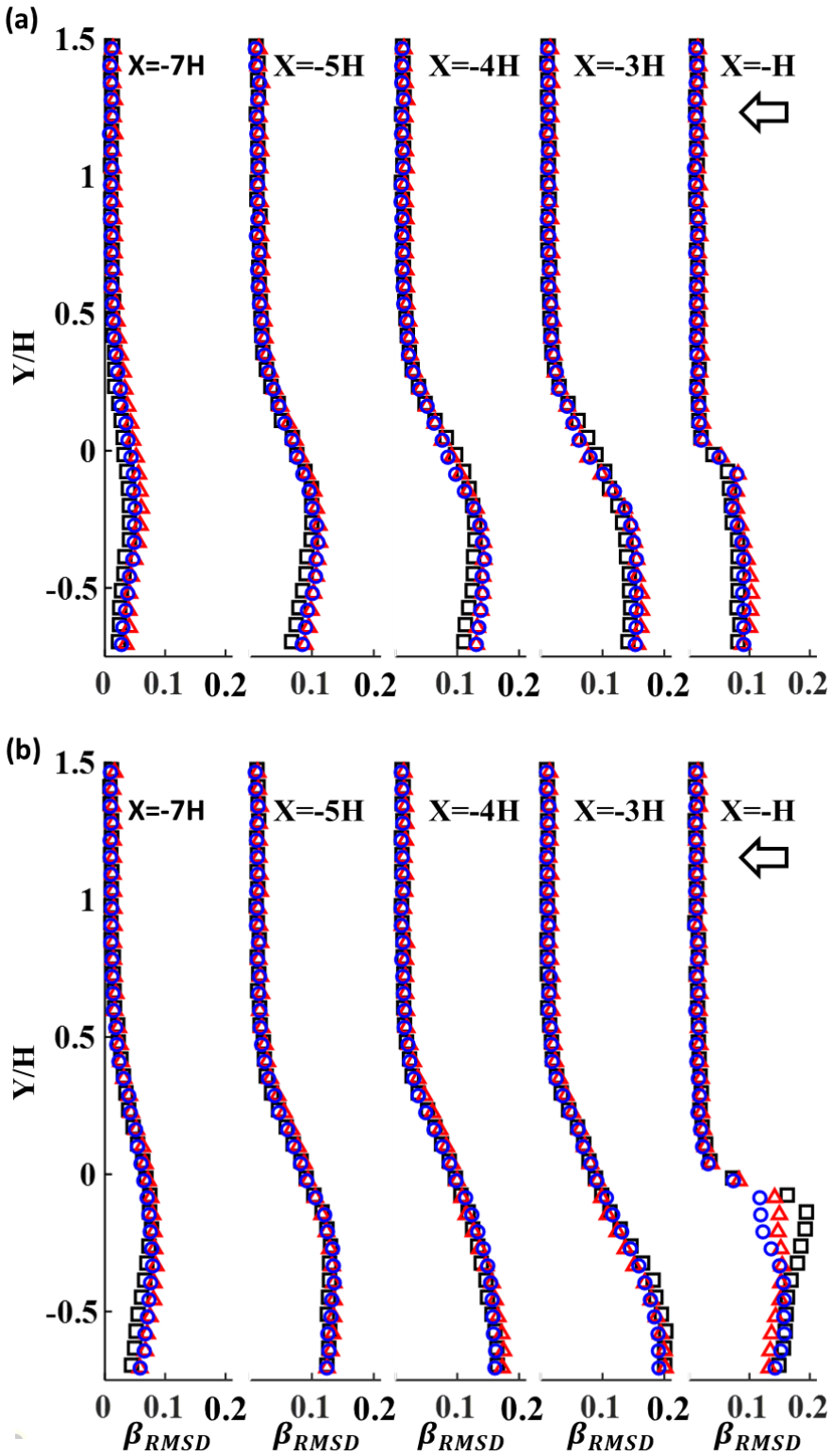

Figure C.2: RMSD values for the three Re; $u_H = 8m/s(\square)$, 10 m/s ($\triangle$) and $12m/s(\circ)$;(a) Type B;(b) Type C. RMSD values for Type B are comparable, meanwhile for Type C, RMSD of cavity void fraction is sensitive to Re. This can be partially attributed to different mean pressures at these Re that affect local pressure fluctuations.

Appendix D

Estimated Speed of Sound for Backward Facing Step

Based on the expression given in equation 3.1, by using void fraction field measurements and static pressure measurements at port locations shown in figure 2.3 (p_i, where i = 1, 2, 3), the local speed of sound can be estimated. The variation of local speed of sound with σ_0 estimated by using 'homogeneous frozen model' and 'homogeneous equilibrium model' is shown in figure D.1. The c_i estimated using 'homogeneous equilibrium model' are almost two orders of magnitude lower than the sound speeds estimated using 'homogeneous frozen model'. All the speed of sound values (c_1, c_2 and c_3) at u_H = 8, 10 and 12 m/s are reported in tables D.1, D.2 and D.3 respectively.

u_0 (m/s)	u_H (m/s)	σ_0	Static Pressure (kPa)			Frozen Model (m/s)			Equilibrium Model (m/s)		
			p_1	p_2	p_3	c_1	c_2	c_3	c_1	c_2	c_3
6.75	8.02	0.88	12	10.08	25.23	13.21	12.11	19.16	0.17	0.15	0.33
6.76	8.03	0.79	8.57	6.43	23.05	7.06	6.11	11.57	0.13	0.1	0.3
6.77	8.04	0.60	6.37	3.87	14.08	5.86	4.57	8.71	0.1	0.06	0.2
6.77	8.04	0.69	7.17	5.44	20.59	6.33	5.52	10.73	0.11	0.09	0.28
6.77	8.05	0.61	6.49	4.02	16.54	5.88	4.63	9.39	0.1	0.07	0.23
6.77	8.05	0.86	11.83	9.72	24.93	11.98	10.86	17.39	0.17	0.14	0.32
6.77	8.05	0.65	6.52	4.4	19.39	5.89	4.84	10.17	0.1	0.07	0.26
6.77	8.05	0.92	12.83	11.04	26.05	13.75	12.76	19.6	0.18	0.16	0.34
6.78	8.06	0.69	7.37	5.34	20.50	6.37	5.42	10.62	0.11	0.09	0.27
6.78	8.06	0.86	11.71	9.56	24.94	11.93	10.78	17.42	0.17	0.14	0.32
6.78	8.06	0.69	7.1	5.08	20.73	6.25	5.29	10.68	0.11	0.08	0.28
6.79	8.07	0.76	8.37	6.70	22.63	7.07	6.32	11.63	0.13	0.1	0.3
6.80	8.09	0.75	8.41	6.59	22.41	7.07	6.26	11.54	0.13	0.1	0.3

Table D.1: Speed of sound estimation using 'homogeneous frozen model' and 'homogeneous equilibrium model' for $u_H = 8$ m/s.

u_0 (m/s)	u_H (m/s)	σ_0	Static Pressure (kPa)			Frozen Model (m/s)			Equilibrium Model (m/s)		
			p_1	p_2	p_3	c_1	c_2	c_3	c_1	c_2	c_3
8.42	10.01	0.67	8.19	6.29	28.07	6.67	5.85	12.35	0.12	0.1	0.36
8.44	10.03	0.73	9.49	7.99	29.93	7.38	6.78	13.12	0.14	0.12	0.38
8.45	10.05	0.79	13.25	11.82	32.44	13.01	12.29	20.36	0.19	0.17	0.41
8.46	10.06	0.72	9.78	8.70	29.92	7.44	7.02	13.02	0.14	0.13	0.38
8.46	10.06	0.56	6.27	4.21	19.59	5.92	4.85	10.46	0.1	0.07	0.26
8.47	10.07	0.55	6.77	4.36	15.68	6.00	4.82	9.13	0.11	0.07	0.22
8.47	10.07	0.78	13.65	11.55	32.27	12.66	11.64	19.46	0.19	0.17	0.41
8.48	10.08	0.55	6.59	4.26	16.54	5.93	4.77	9.39	0.1	0.07	0.23
8.48	10.08	0.61	7.67	5.55	24.87	6.48	5.52	11.68	0.12	0.09	0.32
8.48	10.08	0.66	8.83	6.87	28.59	7.01	6.18	12.61	0.13	0.11	0.37
8.48	10.08	0.78	13.70	11.63	32.47	12.70	11.71	19.56	0.19	0.17	0.41
8.49	10.09	0.60	7.28	5.44	24.81	6.28	5.43	11.60	0.11	0.09	0.32
8.49	10.09	0.67	8.74	7.04	28.67	7.03	6.31	12.74	0.13	0.11	0.37
8.49	10.09	0.71	9.53	8.11	29.87	7.35	6.78	13.02	0.14	0.12	0.38
8.50	10.1	0.82	14.55	13.02	33.75	12.87	12.17	19.6	0.2	0.19	0.42
8.52	10.13	0.59	6.68	4.62	24.61	5.96	4.96	11.44	0.1	0.08	0.32

Table D.2: Speed of sound estimation using 'homogeneous frozen model' and 'homogeneous equilibrium model' for $u_H = 10$ m/s.

u_0 (m/s)	u_H (m/s)	σ_0	Static Pressure (kPa)			Frozen Model (m/s)			Equilibrium Model (m/s)		
			p_1	p_2	p_3	c_1	c_2	c_3	c_1	c_2	c_3
10.14	12.06	0.72	11.52	11.43	40.19	8.16	8.13	15.25	0.17	0.17	0.49
10.16	12.08	0.65	9.24	8.26	37.12	7.17	6.78	14.38	0.14	0.12	0.46
10.17	12.08	0.85	21.25	20.03	47.11	17.52	17.01	26.08	0.28	0.27	0.56
10.17	12.09	0.71	11.70	12.09	40.37	8.24	8.37	15.30	0.17	0.17	0.49
10.18	12.10	0.65	10.72	8.68	38.06	7.83	7.05	14.76	0.16	0.13	0.47
10.18	12.10	0.65	10.68	9.17	38.04	7.77	7.20	14.67	0.16	0.14	0.47
10.18	12.1	0.53	6.24	4.28	17.29	5.85	4.84	9.74	0.1	0.07	0.24
10.19	12.11	0.54	7.38	5.11	19.26	6.27	5.21	10.13	0.11	0.08	0.26
10.19	12.11	0.53	7.29	4.92	18.28	6.28	5.16	9.95	0.11	0.08	0.25
10.19	12.11	0.60	9.22	7.09	33.59	7.06	6.19	13.47	0.14	0.11	0.42
10.19	12.11	0.71	11.92	12.09	40.42	8.29	8.35	15.27	0.17	0.17	0.49
10.19	12.11	0.77	17.96	16.07	43.45	14.87	14.06	23.12	0.24	0.22	0.52
10.19	12.11	0.59	7.76	5.78	32.91	6.43	5.55	13.24	0.12	0.09	0.41
10.20	12.12	0.60	8.91	6.99	33.00	6.93	6.14	13.33	0.13	0.11	0.41
10.20	12.12	0.77	17.83	16.03	43.61	14.85	14.07	23.22	0.24	0.22	0.53
10.20	12.12	0.75	16.54	14.93	42.87	14.99	14.24	24.13	0.23	0.21	0.52

Table D.3: Speed of sound estimation using 'homogeneous frozen model' and 'homogeneous equilibrium model' for $u_H = 12$ m/s.

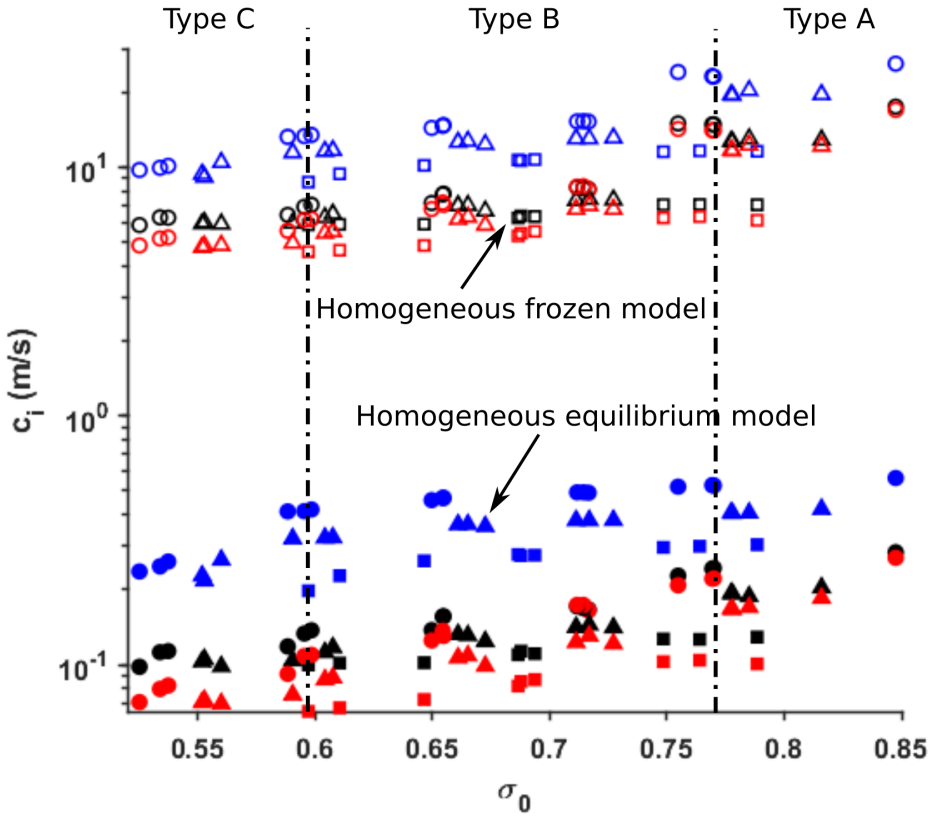

Figure D.1: The variation of c_i with decreasing σ_0 across three different Re estimated using 'homogeneous frozen model' (open symbols) and 'homogeneous equilibrium model' (filled symbols) ; $u_H = 8m/s$ (□□□), $10m/s$ (△△△) & $12m/s$ (○ ○ ○); c_1 (□△○), c_2(□△○) & c_3(□△○).

Appendix E

Measurement of Bubble Size Distribution Downstream of NACA0015 Hydrofoil

A visual snapshot of shedding cavity over the symmetric NACA0015 hydrofoil at $\alpha = 10^{\circ}$ is shown in figure E.1(a). Corresponding schematic of the cavity highlighting different flow features is shown in figure E.1(b).

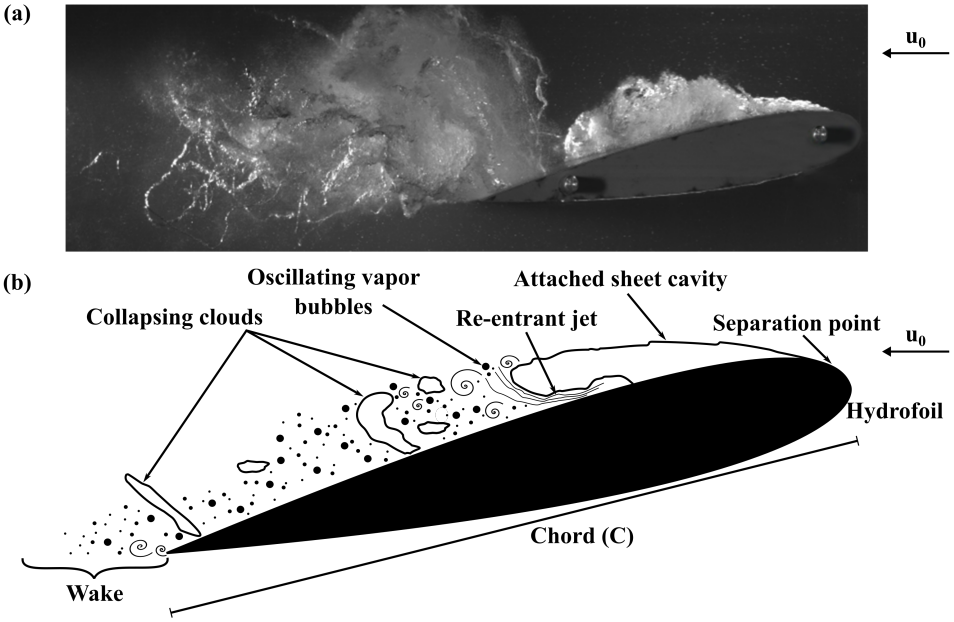

Figure E.1: Cavitation over the symmetric hydrofoil used in current study (a) High speed snapshot showing a typical shedding cavity over the surface of the foil (b) Schematic depicting classical understanding of different flow features (not to scale).

Bubble size and distribution within the cavity can provide information about the extent of homogeneity and sphericity of the vapor phase. The opacity of vapor bubbles and non-uniform reflections make the optical investigation of these vapor bubbles within the cavity very difficult. To mitigate this difficulty bubble size and distribution in the wake of the

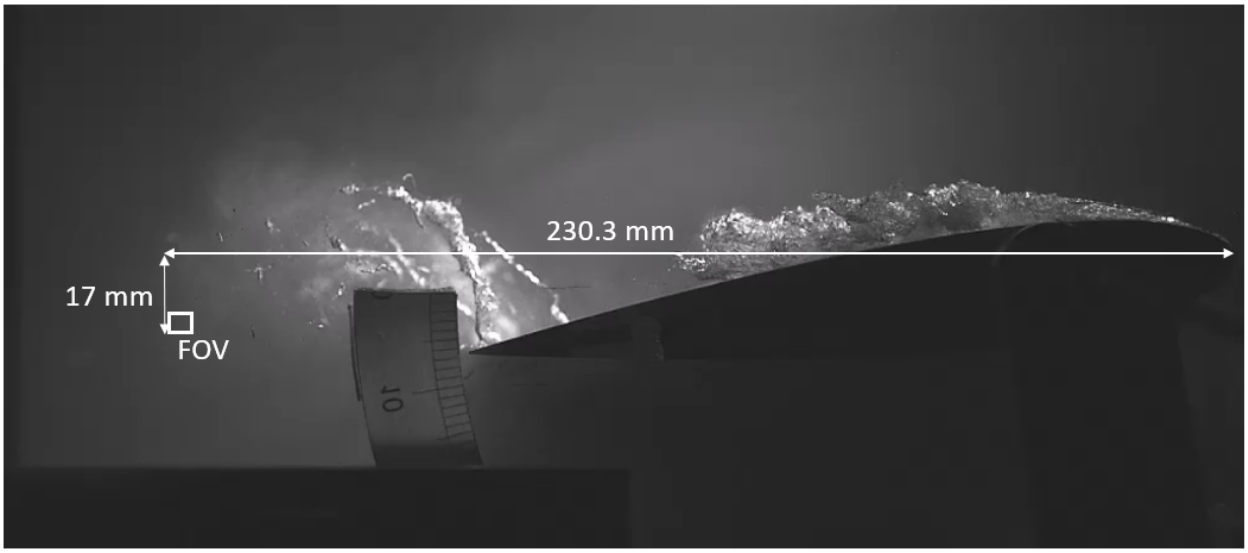

Figure E.2: Questar FOV selected downstream of the cavitating hydrofoil for bubble size and distribution estimations.

hydrofoil are estimated using a Questar microscopic lens with a narrow depth of field. A 1 mm x 1.5 mm FOV was chosen downstream of the foil to acquire high speed snapshots at 13000 frames per second for 0.9 ms exposure time as shown in figure E.2. The FOV has a resolution of 800 x 600 pixels and is calibrated using a 250 μm dot-matrix grid to yield 1 px = 1.8 μm.

The current FOV is selected because by the time vapor bubbles reach the FOV, the pressure has largely normalized and mostly gas bubbles are seen in the FOV. The lighting fluctuations are detrimental to accurately capture the bubble sizes (due to lost frames). It is important to minimize the number of large structures passing through the FOV, hence having the FOV sufficiently far away is desirable. Also, to keep a consistent FOV for shorter cavity lengths ($< 25\%$ chord) as well as longer cavities (upto 85-90% of chord) to minimize the effect of lighting corrections and different of depth of view.

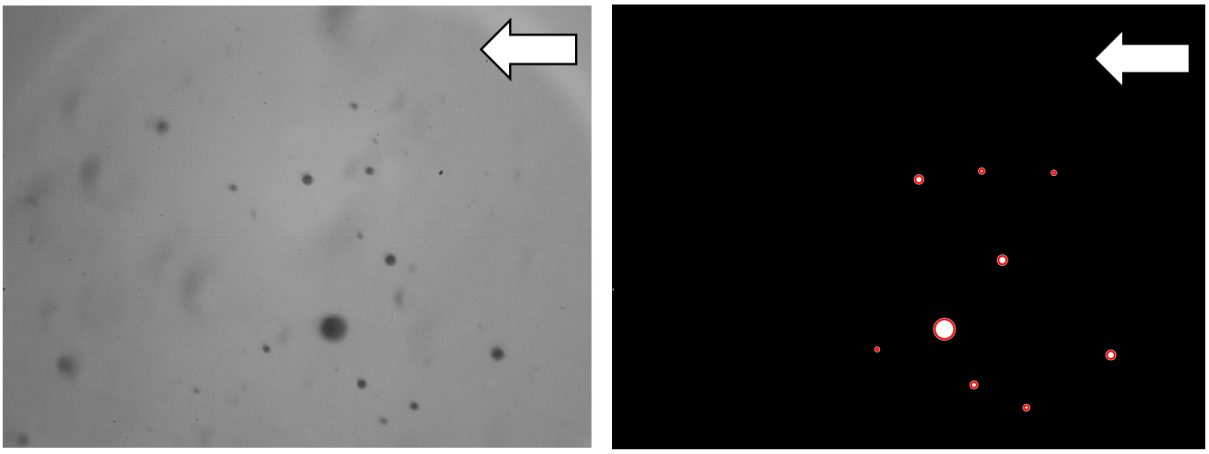

(a) (b)

Figure E.3: Figure depicting the post processing step for each frame of the Questar FOV (a) Raw image captured through the Questar lens (b) Final processed image used for edge detection.

E.1 Post-processing

The high speed snapshots are processed frame by frame. After background subtraction and noise correction, the images are binarized and simple edge detection algorithm is used to estimated size and number of bubbles captured in the field of view. The post processing step is shown in figure E.3.

After processing the bubble size (radii in μm) and distribution for a period of 0.2 s was obtained. The data was appropriately binned and is presented as a histogram of bubble size population. Figure E.4 presents bubble size distribution downstream of two cavities Lc/C = 0.15 and 0.87 respectively for $\alpha = 10°$. Lower the cavitation number, larger the vapor bubble size downstream of the hydrofoil i.e. the larger cavities significantly affect the nuclei content of the cavitating flow.

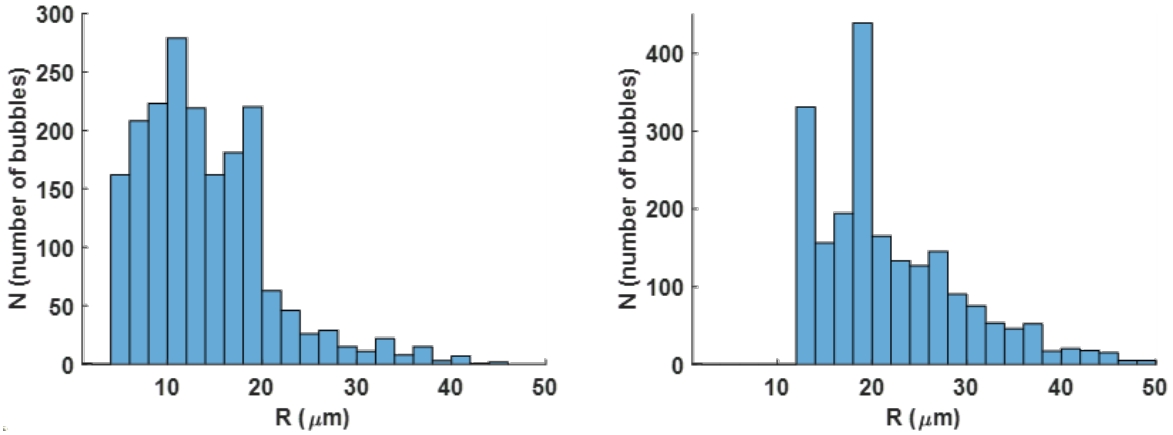

(a) (b)

Figure E.4: Figure depicting the bubble size distribution downstream of the cavity for (a) $\sigma_0 = 2.2$, Lc/C=0.15 (b) $\sigma_0 = 1.6$, Lc/C=0.87. Higher cavitation intensity leads to higher vapor bubble size and concentration downstream of the hydrofoil.

Appendix F

Mean and RMSD β Values for NACA0015 Hydrofoil

The void fraction flow fields ($\beta(X, Y, t)$) for each of the cavity shedding regime can be represented using time averaged flow field called 'mean void fraction fields' and 'root mean square difference(RMSD)' field(variance). They are defined as follows :

$$\beta_{MEAN} = \sum_{N=0}^{786} \frac{\beta(X, Y, N)}{787} \tag{F.1}$$

$$\beta_{RMSD} = \sqrt{\frac{\sum_{N=0}^{786} \left(\beta(X, Y, N) - \beta_{MEAN}\right)^2}{787}} \tag{F.2}$$

All the reported void-fraction values have ≈2% measurement uncertainty associated with them. The mean and RSMD flow fields of each of the cavitation shedding regime are shown in figure F.1.

The maximum void fraction values for different shedding regimes are presented in table F.1.

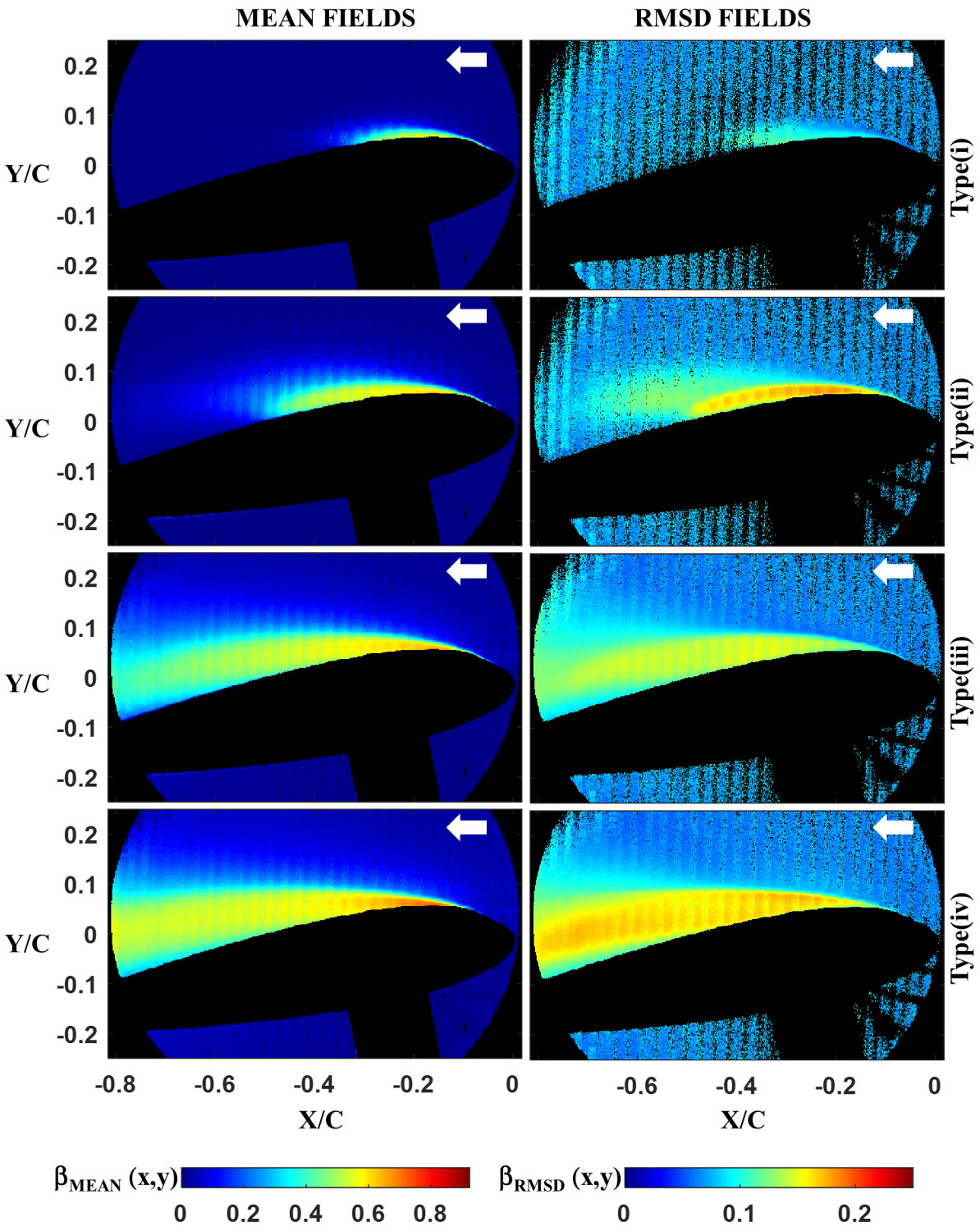

Figure F.1: Mean and RMSD flow fields of the different cavitation shedding regimes. Mean cavity length progressively increases. The striation in RMSD field occurs due to minimum change in measured x-ray intensity across 0.787s.

σ_0	$\sigma_0/2\alpha$	max β_{MEAN}	max β_{RMSD}	Cavity Type
1.43	4.11	0.74	0.17	Type (iv)
1.49	4.27	0.74	0.18	
1.65	4.73	0.72	0.17	
1.73	4.95	0.69	0.22	
1.93	5.52	0.68	0.16	Type(iii)
1.99	5.71	0.71	0.18	
2.18	6.24	0.68	0.18	Type(ii)
2.38	6.82	0.64	0.19	
2.5	7.17	0.7	0.21	
2.65	7.59	0.67	0.19	
2.85	8.17	0.64	0.15	Type(i)
3.04	8.71	0.62	0.14	
3.15	9.03	0.6	0.15	
3.31	9.48	0.55	0.13	Sheet cavity
3.48	9.96	0.5	0.14	or Incipient
3.65	10.45	0.46	0.14	cavity

Table F.1: Max void fraction values in mean and RMSD void fraction filed at $\alpha = 10^\circ$ for different cavitation shedding regimes.

Appendix G

Spectral Content in Cavitating NACA0015 Hydrofoil

G.1 Waterfall Plots for Pressure (dp_1, dp_2) and Void Fraction (β_{LE}, β_{TE}) Signals

Waterfall plots shown in figures G.1 and G.2 illustrate the variation of normalized power spectral densities ($\widehat{PSD}$ is normalized using peak power spectral density values) with change in $\sigma_0/2\alpha$ for $\alpha = 10°$. At higher cavitation number ($\sigma_0 = 3.7$) (steady sheet cavity/beginning of type(i) cavities) the signal strength is comparatively low, which leads to broadband behavior of dynamics detected through transducers. The dominant shedding frequency (St) changes with the reducing $4.2 < \sigma_0/2\alpha < 9.3$. The St for shorter cavities are between 1-2.5. As the cavity length increases and re-entrant flow/shockwaves emerge, the St decreases below 1. This is a consistent observation across all time signals. Emergence of two peaks as the cavity transitions from oscillatory type(i) cavity to shedding type(ii) cavity where both re-entrant flow and shockwaves cause shedding, is observed in the $\sigma_0/2\alpha$ range 6.4-7.8. The normalized PSD content in each peak in St is presented in table G.1. dp_1 and dp_2 signals have a frequency resolution of 0.33 Hz and the β_{LE}, β_{TE} have a frequency resolution of 1.3 Hz.

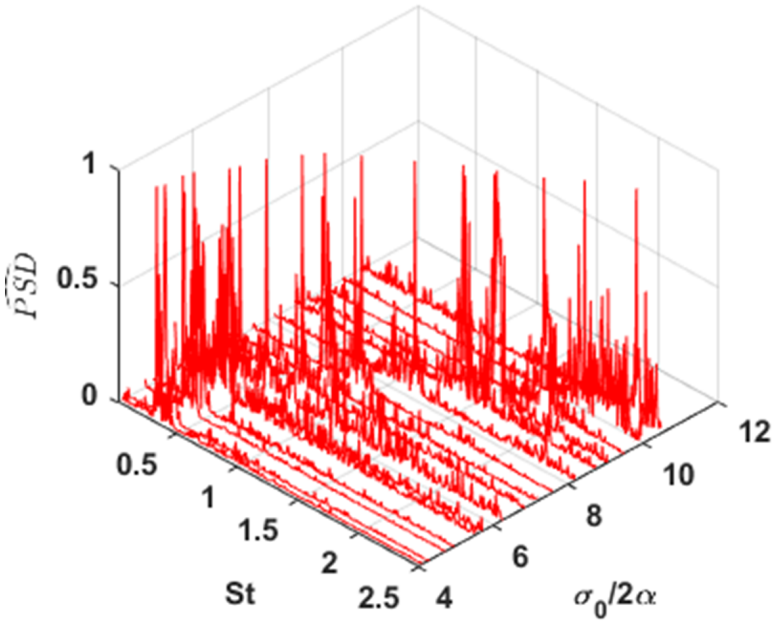

(a) dp_1

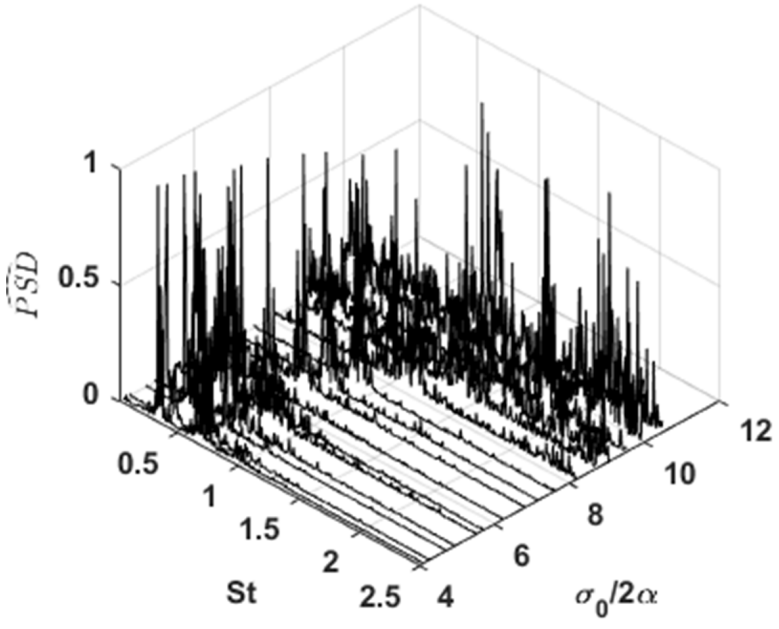

(b) dp_2

Figure G.1: Waterfall plot depicting variation of normalized power spectral density with cavitation parameter ($\sigma_0/2\alpha$), where (a) unsteady surface pressure signal near leading edge (dp_1) (b) unsteady surface pressure signal near trailing edge(dp_2). Presence of two peaks in St for the $\sigma_0/2\alpha$ range between 4 to 8 in signal dp_2. The multiple peaks for type(iv) cavities can be visualized in figure G.3

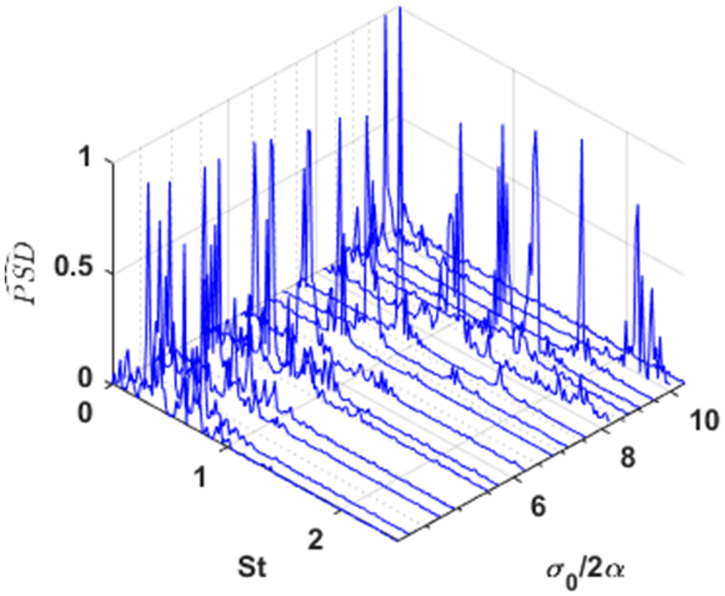

(a) β_{LE}

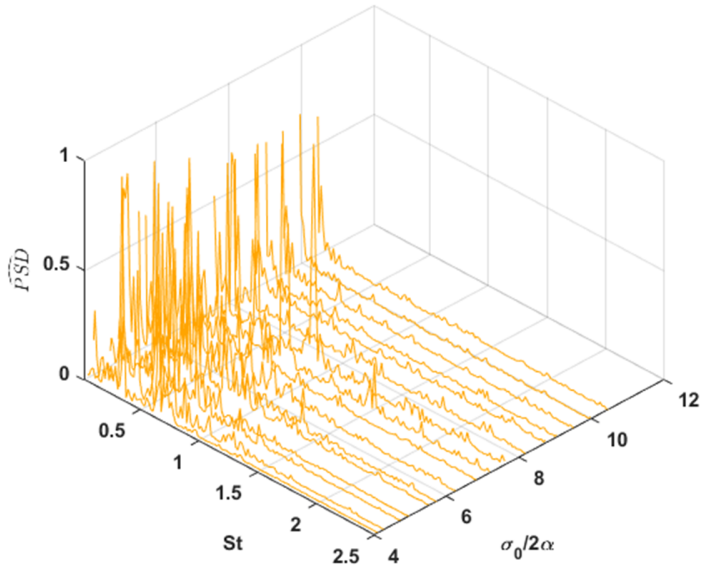

(b) β_{TE}

Figure G.2: Waterfall plot depicting variation of normalized power spectral density with cavitation parameter ($\sigma_0/2\alpha$), where (a) static void fraction probe near dp_1 (β_{LE}) (b) static void fraction probe near dp_2 (β_{TE}). Presence of two peaks in St can be seen in figure G.4

σ_0	$\sigma_0/2\alpha$	St for dp_1				St for dp_2			
		Peak1	$\widehat{PSD}$	Peak2	$\widehat{PSD}$	Peak1	$\widehat{PSD}$	Peak2	$\widehat{PSD}$
1.43	4.09	0.31	1	x		0.31	1	0.64	0.77
1.48	4.25	0.33	1	x		0.34	1	0.65	0.79
1.64	4.69	0.34	1	x		0.34	1	0.69	0.533
1.71	4.91	0.36	1	0.68	0.52	0.36	1	0.68	0.75
1.91	5.48	0.47	1	0.69	0.43	0.50	1	0.75	0.689
1.98	5.66	0.50	1	0.36	0.84	0.50	1	x	
2.17	6.21	0.55	1	1.20	0.82	0.55	1	x	
2.37	6.80	0.67	1	1.24	0.52	0.67	1	x	
2.50	7.16	0.75	1	x		0.75	1	x	
2.65	7.59	0.92	1	x		0.92	1	x	
2.85	8.16	1.18	1	x		1.18	1	x	
3.04	8.70	1.41	1	x		1.42	1	x	
3.15	9.02	1.59	1	x		1.58	1	x	
3.31	9.48	1.84	1	x		1.86	1	x	
3.47	9.95	2.03	1	x		2.22	1	x	
3.65	10.45	2.30	1	x		2.30	1	x	

Table G.1: Table summarizing the change in normalized PSD ($\widehat{PSD}$) for the dominant and secondary peak in St for different σ_0. Only dp_2 sees two peaks for longer type (iv) cavities.

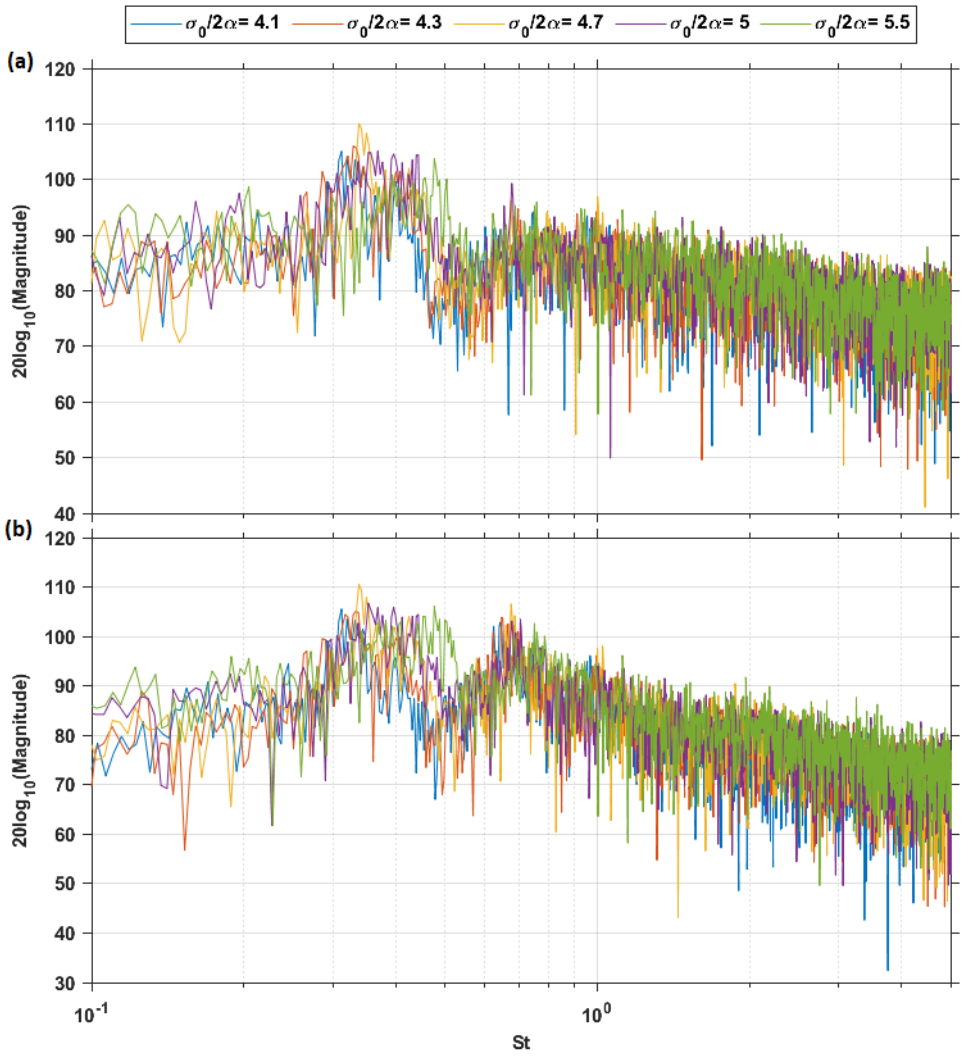

Figure G.3: The variation of St with $\sigma_0/2\alpha$ from surface pressure signals (a) dp_1 (b) dp_2. Two peaks can be seen in the plot for type(iv) and type(iii) cavities.

G.2 Multiple Peaks in type (iii) and (iv) cavities

At lower cavitation numbers ($\sigma_0 = 1.3 - 2.4$) multi-modality (presence of two peaks) as shown in figure G.3 and G.4. The dominant peaks of surface pressure transducers (dp_1 and dp_2) match well with the peaks detected from the void fraction signals (β_{LE} andβ_{TE}).

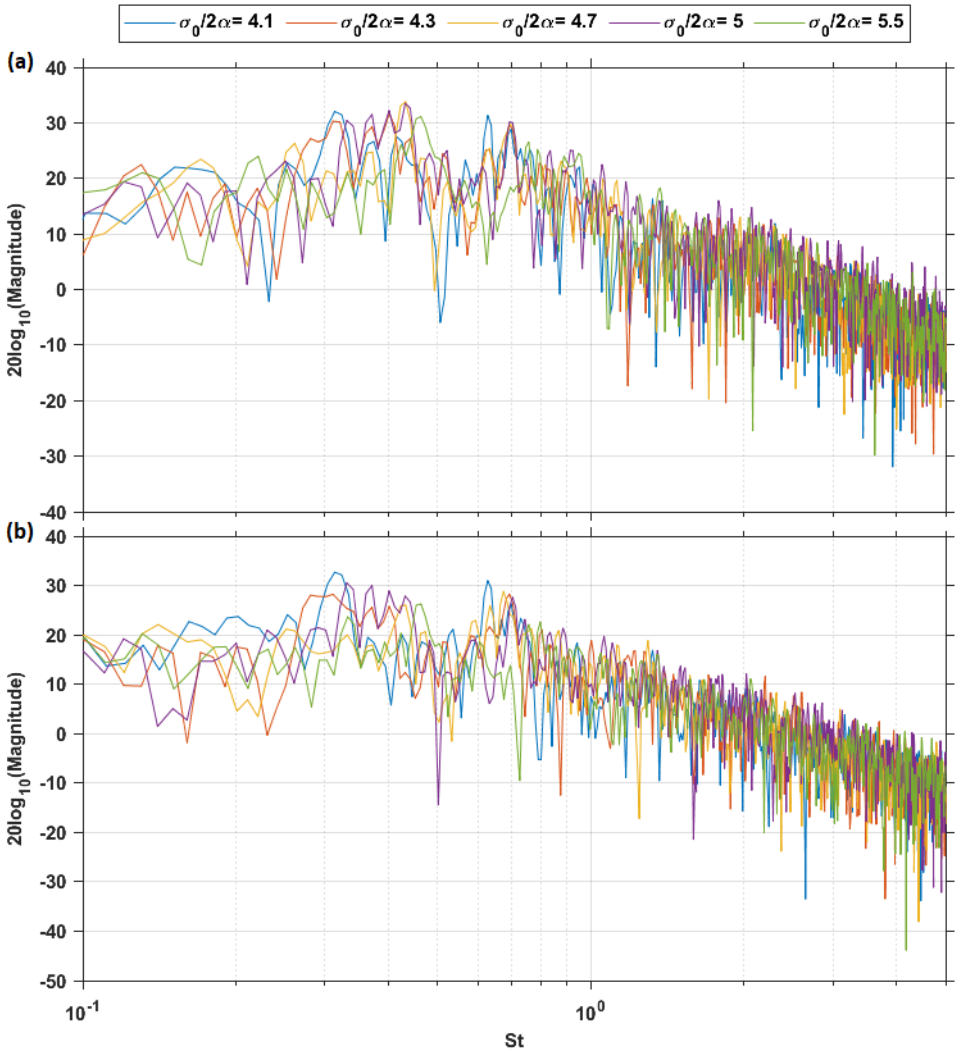

Figure G.4: The variation of St with $\sigma_0/2\alpha$ from surface pressure signals (a) β_{LE} (b) β_{TE}. Two peaks can be seen in the plot for type(iv) and type(iii) cavities.

G.3 Hydrophone signal for type(iv) cavities

The hydrophone monitors the acoustic pressure variations caused by different shedding phenomena with the primary goal to capture the collapse of the cavitation cloud downstream of the foil and correlate to appearance of shockwaves in the system. The peak in hydrophone signal shown in figure 8.20 (7)-(8)

At such low cavitation numbers, the cavity length $Lc/C \geq 0.85$ which makes the surface pressure transducer covered with vapor during most of the shedding cycle. This makes it hard to determine the dominant frequency associated when strong trailing edge cavitation occurs. The interaction between trailing edge cavitation and a shed cloud, shown in figure 8.19, is investigated further by acquiring acoustic pressure through hydrophone.

The power spectral density curves for both surface pressure transducers, void fraction probe near trailing edge defined in figure 9.2, and the hydrophone signal are shown in figure G.5. The hydrophone signal sees a dominant peak at 50 Hz for the type(iv) cavitation, as highlighted in figure G.5(d). This dominant peak appears when the trailing edge cloud cavitation start to occur at $\sigma_0/2\alpha = 6$ as seen in the waterfall plot of hydrophone signal in figure G.6. The mode associated with this 50 Hz peak frequency can be visualized by performing SPOD on the time resolved void fraction data as shown in figure G.7. The closest resolved frequency is 48 Hz which corresponds to the lobe cavitation described in figure 8.19.

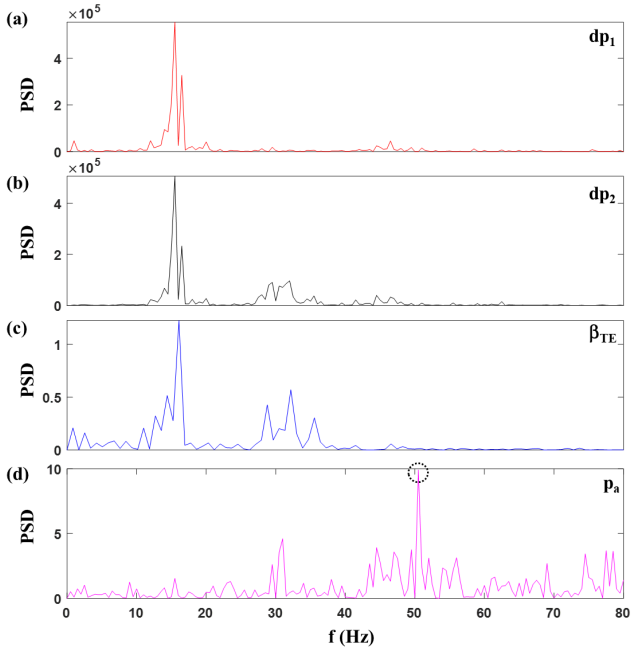

Figure G.5: PSD plots of transducer signals (a) dp_1 and (b) dp_2 along with void fraction signal (c) and acoustic pressure power spectral density (PSD) from hydrophone (d). The peak frequency 50Hz is not seen on either of the transducers. σ_0 =1.5 ($\sigma_0/2\alpha = 4.3$)

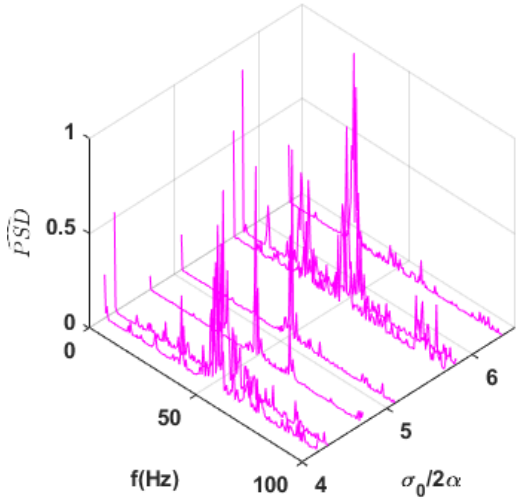

Figure G.6: Waterfall plot showing PSD from hydrophone signal. The TE cavitation occurs as early as $\sigma_0/2\alpha = 6$ and becomes a dominant shedding flow feature for type(iv) cavities. The 50Hz peak is explored further using SPOD.

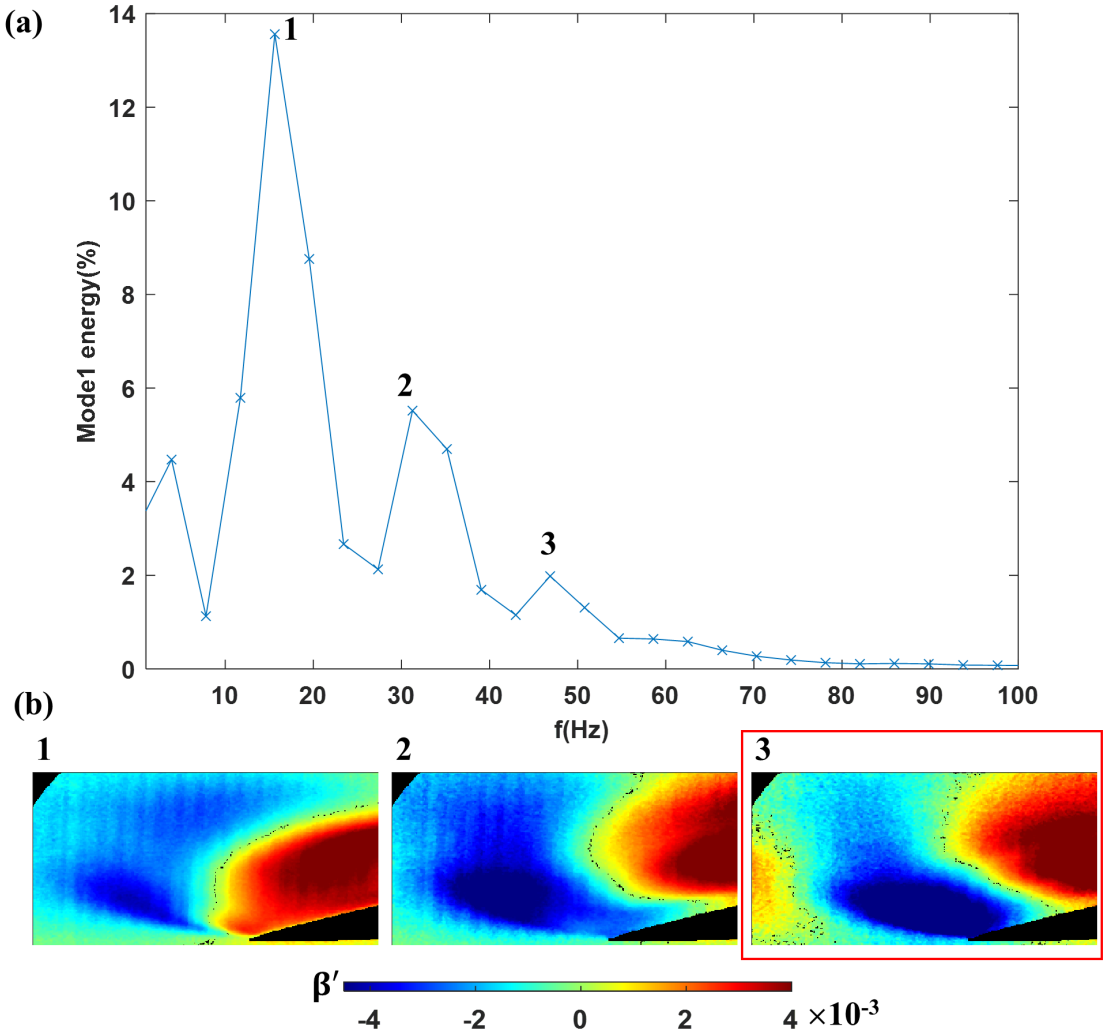

Figure G.7: Resolved frequencies and the model energy (%) at each frequency (a) Three peaks in the resolved frequency, with 15 Hz mode having the highest energy (b) The 48Hz mode is closet to 50Hz peak seen on the hydrophone and is the alternating lobe cavitation shown in figure 8.19. σ_0 =1.5 ($\sigma_0/2\alpha = 4.3$)

Bibliography

Aeschlimann, V., Barre, S., and Legoupil, S. (2011). X-ray attenuation measurements in a cavitating mixing layer for instantaneous two-dimensional void ratio determination. *Physics of Fluids*, 23(5):055101.

Agarwal, K., Ram, O., and Katz, J. (2018). Cavitating structures at inception in turbulent shear flow. In *Proceedings for 10th International Symposium on Cavitation*.

Arndt, R. E. (2012). Some remarks on hydrofoil cavitation. *Journal of Hydrodynamics, Ser. B*, 24(3):305–314.

Arndt, R. E., Song, C., Kjeldsen, M., He, J., and Keller, A. (2000). Instability of partial cavitation: a numerical/experimental approach.

Barwey, S., Ganesh, H., Hassanaly, M., Raman, V., and Ceccio, S. (2020). Data-based analysis of multimodal partial cavity shedding dynamics. *Experiments in Fluids*, 61(4):1–21.

Belahadji, B., Franc, J.-P., and Michel, J.-M. (1995). Cavitation in the rotational structures of a turbulent wake. *Journal of Fluid Mechanics*, 287:383–403.

Bhatt, A., Ganesh, H., and Ceccio, S. (2021). Cavitating flow behind a backward facing step. *International Journal of Multiphase Flow*, 139:103584.

Bhatt, M. and Mahesh, K. (2020). Numerical investigation of partial cavitation regimes

over a wedge using large eddy simulation. *International Journal of Multiphase Flow*, 122:103155.

Billet, M. and Holl, J. (1981a). Scale effects on various types of limited cavitation. *J. Fluids Eng.*, 103(3).

Billet, M. L. and Holl, J. W. (1981b). Scale Effects on Various Types of Limited Cavitation. *Journal of Fluids Engineering*, 103(3):405–414.

Bradshaw, P. and Wong, F. (1972). The reattachment and relaxation of a turbulent shear layer. *Journal of Fluid Mechanics*, 52(1):113–135.

Brennen, C. E. (2005). *Fundamentals of multiphase flow*. Cambridge university press.

Budich, B., Schmidt, S., and Adams, N. A. (2018). Numerical simulation and analysis of condensation shocks in cavitating flow. *Journal of Fluid Mechanics*, 838:759–813.

Callenaere, M., Franc, J.-P., Michel, J.-M., and Riondet, M. (2001). The cavitation instability induced by the development of a re-entrant jet. *Journal of Fluid Mechanics*, 444:223–256.

Crespo, A. (1969). Sound and shock waves in liquids containing bubbles. *The Physics of Fluids*, 12(11):2274–2282.

Eaton, J. and Johnston, J. (1981). A review of research on subsonic turbulent flow reattachment. *AIAA journal*, 19(9):1093–1100.

Franc, J.-P. and Michel, J.-M. (1983). Two-dimensional rotational structures in the cavitating turbulent wake of a wedge.

Ganesh, H. (2015). *Bubbly Shock Propagation as a Cause of Sheet to Cloud Transition of Partial Cavitation and Stationary Cavitation Bubbles Forming on a Delta Wing Vortex.* PhD thesis.

Ganesh, H., Mäkiharju, S. A., and Ceccio, S. L. (2016). Bubbly shock propagation as a mechanism for sheet-to-cloud transition of partial cavities. *Journal of Fluid Mechanics*, 802:37–78.

Hubbell, J. and Seltzer, S. M. (2004). Cross section data for electron–positron pair production by photons: a status report. *Nuclear Instruments and Methods in Physics Research Section B: Beam Interactions with Materials and Atoms*, 213:1–9.

Iyer, C. O. and Ceccio, S. L. (2002). The influence of developed cavitation on the flow of a turbulent shear layer. *Physics of fluids*, 14(10):3414–3431.

Jovic, S. and Driver, D. (1995). Reynolds number effect on the skin friction in separated flows behind a backward-facing step. *Experiments in Fluids*, 18(6):464–467.

Katz, J. and O'hern, T. (1986). Cavitation in large scale shear flows.

Kjeldsen, M., Arndt, R. E., and Effertz, M. (2000). Spectral characteristics of sheet/cloud cavitation. *J. Fluids Eng.*, 122(3):481–487.

Le, Q., Franc, J.-P., and Michel, J.-M. (1993). Partial cavities: global behavior and mean pressure distribution.

Makiharju, S. A. (2012). *The Dynamics of Ventilated Partial Cavities over a Wide Range of Reynolds Numbers and Quantitative Two-Dimensional X-ray Densitometry for Multiphase Flow*. PhD thesis, University of Michigan.

Mäkiharju, S. A., Gabillet, C., Paik, B.-G., Chang, N. A., Perlin, M., and Ceccio, S. L. (2013). Time-resolved two-dimensional x-ray densitometry of a two-phase flow downstream of a ventilated cavity. *Experiments in fluids*, 54(7):1561.

O'hern, T. (1990). An experimental investigation of turbulent shear flow cavitation. *Journal of fluid mechanics*, 215:365–391.

Scarano, F., Benocci, C., and Riethmuller, M. (1999). Pattern recognition analysis of the turbulent flow past a backward facing step. *Physics of Fluids*, 11(12):3808–3818.

Schmidt, O. T. and Colonius, T. (2020). Guide to spectral proper orthogonal decomposition. *Aiaa journal*, 58(3):1023–1033.

Troutt, T., Scheelke, B., and Norman, T. (1984). Organized structures in a reattaching separated flow field. *Journal of Fluid Mechanics*, 143:413–427.

Wade, R. and Acosta, A. (1966). Experimental observations on the flow past a plano-convex hydrofoil.

Watanabe, S. (1998). Linear analyses of cavitation instabilities. In *Proceedings, 3rd Int. Symp. on Cavitation*, volume 1, page 347.

Wu, J. (2019). *Bubbly Shocks in Separated Cavitating Flows*. PhD thesis.

Wu, J., Deijlen, L., Bhatt, A., Ganesh, H., and Ceccio, S. L. (2021). Cavitation dynamics and vortex shedding in the wake of a bluff body. *Journal of Fluid Mechanics*, 917.

Wu, J., Ganesh, H., and Ceccio, S. (2019). Multimodal partial cavity shedding on a two-dimensional hydrofoil and its relation to the presence of bubbly shocks. *Experiments in Fluids*, 60(4):66.

Young, J. and Holl, J. W. (1966). Effects of cavitation on periodic wakes behind symmetric wedges.